technische universität
dortmund

Acceptance tests of PMTs for the mDOM of the IceCube Upgrade

Dissertation zum Erlangen des Grades
Dr. rer. nat.

von
Johannes Werthebach
geboren in Siegen

2025

Lehrstuhl für Experimentelle Physik V
Fakultät Physik
Technische Universität Dortmund

Erstgutachter:	Prof. Dr. Dr. W. Rhode
Zweitgutachter:	Prof. Dr. Julia Tjus
Abgabedatum:	June 25, 2026

Acknowledgments

I want to thank Lasse Halve, who designed and built the first testing facility at RWTH Aachen University. Without his support, this thesis would not have been possible.

Some of the results presented in this thesis have already been published in a paper co-authored by Lasse Halve and me [1], as well as in the ICRC2021 proceedings [2]. I want to clarify that no text blocks or figures from these publications are directly included in this work.

Additionally, I utilized the TU Dortmund Campus-KI as a formulation aid and to structur my text. For spell checking and grammar corrections, I relied on the Pro version of Grammarly. I have thoroughly verified all content myself and take full responsibility for the integrity of this work.

[1]: Abbasi et al. (2024), "Acceptance Tests of More than 10 000 Photomultiplier Tubes for the Multi-PMT Digital Optical Modules of the IceCube Upgrade"
[2]: Halve et al. (2021), "Design of an Efficient, High-Throughput Photomultiplier Tube Testing Facility for the IceCube Upgrade"

Kurzfassung

IceCube ist das bislang größte Neutrinoteleskop und besteht aus 5160 Digital Optical Modules (DOMs), die in einer Tiefe von bis zu 2450 m im Eis am geografischen Südpol eingefroren sind. Das IceCube Upgrade ist für die Feldsaison 2025/26 geplant. Im Rahmen dieses Upgrades werden etwa 700 neue optische Sensormodule, darunter Kalibrier- und Testmodule, im Zentrum des bestehenden IceCube-Detektors installiert. Eine dieser neuen Entwicklungen ist das Multi-PMT Digital Optical Module (mDOM), das 24 Photomultiplier tubes (PMTs) pro Modul kombiniert.

Die PMTs sind die primären Detektionseinheiten in IceCube und müssen vor ihrem Einbau getestet werden. Im Zuge der Messkampagne wurden über 10 000 PMTs an zwei Standorten getestet. Während der Tests wurde bei fast allen Einheiten eine deutlich höhere Dunkelrate als gefordert festgestellt. Diese Abweichung konnte auf eine erhöhte Kontamination durch radioaktive Isotope in der Glasummantelung der PMTs zurückgeführt werden.

Im Rahmen dieser Arbeit wurde ein Teststand entwickelt, konstruiert und in Betrieb genommen, um Massentests der PMTs zu ermöglichen. Das Design mit seinen einzelnen Komponenten, die Messverfahren, die Herausforderungen bei der Inbetriebnahme des Aufbaus in Dortmund sowie die Testergebnisse der PMTs werden vorgestellt.

Abstract

IceCube is the largest neutrino telescope to date and consists of 5160 Digital Optical Modules (DOMs) embedded up to 2450 m deep within the ice at the geographic South Pole. The IceCube Upgrade is scheduled for installation during the 2025/26 field season. During the upgrade, approximately 700 new optical sensor modules, including calibration and test devices, will be installed at the center of the existing IceCube detector to enhance detection capabilities and improve precision measurements. One of these new designs is the Multi-PMT Digital Optical Module (mDOM) combining 24 photomultiplier tubes (PMTs) per module.

As PMTs serve as the primary detection units in IceCube, testing is required to ensure their performance meets specifications. Over 10 000 PMTs were tested at two independent sites during this campaign. A significantly higher dark rate than specified was identified in almost all units during testing. This discrepancy was traced back to elevated contamination levels of radioactive isotopes in the glass envelope of the PMTs.

In this work, a test bench was developed, constructed, and commissioned to facilitate large-scale PMT testing. The design, procedures, challenges, and results are presented.

Contents

Fundamentals 1

1 Neutrino Astronomy 3
- 1.1 Neutrino Properties . . . 4
- 1.2 Cosmic Rays . . . 7
- 1.3 Multi-Messenger Astronomy . . . 12

2 Large Volume Neutrino Telescopes: The IceCube Observatory 15
- 2.1 Operation Principle . . . 15
- 2.2 The IceCube Neutrino Observatory . . . 19

3 Photomultiplier Tube 35
- 3.1 Photoelectric Effect . . . 36
- 3.2 Secondary Emission Multipliers (Dynodes) . . . 38
- 3.3 PMT Characteristics . . . 39

mDOM PMT and Acceptance Testing 49

4 IceCube Upgrade mDOM and PMT 51
- 4.1 mDOM . . . 52
- 4.2 The mDOM PMT . . . 54

5 The mDOM PMT Test Bench 61
- 5.1 Design . . . 62
- 5.2 Implementation at the TU Dortmund University . . . 67
- 5.3 Calibration . . . 80
- 5.4 A Complete Testing Cycle . . . 92
- 5.5 The Measurements . . . 95

6 Results 119
- 6.1 Technical Challenges of the Test Bench . . . 119
- 6.2 Summary of PMT Testing Results and Voltage Classifications . . . 122
- 6.3 Key Findings from PMT Testing . . . 124

6.4 Stability and Channel Dependency of the Results 129
6.5 Comparison with Aachen and Hamamatsu 136

7 Resume and Outlook **141**

Appendix **145**

A Results of Single Measurements **147**

B Estimation of the Measurement Precision **173**

Bibliography **181**

Fundamentals

1 Neutrino Astronomy

Contents

1.1 Neutrino Properties **4**

1.2 Cosmic Rays **7**

1.3 Multi-Messenger Astronomy **12**

Astronomy is one of the oldest sciences of humankind. Ancient societies all around the world aligned stone circles and buildings with stars and the Sun. These early calendars were essential for the development of society, predicting the seasons, legitimizing power, and, as religious sites, bringing communities closer to their gods [3]. Since the currently oldest known astronomical site, Nabat Playa, was built more than 7000 years ago in Egypt [4], astronomy in visible light has proven to be a valuable resource for gaining insight into our universe. Roughly a century ago, Viktor Hess discovered a constant bombardment of charged particles, called cosmic rays (CR), opening a whole new window to our universe [5]. The chemical composition of stars was discovered shortly after in 1926 by Cecilia Payne [6]. In 1968, Jocelyn Bell discovered the first "scruff" leading towards the discovery of pulsars [7]. The electromagnetic spectrum of extraterrestrial sources has been and continues to be used as a robust tool to study astronomy. In recent years, new observations outside the electromagnetic spectrum have flourished. IceCube detected the first high-energy cosmic neutrino in 2013 [8] and in 2015 the merging of two black holes was observed by LIGO and VIRGO [9]. Multi-messenger astronomy studies our universe by utilizing combined information from various messengers, such as electromagnetic waves, gravitational waves, and neutrinos.

[3]: Darvill (2022), "Keeping Time at Stonehenge"
[4]: McKim Malville (2015), "Astronomy at Nabta Playa, Southern Egypt"
[5]: Hess (1912), "Über Beobachtungen Der Durchdringenden Strahlung Bei Sieben Freiballonfahrten"
[6]: Payne-Gaposchkin (1925), "Stellar Atmospheres"
[7]: Hewish et al. (1968), "Observation of a Rapidly Pulsating Radio Source"
[8]: Aartsen et al. (2013), "Evidence for High-Energy Extraterrestrial Neutrinos at the IceCube Detector"
[9]: Abbott et al. (2016), "Observation of Gravitational Waves from a Binary Black Hole Merger"

Section 1.1 investigates the properties of neutrinos, covering their oscillations and interactions with matter. A short introduction to cosmic rays (CRs) focuses on their acceleration mechanisms and sources as well as their interaction with the atmosphere in section 1.2. The last section 1.3 connects neutrinos, CRs, and the electromagnetic spectrum into multi-messenger astronomy.

1.1 Neutrino Properties

A neutrino is an elementary particle in the Standard Model of particle physics, only interacting through weak interaction and gravity [10]. It is characterized by a neutral electrical charge, a spin of $1/2$, and a tiny mass of $< 0.120\,\mathrm{eV}$ [11]. The gravitational interaction is neglected in the framework of particle physics due to the neutrinos' tiny mass. Additionally, neutrinos neither participate in the electromagnetic nor the strong interaction. As a result, neutrinos only interact via the weak force and usually travel through ordinary matter without being absorbed or deflected, remaining hard to detect [10].

Neutrino Oscillations

Neutrinos are produced and again projected onto flavor eigenstates $|\nu_\alpha\rangle$, with $\alpha = e, \mu, \tau$ through weak interactions associated with the respective charged lepton. However, the flavor eigenstates are superpositions of the mass eigenstates of neutrinos, which themselves are stationary solutions of the Hamiltonian for a free particle H. The time evolution of the Schrödinger equation gives the propagation in space,

$$H\,|\Psi\rangle = i\frac{\delta\,|\Psi\rangle}{\delta t} = E\,|\Psi\rangle\,, \tag{1.1}$$

where Ψ is the eigenstate of the Hamiltonian and E, the eigenvalue, the energy of the particle. The distinction between the three eigenstates is visualized in Figure 1.1.

When neutrinos propagate, their mass eigenstates evolve at different frequencies, leading to a phase difference due to the different masses of the eigenstates.

[10]: Close (2012), *Neutrino*
[11]: Giaré et al. (2022), "Cosmological Forecasts on Thermal Axions, Relic Neutrinos and Light Elements"

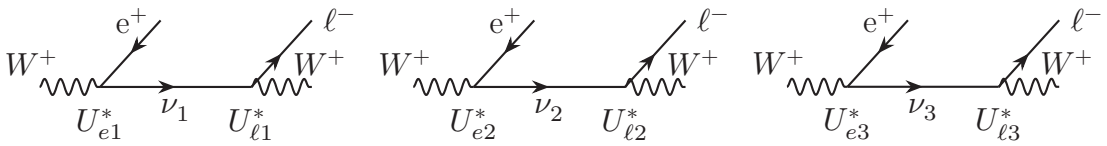

Figure 1.1: Visualization of the superposition of mass eigenstates.

$$\Delta m_{ij}^2 = m_i^2 - m_j^2. \tag{1.2}$$

The relation between mass eigenstates and flavor eigenstates is described by a unitary matrix, which is called the Pontecorvo–Maki–Nakagawa–Sakata (PMNS) matrix. Consisting of 18 initial parameters, the PMNS reduces to three absolute mixing angles θ_{ij} and one complex phase δ when applied to neutrino oscillations.

$$U_{\text{PMNS}} = \begin{pmatrix} 1 & 0 & 0 \\ 0 & c_{23} & s_{23} \\ 0 & -s_{23} & c_{23} \end{pmatrix} \begin{pmatrix} c_{13} & 0 & s_{13}e^{-i\delta} \\ 0 & 1 & 0 \\ -s_{13}e^{-i\delta} & 0 & c_{13} \end{pmatrix} \begin{pmatrix} c_{12} & s_{12} & 0 \\ -s_{12} & c_{12} & 0 \\ 0 & 0 & 1 \end{pmatrix} \tag{1.3}$$
$$c_{ij} = \cos\theta_{ij} \text{ and } s_{ij} = \sin\theta_{ij}$$

When a neutrino is generated through weak interaction, it exists as a superposition of three distinct mass eigenstates $|\Psi\rangle = \sum_{i=1}^{3} U_{ei}^* |\nu_i\rangle$. Each state has a slightly different mass m_i, leading to distinct phase accumulation rates as the neutrino travels, which causes the superposition to evolve. The oscillation between mass and flavor eigenstates implies that the likelihood of observing a neutrino in a different flavor state depends on the mass-splitting parameters Δm_{ji}^2. Observation of this flavour-changing oscillation confirms the presence of at least two non-zero mass eigenstates with different masses [12].

When neutrinos travel through matter, an additional potential V is added to the Hamiltonian $H = H_0 + V$ in equation (1.1), induced mainly due to interactions with electrons. This leads to a different effective mass of the neutrino mass eigenstates and, in turn, to different oscillation dynamics due to changed mass-splitting parameters Δm_{ji}^2. This phenomenon, which is known as the Mikheyev–Smirnov–Wolfenstein (MSW) effect, arises from an additional effective potential present in dense environments like the Sun. It, therefore, enhances oscillation probabilities under

[12]: Spurio (2018), "Low-Energy Neutrino Physics and Astrophysics"

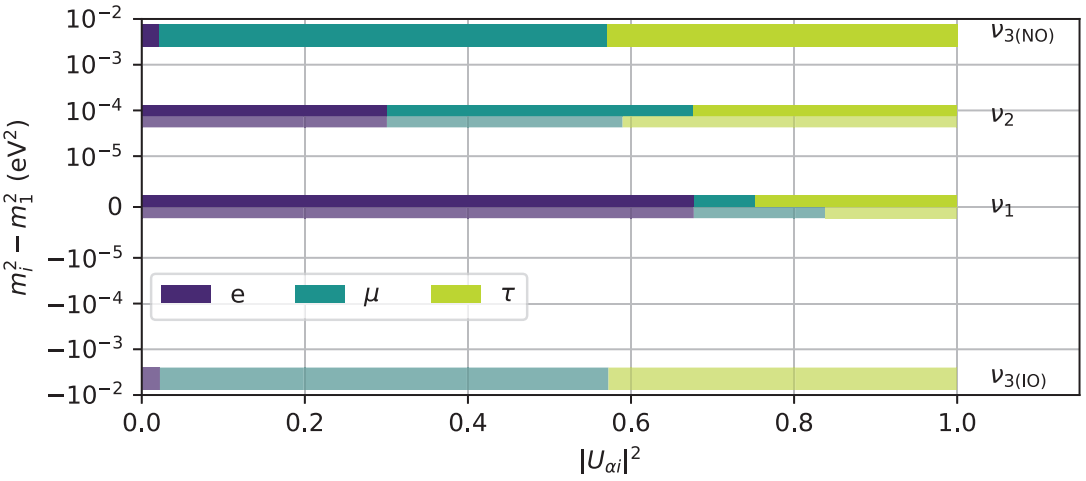

Figure 1.2: Neutrino mass ordering relative to m_1^2 in the normal (NO) and inverted (IO) order (y-axis). The x-axis depicts the superposition of the flavor eigenstates α in one mass eigenstate i $|\Psi\rangle = \sum_{i=1}^{3} U_{\alpha i}^* |\nu_\alpha\rangle$. Colours indicate the contribution of each flavour eigenstate towards the mass eigenstate. Values for the plot are taken from [13].

certain conditions [14]. Experimental observations strengthen the fundamental properties of neutrino oscillations. Solar neutrino experiments, for instance, have shown that $\Delta m_{21}^2 > 0$, which provides insight into the mass hierarchy. However, the sign of Δm_{31}^2 remains unknown, leaving the absolute ordering of neutrino masses undetermined [15].

The current best values for the neutrino mass hierarchy and the contributions of each flavor state are visualized in Figure 1.2. Since only a limited subset of PMNS matrix parameters can be measured in a single oscillation experiment, oscillations alone cannot determine the absolute neutrino masses. The KATRIN experiment aims to measure the absolute mass of the electron antineutrino, providing an upper limit of less than $0.8\,\mathrm{eV/c^2}$ [16]. Notably, this indicates that neutrinos possess a non-zero mass beyond the scope of Einstein-Cartan torsion, requiring an adjustment to the Standard Model of particle physics [10].

[14]: Giunti (2007), "Neutrino Oscillations In Matter"
[15]: Esteban et al. (2020), "The Fate of Hints"
[16]: The KATRIN Collaboration et al. (2022), "Direct Neutrino-Mass Measurement with Sub-Electronvolt Sensitivity"
[10]: Close (2012), *Neutrino*

High Energy Neutrino Interactions with Matter

Neutrinos interact only through the weak force, which is mediated by Z and W bosons. At energies relevant to neutrino astronomy, neutrinos undergo deep-inelastic scattering with nucleons via these bosons. These scattering processes are distinguished by the boson that mediates the interaction: Neutral current interactions, mediated by neutral Z bosons, alter the neutrino's path without changing its quantum properties. In Charged current interactions, neutrinos interact with matter and charged leptons ($e, \mu,$ or τ) are produced mediated by charged W bosons, transferring electric charge in the process. In both cases, the interaction results in a hadronic shower when nucleons break up [17]. The two different modes of deep-inelastic scattering are depicted in Figure 1.3, where X labels the resulting hadronic shower.

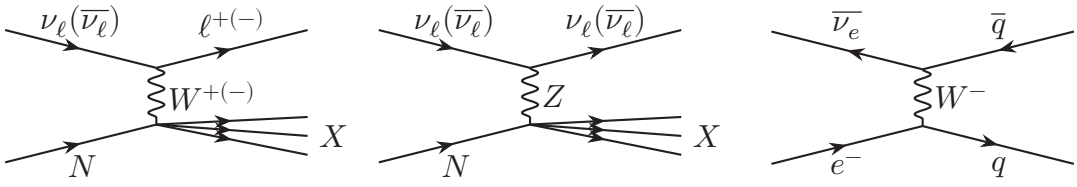

(a) Charged current interaction **(b)** Neutral current interaction **(c)** Glashow resonance

Figure 1.3: The different modes of deep-inelastic scattering of neutrinos with nuclei.

A third interaction becomes relevant at even higher neutrino energies. If the center-of-mass energy $\sqrt{s}$ is equal to the mass of the W^- boson $m_{W-} = 80.38\,\text{GeV}$, the interaction of an electron antineutrino with an electron is resonantly enhanced. This phenomenon is known as the Glashow resonance [18] and results in a resonant neutrino energy of $E_{\overline{\nu}_e R} \approx M_W^2/(2m_e) \sim 6.3\,\text{PeV}$ [19].

1.2 Cosmic Rays

Particles originating from outer space with high energies are summarised under the term cosmic rays (CRs). CRs predominantly comprise ionized nuclei, about 90%

[17]: Vannucci (2017), "Interactions of Neutrinos with Matter"
[18]: Glashow (1960), "Resonant Scattering of Antineutrinos"
[19]: Aartsen et al. (2021), "IceCube-Gen2: The Window to the Extreme Universe"

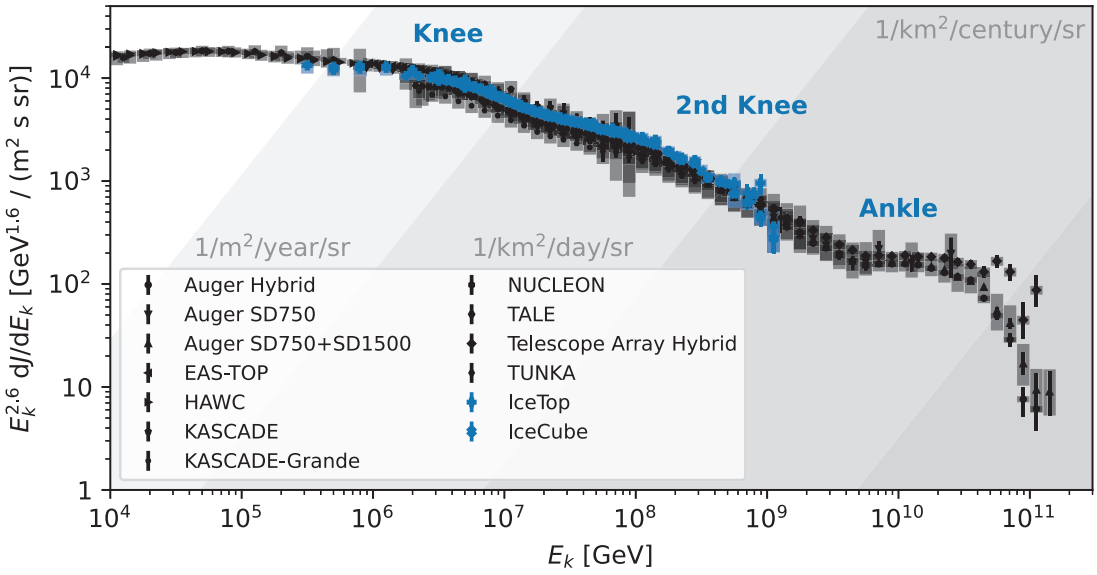

Figure 1.4: Cosmic ray spectrum basen on the data from the Cosmic-Ray Data Base [20]. To highlight the characteristics of the differential energy spectrum, it was multiplied by $E^{2.6}$.

protons, about 9% alpha particles, and roughly 1% heavier nuclei, but also include a small electron component. These proportions can fluctuate significantly, which depends on the energy inherent to the CRs. A tiny fraction of CRs consist of stable antimatter particles, such as positrons or antiprotons, with ongoing research seeking to clarify this remainder [21].

These particles travel close to the speed of light and, therefore, possess high energies, extending from about 10^9 eV to more than 10^{20} eV. A general distinction is made between primary and secondary CRs. While primary CRs originate in outer space, secondary CRs are produced in the Earth's atmosphere [22].

The spectrum of the primary charged CR flux above 10 TeV is illustrated in Figure 1.4. The spectrum of non-thermal particles can be described by power laws of the form $A \cdot E^{-\alpha}$. For particularly steep fluxes, like the CR flux, the y-axis is often weighted by a power of energy E^{β}, where a straight line represents a power law on a double-logarithmic plot. [23, p. 11].

[21]: Supanitsky (2022), "Determination of the Cosmic-Ray Chemical Composition"
[22]: De Angelis (2023), "The Highest Energies in the Universe"
[23]: Spurio (2018), *Probes of Multimessenger Astrophysics*

Up to approximately 1 PeV, the spectral index is $\alpha \approx 2.7$ until the so-called knee, where the flux steepens to $\alpha \approx 3.1$. This change in spectral index is correlated with the reduced flux from galactic sources, which reach their acceleration limit [24, p. 525]. A further steepening occurs around 10^8 GeV, at the second knee, with $\alpha \approx 3.3$. The region between the first and second knee represents the acceleration limit of the individual components of CRs. It is assumed that the maximum achievable energy of a particle depends on its charge Z. Initially, the contribution of protons decreases, and at the second knee, the acceleration limit of iron ions in galactic sources is reached. At 5×10^9 GeV, the spectrum flattens at a feature known as the ankle, where the flux hardens to $\alpha \approx 2.6$. The ankle is generally linked to the emergence of CRs from extragalactic sources [25, p. 12]. At energies exceeding $\sim 7 \times 10^{10}$ GeV, CR propagation over extragalactic distances is expected to be suppressed due to inelastic interactions with the cosmic microwave background (CMB), a phenomenon known as the Greisen-Zatsepin-Kuzmin (GZK) effect [26].

Ongoing experiments have steadily improved our understanding of CR origins. In 2009, researchers from the Pierre Auger Observatory in Argentina announced at the International Cosmic Ray Conference (ICRC) that they had detected ultra-high-energy CRs coming from the surroundings of the radio galaxy Centaurus A. A lack of correlation between gamma-ray bursts and CRs led to an upper limit being set on the flux of CRs from gamma-ray bursts in the range of 1 GeV to 1 TeV, with a flux limit as low as 3.4×10^{-6} erg/cm^2 [27]. Observational data from the Very Large Telescope (VLT) identified supernovae as a CR source, with each event releasing approximately 3×10^{42} J to 3×10^{43} J in CRs. However, further investigation showed that the spectra of hydrogen and helium nuclei do not fit a single power law, indicating a more complex formation process and leaving the precise contribution of supernovae unresolved [28, 29].

[24]: Workman et al. (2022), "Review of Particle Physics"
[25]: Gaisser et al. (2016), *Cosmic Rays and Particle Physics*
[26]: Spurio (2018), "The Extragalactic Sources and Ultra High Energy Cosmic Rays"
[27]: Abreu et al. (2010), "Update on the Correlation of the Highest Energy Cosmic Rays with Nearby Extragalactic Matter"
[28]: Adriani et al. (2013), "Measurements of Cosmic-Ray Proton and Helium Spectra with the PAMELA Calorimeter"
[29]: Ackermann et al. (2013), "Detection of the Characteristic Pion-Decay Signature in Supernova Remnants"

Acceleration Mechanisms and CR Sources

Diffuse shock acceleration (DSA) plays a central role in high-energy CR research, serving as a key process for accelerating charged particles in astrophysical environments. Unlike static magnetic fields, which do not facilitate energy transfer due to the absence of large-scale electric fields - often disrupted by the presence of plasma - DSA operates effectively in dynamic settings where magnetic variations are prevalent. These variations can occur at the magnetic boundaries of colliding plasma, leading to elastic scattering of charged particles, which is crucial for acceleration. When charged particles encounter a shock front, they experience an increase in energy proportional to the factor:

$$1 + \frac{v_s}{c} \tag{1.4}$$

In this term, c represents the speed of light, and v_s is the speed of the shock front. This interaction allows particles to gain energy as they cross the shock front, and repeated crossings can significantly enhance their energy levels. The likelihood of a particle escaping the acceleration region after each crossing significantly influences the resulting energy spectrum of E^{-2}. The maximum energy E_{max}, a particle can attain during this process, depends on the strength of the magnetic field B, its charge Z, as well as the acceleration region's size R. This relationship is encapsulated in the Hillas criterion, a geometrical constraint that serves as a guideline for identifying potential sites for cosmic-ray acceleration. The Hillas criterion is obtained by demanding that the particle's Larmor radius should not exceed the size of the acceleration area, and can be mathematically expressed as:

$$\epsilon_{\mathrm{max}} \simeq ZBR \tag{1.5}$$

Figure 1.5 uses the Hillas criterion to visualize how different astrophysical objects and environments fit into the context of particle acceleration. Smaller objects (e.g., neutron stars, white dwarfs) can generate stronger magnetic fields but are limited by their small size. Larger objects (e.g., galaxy clusters) have weaker magnetic fields but can influence particles across vast distances. Features in the CR spectrum (knee, ankle, GZK) can be drawn into the plot and link different astrophysical processes and environments based on their location in the Hillas diagram. Sources on the left side of a red dashed line cannot accelerate protons to the corresponding energy.

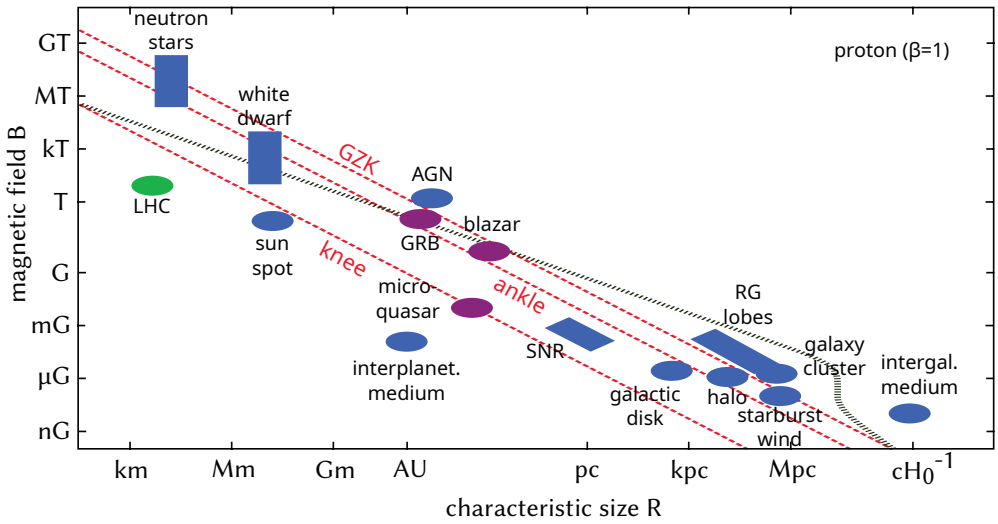

Figure 1.5: Potential astronomical accelerators are displayed according to their characteristic size and magnetic field strength. The maximal energy a proton can be accelerated to, as predicted by the Hillas criterion at the energies of the knee, ankle, and GZK (cf. Figure 1.4), are shown as red dashed lines. Figure adapted from [30, p. 6].

One of the most luminous objects in the universe are active galactic nuclei (AGNs). They are considered the primary source of CRs above the ankle. This hypothesis is supported by two high-energy neutrinos detected with the IceCube Neutrino Observatory that show evidence to originate from two AGNs [31, 32]. The detection of a neutrino from the blazar TXS 0506+056 in its flaring state triggered an extensive multi-wavelength campaign. Measurements were taken across the entire electromagnetic spectrum, from radio to γ-particles, and this campaign is regarded as a milestone in multi-messenger astronomy.

[31]: Aartsen et al. (2018), "Multimessenger Observations of a Flaring Blazar Coincident with High-Energy Neutrino IceCube-170922A"
[32]: Abbasi et al. (2022), "Evidence for Neutrino Emission from the Nearby Active Galaxy NGC 1068"

1.3 Multi-Messenger Astronomy

The link between the origin of CRs and other cosmic messengers, like photons and neutrinos, is rooted in the hadronic model of particle acceleration. Figure 1.6 illustrates the production of γ-rays via leptonic processes and CRs and neutrinos via hadronic processes in the vicinity of a jet. Here, a key mechanism is synchrotron radiation, in which charged particles rotate around magnetic fields, emitting photons in the energy range from radio to X-rays. Higher-energy photons can be produced through leptonic models, such as Synchrotron Self-Compton (SSC), where the same electrons that produce synchrotron photons upscatter them via inverse Compton scattering to higher energies ranging from GeV to TeV [33].

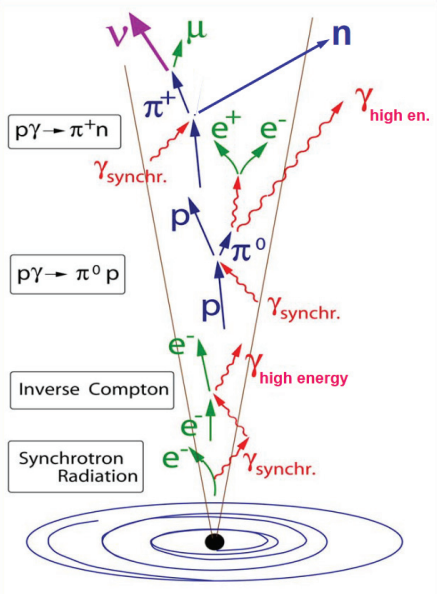

Figure 1.6: Visualization of the production of CRs, γ-rays and neutrinos via the leptonic and hadronic model in the vicinity of a jet. Figure from [34, p. 656]

In hadronic models, high-energy protons interact with ambient matter and radiation, producing various secondary particles. Here, neutrinos and photons are mainly generated by decaying pions. Charged pions dominantly undergo the decay chain:

$$\begin{aligned} \pi^+ &\to \nu_\mu + \mu^+ \\ &\qquad \hookrightarrow \mu^+ \to \overline{\nu}_\mu + \nu_e + e^+, \\ \pi^- &\to \overline{\nu}_\mu + \mu^- \\ &\qquad \hookrightarrow \mu^- \to \nu_\mu + \overline{\nu}_e + e^-, \end{aligned} \tag{1.6}$$

while neutral pions dominantly decay into γ-rays:

$$\pi^0 \to \gamma + \gamma \tag{1.7}$$

The pions are produced with approximately the same branching ratio between π^0, π^+, and π^- in proton-proton collisions via

$$p + p \to \pi^\pm, \pi^0, K^\pm, \dots . \tag{1.8}$$

[33]: Spurio (2018), "The Sky Seen in -Rays"

Another mechanism is the photoproduction process, where the high-energy proton interacts with low-energy photons, producing a Δ^+ resonance. The same process is responsible for the GZK cut-off, where protons interact with photons from the CMB:

$$\begin{aligned} p + \gamma_\epsilon \rightarrow \Delta^+ &\rightarrow \pi^0 + p, \\ &\rightarrow \pi^+ + n. \end{aligned} \tag{1.9}$$

Here, the branching ratio for the decay into a π^0 is twice as high as for the π^+. This leads to three neutrinos for every four photons, in contrast to six neutrinos for every two photons in proton-proton collisions. Equation (1.6) shows that the flavor composition $\nu_e : \nu_\mu : \nu_\tau$ at the source is $1:2:0$. However, due to the immense size of the acceleration regions compared to the oscillation length, the neutrino flux composition should be close to $1:1:1$ when reaching Earth.

CRs reaching the Earth, interact with its atmosphere. Figure 1.7 shows an extensive air shower initiated by a CR in the atmosphere. These showers have a hadronic core, where short-lived hadrons decay and generate electromagnetic sub-showers. The electromagnetic sub-showers are mainly generated by the decay of neutral pions $\pi_0 \rightarrow 2\gamma$, undergoing pair production $\gamma \rightarrow e^- + e^+$ when the photon energy is above 20 MeV, creating electron-positron pairs. Charged mesons, such as charged pions ($\pi^\pm$), decay into muons and neutrinos as described in equation (1.6), contributing to the conventional atmospheric neutrino flux [34]. The interactions can also produce heavy, unstable charmed mesons at high energies. Due to their short lifetimes, these mesons are unlikely to in-

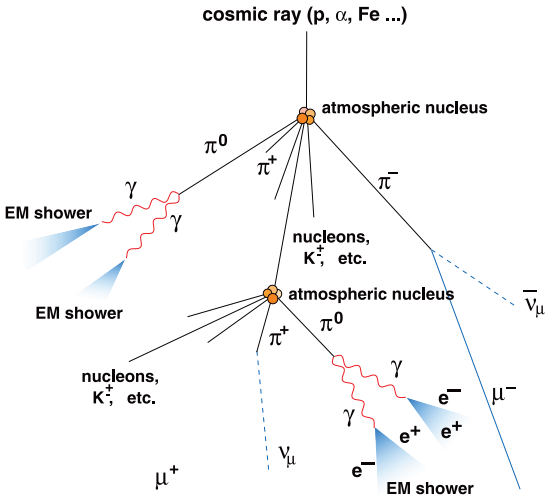

Figure 1.7: Schematic description of an air shower initiated by a CR in the earth atmosphere. The electromagnetic component is highlighted by blue cones. Figure from [35, p. 44]

[34]: Katz et al. (2012), "High-Energy Neutrino Astrophysics"

teract before decaying, resulting in a unique energy spectrum similar to that of the cosmic rays. This phenomenon is called the prompt flux, which becomes significant only at very high energies. As of today, this prompt flux has not yet been measured. [36].

Neutrino astronomy, therefore, presents a compelling case for advancing our understanding of the universe, primarily because neutrinos serve as the smoking gun for hadronic acceleration processes. Unlike charged cosmic rays, deflected by magnetic fields and through that losing directional information about their sources, neutrinos travel straight from their origins, providing direct evidence of the high-energy processes that produce them. Their ability to escape dense environments, such as those found in supernova remnants and active galactic nuclei, enables them to probe the strongest accelerators in the universe. This distinctive feature makes neutrinos essential for studying phenomena that are invisible to traditional electromagnetic observations, thereby providing a new perspective on the cosmos's most energetic incidents. By harnessing the potential of neutrino astronomy, we can deepen our understanding of cosmic particle acceleration and the fundamental processes that govern the universe [34].

[36]: Van Santen (2015), "Probing Extraterrestrial Neutrino Fluxes and Atmospheric Charm with Contained Neutrino Events above 1 TeV in IceCube"
[34]: Katz et al. (2012), "High-Energy Neutrino Astrophysics"

2 Large Volume Neutrino Telescopes: The IceCube Observatory

Contents

2.1 Operation Principle **15**

2.2 The IceCube Neutrino Observatory **19**

Building and operating large-volume neutrino detectors that are suitable for detecting neutrinos coming from outside our solar system comes with some challenges. Section 2.1 describes the basic operation principle of these detectors, including Cherenkov radiation and light signatures. The IceCube Neutrino Observatory, its components, operation, and planned upgrades are discussed in section 2.2.

2.1 Operation Principle

Cosmic rays that enter the atmosphere interact with its main components, including oxygen and nitrogen. This triggers a chain reaction known as an air shower. This cascade generates a variety of secondary particles, such as x-rays, alpha particles, protons, muons, pions, electrons, neutrons, and neutrinos. These particles spread out but remain primarily aligned with the trajectory of the original cosmic ray, typically within about one degree. Among the particles produced in these high-energy collisions are neutrons and positively and negatively charged mesons. Many of these particles undergo decay, producing muons and neutrinos that can travel through the atmosphere and reach the Earth's surface [37]. Neutrinos produced by the interactions of secondary and primary cosmic rays may exhibit every kind of flavor, depending on how they interact with atmospheric particles. Atmospheric neutrinos span an energy spectrum that is similar to that of cosmic rays. Secondary hadrons penetrating the Earth's crust are generally low in energy. As these particles travel through the dense terrestrial medium, they quickly dissipate a big part of their energy through hadronic collisions and ionization over comparably brief distances.

[37]: Spurio (2018), "Indirect Cosmic Ray Detection"

The same holds for muons, but with longer distances. High energy muons can travel several km through the earth. Consequently, unstable particles such as pions, kaons, and muons tend to decay almost at rest, resulting predominantly in low-energy muon and electron neutrinos, along with their corresponding antineutrinos [38].

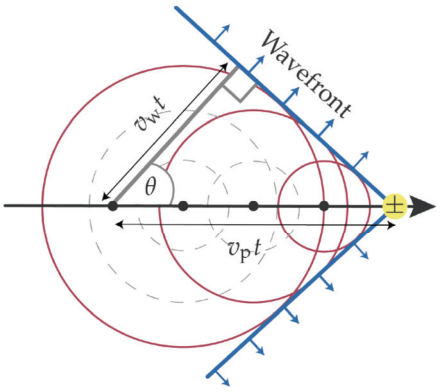

Figure 2.1: Schematic build-up of a Cherenkov wavefront. Constructive interference occurs when, in a time interval t, the charged particle moves further than the photons $v_p t > v_w t$. Figure from [39, p. 16].

The IceCube Neutrino Observatory is a large-scale Cherenkov detector designed to detect high-energy neutrinos originating from outer space.

Large neutrino detectors operate by utilizing Cherenkov radiation. Charged particles move through a dielectric medium, interact with the material's electric field, and cause the medium to become polarized. As the medium returns to its equilibrium state, it emits electromagnetic wavelets. If the velocity of the charged particle is lower than the speed of light within the medium, these wavelets interfere destructively, preventing the formation of a coherent wavefront. However, if the particle's velocity exceeds the speed of light in that medium, constructive interference occurs. This leads to the formation of a wavefront and results in the emission of coherent photons, producing a distinct light deposition signature that propagates through the material, as illustrated in Figure 2.1. This wavefront has a characteristic opening angle Θ with respect to the particle trajectory. The opening angle can be calculated by:

$$\cos(\Theta) = \frac{v_w t}{v_p t} = \frac{1}{\beta n}$$
$$\text{and } \beta = \frac{v_p}{c},$$

with the velocity of the particle v_p, the wavefromt velocity $v_w = c/n$ and a given time interval t.

[38]: Grieder (2001), "Cosmic Rays Underground, Underwater and Under Ice"

In Cherenkov detectors, the medium is typically a significant, transparent substance like water or ice. It is usually surrounded or interspersed by an array of PMTs, serving as a detector. For IceCube, the interacting medium is ice, and the PMTs are organised in so-called optical modules, which consist of a photomultiplier, a computer board, and an LED board for calibration, all enclosed in a waterproof glass sphere. When a neutrino passes through this detector and interacts with a nucleus, a high-energy charged lepton is generated. Due to its high velocity, which exceeds the speed of light in the medium, it emits Cherenkov radiation in a characteristic cone-shaped pattern. This cone of light is called a light deposition signature and appears as a ring of activity in the PMT array [40].

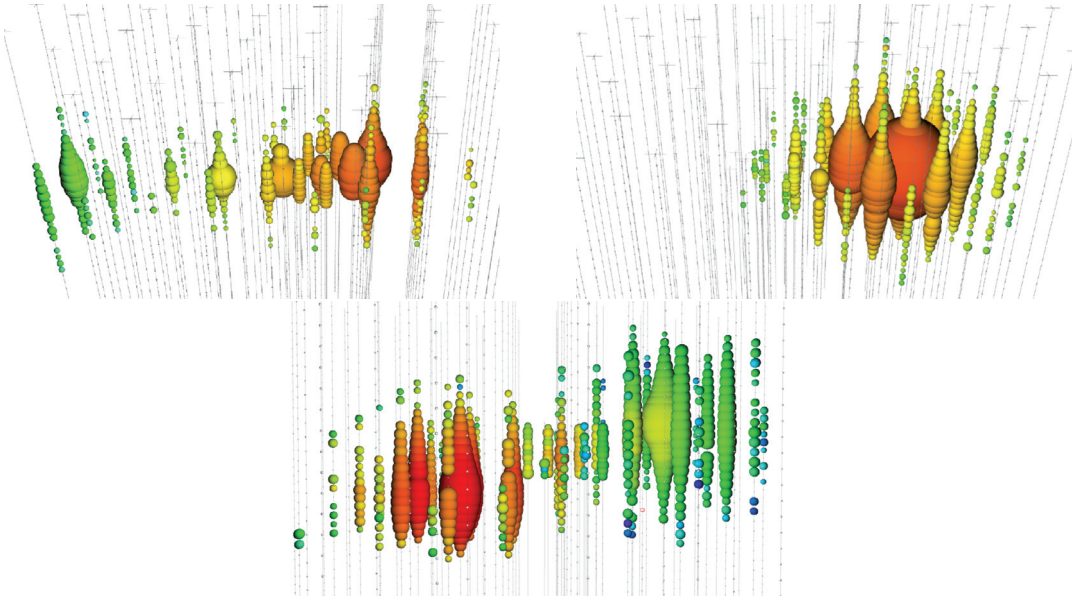

Figure 2.2: Examples of light deposition signatures detected by IceCube. Tracks (left), cascades (right), and double-bang events (bottom). The light detection time is decoded by color, ranging from early (red) to late (blue). The size of the spheres corresponds to the number of detected photons in a module. Figures courtesy of the IceCube collaboration.

By analyzing the light deposition signature, it is possible to determine the direction, energy, and flavour of the incoming neutrino based on the properties of the emitted Cherenkov radiation [40]. In general, light deposition signatures can be grouped into three primary categories. Figure 2.2 illustrates examples of each: track-like patterns arising from the charged-current interactions of muon neutrinos (left); cascade-like

[40]: Gaisser et al. (2014), “IceCube”

patterns generated by interactions of all neutrino flavours (right); and more complex signatures from extremely high-energy tau neutrinos, such as the rare and thus simulated double-bang event (bottom) [19].

[19]: Aartsen et al. (2021), "IceCube-Gen2: The Window to the Extreme Universe"

2.2 The IceCube Neutrino Observatory

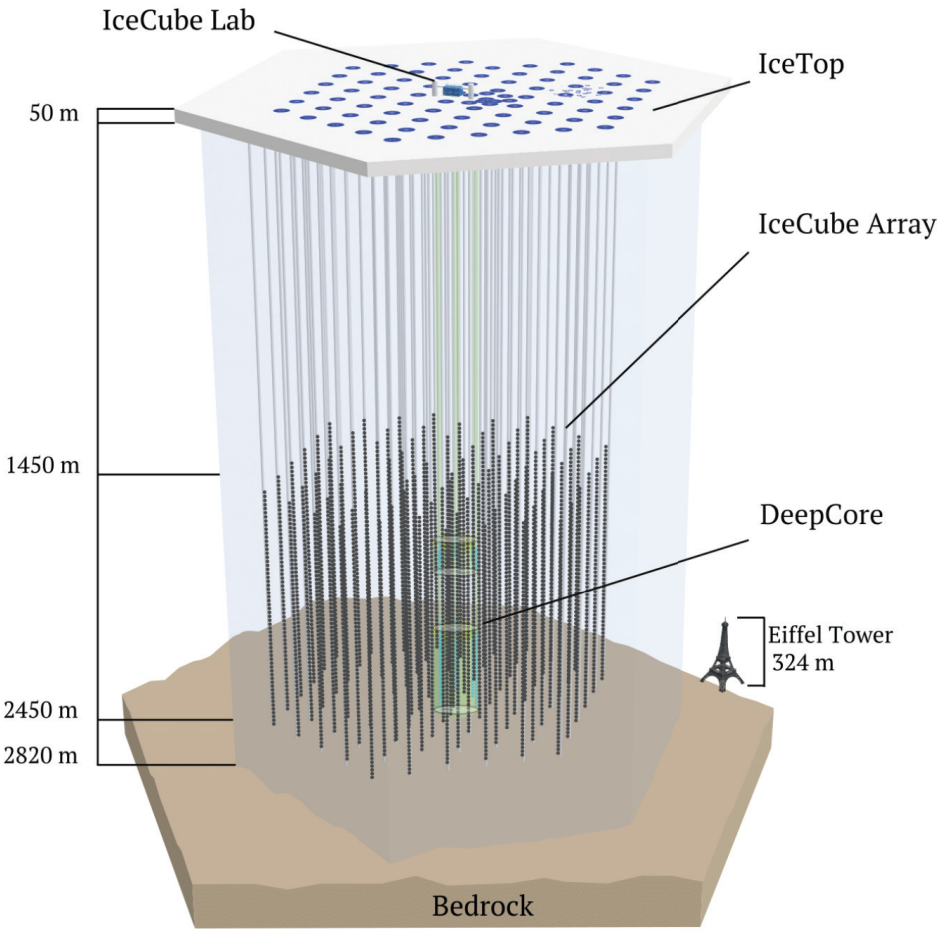

Figure 2.3: Schematic layout of the IceCube Neutrino Observatory and its infrastructure. The blue circles at the surface represent the IceTop component, vertical lines depict strings with black dots for the DOMs. The highlighted section consists of high quantum efficiency DOMs of the DeepCore. Figure courtesy of the IceCube collaboration.

The IceCube detector system consists of 86 vertical strings anchored embedded in the Antarctic ice at a depth of 1450 m to 2450 m. Every string has 60 susceptible optical sensors, the DOMs sensitive to light generated when high-energy neutrinos interact with ice molecules. This allows researchers to measure the direction, energy, and type of neutrinos, providing valuable information about their astrophysical

origins. DeepCore is a special subarray within the IceCube detector developed to increase the sensitivity for neutrinos with lower energies. It consists of 8 additional strings strategically placed in the central area of the in-ice array and contains 480 optical sensors spaced closer together. This arrangement enables the detection of neutrinos with energies below 5 GeV, which is crucial for studying neutrinos of solar and atmospheric origin. The surface component of the IceCube detector, known as IceTop, is built of 81 stations spread across 1.5 km^2. Each station has four optical sensors that measure the air showers produced by high-energy cosmic rays. IceTop enables the analysis of the composition and energy of cosmic rays within the range of 300 TeV to over 1 EeV, offering crucial data that complements the in-ice array's results. The IceCube Laboratory (ICL), which is placed at the surface in the center of the IceCube array's hexagonal layout, plays a key role in processing and transmitting data for the entire detector system. It houses a state-of-the-art computer infrastructure responsible for processing the data collected by the detectors, including calibrating the sensors and analyzing the experimental data. In addition, the laboratory serves as a coordination centre for maintaining and monitoring the systems and conducting experiments [40].

2.2.1 Location and Environment



Figure 2.4: The ICL (left building) at the center of IceCube's hexagonal footprint on the surface. The orange flags mark the positions of some strings.

The harsh conditions of remote Antarctica present significant challenges for IceCube,

[40]: Gaisser et al. (2014), "IceCube"

including extreme cold, isolation, and logistical issues. To address these, IceCube employs automated systems for data collection and filtering that continuously process the data from the detectors. Specifically, IceCube relies on a network of around 400 identical filtering and calibration processors that automatically gather and analyze data from the detectors. The detectors and the entire infrastructure are designed for extreme temperatures and weather conditions. Materials and components have been selected to withstand the challenges of cold and ice, and the systems are designed to require minimal maintenance. Several communication channels have been set up to ensure communication with the outside world, including email and VOEvent messages. These systems allow for the quick transmission of alarms and data to other observatories, enabling extensive multi-wavelength follow-up campaigns [41]. This led, among other things, to the observation of the potential high-energy neutrino source TXS 0506+056 [31].

The characteristics of the deep Antarctic glacial ice at the South Pole are essential for neutrino experiments, as the ice serves as the medium for detecting high-energy neutrinos. The glacial ice is essentially free from optical background that water-based experiments must consider, such as bioluminescence and the decay of ^{40}K isotopes in saline water.

For event reconstruction based on the detected Cherenkov photons produced from secondary particles, an accurate description of the properties of the glacial ice is crucial.Optical properties of these glaciers, including light scattering and absorption, change with depth and dust concentration, which in turn affects the performance of the photomultiplier tubes that detect Cherenkov light. At lower depth, the scattering length is reduced by a high concentration of air bubbles in the ice. With increasing depth and pressure, air bubbles compress and eventually transform into the solid air-hydrate clathrate phase. Below $\sim$1500 m all air bubbles have gradually transformed into the solid phase [43]. The resulting clathrate hydrate has a refractive index within 5.3 permill of that of the surrounding ice and appears nearly transparent [44], and the optical properties at these depths depend primarily on the dust concentration in the ice. The concentration of dust in the ice varies

[41]: Aartsen et al. (2017), “The IceCube Realtime Alert System”
[31]: Aartsen et al. (2018), “Multimessenger Observations of a Flaring Blazar Coincident with High-Energy Neutrino IceCube-170922A”
[43]: Ackermann et al. (2006), “Optical Properties of Deep Glacial Ice at the South Pole”
[44]: Uchida et al. (1995), “Refractive-Index Measurements of Natural Air–Hydrate Crystals in an Antarctic Ice Sheet”

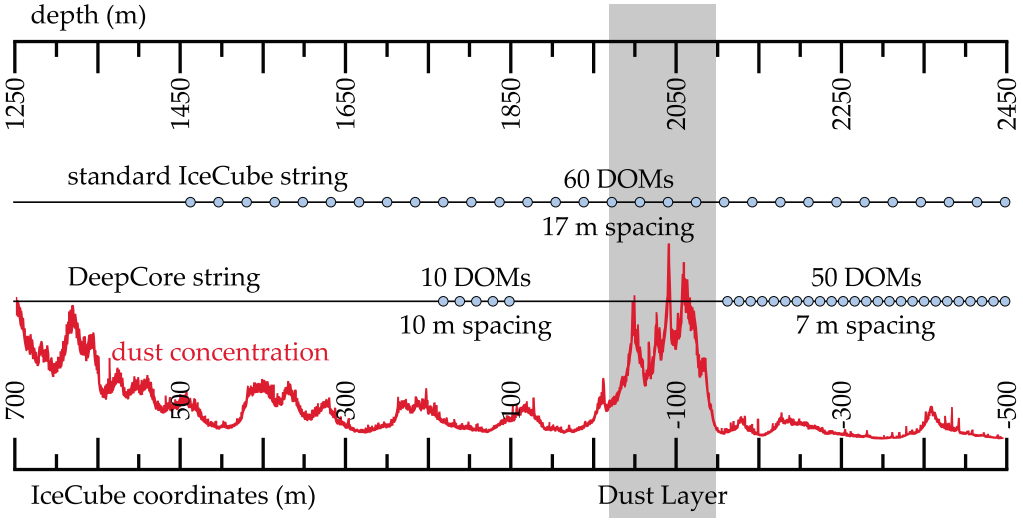

Figure 2.5: Vertical cross-section of the instrumented ice showing sensor spacing and dust concentration. Figure from [42, p. 44].

with depth, depending on historical atmospheric deposition at the time of ice sheet formation. It typically increases with increasing depth, increasing optical absorptivity, and scattering coefficient [43]. However, in depths instrumented by the IceCube detector, the dust concentration is primarily constant. The most prominent dust layer in this region corresponds to the so-called marine isotope stage 4 (MIS4), a period of increased atmospheric dust deposition. This distinct peak in dust concentration, located between approximately 1950 m and 2100 m and depicted in Figure 2.5, has a notable impact on the detector's response to particle physics events [45]. Overall, the effective scattering coefficient varies with depth and ranges from $0.01\,\mathrm{m}^{-1}$ to $0.08\,\mathrm{m}^{-1}$ and $0.1\,\mathrm{m}^{-1}$ to $0.2\,\mathrm{m}^{-1}$ in the MIS4. The absorptivity of the ice also shows a dependence on depth and dust concentration, with typical values of $0.005\,\mathrm{m}^{-1}$ to $0.02\,\mathrm{m}^{-1}$ and $0.03\,\mathrm{m}^{-1}$ to $0.055\,\mathrm{m}^{-1}$ in the MIS4 [46]. Additionally, the optical properties show a strong wavelength dependence, with scattering being more pronounced in the UV range and absorption increasing in the red range [43].

Recent findings have revealed a birefringent dependency in the optical properties of

[43]: Ackermann et al. (2006), "Optical Properties of Deep Glacial Ice at the South Pole"
[45]: The IceCube Collaboration (2013), "South Pole Glacial Climate Reconstruction from Multi-Borehole Laser Particulate Stratigraphy"
[46]: Aartsen et al. (2013), "Measurement of South Pole Ice Transparency with the IceCube LED Calibration System"
[43]: Ackermann et al. (2006), "Optical Properties of Deep Glacial Ice at the South Pole"

the Antarctic glacial ice, indicating improved light transmission along the direction of glacial flow in a NW direction with approximately 10 m/year[47]. This discovery is crucial for understanding photon propagation in the IceCube detector and serves as a foundation for implementing the Pencil Beam concept in the IceCube Upgrade. The Pencil Beam is a special calibration device that emits focused beams of light with an opening angle of less than one degree in any direction, achieving a precision of 0.1°. By leveraging this directional dependency, the Pencil Beam design aims to optimize detection capabilities and enhance the precision of measurements within the upgraded observatory [48].

The reconstruction of events depends on ice properties. Deviations from the used ice models result in significant systematic uncertainties. Another source of such uncertainties is the so-called bubble column. The bubble column forms when the boreholes refreeze from the outside to the inside of the hole. During this process, bubbles and dust particles are pushed towards the centre, forming the bubble column. Photons scatter at these bubbles, but the scattering length of the column remains unknown, leading to further uncertainties, especially during the reconstruction of low-energy events [49].

2.2.2 The Digital Optical Module

The Digital Optical Module (DOM) serves as the data acquisition unit in the IceCube detector. It is the primary light sensor. Housed in a spherical glass casing, it features a PMT that faces downwards with a 10-inch (25.4 cm) diameter, along with integrated circuit boards. The Main Board, a ring-shaped circuit board around the PMT neck, handles calibration, communication, control, data acquisition, and also low-voltage power conversion. Additional circuit boards delay the PMTs' signals, provide high voltage to the PMT, manage PMT pin interfaces, and emit calibration light flashes, capable of reaching other DOMs. The PMT detects Cherenkov light from particle interactions in the ice. The detector is sensitive to neutrino energies from about 10 GeV up to 10 PeV, with light from high-energy events detectable over distances of several hundred meters. It operates at a gain of 10^7 and produces

[47]: Rongen et al. (2021), *A Novel Microstructure-Based Model to Explain the IceCube Ice Anisotropy*
[48]: Ishihara (2019), "The IceCube Upgrade - Design and Science Goals"
[49]: Ishihara et al. (2019), *Calibration LEDs in the IceCube Upgrade D-Egg Modules*

waveforms with pulse widths ranging from 12 ns to 1500 ns and amplitudes that range from 1 mV to approximately 2 V. To handle this diverse signal range, it employs many digitizers at different sampling speeds and with overlapping dynamic ranges. Each DOM detects single photons and records PMT waveforms independently, capturing additional photons arriving within a 6.4 µs window in the same waveform. These events constitute a so-called hit. It is impossible to send the full waveform for every recorded hit to the surface, and the amount of information stored with every hit depends on a local coincidence logic implemented in the DOMs. If a nearest or next-to-nearest DOM signals a hit within a 1 µs time window, the waveform is digitized, compressed, and included in the hit record. For isolated events without a local coincidence, the digitization is aborted, and only a timestamp and charge summary are sent. For this purpose, DOMs are interconnected through dedicated local coincidence wiring that links them to their neighbouring DOMs above and below. The DOM temporarily stores hit data for roughly one second, in which the trigger decision is made and the hit is transmitted in a batch to the surface computers, called DOMHubs. This setup enables rapid detection of coincident hits between neighbouring or next-to-nearest DOMs within a configurable time window.

DOMs communicate with the DOMHubs in the ICL via twisted wire pairs, which also serve as their power supply. The wire pairs are bundled into horizontal surface cables and vertical in-ice cables. Every one of the pairs serves two DOMs. The data transfers are initiated by the computers at the surface [50].

In IceCube, the basis for measurements of energies is the deposited charge, relying on two calibration constants: the pedestal (baseline digitizer value at zero voltage) and the gain (voltage change per ADC count). These constants convert raw digitizer readings into voltage for charge calculations. Digitizer baselines are highly sensitive to operating conditions, making it essential to continuously monitor them during normal data collection. This is achieved using a forced trigger mechanism, operating at a rate of 1.2 Hz for the in-ice DOMs and 4.8 Hz for the IceTop DOMs. These real-time baselines are preferred over those obtained during the DOMCal (see next paragraph), as the latter cannot replicate the exact conditions present during regular operations. The baselines remain highly stable, only shifting annually with a maximum 0.2 counts, equal to voltage changes of 0.018 mV to 0.025 mV. In-ice

[50]: Aartsen et al. (2017), "The IceCube Neutrino Observatory: Instrumentation and Online Systems"

DOMs undergo calibration annually, while IceTop DOMs requires monthly calibration to account for seasonal temperature variations that can affect its performance. The recalibrations may induce baseline shifts as far as to 0.6 counts, equivalent to 0.54 mV. Stability of the DOM's gain, which is essential for precisely amplifying the charge from detected photons, relies on the steady operation of components like the digitizers, PMT high-voltage, and mainboard amplifiers. Historical calibration data and ongoing monitoring of Single Photoelectron (SPE) charge during operations are used to assess stability. Annual calibration results show 0.1%, 0.2%, and 0.5% variations for the high-, medium-, and low-gain channels of the in-ice DOMs, respectively [50].



Figure 2.6: Photo of an IceCube DOM sitting inside the harness. Figure courtesy of the IceCube collaboration.

The PMT waveform calibration process for DOMs is realized using the DOM calibration software (DOMCal). It converts the samples into precise time and voltage measurements, factoring in the PMT's gain. This is done using calibration constants specific to each DOM, which are autonomously determined by the DOMs through the DOMCal system. Key elements in this calibration process include a precise electronic pulser circuit that provides known charge values, the timing reference represented by a 20 MHz oscillator on the mainboard, a reference circuit offering a stable DC bias voltage and SPE signals, which can come from natural dark noise photons or a LED with low intensity located at the mainboard. Free-running clocks of individual DOMs are synchronized with the surface clocks using Reciprocal Active Pulsing Calibration (RAPCal), a continuous process that ensures timing accuracy down to the nanosecond level. This synchronization enables the translation of hit timestamps from DOM clocks to a unified array time base and finally to Coordinated Universal Time (UTC). The process involves transmitting a calibrated bipolar pulse to each DOM via the power/communication wire pair, pausing data transmission during the operation. The Event Builder, which coordinates data

[50]: Aartsen et al. (2017), "The IceCube Neutrino Observatory: Instrumentation and Online Systems"

collection by processing requests from the Global Trigger, then uses the DOM data and their clock offset tracked by RAPCal to construct events [50].

2.2.3 Operation

IceCube's online systems encompass the hardware and software at the detector that handle data acquisition and management, monitoring, and event selection during operation. Optimized to maximize uptime, which is the proportion of time the detector is capable of detecting neutrino interactions, these systems are built in a modular way, allowing individual component failures to be isolated without disrupting essential data collection. Furthermore, comprehensive monitoring tools notify detector operators of any anomalies. The online data flow begins with photon detection in the ice. It progresses through multiple reduction and event selection stages, including secondary monitoring and auxiliary data streams, targeting potential astrophysical events [50].

Two detector operators are present at the Amundsen-Scott South Pole station year-round. The so-called winterovers respond to any anomalies during detector operation, plan and execute special runs like the DOMCal runs, upgrade the systems in the summer, and do basic maintenance tasks. They also participate in public outreach events and are the point of contact for members of the collaboration regarding detector operations.

During my 2017/18 season as a winterover, an uptime of 99.78% was achieved, 840 TB of scientific data recorded, and 28 TB of event data transmitted via Tracking and Data Relay Satellites (TDRS) for real-time alerts and complex off-site reconstructions.

The Data Acquisition (DAQ) system collects and processes data from the detector, including secondary monitoring and auxiliary data streams aimed at identifying potential physical events. DOM hits are classified into two categories: Hard Local Coincidence (HLC) hits, which contain full digitized waveforms, and Soft Local Coincidence (SLC) hits, which store only minimal information after compression. Local Coincidence hits orruce, if directly or indirectly neighbouring DOMs signal a launch within a time frame of $\pm 1\,\mu s$. These hits are transmitted to surface-based

[50]: Aartsen et al. (2017), "The IceCube Neutrino Observatory: Instrumentation and Online Systems"

computers for further analysis. Using parallel trigger algorithms, the DAQ generates software triggers by analyzing the spatial and temporal patterns of HLC hits all over the detector. Events are produced by grouping hits within a given time window. The event rate fluctuates seasonally based on atmospheric muon flux, averaging 2.7 kHz, while the total DAQ rate is approximately 1 TB per day. In addition to event data, the DAQ generates secondary data streams, including monitoring, time calibration, and DOM scaler data. The scaler data tracks the hit rate of each DOM and is used for supernova detection, while time calibration and monitoring streams ensure system health and data quality [50].

The event data from the DAQ is then processed in the Processing and Filtering (PnF) system, where about 25 filters are applied to select a subset of about 15% of events for transmission via satellite. These filters are managed by a computing cluster optimized to identify events that are appropriate for specific physics analyses. Due to limitations in processing power, the filters only use energy and fast directional reconstructions. Additionally, the PnF system applies the most current calibration to the data received from the DAQ. Finally, the JADE system manages data movement, including local archival storage and satellite data handoff. In addition, real-time communication for experiment control and monitoring is provided by the IceCube Messaging System (I3MS), and detector operations are handled by the IceCube Live software [50].

IceCube utilizes 19 racks of network and computing equipment, called South Pole System (SPS). These systems house the hardware for all the aforementioned components, along with additional equipment such as Iridium modems, GPS clocks, network infrastructure, DOMHubs, and experimental setups that operate independently of the IceCube detector. The DOM surface cables are linked to custom computers, so-called DOMHubs, which are part of the SPS. Each in-ice string is assigned to a DOMHub. Eleven additional DOMHubs are assigned to IceTop. Each DOMHub is encased in a chassis containing specialized components for communication, timing, and power. The SPS computers interface through switches installed in each rack, which offer redundant connections to a high-speed 10 Gbps network backbone. Each DOMHub connects to the rack switches using dual-bonded 1 Gbps links, ensuring reliable and efficient data transmission. [50].

[50]: Aartsen et al. (2017), “The IceCube Neutrino Observatory: Instrumentation and Online Systems”

2.2.4 The Future of IceCube

IceCube Upgrade

The IceCube Upgrade, set for deployment during the 2025/26 Antarctic summer, represents the next phase of the IceCube project. It will include seven new strings with approximately 700 optical sensors distributed among the strings. The IceCube Upgrade is strategically placed near the bottom centre of the current IceCube detector, as shown in Figure 2.7.

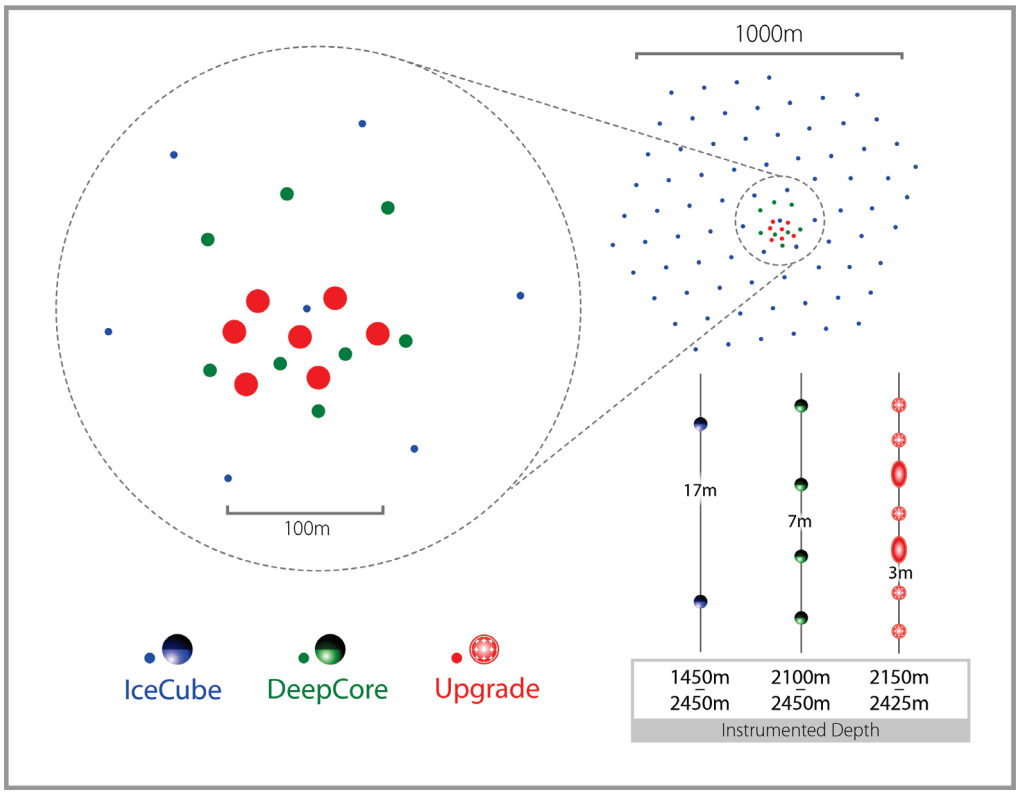

Figure 2.7: The layout of the IceCube Upgrade. The seven new strings (red) are located in the center of IceCube (blue) within the DeepCore region (green). The lower right box shows the depths of the instrumentation. Only the physics region is considered for DeepCore and Upgrade.
Image courtesy of the IceCube collaboration.

It forms a grid of sensors spanning 20 meters horizontally and 3 meters vertically at depths between 2150 and 2425 meters. This region, known as the physics region, is characterised by apparent glacial ice and minimal atmospheric muon interference.

Above and below the physics region, there are sparsely instrumented zones in depths between 1450 and 1850 meters, with sensors spaced approximately 25 meters apart vertically. These areas serve multiple purposes: providing an atmospheric muon veto, enabling calibration, and supporting research and development (R&D) for sensors tailored to the future IceCube-Gen2. The IceCube Upgrade will feature mDOMs and dual Optical Sensors in Ellipsoid Glassdomes (D-Eggs). Both have been chosen as the primary sensors [48]. The mDOMs represent a significant evolution in optical module design, incorporating 24 PMTs of 80 mm diameter each. These PMTs are arranged within a 3D-printed support structure equipped with reflectors, which enhance photon detection efficiency by capturing and redirecting photons arriving from off-axis directions [51]. This multi-PMT design, initially pioneered by the KM3NeT Collaboration for deep-sea detectors, has a reduced diameter of 356 mm and offers significant advantages over the traditional single-PMT approach, including superior solid-angle coverage and an increased photocathode area per module [52]. A total of 310 D-Egg modules have been produced, with 288 to be deployed in the IceCube Upgrade. In contrast to the current-generation single-PMT IceCube DOMs, D-Eggs incorporate two high-efficiency 8-inch (20.32 cm) PMTs. These PMTs are vertically aligned, facing in opposite directions. They are part of an integrated assembly with high-voltage supply bases, a front-end circuit board, magnetic shielding, and calibration devices. All components are enclosed within a durable, ellipsoidal pressure-resistant vessel made of UV-transparent borosilicate glass, offering superior UV transmissivity compared to the traditional IceCube DOM vessel [53].

Furthermore, the IceCube Upgrade introduces advanced calibration capabilities for the existing IceCube detector. Each optical module has multiple calibration tools, including ultra-fast LEDs, CCD cameras, pressure, temperature, magnetic field, and acceleration sensors. The IceCube Upgrade will incorporate a variety of stand-alone calibration devices, such as the Precision Optical Calibration Module (POCAM), Pencil Beam emitters, and acoustic sources [48]. In addition, experimental photosensor designs, including the Wavelength-Shifting Optical Module (WOM) [54] and the

[48]: Ishihara (2019), "The IceCube Upgrade - Design and Science Goals"
[51]: Basu et al. (2021), "A Next-Generation Optical Sensor for IceCube-Gen2"
[52]: Anderson et al. (2021), "Design and Performance of the Multi-PMT Optical Module for IceCube Upgrade"
[53]: Hill et al. (2021), *Performance of the D-Egg Optical Sensor for the IceCube Upgrade*
[54]: Rack-Helleis et al. (2021), *The Wavelength-shifting Optical Module (WOM) for the IceCube Upgrade*

Long Optical Module (LOM) [51], will also be installed as part of the deployment.

The IceCube Upgrade amplifies scientific capabilities with its densely packed, high-efficiency photosensors, which detect a more significant number of photons originating from secondary charged particles which are originating from interactions of neutrinos in the $\mathcal{O}(1\,\text{GeV to } 10\,\text{GeV})$ energy range, reducing the low-energy neutrino threshold to 1 GeV closing the gap to other lower energy neutrino experiments, like Super-K [55]. This enhanced photon detection enables more precise event reconstruction at lower energies than those typically studied by DeepCore. The IceCube Upgrade also facilitates highly accurate measurements of tau neutrino appearances with a precision of at least 6%. It, therefore, represents the most rigorous test to date of the unitarity of the PMNS matrix as introduced in section 1.1. Concerning oscillation measurements, including parameters such as Δm^2_{23} and $\sin^2\Theta_{23}$, the IceCube Upgrade achieves precision comparable to leading long baseline accelerator experiments like NOνA, T2K, and MINOS [48, 56–58].

Further improvements could be achieved through the calibration of the refrozen ice. The IceCube Upgrade's D-Egg modules will feature a calibration system, consisting of downward-facing LEDs. It will be used to assess the drill holes' optical properties, referred to as hole ice. Within the hole ice, an area known as the bubble column contains impurities that alter the ice's optical characteristics. Precise measurement of those impurities is essential for the existing array and the IceCube Upgrade, as the refrozen ice contributes substantial systematic uncertainties in the reconstruction of neutrinos with low energies. The D-Egg modules are equipped with four downward-facing flasher LEDs, unlike current IceCube DOMs, which lack fully vertical LEDs and are thus less suited for directly measuring hole ice. These LEDs help by reducing the uncertainty associated with the hole ice. Critical parameters such as the bubble column's effective scattering length λ_e and its diameter will be determined by the D-Eggs [49]. A crucial component for investigating anisotropy in the IceCube Upgrade is the Pencil Beam emitters, which generate a laser beam that can be aimed in any desired direction, allowing for systematic scans across different receiver

[51]: Basu et al. (2021), "A Next-Generation Optical Sensor for IceCube-Gen2"
[55]: Suzuki (2019), "The Super-Kamiokande Experiment"
[48]: Ishihara (2019), "The IceCube Upgrade - Design and Science Goals"
[56]: Bian (2013), *The NOvA Experiment*
[57]: Abe et al. (2011), "The T2K Experiment"
[58]: Evans (2013), *The MINOS Experiment*
[49]: Ishihara et al. (2019), *Calibration LEDs in the IceCube Upgrade D-Egg Modules*

orientations. Due to deflection caused by birefringence, the direction of the maximum received intensity shifts from the receiver's geometric alignment, producing a unique signature. By analyzing sweeping profiles across multiple emitter-receiver pairs with varying orientations, the effects of absorption and birefringence in contributing to the observed anisotropy can be precisely separated [59]. While the novel calibration instruments will only be deployed in future IceCube expansions, the newly acquired calibration parameters can be applied retroactively to the entire IceCube data archive and thus improve the data already recorded [49].

IceCube-Gen2

IceCube has been a pioneer in detecting high-energy astrophysical neutrinos, but higher sensitivity is needed to identify individual neutrino sources. Therefore, IceCube-Gen2 has been designed to overcome these limitations. Its primary objective is to map the high-energy neutrino sky across a broad energy spectrum, from TeV to EeV. By integrating multi-messenger observations, it aims to investigate the mechanisms of cosmic particle acceleration and examine the correlation between neutrinos and other astrophysical signals. The observatory seeks to identify the sources and propagation characteristics of the universe's most energetic particles, providing a deeper understanding of their origins and behaviour.

Additionally, IceCube-Gen2 will use high-energy neutrinos as tools to test the laws of nature under extreme conditions. The planned upgrades include significantly enhancing the sensitivity of the existing detector. This aims to increase the annual neutrino detection rate tenfold and improve the detector's sensitivity by a factor of five, making the discovery of neutrino sources much more likely. A newly integrated radio array will further extend the observatory's sensitivity to higher energy ranges, enabling studies across several orders of magnitude [19].

To achieve its scientific objectives, IceCube-Gen2 aims to expand the current detector by adding four novel components: a low-energy core (IceCube Upgrade), an in-ice optical array, an expanded radio detector array, and a surface air shower array. The top-down view of the planned IceCube-Gen2 layout, shown in Figure 2.8,

[59]: Rongen et al. (2021), "Advances in IceCube Ice Modelling & What to Expect from the Upgrade"
[49]: Ishihara et al. (2019), *Calibration LEDs in the IceCube Upgrade D-Egg Modules*
[19]: Aartsen et al. (2021), "IceCube-Gen2: The Window to the Extreme Universe"

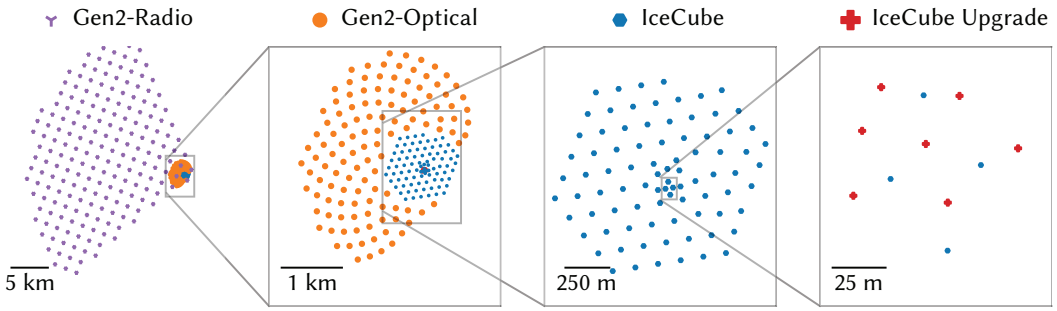

Figure 2.8: Top-down view of the proposed IceCube-Gen2 Neutrino Observatory. Left: Radio array with stations for ultra-high-energy neutrino detection. Center: IceCube-Gen2 optical high-energy array new strings (in orange), and the current IceCube array (in blue). Right: Layout of the IceCube Upgrade strings relative to the IceCube detector. Figure from [19]

illustrates the elements, each designed with advanced technologies optimized for specific energy ranges. On the left, the radio array consists of 200 stations intended to detect neutrinos with ultra-high energies. In the center, the optical high-energy array includes 120 new IceCube-Gen2 strings (represented by orange points), with a spacing of 240 m, where each string features 80 optical modules distributed vertically over 1.25 km. This expansion will increase the instrumented volume by a factor of 7.9 compared to the current detector (indicated by blue points). Nevertheless, the final design of the optical modules has not been chosen yet. On the right of Figure 2.8 are the seven new strings of the IceCube Upgrade, relative to the current IceCube infrastructure. The surface array will be placed directly over the optical array. Critical considerations for enhancing the sensitivity of both radio- and optical-based neutrino detectors were guided by the need to ensure cost-effectiveness. One strategy involves deploying longer strings, taking advantage of the 125 meter of ice above and below the current instrumented volume, where the optical properties are sufficient for detection. Expanding the string spacing offers significant potential improvements in the effective detection area and volume, enhancing the high-energy neutrino event detection rate while being cost-effective. Larger inter-DOM and string spacing present new challenges, especially for the calibration of the detector. The original IceCube design used a string spacing of 125 m to meet specific requirements, such as using LED-based flashers for precise geometry and timing calibration and maintaining adequate sensitivity to TeV-scale muons. For IceCube-Gen2, these constraints are removed by advances in calibration methods, such as using cosmic

ray muons, camera systems, and acoustic calibration modules. The proposed optical array geometry effectively suppresses the atmospheric contribution of through-going muons. The effective lower energy threshold has increased from 10 TeV to around 30 TeV, surpressing the atmospheric muon background that dominates below 10 TeV. Therefore, this adjustment minimally impacts sensitivity to astrophysical neutrino fluxes, as high-energy events can still be reconstructed accurately despite larger string spacings [19].

For further cost-effectiveness, the new LOM has been designed accordingly and is the main candidate for the IceCube-Gen2 optical modules. Its sensor diameter has been reduced to allow deployment in narrower boreholes, significantly cutting drilling time and fuel costs. To maximize effective area while preserving omnidirectional sensitivity, the LOM incorporates multiple PMTs. Key to this design is the use of new 4-inch (10.16 cm) diameter PMTs, enabling the LOM to match the effective area of the mDOM with fewer channels. This reduction in channel count also decreases the power demands for digitization and data processing. The design of the pressure vessel is critical for determining the size of the LOM and the number of PMTs it can accommodate. Two configurations are currently developed, featuring 18 and 16 PMTs. Simulations indicate that the 18-PMT module achieves an effective area of 118 cm^2 (at 400 nm), while the 16-PMT module reaches 105 cm^2. Both designs represent a 3.2 to 4.2-fold increase in Cherenkov-averaged effective area compared to the first generation DOM, utilising PMTs with 25% quantum efficiency. The LOM will utilize gel pads specifically moulded to fit between the PMTs and the vessel using total internal reflection at the conical surface around the PMT to mitigate the need for a reflector with comparable results [51].

[19]: Aartsen et al. (2021), “IceCube-Gen2: The Window to the Extreme Universe”
[51]: Basu et al. (2021), “A Next-Generation Optical Sensor for IceCube-Gen2”

3 Photomultiplier Tube

Contents

3.1 Photoelectric Effect **36**

3.2 Secondary Emission Multipliers (Dynodes) **38**

3.3 PMT Characteristics **39**

This chapter provides a selective summary of the various manufacturers' handbooks on PMT, focusing on information relevant to this work. *Photomultiplier Tubes: Basics and Applications (4th ed.)* (i.e. chapters 2 + 4) by Hamamatsu [60] as well as *Photomultiplier Tubes: principles & applications (2nd ed.)* (i.e. chapters 1 through 5) by Photonis [61] are used. A good overview is also given by the sales handout *Photomultiplier tube basics* from Photonis [62]. Information taken from other sources, data, or images is cited as usual.

The basic principle of a PMT is simple: a photon interacts with the photocathode, is converted into an electron, and amplified to a measurable current.

To achieve this, every PMT consists of a photocathode, focusing electrodes, electron multipliers, and an anode inside a vacuum tube. A schematic PMT is depicted in Figure 3.1 as an example showing all listed components. Its function is based on two basic principles: the photoelectric effect and the secondary emission multipliers (dynodes). Light detection in a PMT follows a sequence of stages, from photon entry to signal amplification at the output:

1. Light hits the input window and excites the electrons in the photocathode, which are then released into the vacuum.
2. The focusing electrode accelerates and focuses the photoelectrons towards the first dynode. At each dynode, the electrons are multiplied through secondary emission and accelerated towards the next dynode.
3. After the last dynode, the anode collects all electrons, and a signal can be measured.

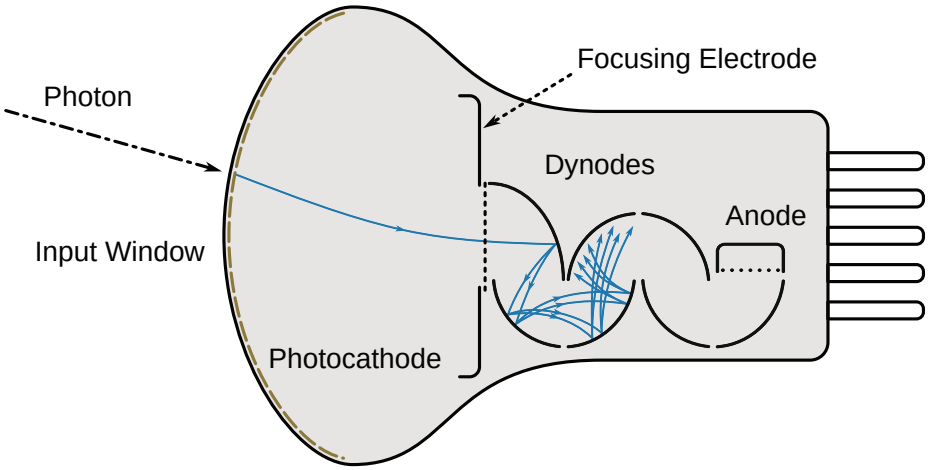

Figure 3.1: Schematics of a photomultiplier tube based on the mDOM-PMT depicting basic components.

3.1 Photoelectric Effect

The photoelectric effect was discovered by Hertz in 1887 [63] and has been the subject of many discussions and a variety of experiments until Einstein proposed a theory of the photoelectric effect utilizing the quantum nature of light [64]. In his concept from 1905, the radiation energy is localized in photons rather than continuously distributed over the whole wavefront. Each photon carries an energy $E = hv$ proportional to its wavelength v and can remove an electron from its atomic binding when the photon's energy is greater than the binding energy. In solid-state physics, the binding energy is described by the work function W and depends on the crystal face and surface contamination. The released electron, a photoelectron, can have a maximum kinetic energy of $E_{\text{kin}} = hv - W$. Suppose the photoelectron is emitted into the vacuum, it is called the external photoelectric effect. The internal photoelectric effect is when the photoelectron stays in the material and is excited into the conduction band. The external photoelectric effect is used in PMTs while the internal effect is utilized by, e.g., photoconductors.

Band models for semiconductors can describe the photoelectric effect in a photocathode. In this model, the valence and conduction bands are separated by

[63]: Hertz (1887), "Über Einen Einfluss Des Ultravioletten Lichtes Auf Die Elektrische Entladung"
[64]: Einstein (1905), "Über Einen Die Erzeugung Und Verwandlung Des Lichtes Betreffenden Heuristischen Gesichtspunkt"

an energy gap that electrons cannot occupy. The electron affinity is defined by the energy interval between the conduction band and the vacuum level barrier. The lower the electron affinity, the easier it is to excite electrons to a level where they are emitted into the vacuum. The work function W, or binding energy of the electron, is the energy difference between the Fermi level E_{F} and the vacuum level barrier E_{vac}. Electrons absorb incoming photons in the valence band, which become excited and diffuse towards the surface. If the absorbed energy is big enough to overcome the vacuum level barrier, the excited electron is emitted into the vacuum. The quantum efficiency (QE) $\eta(v)$ expresses the probability of incoming photons emitting a photoelectron and is given by:

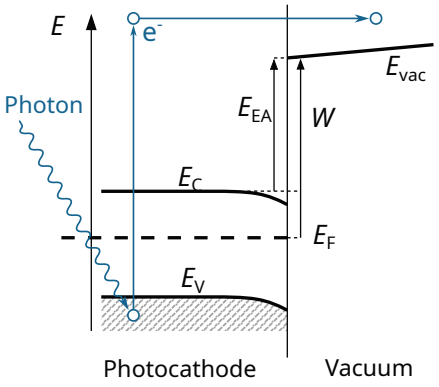

Figure 3.2: Band model of a semiconductor-vacuum transition showing the energy gap $\Delta E = E_{\mathrm{C}} - E_{\mathrm{V}}$ between the conduction E_{C} and valence band E_{V}. The electron affinity E_{EA} is defined as the energy interval between the conduction band edge E_{C} and the vacuum energy E_{vac}. The work function W is the energy difference between the Fermi level E_{F} and the vacuum level barrier. Figure based on [60, p. 15].

$$\eta(v) = (1 - R)\frac{P_{\mathrm{v}}}{k} \cdot \frac{1}{1 + \frac{1}{kL}} \cdot P_{\mathrm{s}} \tag{3.1}$$

with:

- R = reflection coefficient
- k = full absorption coefficient of photons
- P_{v} = probability that light absorption excites electrons above the vacuum level
- L = mean escape length of excited electrons
- P_{s} = probability that excited electrons at the surface are released into the vacuum
- v = frequency of light

All these parameters can be optimized towards a particular frequency by choosing a suitable material. R, k, and P_{v} are determined by the material, and the dominating factors will be L and P_{s}. The electron affinity significantly affects the probability that electrons at the surface are emitted into the vacuum, and a better crystal increases the mean escape length of excited electrons.

In the first step of measuring light, the light is transformed into an electron via the photoelectric effect. The photoelectron can be emitted in two general ways: either in the direction of the incident light, called transmission mode, or in the opposite direction, called reflective mode. For the transmission mode, a thin film of photocathode material is usually applied onto an optically transparent glass window. The reflective mode is achieved by applying the photocathode material onto a metal plate.

3.2 Secondary Emission Multipliers (Dynodes)

Studying the reflection behavior of cathode rays in 1902, Austin and Starke observed an emission of secondary electrons under certain circumstances [65]. With this discovery, primary electrons can be multiplied, making it possible to amplify a single electron into a measurable current.

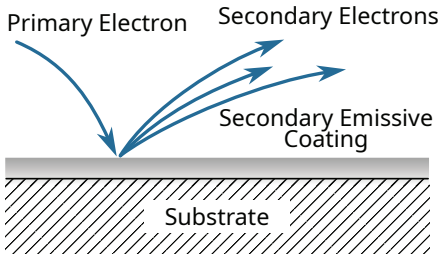

Figure 3.3: Secondary emissive materials are coated on a metal substrate to enhance the discharge of secondary electrons. Amplifications can range from 10 to more than 100. Figure based on [60, p. 19].

Today's electron multipliers are optimized toward collection efficiency and transit time spread by analyzing the trajectories of the electrons. Electric fields within the PMT influence the movement of electrons, which in turn is dominated by the dynode shape, arrangement, and applied voltage.

After the primary photoelectron is emitted at the photocathode, it must be multiplied to create a measurable current. This happens in the electron multiplier. The first part of the electron multiplier is the focusing electrode, which focuses the primary photoelectron onto the first dynode. This step is a crucial part of achieving high collection efficiency. For the collecting efficiency of the first dynode, the ratio of photoelectrons hitting the dynode to the total number of emitted photoelectrons is used. Efficiencies between 60% and 90% are typical for the first dynode. The

[65]: Austin et al. (1902), "Ueber Die Reflexion Der Kathodenstrahlen Und Eine Damit Verbundene Neue Erscheinung Secundärer Emission"

arrangement and configuration of the dynodes are optimized towards enhanced collection efficiency and minimal transit time spread. The transit time is the period between the release of a photoelectron in the photocathode and the measurement of the pulse. Different tradeoffs between the characteristics of a PMT depend on the use case. At the same time, the design must prevent ion or light feedback from earlier dynodes. The mostly curved dynodes consist of a substrate electrode and an emissive material. The number of secondary electrons depends on the chosen emissive material and the accelerating voltage. The voltage can be easily adjusted to modify the amplification or gain. A successively rising potential at each dynode accelerates secondary electrons toward the next dynode. The anode collects the secondary electrons of the last dynode. The anode is the final part of the electron multiplier and has the shape of a rod, plate, or mesh.

The space charge effect at high currents limits the linearity of a PMT. The space charge effects occur when the charge of the electrons themselves creates an electric field, significantly distorting the field distribution within the electron multiplier. Thus, the space charge can influence the electron trajectory and even cause electrons to return to the dynode from which they were released, causing collection losses. As the current density is usually highest between the last dynode and the anode, a high electric field must be applied to prevent space charge effects. In most cases, the voltage distribution between the last dynode and the anode is higher than between earlier stages to account for such effects. The so-gathered current is output to an external circuit and can be further analyzed.

3.3 PMT Characteristics

The performance of PMTs is influenced by the design, arrangement, and choice of materials used inside the photomultiplier tube. The characteristics of a PMT can be divided into characteristics of the photocathode, the dynode, and general performance characteristics such as operating stability, time response, sensitivity, or signal-to-noise ratio.

3.3.1 Characteristics of the Photocathode System

The choice of material for the photocathode can be tailored to extend towards the desired characteristics. The materials differ in their sensitivity to different spectral regions and in their electrical resistance. A lower resistance is more suited for applications with higher light intensities.

The photocathode material defines the upper bound of the sensitivity range of a PMT. The window material defines the lower bound. Different window materials offer varying levels of ultraviolet radiation transmission and are chosen in combination with the photocathode material.

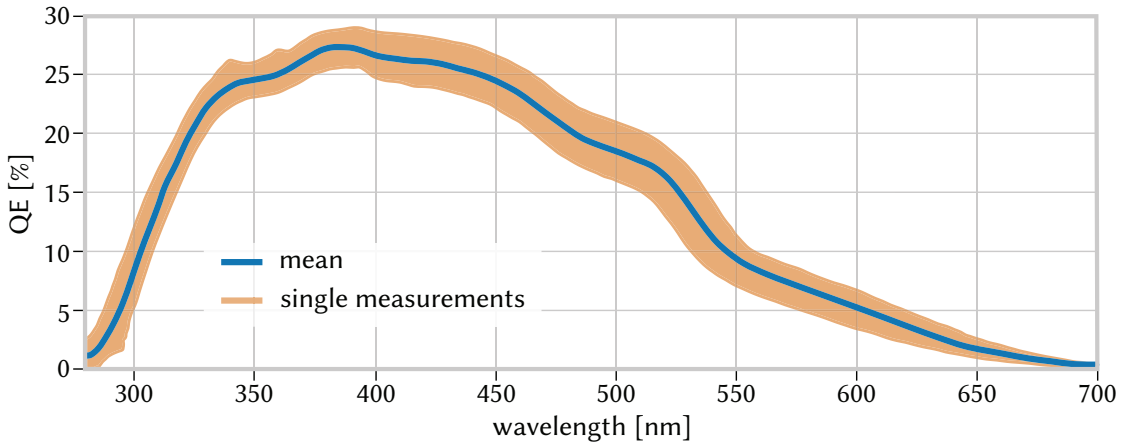

Figure 3.4: Wavelength dependency of the mDOM PMT QE. Figure adapted from [66].

The quantum efficiency (QE) quantifies the quality of the chosen photocathode and window material combination. It represents the number of emitted photoelectrons divided by the number of incoming photons and is typically expressed as a percentage. The QE for most materials is around 15–25% but can be as high as 40% for GaAsP in a vacuum without a window. As described in section 3.1, the incoming photon energy is deposited in a valence band electron, and the electron will be released into the vacuum with a certain probability. Because photons at shorter wavelengths carry higher energies, they are more likely to emit a photoelectron. The photocathode material limits the spectral response range at long wavelengths because minimal energy is required to emit a photoelectron, while the window material limits the range at short wavelengths. The photon's energy is higher at short wavelengths, causing the window material to become non-transparent to higher-energy photons.

The resulting wavelength-dependent QE for the PMTs used in the mDOM is shown in Figure 3.4.

3.3.2 Characteristics of the Dynode System

As described in the section 3.2, each dynode varies in building type and number of stages. Each type exhibits different characteristics, like gain, time response, linearity, or collection efficiency, and is selected to offer the best results in each application. Widely used types include circular-cage, box-and-grid, and linear-focused types, while more exotic types include the microchannel plate, metal channel dynode, and electron bombardment type.

The collecting efficiency of the first dynode is the probability that the photoelectron follows the predicted trajectory and lands on the effective area of the first dynode. The effective area refers to the region on the first dynode where the photoelectron is multiplied in each subsequent stage, without deviating greatly from the favorable trajectory. At later stages, electrons not following the favorable trajectory are present but contribute less to the total collection efficiency as the number of electrons increases significantly with each stage. Therefore, the collection efficiency of the first dynode contributes the most to the total collection efficiency. The voltage between the photocathode and the first dynode is essential for good collection efficiency. A low voltage leads to a more extensive spread, resulting in fewer electrons reaching the effective area of the first dynode, and consequently, the collection efficiency decreases. Collection efficiencies up to 100% can be achieved with a sufficient voltage. Together with the previously described QE, it forms the detection efficiency of a PMT, which is the ratio of incoming photons to the detected signal.

The gain G is the defining characteristic of a PMT and describes the amplification of the photocathode current I_c into a measurable current I_a at the anode.

$$G = \frac{I_\mathrm{a}}{I_\mathrm{c}} \tag{3.2}$$

The electric fields between each dynode pair cause the incoming electrons to hit the next dynode with an energy of a few hundred electron volts, amplifying the current from dynode to dynode via secondary emission. The amplification depends on two characteristics: the secondary emission coefficient δ_i of the n-th dynode and the

collection efficiency c_{n-1} of the *(n-1)*-th dynode. Both increase with the voltage U_i between the two dynodes.

$$g_i = c_{n-1}\delta_i = a_i U_i^k \tag{3.3}$$

Where a is a constant and k is defined by the structure and material of the dynodes. Using this expression, the gain simplifies to

$$\begin{aligned} G &= \prod_{i=1}^{n} g_i = A \cdot U^{kn} \\ \text{and } A &= \frac{a^n}{(n+1)^{kn}}, \end{aligned} \tag{3.4}$$

if the collection efficiency of all dynodes is 100%, where n denotes the number of dynodes. This equation shows that the gain is proportional to the kn-th power of the total supply voltage and can, therefore, be adjusted after the PMT is fabricated. It also implies that changes in the supply voltage due to temperature changes, drift, ripples, or unstable regulation will result in gain changes and must be considered in the design of the power supply. One way to measure the gain of a PMT is by calculating the measured charge at the output of the PMT and dividing it by the electric charge of a single electron, assuming the incident light is so sparse that only single photons hit the photocathode.

3.3.3 Timing Characteristics

Besides amplifying a single photoelectron to a measurable current, the timing characteristics, such as response time or transit time spread (TTS), are other essential features of PMTs. The dynode type dominates the time response of a PMT. Nevertheless, the supply voltage has a significant effect, too, as increasing electric fields accelerate electrons faster, resulting in higher transit speeds followed by a shorter transit time and an improved time response. Several time response characteristics, such as rise, fall, and transit time, can be measured.

Single photon pulses can be used to measure the electron transit time, as well as its rise and fall times. The electron transit time is then defined by the time difference between the light source trigger pulse and the pulse's maximum. To measure the transit time within the PMT, a reference photodiode is needed at the same place as the PMT to rule out effects from the light source system. As seen in Figure 3.5, the rise and fall time is defined between 10 to 90% of the pulse height. The rise time

is defined as the time the output requires to rise from 10 to 90% of the maximum pulse height. The fall time is the time the output needs to decrease from 90 to 10%. Commonly, the fall time is larger than the rise time.

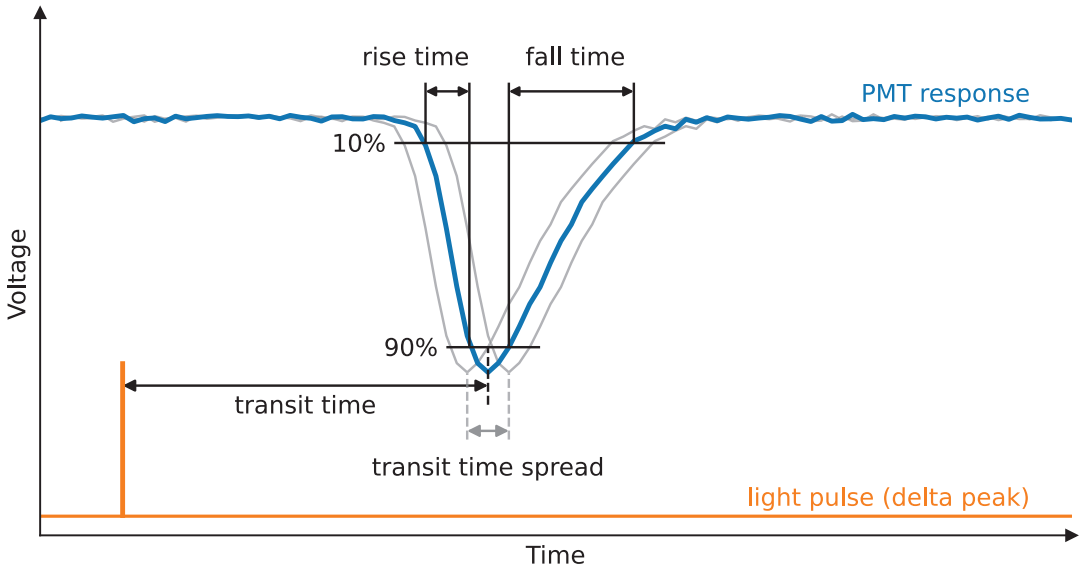

Figure 3.5: Sketch of a PMT response to a dealt peaked light pulse defining the rise/fall times and transit time.

Using single photons for the timing measurements allows for measuring the transit time spread. The transit time for each pulse through the PMT fluctuates, and a slight transit time difference occurs depending on the position where the photon hits the photocathode. As seen in Figure 3.6, a simple measurement setup will measure the combined TTS. A small TTS is essential to measurements where the number of photons and their arrival times are needed. This could be for coincidence measurements or arrays of PMTs used to reconstruct event directions based on photon arrival times, like in the IceCube detector.

To count the number of photons in one pulse, the PMT must exhibit a good linearity over a wide dynamic range from single photons up to several hundred per pulse. At high incident light levels, the output starts to deviate from the linear response. If an intense light pulse hits the PMT, a large current is produced in the final dynode stages. This high current causes high space charge densities and leads to current saturation. The current cannot increase proportionally to the light intensity anymore. The space charge effect depends on the electric field between the dynodes.

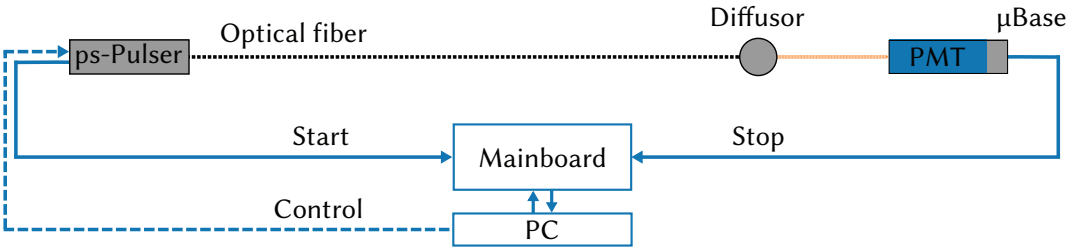

Figure 3.6: Block diagram for the TTS measurement.

Proximity to the next dynode provides higher field strength; bigger dynodes reduce the electron density and, therefore, the space charge effect. A higher supply voltage increases linearity as the field strength between the dynodes increases. However, the positive impact is counteracted by the gain increase and higher currents. For a PMT used in pulse mode operation, the linearity can be measured by increasing the light intensity in defined steps and comparing the output response. If the output ratio starts to differ from the light intensity ratio, the PMT response is no longer linear.

3.3.4 PMT Noise

Every PMT exhibits a small output of current, even in complete darkness. This current is called dark current and is later referred to as the baseline. Part of the dark current is a side-effect of the high operating voltages of up to 3000 V applied to the PMT. A minimal leakage current is present, even with high-quality insulation between all parts of the PMT. A clean PMT and low humidity can effectively lower the leakage current.

Other sources can contribute to the dark current when the PMT is used in DC mode or generate undesired pulses in pulse mode. When the PMT is used in pulse mode, as it will be for the IceCube Upgrade, the following causes are combined in the dark noise or dark rate of the PMT. The dark rate is the number of pulses measured by the PMT in complete darkness.

Uncorrelated Noise

Thermionic emission is the spontaneous emission of electrons from the photocathode or dynode surfaces. In the band model of the photocathode, some electrons can move freely within the band, and their energy follows a Fermi-Dirac distribution. Some electrons will have enough energy to overcome the work function and be released in the vacuum. W. Richardson described this effect in 1901 and stated that the thermionic emission is a function of the work function and absolute temperature T. [67, 68]

$$I = AT^2 \exp\left(-\frac{W}{kT}\right) \tag{3.5}$$

I is the thermionic emission current, A a constant, W the material's work function as described in section 3.1, and k the Boltzmann constant. This equation shows that cooling the PMT effectively lowers the thermionic emission and, therefore, the dark current.

Scintillation in the surrounding glass or window can be caused by stray electrons that deviate from the preferred trajectory and enter the glass envelope. This effect can be minimized by applying a so-called HA coating to the outside of the PMT. This conductive coating is connected to the cathode potential and is a barrier to the usually grounded cage around the PMT.

Field electron emission may occur when high supply voltages are used. This can be observed by a fast rise in dark rates above a specific supply voltage. Operating the PMT within the specified rating effectively prevents field electron emission by the dynodes.

Environmental gamma radiation and particles from cosmic ray air showers can also introduce false output pulses. Especially muons produced in cosmic ray air showers can be an important source of dark noise. When muons travel through the glass, Cherenkov radiation is emitted if the velocity of the muon exceeds the velocity of light inside the glass. This Cherenkov photon can interact with the photocathode and create a false pulse. Good shielding can block part of the environmental

[67]: Richardson (1929), *Thermionic Phenomena and the Laws Which Govern Them*
[68]: Coates (1972), "Thermionic Emission from Photocathodes"

radiation, but muons are especially difficult to block as they can travel several kilometers in water.

Radioisotopes in the glass envelope are the last source of dark pulses discussed in this scope. As most glasses contain potassium, a small amount of ^{40}K is also present inside the glass. ^{40}K is a radioactive element with a long half-life of 1.25 billion years. Together with other radioactive trace particles like Uranium and Thorium that enter the glass during melting and production, their decay releases beta and gamma rays inside the glass. As it is impossible to shield against radiation inside the glass envelope, the decay can trigger dark noise and must be managed for low-noise applications.

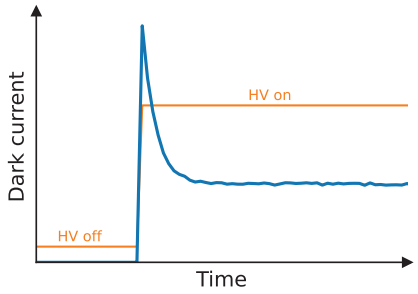

Figure 3.7: Illustration of dark-current behavior after switching on the high voltage.

All of the aforementioned dark pulses are independent of an incident photon and, therefore, happen randomly. The rate at which they occur can be reduced by operating at lower temperatures or a burn-in of the PMT before use.

The burn-in describes a time period in which the PMT is connected to its high supply voltage but not used for measurements. When a PMT is exposed to ambient light, the cathode excites, and the dark current can initially be several orders of magnitude larger. The burn-in allows the dark current to settle after switching on the high voltage. Figure 3.7 shows an exemplary dark current and behavior after switching on the high voltage. The time to achieve average dark-current levels depends on several factors, such as previous illumination levels or the form of magnetic shielding.

Correlated Noise

In contrast to the random dark pulses, there are pulses highly time-correlated with the initial photon. These pulses are called pre-, delayed-, and after-pulses. Figure 3.8 shows a typical transit-time distribution measured in Dortmund with the Hamamatsu R15458-20 PMT.

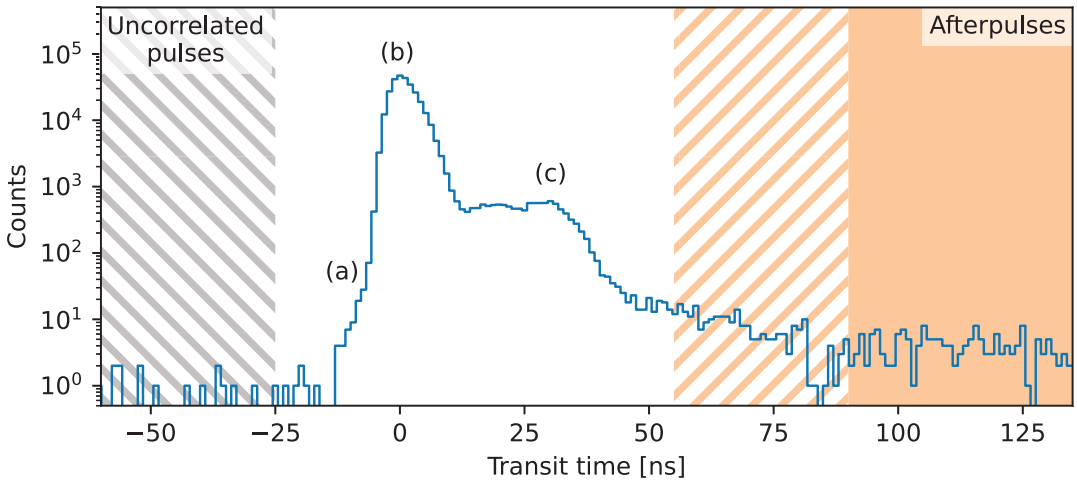

Figure 3.8: Single-photoelectron transit-time distribution of Hamamatsu R15458-20 PMT (DM00373). The mean transit-time is 53 ns corresponding to the maximum of the distribution. (b) denotes the main peak and (a) the distribution of the prepulse. Delayed pulses are in (c).

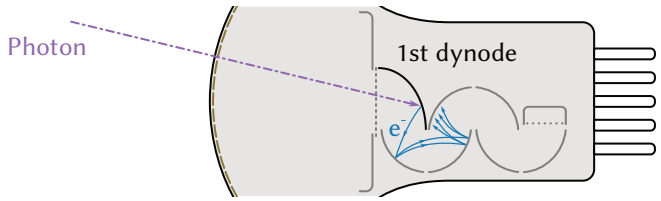

Figure 3.9: Illustration of a pre pulse. The photon moves through the photocathode and frees an electron on the first dynode.

Prepulses (a) are triggered by photons traversing through the transparent photocathode and interacting with the first dynode, creating a photoelectron. Since light travels the distance to the first dynode faster than an electron, this results in a pulse that is a few tens of nanoseconds earlier than expected. As these pulses skip the first dynode, they exhibit lower amplification, resulting in a less pronounced pulse.

Delayed pulses (c) are fully developed pulses that arrive some ten nanoseconds after the expected signal time. They appear as photoelectrons bounce off the first dynode and are subsequently accelerated back towards it, initiating the cascade slightly later and leading to an output pulse at the anode.

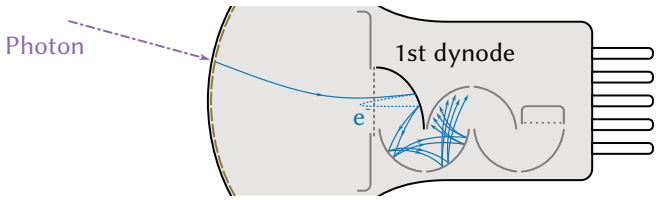

Figure 3.10: Illustration of a delayed pulse. The photoelectron bounces off the first dynode.

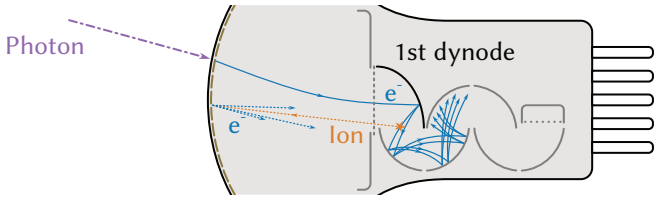

Figure 3.11: Illustration of an afterpulse. Electrons from the avalanche can ionize residual gas inside the PMT. If the ion interacts with the photocathode, an afterpulse can be measured.

Afterpulses are caused by ionized gas inside the PMT. Even as the inside of the PMT is kept in a vacuum, some residual gas remains. Electrons can collide with the residual gas and ionize single atoms. If a positive ion strikes the active surface of the photocathode or dynode, it can release secondary electrons, resulting in a large output pulse. Over time, the vacuum might get contaminated by the decay products of radioisotopes inside the glass envelope, making pulses initiated by ionization more likely. This increase in afterpulses needs to be considered when planning experiments with a long lifetime, such as IceCube.

mDOM PMT and Acceptance Testing

4 IceCube Upgrade mDOM and PMT

Contents

4.1 mDOM **52**

4.2 The mDOM PMT **54**

Since its completion in 2011, the IceCube Neutrino Observatory at the geographic South Pole has led to numerous new findings in high-energy astroparticle physics. In addition to the detection of an astrophysical neutrino flux in 2013 [8, 69], the first candidates for neutrino sources outside our solar system have also been found in recent years [31, 32]. In parallel to the high-energy neutrino events, IceCube records low-energy neutrinos starting at a few GeV [70]. IceCube Upgrade is one of two planned extensions of the IceCube Neutrino Observatory. It consists of seven additional strings equipped with a total of about 700 optical sensor modules at a depth between 2150 and 2425 m and will be installed in the center of the existing IceCube detector. The higher density of the sensors with 20 m spacing between the strings and only 3 m vertical spacing increases the sensitivity at low energies and enables better reconstruction of these low-energy events.

The mDOM consists of 24 3 inch PMTs in a 356 mm pressure housing. The arrangement of several small PMTs in one housing offers several advantages over the DOM:

- larger active photocathode area
- better photon capture and later saturation
- better angle acceptance and sensitivity
- local coincidence for triggering

[8]: Aartsen et al. (2013), "Evidence for High-Energy Extraterrestrial Neutrinos at the IceCube Detector"
[69]: Aartsen et al. (2013), "First Observation of PeV-Energy Neutrinos with IceCube"
[31]: Aartsen et al. (2018), "Multimessenger Observations of a Flaring Blazar Coincident with High-Energy Neutrino IceCube-170922A"
[32]: Abbasi et al. (2022), "Evidence for Neutrino Emission from the Nearby Active Galaxy NGC 1068"
[70]: Aartsen et al. (2018), "Measurement of Atmospheric Neutrino Oscillations at 6–56 GeV with IceCube DeepCore"

In addition, each mDOM is equipped with calibration modules such as cameras and LED flashers. The PMTs are the eyes of every mDOM and must be checked for function before installation. In addition, the more than 10 000 PMTs will be divided into so-called voltage classes. This classification allows the installation of PMTs with a similar operating voltage in one mDOM. This will reduce the leakage current as the potential difference between the individual PMTs is reduced.

The next chapter discusses the mDOM in more detail before section 4.2 takes a look into the mDOM PMT and its specifications.

4.1 Multi-PMT Digital Optical Module (mDOM)

The design of the mDOMs is based on the optical modules with multiple PMTs used for the first time in KM3NeT [71] and was adapted to the special conditions at the South Pole [72]. These conditions include a diameter of <360 mm, operating temperatures up to −45 °C, a temperature shock from −45 to 20 °C or pressures of up to 700 bar. Such a temperature difference occurs when the mDOM is immersed in the borehole. The high pressure appears during the refreezing of the borehole, starting on the surface and gradually freezing to the bottom. Once the upper part is frozen, the water can no longer expand, resulting in high pressures, especially in the lowest mDOMs. [50].

A schematic representation of the mDOM with all components can be seen in Figure 4.1. The outer pressure vessel, in which all other components are housed, is made of borosilicate glass and has a wall thickness of 13.5 mm. The outer diameter is 356 mm, and simulations by the manufacturer Nautilus GmbH show a pressure resistance of 1050 bar. The pressure housing is divided into two hemispheres, which merge at their contact surfaces into a cone with a length of 27.5 mm and a wall inclination of 2.8°. As a result, the entire module is slightly higher than the diameter. A 3D-printed support structure made of nylon 12 (PA12) holds all components within the half module and serves as a barrier for the optical gel. The optical gel couples the PMT and the pressure vessel optically and consists of two individually

[71]: Bruijn (2019), “The KM3NeT Digital Optical Module and Detection Unit”
[72]: Classen (2017), “The mDOM - a Multi-PMT Digital Optical Module for the IceCube-Gen2 Neutrino Telescope”
[50]: Aartsen et al. (2017), “The IceCube Neutrino Observatory: Instrumentation and Online Systems”

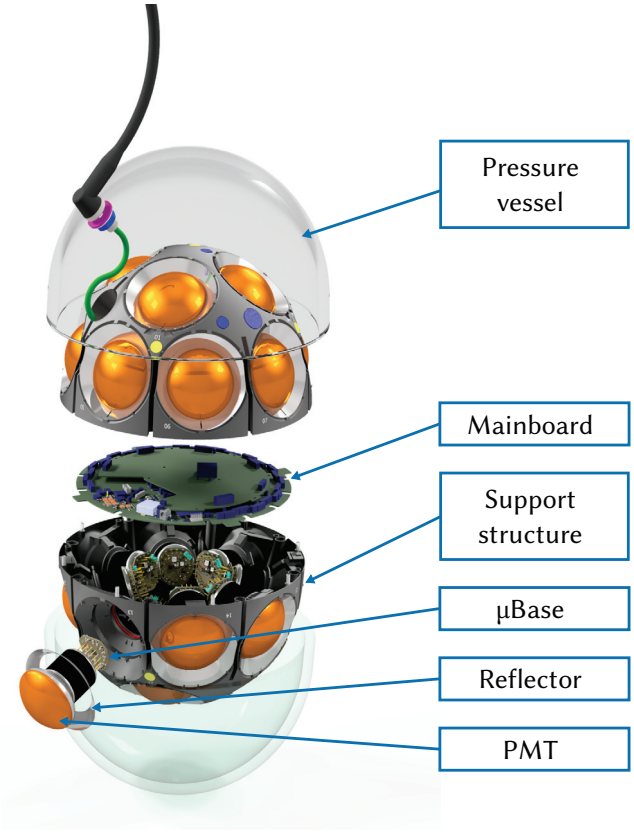

Figure 4.1: Exploded view of an mDOM. Image courtesy of the IceCube collaboration.

liquid components that harden slowly after mixing. At the same time, it fixes all components in place and dampens vibrations during transportation. The glass of the pressure vessel, the gel, and the glass of the PMTs are optimized for high transparency to wavelengths down to ∼300 nm [72].

Each half module contains 12 PMTs, and the lower half module also houses the mDOM mainboard. The PMTs are aligned in different directions and surrounded by a reflector ring. This reflector increases the active area of the PMTs by reflecting incident photons onto the PMTs.

There are three basic ways to collect data with the mDOM mainboards:

1. **Waveform measurement**: Waveforms, as described in section 4.2, are recorded by the mainboards, and all essential information, such as the charge or arrival time, is later extracted from the waveform. The length of the waveform can be adjusted via a configuration file. The advantage of this

[72]: Classen (2017), "The mDOM - a Multi-PMT Digital Optical Module for the IceCube-Gen2 Neutrino Telescope"

readout mode is that the waveform is retained and can be analyzed later. However, considerably more data must be transferred from the mainboards to the PC, resulting in longer measurements and higher storage usage.

2. **Chargestamp measurement**: The waveform is analyzed on the mainboard, and only a charge stamp, consisting of charge and arrival time, is transmitted. Additional information, such as integration window or assumed analog front-end (AFE) gain, is also included in the charge stamp. The waveform is lost and cannot be analyzed; for example, adjusting the integration window is impossible. However, data transmission is significantly faster.
3. **Scaler measurement**: In a scaler measurement, the PMT signal is only examined to determine whether the discriminator threshold is exceeded or not. A predefined deadtime in which no new pulse is counted is set after each discriminator crossing. Only the number of discriminator crossings in a given time window is sent to the PC. This measurement method is used for dark rate measurement.

4.2 The IceCube Upgrade mDOM PMT: Hamamatsu R15458-20

Hamamatsu Photonics manufactures the PMT model R15458-02 for the IceCube Upgrade mDOM. The R15458-02 is based on the PMT type R12199-02 developed for the KM3NeT experiment and adjusted for the unique requirements of IceCube. The main difference is a reduced length from 98 mm to 91 mm and an HA coating around the base of the R12199-02. The HA coating reduces and stabilizes the intrinsic background of the PMT. A µBase is soldered to the PMT's flying leads at the factory, and the PMT-µBase unit forms the mDOM PMT R15458-20. A photograph of the R15458-20 is shown in Figure 4.2.

µBase

The main function of the custom-designed µBase is to supply a stable and controllable high voltage to the PMT and to provide a break-out connection for the PMT signal. Figure 4.3 shows a µBase attached to a PMT. The main components used to generate



Figure 4.2: Picture of the Hamamatsu R15458-20 PMT.

and control the high voltage are composed of a microcontroller, an LC resonator, and a Cockcroft-Walton multiplier.

The microcontroller produces a high frequency sqaure wave between 0 V to 3.3 V at a typical frequency of 110 kHz. The square wave is fed into an LC resonator, resulting in an output sine wave with a peak-to-peak amplitude between 75 V to 150 V. This amplitude V_{max} can be adjusted by changing the frequency of the square wave. When setting the high voltage, the microcontroller performs a frequency scan, measuring the output voltage for different frequencies. The frequency is chosen so that V_{max} is about 7.5% above the desired output value. The output voltage V_{out} is precisely adjusted by altering the square wave's duty cycle D. This is possible as the LC resonator primarily responds to the lowest sine wave component of the Fourier decomposition.

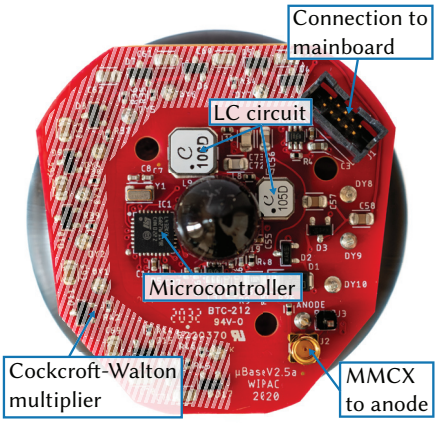

Figure 4.3: A µBase attached to the flying leads of a PMT showing the different main parts of the electronic circuit.

The Cockcroft-Walton multiplier generates a high DC voltage from a low AC voltage input and consists of a series of diodes and capacitors. At each stage of the multiplier,

the voltage of the previous stage is doubled, resulting in a 13-stage multiplier on the µBase. The Cockcroft-Walton multiplier on the µBase follows approximately a ratio of 1:1:1:1:1:1:1:1:1:1:3 starting at the anode and ending with a negative high voltage at the cathode. RC filters at each output of the Cockcroft-Walton multiplier smooth the DC voltage before being applied to the dynodes and anode.

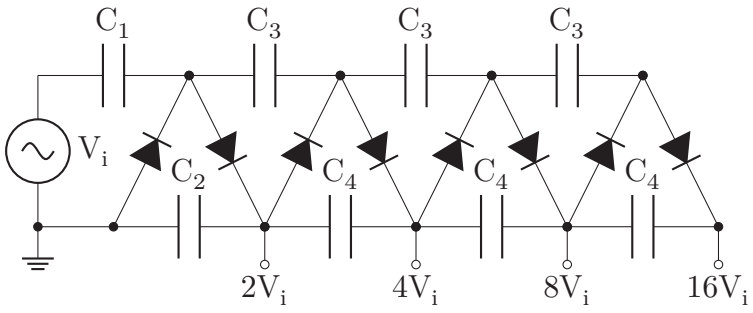

Figure 4.4: A basic four stage Cockcroft-Walton multiplier. The connection points marked are where the voltage is two, four, eight, and sixteen times the input voltage.

To maintain the desired high voltage stability, a control loop is implemented in the microcontroller. It performs measurements ten times per second at the first stage (corresponding to dynode 10) of the Cockcroft-Walton multiplier and adjusts the duty cycle accordingly.

The anode signal is tapped out via a coax cable with an MMCX connector. The communication with the µBase and the provision of the operating voltage are done via a 10-pin ribbon cable. The firmware on the µBase can be updated remotely.

Specifications

With an outer diameter of 356 mm, the mDOM is only slightly larger than the original IceCube DOMs. The R15458-20 has a diameter of 80 mm and a length of 91 mm without the µBase. The compact form factor is a prerequisite for accommodating the 24 PMTs in the mDOM. Nevertheless, for good results, the electronic requirements also need to fit IceCubes' use case and are listed in Table 4.1 as agreed with the manufacturer [73].

[73]: Kappes (2019), *mDOM PMT Tender Specifications*

Table 4.1: The specifications of the PMTs agreed with the manufacturer.

Metric		Specification	Conditions
Operating temperature		−45 °C to 30 °C	
Storage temperature		−60 °C to 50 °C	
High Voltage		950 V to 1350 V	@ gain=5×10^6
Quantum efficiency		> 7%	@ 325 nm
		> 25%	@ 380 nm
		> 15%	@ 500 nm
avg. SPE amplitude		> 6 mV	@ (gain=5×10^6, 50 Ω impedance)
TTS (sigma)		< 2 ns	
Rise time		>1 ns and <5 ns	(10 – 90%)
SPE resolution (sigma)		< 0.7 pe	
Peak-to-valley ratio		> 2.0	
Linearity		within 10%	> 100 pe
Prepulsing	[−20 ns, −10 ns]	< 1%	@ (gain=5×10^6, T=−20 °C, 0.2 pe threshold)
Delayed pulses	[15 ns, 80 ns]	< 5%	@ (gain=5×10^6, T=−20 °C, 0.2 pe threshold)
Afterpulsing	[100 ns, 12 µs]	< 15%	@ (gain=5×10^6, T=−20 °C, 0.2 pe threshold)
Dark rate		< 150 Hz	@ (gain=5×10^6, T=−20 °C, 0.2 pe threshold, 100 ns dead time, photocathode in air, after 5 h in dark)

PMT Opperation

The PMTs in the mDOM are operated in pulse mode. In contrast to DC mode, in which the intensity of the incident light is so high that a constant current is measured at the anode, in pulse mode, the incident photons or photon packets are so rare that they can be detected as individual pulses at the anode. The two modes differ in the downstream readout electronics. The output of the PMT can

be regarded as a current source. A time interval of the current measured at the output is referred to as a waveform and forms the basis for all measurements. If the readout of the waveform is triggered externally, the waveform always contains the dark current and, in some cases, a pulse. An example of a waveform for both cases is shown in Figure 4.5.

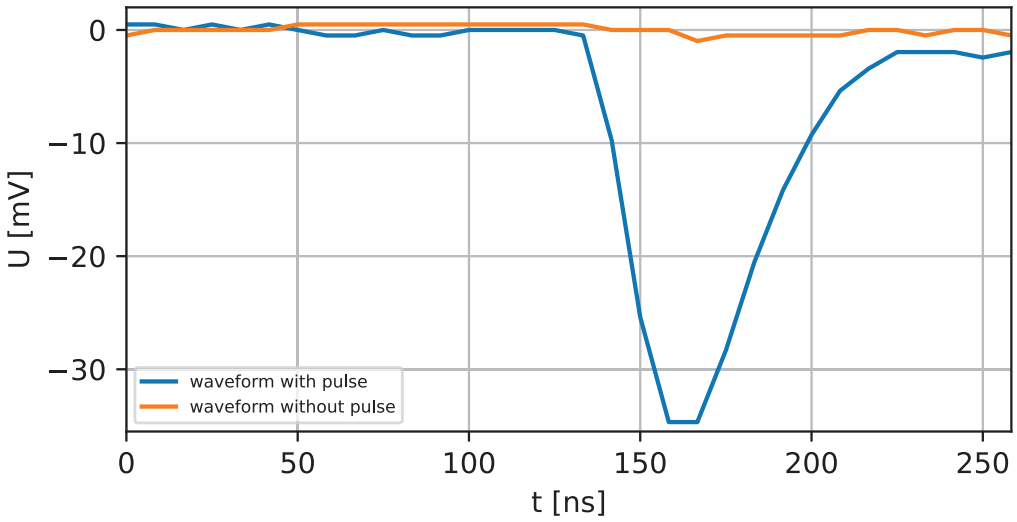

Figure 4.5: Two waveforms, measured with the PMT DM00230 at −20 °C. Both show the dark current, which has already been subtracted from the voltage values. The blue data also contains a photon pulse.

The anode current is converted into a voltage in the readout electronics and transformed into a digital signal via a flash analog-to-digital converter (FADC). The internal or external trigger signal also defines the readout interval as the time window before and after the trigger time. This way, specific waveform properties can be defined, e.g., a time interval before the pulse for dark current correction or the expected time interval in which the pulse should be located.

The period for the dark current correction is indicated by the orange area in Figure 4.6. Only the dark current is expected in this area, and the median is subtracted from the entire waveform. A photoelectron triggered the subsequent voltage pulse, and an external signal triggered the waveform. The photon pulse is expected in the blue region, and the voltage signal can be converted into a charge via integration. If there is no pulse in the waveform, the average charge in this area

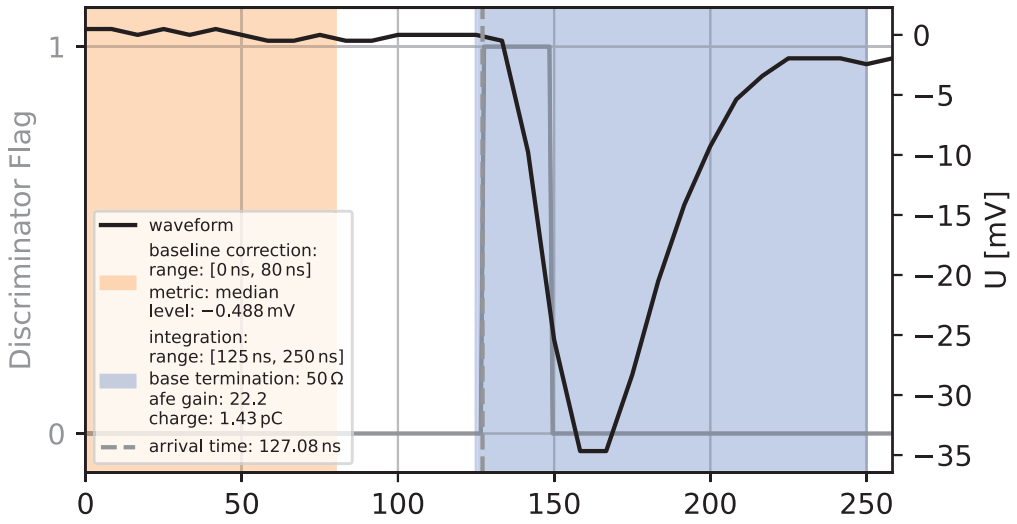

Figure 4.6: A waveform with pulse measured with the PMT DM00230 at −20 °C. The area marked in orange is used for dark current correction. The median of the voltage measured in this range is subtracted from the total waveform, setting the noise to zero. The voltage is integrated over the second time interval (blue) of 125 ns to 250 ns, and the charge is calculated.

is zero. The charge is calculated as follows

$$Q = \int \frac{U}{R} dt \tag{4.1}$$

where Q is the charge, U is the voltage, R is the impedance of the signal output and dt is the time interval over which it is integrated. The impedance for this PMT and this measurement setup is 50 Ω.

5 The mDOM PMT Test Bench

Contents

5.1 Design **62**

5.2 Implementation at the TU Dortmund University **67**

5.3 Calibration **80**

5.4 A Complete Testing Cycle **92**

5.5 The Measurements **95**

Lasse Halve developed and implemented the idea and concept of the test bench at the RWTH Aachen [74]. While the idea and concept remained the same, the design and implementation needed significant adjustments to suit the conditions in Dortmund.

The main goal of the test bench is to ensure the functionality and conformance to the requirements (see section 4.2) of each PMT. The entire mDOM is later subjected to further functional tests. However, opening a sealed mDOM to replace a component is very labor-intensive and time-consuming and, therefore, not feasible on a large scale. In addition, the required operating high voltage (HV), photodetection efficiency, linearity, temporal resolution, probabilities of pulses just before, just after, and an extended time after photons arrive are calibrated, and a dark pulse rate measurement is performed. A classification of PMTs based on their operating HV is also conducted. PMTs with the same operating HV are preferably used in one module to avoid possible leakage currents between PMTs. All tests are performed at a temperature of $-20\,°C$. This temperature corresponds to the average operating temperature of IceCube DOMs in the Antarctic ice [50, 75] and is stated in the manufacturer's specifications.

The following demonstrates that the idea and concept created by Lasse Halve are transferable, adaptable, and expandable to other sites, allowing easy expansion of

[74]: Halve (2024), "Validation of Optical Sensors for the mDOM of the IceCube Upgrade"
[50]: Aartsen et al. (2017), "The IceCube Neutrino Observatory: Instrumentation and Online Systems"
[75]: Price et al. (2002), "Temperature Profile for Glacial Ice at the South Pole: Implications for Life in a Nearby Subglacial Lake"

test capabilities in preparation for building IceCube-Gen2.

Section 5.1 will discuss the concept of the test bench and the software used. The realization in Dortmund and the final setup will be described in section 5.2. The necessary calibration measurements will be discussed in section 5.3. The final section 5.4 explains the tests performed and the sequence of a test cycle.

5.1 Design

More than 10 000 PMTs were ordered from Hamamatsu Photonics for the 402 mDOMs of the IceCube Upgrade, some test modules, and spare PMTs. Of these, 4793 PMTs were tested in Dortmund. To meet production deadlines, the throughput of the two test benches in Aachen and Dortmund must be several hundred PMTs per week. This is achieved by simultaneously testing approx. 90 PMTs per test cycle and a cycle time of less than 24 h. While the measurements run, the next PMTs can be prepared for the next cycle. This reduces the time between two cycles from several hours to only approx. 30 minutes.

In preparation for the IceCube-Gen2 high-energy extension, the test bench must be capable of testing other PMT types. A modular design, 3D-printed mounts for the PMTs, and the mainboards used in the mDOMs to digitize the PMT pulses allow for easy expansion and adaptation to new requirements.

5.1.1 Hardware

The test bench concept described below was implemented differently at two locations: first at the RWTH Aachen by Lasse Halve, and then at the TU Dortmund University as part of this work. Despite differences in implementation, the concept and software used remain the same, allowing for easy scaling of test capacities by setting up additional sites. Section 6.5 proves that both sites provide comparable results.

Figure 5.1 shows the concept of the site at Dortmund. A cooling chamber divides the test bench into two areas: a temperature-controlled area that can be cooled down to −25 °C and an outside area that is not temperature-controlled.

Inside the cooling chamber is a rack on which 94 PMTs can be mounted in one plane using so-called Vogelstangen. On the opposite side, an optical fiber couples

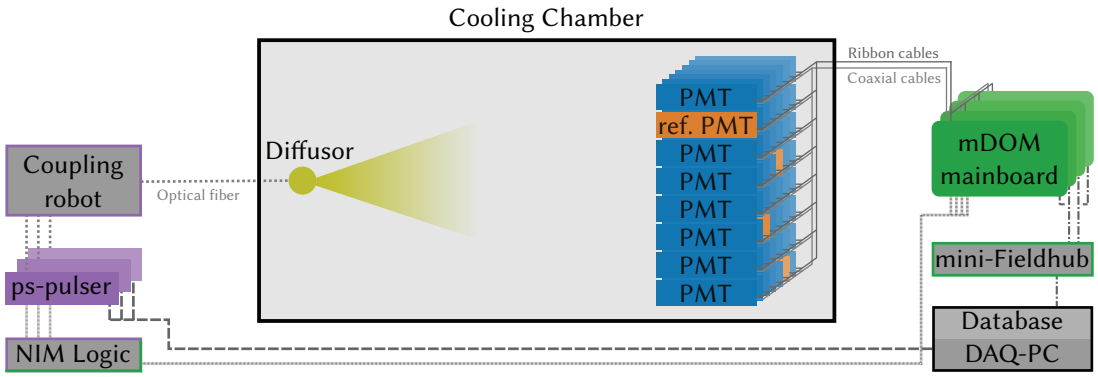

Figure 5.1: The concept of the test bench with all functional components. Divided into the temperature-controlled (light gray background) and the non-temperature-controlled area.

short light pulses into the cooling chamber. These light pulses are scattered by a diffuser almost homogeneously (see section 5.3) onto the plane of the PMTs. Signal and control lines are attached to the µBase and organized in cable bundles. On each PMT position, one signal and control cable pair is led out of the bundle. All cables are led through a hole to the outside of the cooling chamber.

A second rack outside the cooling chamber, identical to the one inside the chamber, is used to prepare the PMTs for the next measurement. This reduces the time between two measurements from approx. 4 hours needed to exchange all 94 PMTs for new ones to just 30 minutes.

The control and signal lines are routed to the mDOM mainboards. The mainboards digitize the signal and control the operating voltage of the PMTs. A maximum of 24 PMTs can be connected to each mainboard. The four mainboards are, in turn, connected to a so-called miniFieldhub. The miniFieldhub communicates with the mainboards, initializes them, and bundles the communication with a PC. This PC is responsible for controlling the entire system. It monitors and controls the temperature in the cooling chamber, reads the mainboards, and controls the light sources. Three different light sources are based on a ps-pulser design by Martin Rongen [76]. Two pulsers generate light pulses smaller 1 ns with 375 nm and 505 nm. A third pulser was modified to generate light pulses with approx. 10 ns length at a 505 nm LED. To guide only one light source into the cooling chamber at a time, the

[76]: Rongen et al. (2018), "Design and Evaluation of a Versatile Picosecond Light Pulser"

corresponding LED is coupled into the optical fiber, and the other two are switched off completely.

All settings, temperatures, and measurement results are stored in a database on the PC. A software (`pmt_taco`) handles the automation of the entire test bench. It controls all components, starts the measurements, evaluates them, and stores everything in the database.

5.1.2 Software

Like the hardware, the software is designed for expandability and flexibility. It is based on Python 3 and has a modular design. This makes it easy to add new modules to the software and adapt existing ones without making fundamental changes. This is especially necessary concerning the use of different hardware at the two sites and for future IceCube-Gen2 applications.

The software written for this project is called **PMT T**esting **A**nd **Co**ntrol (`pmt_taco`) and was developed by Lasse Halve at RWTH Aachen University. Necessary adaptations to the TU Dortmund University hardware, writing of essential modules, new measurements, and debugging were done during this project. The software can be found on GitHub in the `WIPACrepo`. It is currently only available to members of the IceCube Collaboration, as the software and measurements were developed specifically to communicate with IceCube modules. The structure of `pmt_taco` follows the layout of a typical *run*and is shown in Figure 5.2.

The individual modules of `pmt_taco` are divided into six main sections:

scripts The folder most frequently used by the user. All scripts for measurements and analysis, as well as configuration files, are stored here.

core Contains all functions that have a higher-level function and are necessary for the operation of the test bench. For example, the Serial-to-TCP server, various controllers, and scanner service can be found here.

hardware All functions for addressing, controlling, and reading the various hardware components are located here.

analysis The analysis scripts for the various measurements are located here.

special Contains scripts and functions not fitting into the sections above, e.g., a measurement to power down the PMTs.

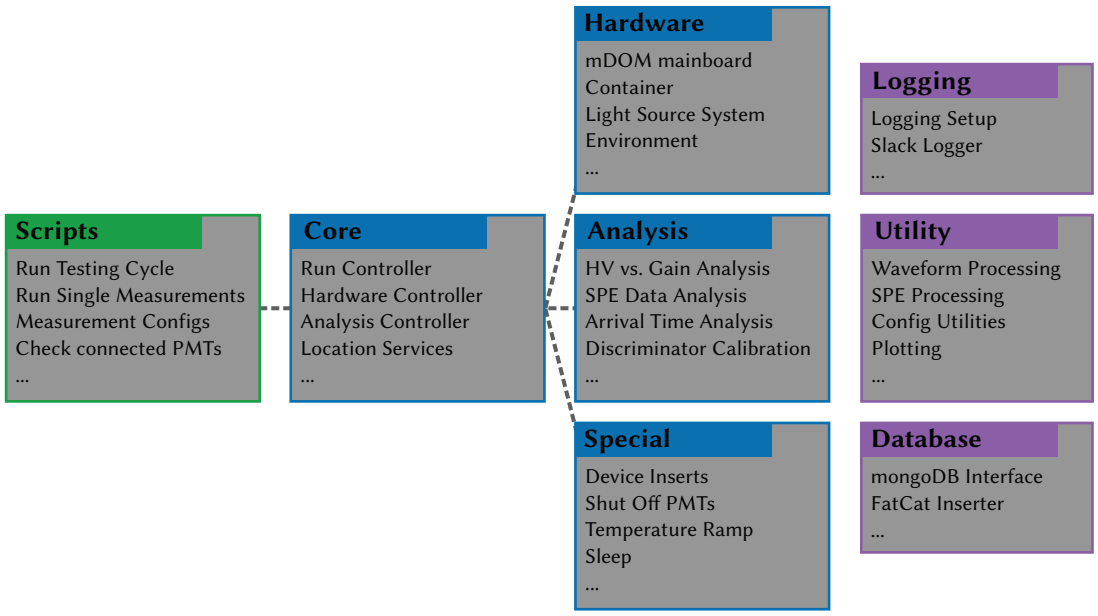

Figure 5.2: Architecture of `pmt_taco`. Following a typical run: The scripts in green are executed by the shifter, the core module handles the three different measurement types (hardware, analysis, special) depicted in blue, and supporting modules are on the right in purple.

utility Supporting functions like plot scripts or waveform editing.

database The interface to the local MongoDB and the fatcatDB hosted in Madison, WI, is defined here.

logging Everything related to log messages and handling Slack alerts can be found here.

Each section contains a folder with configuration files. These files store all variables, names, and settings. The number of hard-coded values is minimized, allowing for easy adaptation to other setups or hardware implementations.

The layout of the software is designed to mimic the structure of a test *run*. The shifter executes a Python script initiating a *Run Controller*. The *Run Controller* is the core module steering the three different measurement types (hardware, analysis, special). It receives an *iterator* over configuration dictionaries for the measurements. Depending on the measurement type, the configuration is relayed to the correct submodule.

- **Hardware** measurements are handled by the *Hardware Controller*. Data

from the PMTs are recorded and stored in the local MongoDB.

- **Analysis** measurements are handled by the *Analysis Controller*. Data are retrieved from the local MongoDB, analyzed, and the results are stored there and vetted against the specifications. This is fully parallelized with one process for each PMT.
- **Special** measurements are handled by the *Special Controller*. Everything that does not fall into the previously mentioned categories (e.g., device inserts, temperature ramps) is handled here.

Besides `pmt_taco`, other software is used to run the test bench. One is the already mentioned MongoDB database for local storage of settings, logs, measurements, and analysis results. Others are the `fatcat_db` and the `fh_server`. Both are software packages developed and maintained by the IceCube collaboration. The `fatcat_db` provides an interface to the IceCube production database. This database stores all individual parts, assemblies, and modules, and links the results of tests or calibrations to the components. The `fh_server` software package provides a network interface to the miniFieldhub and contains the current firmware of the mDOM mainboards and PMTs.

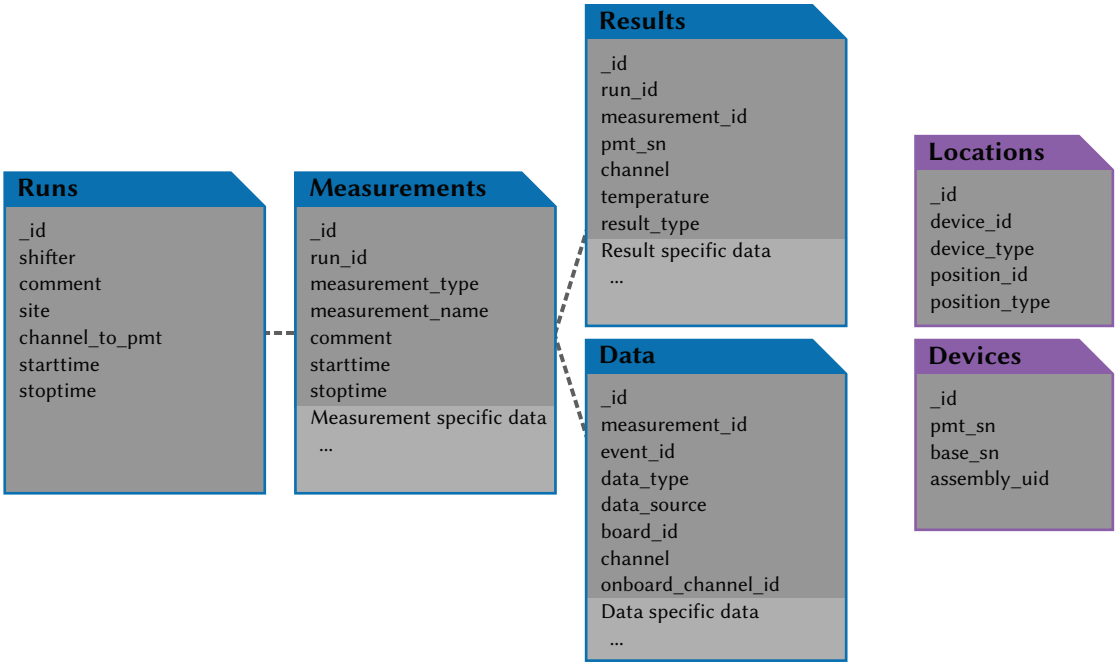

Figure 5.3: Structure of the local MongoDB database.

5.2 Implementation at the TU Dortmund University

When implementing the concept described in the previous chapter, some special considerations have to be taken into account in Dortmund. The test bench is set up in a former server room. This has the advantage that the existing room is temperature-controlled and can effectively dissipate waste heat from the cooling chamber, maintaining a constant temperature. At the same time, the room's size limits the cooling chamber's dimensions. Furthermore, only budgetary funds are available for this project, necessitating some improvisation without restricting the functionality of the test bench. A comparison with the test bench at RWTH Aachen shows the full functionality and consistency of the developed setup in Dortmund despite the different hardware implementations.

5.2.1 Cooling Chamber

The cooling chamber used is a Viessmann TectoCell Standard Plus. This cooling chamber for food operations can be adapted to individual needs in various dimensions. With an inner space of 3.7 m in length and 2.3 m in width, the cooling chamber is large enough to accommodate the PMT rack, provides sufficient distance from the light source, and leaves enough space to handle the PMTs behind the rack. Viessmann's TectoRefigo WMF2 240 cools the cell down to −25 °C. Since only −20 °C is required for the tests, there is sufficient margin to ensure continuous operation. The unit can be easily replaced if it breaks down or becomes insufficient for future studies, and a more powerful model is needed. Since the cooling chamber is used in the food industry, some modifications must be made before it is suitable for testing PMTs. The walls are lined with black stage fleece to avoid reflections inside the chamber. The fleece is non-destructively attached to the walls and ceiling with magnets. The floor is covered with black rubber flooring, which reduces reflections and ensures good slip resistance. Two penetration holes were drilled into the walls of the cooling chamber. There is a small passage under the cooling unit for the optical fiber and a bigger passage on the opposite side for the signal and control lines. The last modification is a sensor applied to the door that monitors whether the door is closed or not. When the door is open, the power supply to the miniFieldhub is interrupted, and the PMTs are disconnected. This prevents



Figure 5.4: The lab with the cooling chamber, a workstation, electronics, and the second rack outside the cooling chamber. The space constraints faced can be seen in this picture.

unintentional destruction of the PMTs when a high incidence of light hits the PMTs while the HV is enabled.

An Arduino Uno controls the cooling unit. This Arduino receives commands from the PC and translates them into commands the cooling unit can understand. For this purpose, it mimics a master device sending commands to the actual cooling unit. With this solution, it is possible to switch the cooling unit on and off, read and set the temperature set point, get the current temperature, and read error codes in case of malfunction.

5.2.2 PMT Rack

The rack is shown in Figure 5.5 and consists of a sturdy aluminium frame and eight Vogelstangen. Each Vogelstange has space for 12 PMTs and is shown in Figure 5.7 as a 3D model. This leads to a maximum capacity of 94 PMTs. Existing Rose+Krieger (RK) aluminum profiles are repurposed from an older project and

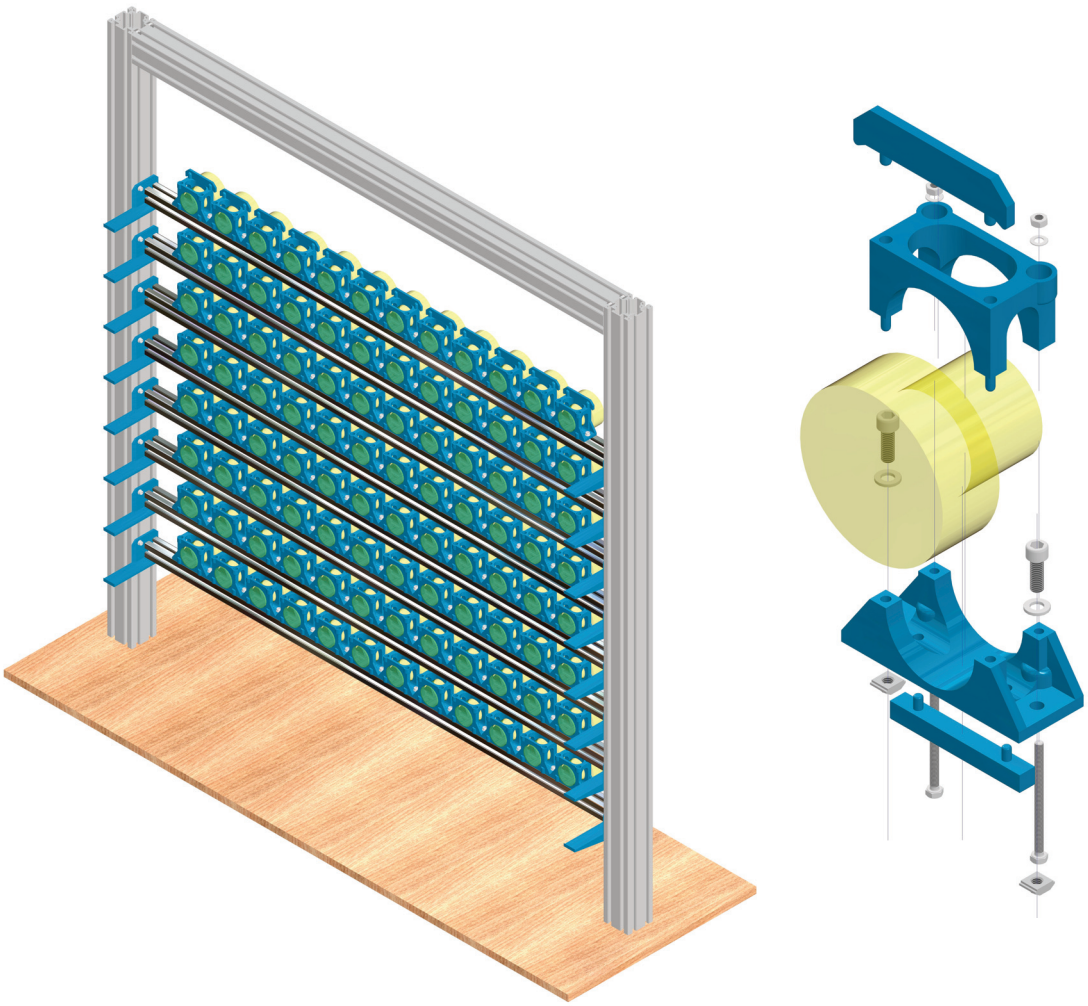

Figure 5.5: On the left is the 3D model of the complete rack. It consists of a base plate, a frame, and eight Vogelstangen, each with 12 PMT mounts. On the right are the individual components of the PMT mount in blue and a simplified model of a PMT in yellow.

used for the frame and the Vogelstangen. The minimalist design was chosen to accommodate the material at hand. The frame is mounted on a 600 mm × 1800 mm base plate and consists of three 80 mm RK profiles that are bolted together. Eight support points for the Vogelstangen are attached on the inside of each vertical RK profile and depicted in Figure 5.6.

The Vogelstangen are made of 40 mm RK profiles and are inserted into these support points. Walls at the front of the support points and a slight elevation help to insert

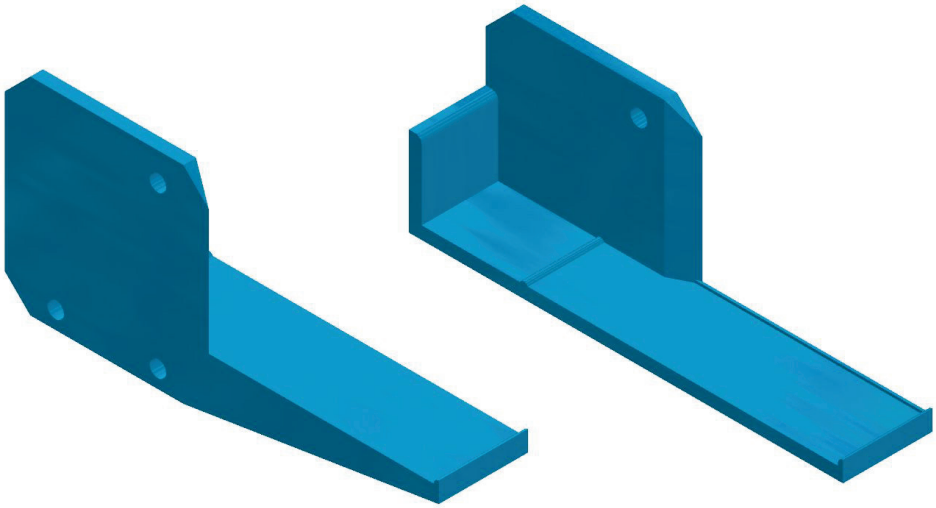

Figure 5.6: 3D model of the support points for the Vogelstangen.

the Vogelstangen correctly and prevent them from accidentally shifting. The support surface is extended to the rear to assist in removing and inserting the bars. On each Vogelstange 12 PMT holders are attached, into which the individual PMTs can be inserted. The PMT holders, as shown in Figure 5.5, are designed to be guided by the RK profiles and locked in place with two screws. They consist of a lower half-shell where the PMT is placed and an upper half-shell that secures the PMT in the holder. The upper half shell has an open design so that the barcodes on the PMTs are visible and can be scanned even after mounting. Due to the modular design of the Vogelstangen, the PMT holders can be easily exchanged for other PMT holders with different dimensions. This makes it easy to adapt the design to new circumstances.

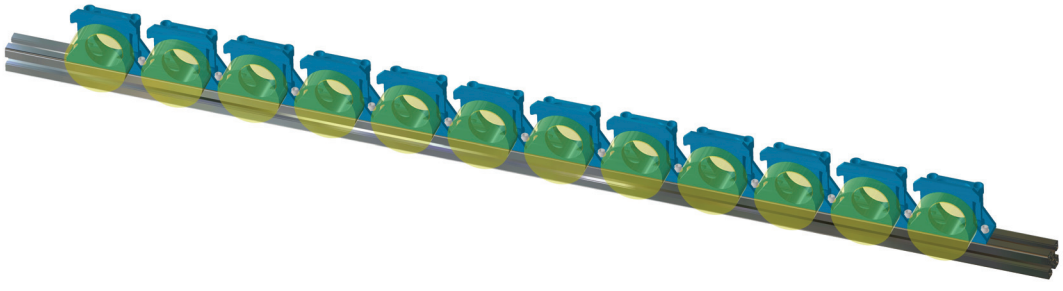

Figure 5.7: The 3D model of the Vogelstangen including the twelve 3D-printed PMT mounts (blue). The PMTs are indicated in yellow.

The entire rack was designed using Autodesk Inventor, and the PMT mounts, Vogelstangen support points, and a cable management support system were printed using a Prusa MK3. After prototyping, two 3D printers were used to print all the needed parts. The total printing time was about 1500 hours and needs to be considered when setting up a new testing facility.

Cable Management



Figure 5.8: This image shows the back of the rack. The two upper rows are completely equipped with PMTs. Additional reference PMTs are connected in the middle. The cable routing of the individual Vogelstangen is clearly visible. Unused cable harnesses can be attached to the wall of the cooling chamber. QR codes of the Vogelstangen, PMT holders, and the position of the Vogelstangen can be seen.

Each PMT position in the rack is wired to a specific channel of a mainboard via the signal and control line. Figure 5.8 shows the back side of the rack with cables

attached to the installed PMTs. The cables for one Vogelstange are bundled together in a cable harness. At each PMT position, a signal/control line pair is led out of the bundle. This minimizes the risk of confusing the cables for each position. For control purposes, each pair of cables is marked with the number of the row and the PMT position. Unused cable harnesses can be attached to the wall of the cooling chamber.

Each PMT holder on a Vogelstange is given an identification (ID) number. A label with the ID and a QR code decoding the ID is attached below each holder. To record the location of the PMTs at any time, each Vogelstange, each position of the Vogelstangen in the rack, and each PMT storage box has its own ID. These QR codes are scanned in pairs whenever a PMT or Vogelstange is moved to a different location. The `scanner_service` stores pairs of movable devices and their positions in the local database. That way, it is possible to track the movement of PMTs through the test bench and link the PMT serial number to the channel of a mainboard. This makes it possible to trace which PMT was tested on which channel at any time.

5.2.3 Light System

The light system is capable of producing light in two wavelengths at Single Photoelectron (SPE) level and one wavelength at approx. 50 photoelectron(PE) intensities. It consists of four essential components: the ps-pulser, the LED, a robot to couple the light into the optical fiber, and a diffuser at the other end of the optical fiber inside the cooling chamber. A detailed schematic of the light system is depicted in Figure 5.9.

Three ps-pulsers drive the LEDs according to the design by M. Rongen and M. Schaufel [76], published under the Creative Commons license. The ps-pulser generates voltage pulses in the 100 ps range and can drive a wide range of LEDs or vertical-cavity surface-emitting lasers (VCSELs). The pulsers are based on the circuit of J. Williams [77], which generates pulses with an avalanche transistor (2N2369) and is shown in Figure 5.10. For this purpose, the collector voltage is set to a value just below the breakdown voltage, and a discharge capacitor C_{D} is charged simultaneously. The capacitor stores the energy, which is later available

[76]: Rongen et al. (2018), "Design and Evaluation of a Versatile Picosecond Light Pulser"
[77]: Williams (1994), "Practical Circuitry for Measurement and Control Problems"

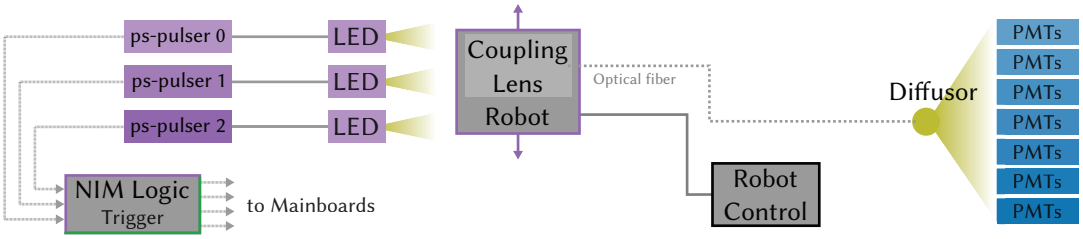

Figure 5.9: Schematics of the light source system. Three ps-pulsers control LEDs positioned within a dark box. The emitted light is directed into an optical fiber through a coupling lens attached to a movable robot. This optical fiber extends into a diffuser to fairly homogeneously illuminate the PMTs inside the cooling chamber.

to the LED in case of an avalanche breakdown. When a voltage is applied to the base, avalanche breakdown occurs, resulting in a steeply rising voltage pulse at the emitter, and the discharge capacitor C_D discharges through the emitter. The collector voltage drops, the transistor resets itself, and can be triggered again. In this case, the pulse height and width can be scaled with the discharge capacitor and must be adjusted for the used LED.

The pulsers communicate with the PC via a serial connection and can be switched on and off separately. In addition, the frequency (0 kHz to 25 kHz) of the pulses can be selected, and a bias voltage (−2.4 V to 0.7 V) can be used to vary the brightness of the LED. The pulse generators are outside a dark box that contains the LEDs (see Figure 5.11). The three silver boxes in the lower right picture are the pulsers. Each pulser is connected to the USB hub in the center of the picture via a USB cable. The thin cable connected to the bottom of the pulser passes the trigger signal to the mainboards, and the top cable connects the LEDs in the dark box.

Four LEDs with two different wavelengths of 375 nm (XSL-375-3E [78]) and 505 nm (B3B-443-B505 [79]) are used. Two, one of each wavelength, are connected to the ps-pulsers, creating dim sub-nanosecond light pulses. The remaining two LEDs with 505 nm are connected in parallel to the third ps-pulser that was modified to produce ∼9 ns long bright light pulses used for the charge response linearity measurement.

Along with the LEDs, a robot is in the dark box shown in Figure 5.12. On top of

[78]: (2014), *XSL-375-3E Data Sheet*
[79]: (2010), *B3B-443-B505 Data Sheet*

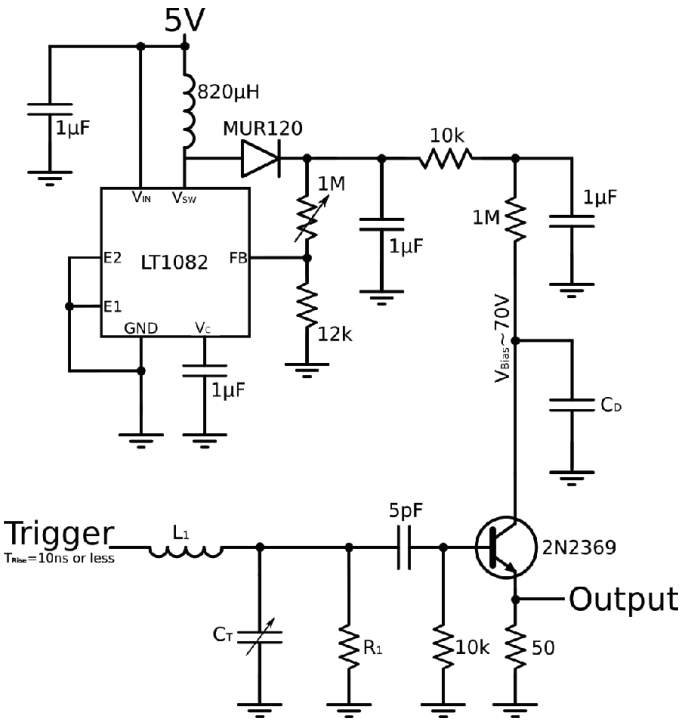

Figure 5.10: Circuit diagram of a triggered pulser according to J. Williams. Figure taken from [76, p. 2].

the robot is the converging lens, which is attached to an optical fiber. The robot can move to the different positions of the LEDs and couple the corresponding LED into the optical fiber. To do this, the robot moves on rails from one position to the next. A reference position (left) is approached each time the robot is initialized. From there, the positions of the LEDs are defined as distances. The distance traveled is measured by the revolutions of the wheels. Slipping wheels would lead to inaccuracies in the approached position and should be prevented. For this purpose, the track is covered with sandpaper to obtain high friction.

Additionally, a steel weight is attached to the robot, increasing the contact pressure of the wheels and thus preventing slippage. The robot and its controller are realized with LEGO MINDSTORMS EV3 [80]. The EV3 runs a Debian Linux distribution called ev3dev [81]. A Python program implements communication with the PC and controls the robot.

The optical fiber ends inside the cooling chamber, and the diffuser is located 2.26 m

[80]: (2013), *LEGO MINDSTORMS EV3*
[81]: (2025), *Ev3dev - Debian Linux for LEGO MINDSTORMS EV3*

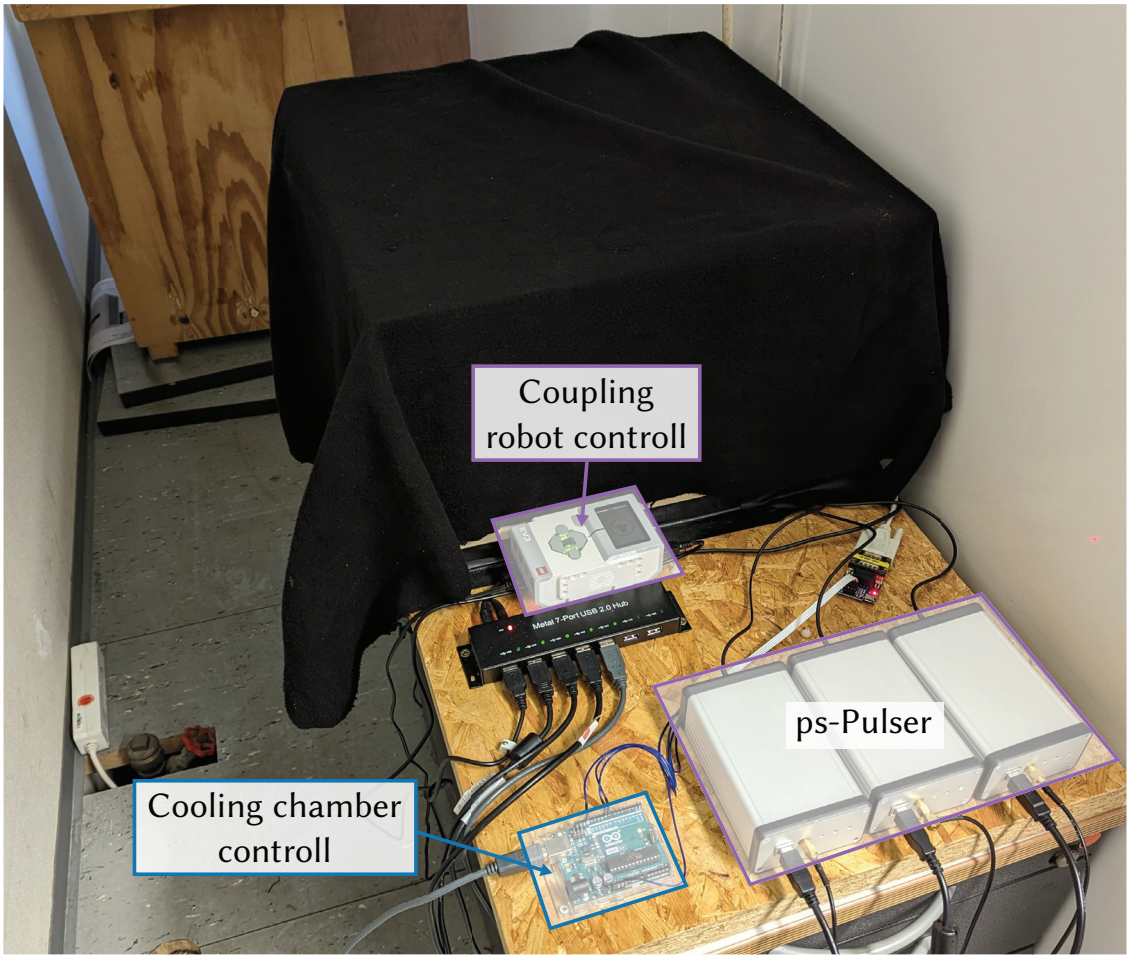

Figure 5.11: The pulses from the three ps-pulsers are fed into the dark box, where they are coupled into the optical fiber via an LED. A LEGO MINDSTORMS EV3 controls the coupling robot. A USB hub connects all the devices to the PC, while an Arduino Uno board is used to facilitate communication between the PC and the cooling chamber.

in front of the center of the rack. It diffuses light from the optical fiber evenly into the room, illuminating each PMT position in the rack as homogeneously as possible. The diffuser is an integrating sphere from the POCAM [82] and is specifically designed to scatter light as isotropically as possible in space. The diffuser and its designed mounting structure for the optical fiber can be seen in Figure 5.13. The diffuser used is made of Polytetrafluorethylen (PTFE) and is not perfectly isotropic. The illumination of the rack is measured and evaluated in section 5.3.

[82]: Khera et al. (2021), *POCAM in the IceCube Upgrade*

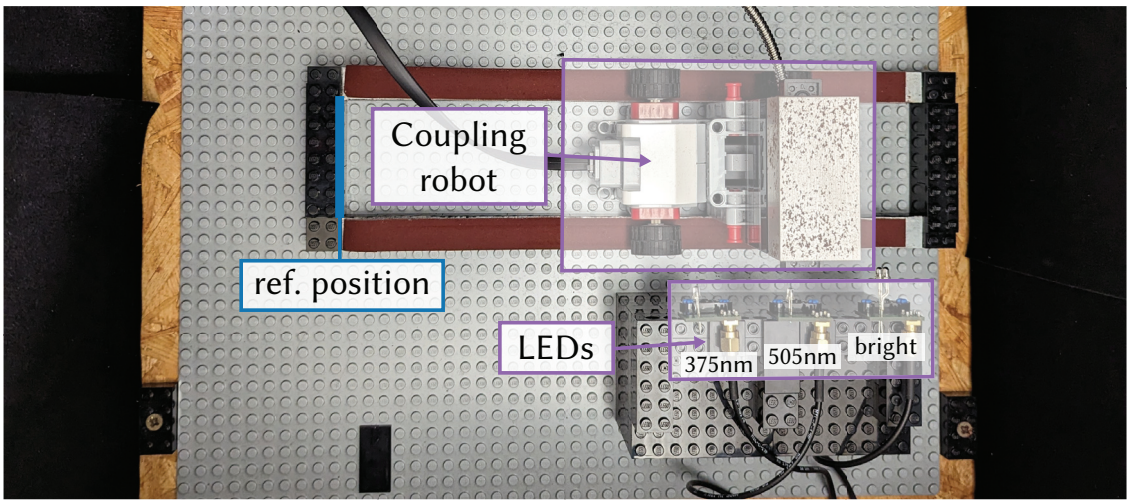

Figure 5.12: Inside the dark box are three LEDs and a robot carrying a converging lens that couples the light pulses into the optical fiber. The sandpaper and metal block on the robot prevent the wheels from slipping.

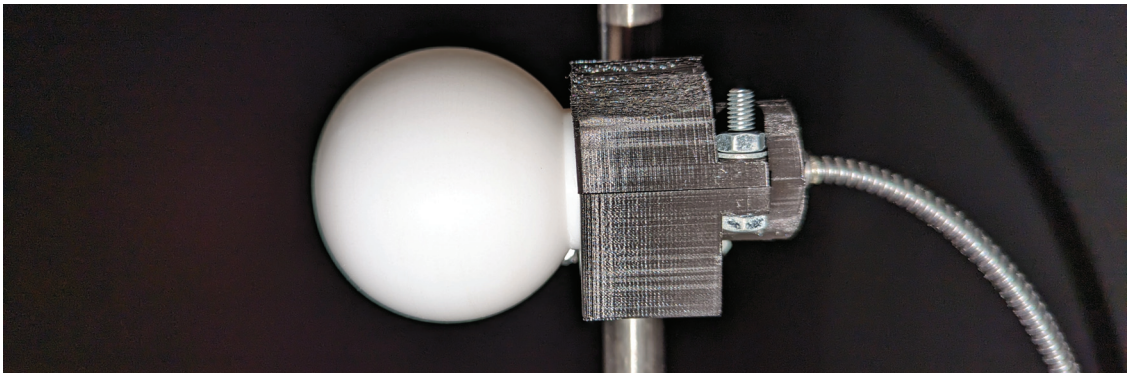

Figure 5.13: The light enters the cooling chamber through an optical fiber and is diffused by the white PTFE sphere. The black holding structure is 3D-printed, holds the end of the optical fiber in place, and fixes the diffuser at the desired height on the metal rod.

5.2.4 Data Acquisition

To digitize and analyze the pulses measured by the PMTs, a Data Acquisition system is needed and housed in an electronics rack. Figure 5.15 shows the electronics rack and its components. Four mDOM mainboards [83, 84] are connected to a desktop

[83]: IceCube et al. (2023), "Design and Performance of the mDOM Mainboard for the IceCube Upgrade"

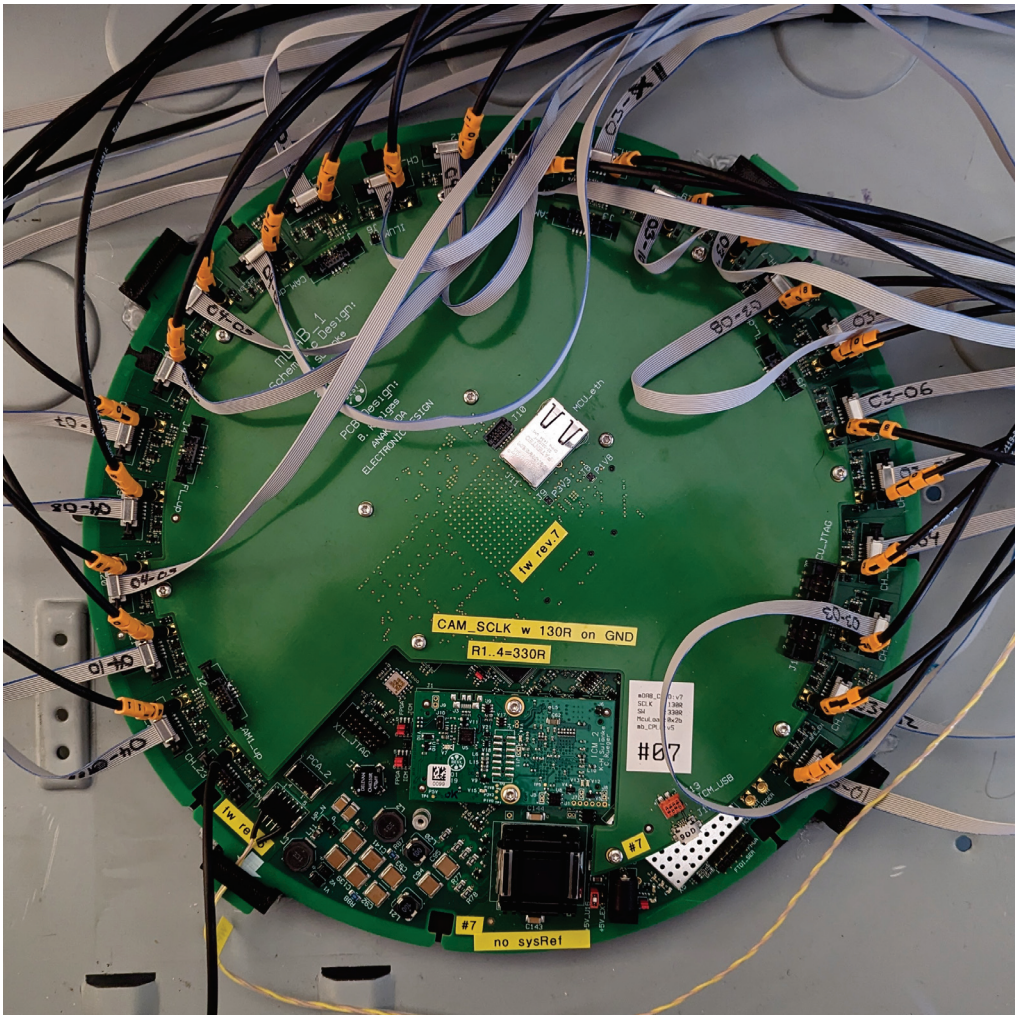

Figure 5.14: An mDOM mainboard Rev.1 with all channels connected. The yellow-purple cable pair connects the mainboard to the miniFieldhub.

PC via a miniFieldhub [85]. A trigger logic is housed inside a Versa Module Eurocard (VME) crate [86] and readout electronics for environmental sensors, as well as the interlock system, are mounted on top of the rack.

The mainboards are precursor models to the final design of the mDOMs. The functional scope of the Rev.1, used in this setup, and Rev.2, used in the mDOMs, is identical. Therefore, the firmware API developed for the mDOMs can be utilized,

[84]: Sulanke (2023), *mDOM Mainboard Design Status and Notes (DSN)*
[85]: Sulanke (2023), *Mini Fieldhub Design Status and Notes (DSN)*
[86]: (1995), *American National Standard for VME64*

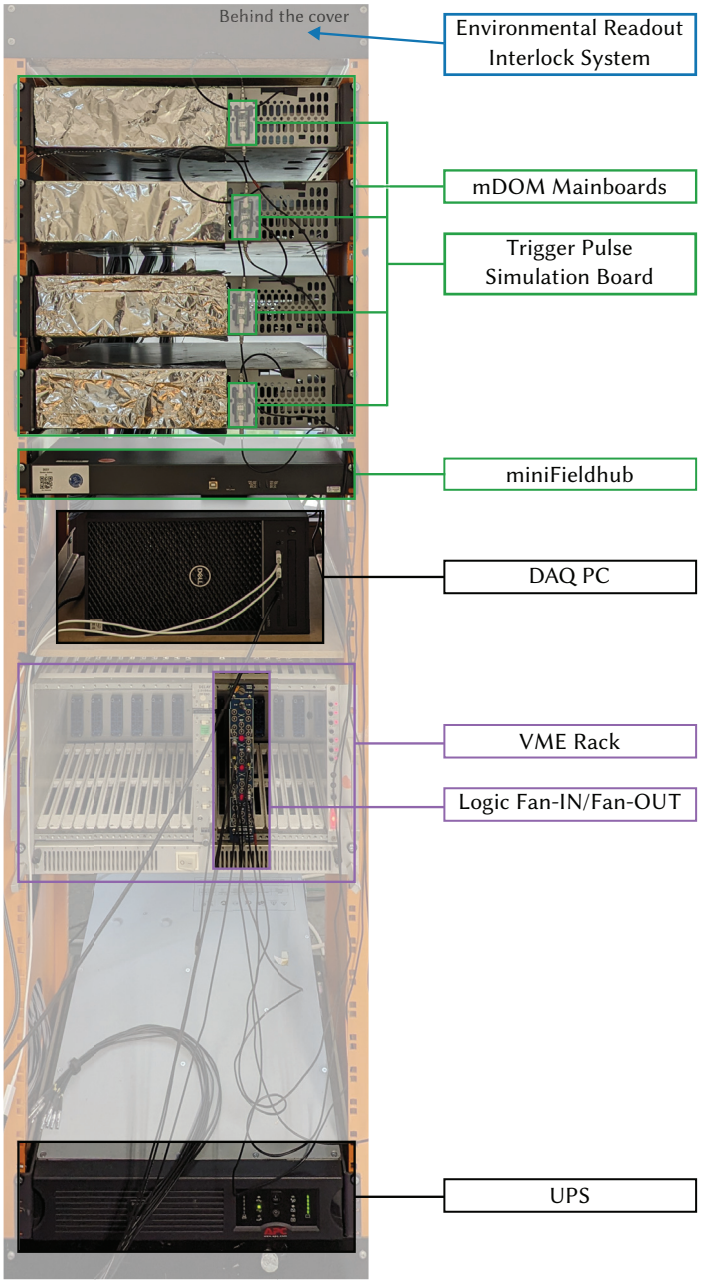

Figure 5.15: The image shows the complete DAQ setup. From top to bottom: Behind the black panel are the Arduinos for the environmental sensors and the interlock system. Below that, the mainboards can be seen in four housings. The control and signal lines are fed into the housings from the back. In front, the trigger signal lines can be seen. The small boards galvanically isolate the trigger signal from the mainboard. Below the mainboard sits the miniFieldhub, followed by the PC. Underneath is the logical fan-in/fan-out for trigger forwarding. At the bottom of the rack is an uninterruptible power supply to cover short power outages in the building.

and no software has to be adapted specifically for the test bench. Each mainboard has 24 readout channels in which the signal from the PMT is first amplified and then digitized using an FADC. The numbering of the channels goes from 0 to 23, where the trigger signal of the pulser is always connected to channel 23. A total of four mainboards are installed, giving a maximum capacity of 96 PMTs. The actual capacity is reduced to 87 PMTs. Four channels are used for triggers and reference

PMTs, respectively. One channel proved unreliable during test bench setup and is therefore not used.

The trigger signals of the pulsers cannot be connected directly to the main boards. The three trigger signals of the different pulsers must be multiplied and forwarded to the four channels of the main boards. For this purpose, a Logic Fan-IN/Fan-OUT board model 429A [87] from LeCroy is used. The three trigger signals are connected as inputs to the board, and four outputs are connected via galvanic isolation to channel 23 of the four main boards. The channel to which the trigger signal is connected can be individually configured on the mainboard. Channel 23 was chosen because it corresponds to a position at one end of the Vogelstangen.

The mainboards are connected to a miniFieldhub. The miniFieldhub will be located on the surface of the IceCube upgrade at each hole, and all mDOMs of the string will be connected to it. The signals are forwarded to the ICL from there. It bundles the communication with the mainboards and supplies them with the operating voltage simultaneously. A special feature of the test bench, however, is that the power supply to the miniFieldhub is interrupted as soon as the door of the cooling chamber is opened. This protects the PMTs from excessive light intensities when the HV is switched on.

The miniFieldhub, pulsers, and all other devices are connected to a desktop PC via USB. The PC serves as the control center for the test bench. It is a Dell Precision 3600 with Ubuntu 20.04 as the operating system. In addition to the standard configuration, two 12 TB hard drives are installed and connected with ZFS in Raid 1, storing the local database. Besides the database, other essential services run in the background on the PC. A serial-to-TCP server forwards the TCP communication to the serial USB interface. It thus ensures that all connected devices can simultaneously connect to `pmt_taco`. `pmt_taco` itself is also installed and configured on the PC. Remote access is provided via SSH.

5.2.5 Environmental Sensors

Four temperature sensors and two humidity sensors are used inside and outside of the cooling chamber to monitor the environmental conditions during a testing cycle.

[87]: LeCroy (1995), *429A QUAD LOGIC FAN-IN/FAN-OUT*

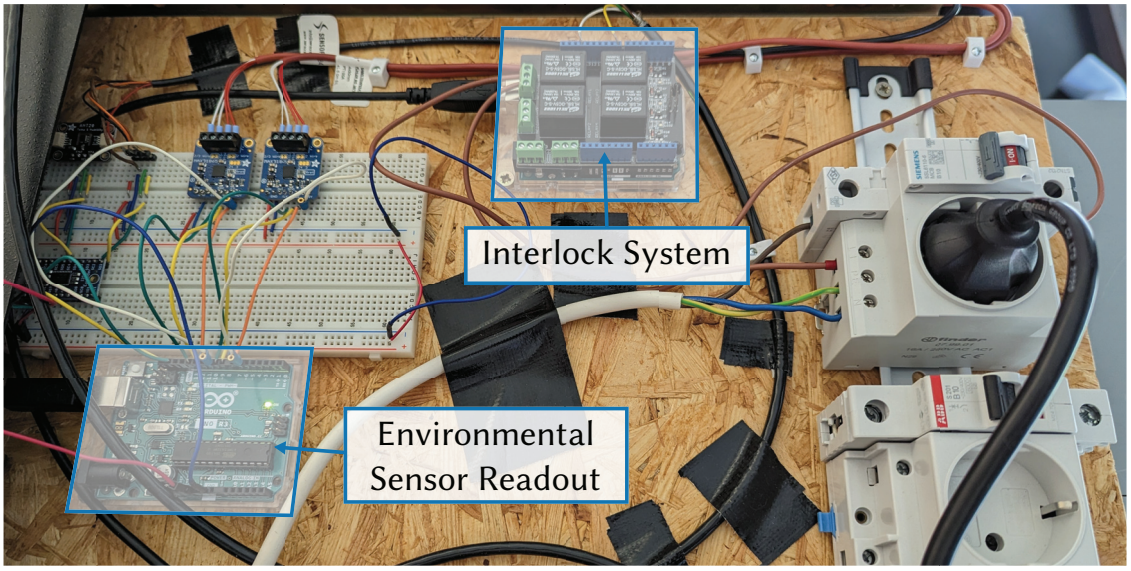

Figure 5.16: Environmental sensor readout and interlock setup on top of the electronics rack.

Inside the cooling chamber, two PT-100 temperature sensors [88] with amplifiers [89] are integrated into the cable harness of rows 2 and 8, respectively. An additional temperature and humidity sensor [90] is installed in the harness for row 4 and sits in the middle of the rack. On the outside, a second temperature and humidity sensor is placed on top of the DAQ rack. All environmental sensors are read out via an Arduino Uno R3 [91]. The temperature readback is used to monitor the temperature within the cooling chamber, and measurement is suspended if the specified conditions are not met.

5.3 Calibration

Before operating the test bench, several calibration tasks are necessary to ensure functionality and reliable, consistent measurements. The ps-pulsers must be set up and tuned to match the used LEDs in order to achieve the specified pulse length and light output. Additionally, the AFE amplification gains must be determined in order

[88]: otom Group GmbH (2025), *Kabelfühler - Durchmesser 4mm (KS-PT100A-4L-5.0-430)*
[89]: ada (2024), *Adafruit MAX31865 RTD PT100 or PT1000 Amplifier*
[90]: Rembor (2024), *Adafruit AHT20 Temperature & Humidity Sensor*
[91]: Arduino (2025), *Arduino Uno R3 Data Sheet*

to be able to compensate for the AFE contributions from the mainboard. Finally, variations in light yield across different positions within the PMT rack need to be measured to account for the not-perfect isotropy of the diffuser. These calibrations rely on reference PMTs previously tested at RWTH Aachen to ensure compatible results between both testing sites despite differences in implementation.

5.3.1 Tuning the ps-Pulser

As described in the previous chapter, the pulser can be operated with different LEDs. The discharge capacitor C_{D} of the Williams pulser in Figure 5.10 must be chosen to match the LED, as it has a considerable influence on the pulse width and shape. The higher the capacitance of the capacitor, the wider the generated pulse will be. In two pulsers, the capacitor has a value of 12 pF. These pulses are used for single-photon measurements. A third pulse generator is modified for linearity measurements and emits pulses with a width of about 9 ns. For this purpose, a capacitor with 1.2 nF is chosen.

Setting the Collector Voltage

For all three pulsers, the correct collector voltage must be set before operation. To do so, the signal and trigger outputs are connected to two channels of a LeCroy Waverunner 6 oscilloscope, and the pulse generator is switched on. The timing setting of the oscilloscope is configured to show several trigger signals simultaneously as depicted by the blue line in Figure 5.17. Then the collector voltage (usually 70 V) is increased with the adjustable resistor (1M in Figure 5.10) until more untriggered signal pulses appear between the trigger pulses (top panel of Figure 5.17). This happens when the breakdown voltage is reached and random breakdowns occur. The collector voltage is now reduced until these random signal pulses disappear, as shown in the lower panel. The collector voltage is now just below the breakdown voltage.

Adjusting the LED Brightness

In the second step, the brightness of the LEDs is adjusted via the bias voltage. Here, the procedure differs between the pulse generators used for single photon

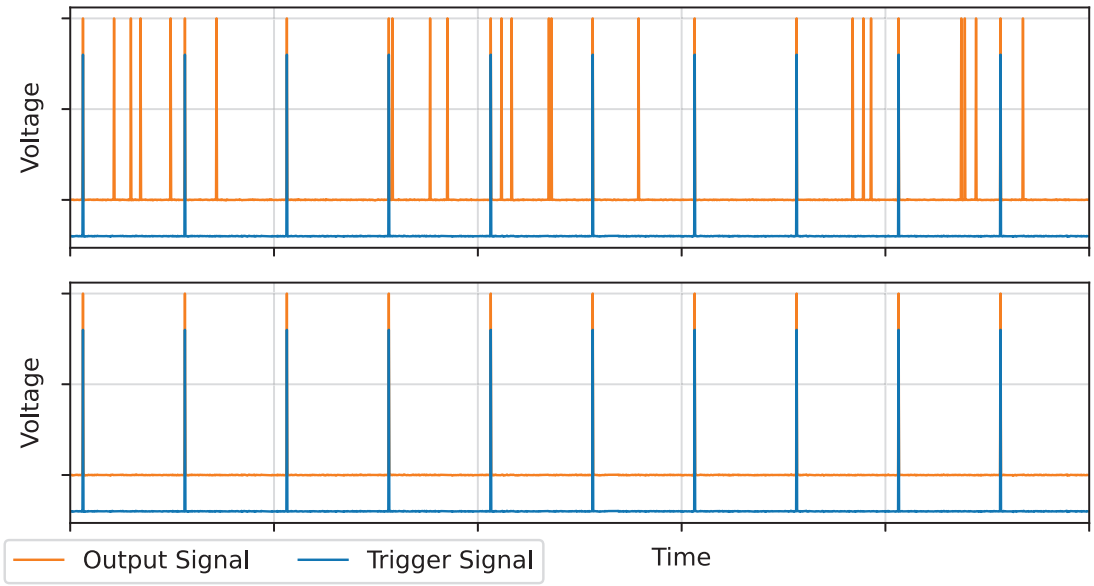

Figure 5.17: Visualization of collector voltage adjustment. Upper panel: The collector voltage is above the breakdown voltage, and random pulses appear. Lower panel: The collector voltage is just below the breakdown voltage, and no random pulses occur.

measurements and the one used for linearity measurements.

To ensure that only single photons are measured for each pulse, the brightness of the LED is adjusted via the bias voltage until only one pulse is measured in 5 to 15% of the waveforms.

Poisson's statistics can describe the number of triggered photoelectrons at low light intensities.

$$P(i, \lambda) = \frac{\lambda^i e^{-\lambda}}{i!} \tag{5.1}$$

If, for example, the average number of photoelectrons per waveform is assumed to be $\lambda = 0.1$, then approximately 9.97% of all waveforms contain a pulse and the probability that this pulse is caused by exactly one photoelectron is $P(1, 0.1) = 9.45\%$. The probability to measure more than one photon simultaneously decreses with the number of photons: for two photos the probability is just $P(2, 0.1) = 0.5\%$ and for three photos it is only $P(3, 0.1) = 0.02\%$.

Occupancy is defined as the ratio of the number of externally triggered measurements in which the waveforms contain a pulse to the sum of all externally triggered measurements and can therefore be written as:

$$\text{occupancy} = \sum_{1}^{\infty} P(i, \lambda) = 1 - P(0, \lambda) \tag{5.2}$$

The standard SPE measurement and analysis, which also determines the occupancy, is used. Several measurements with different bias voltages are performed, and the bias voltage meeting an occupancy between 0.05 and 0.15 is chosen and entered into the configuration files. The following values are employed for the two pulse generators:

375 nm**:** −0.1 V (for 7% occupancy).
505 nm**:** −0.9 V (for 9% occupancy).

The highest bias voltage of 0.7 V is used for the pulse generator of the linearity measurement. Figure 5.18 shows the final settings for the bright pulser with a bias voltage of 0.7 V measured with PMT `DM00231`. The charge is fitted with a Gaussian and determined to (44.8 ± 0.1) pC. This corresponds to ~ 56 photoelectrons per pulse at a charge of 0.8 pC per incident photon determined in a previous SPE measurement. The goal of 100 photoelectrons as specified in Table 4.1 is not achieved with this setup, and another light system would be needed. How this affects the linearity measurements will be discussed in section 5.4.

5.3.2 Correction Factors for AFE

The gain of the photoelectron does not depend solely on the PMT itself. Each channel has its own analog front-end shaping and amplifying the signal from the PMT before reaching the FADC. In order to measure the PMT gain, the measured amplification needs to be corrected by the AFE gain. Each channel has its own AFE electronics and, therefore, a slightly different response to a pulse. The reason for these slight variations in the AFE gain is the components' tolerances. A component with the same nominal value always has a slightly different real value. This variation depends on the component tolerance and can be minimized, but not eliminated, by using components from a single production batch. This variation will not affect the final signal capture in the detector because the PMTs will remain connected to

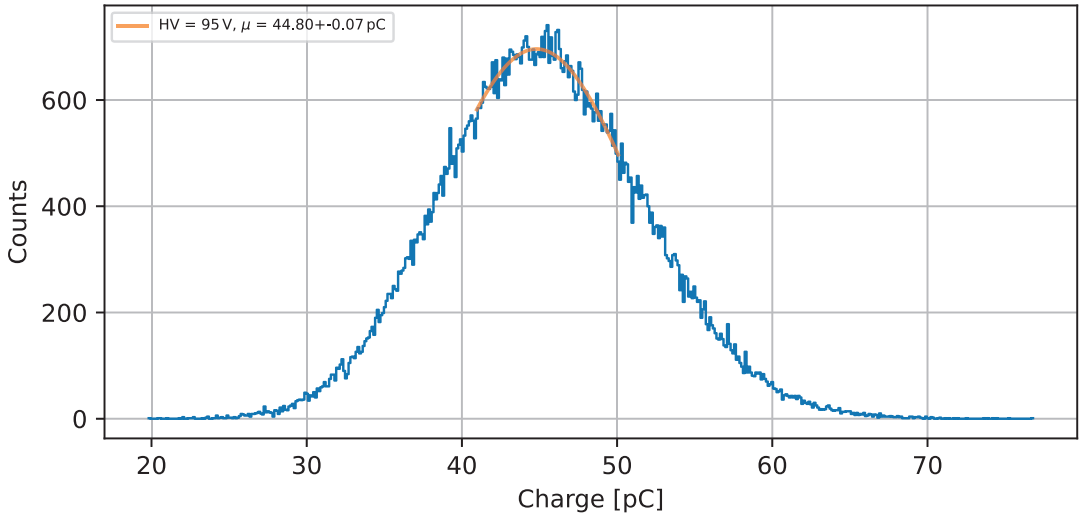

Figure 5.18: Charge spectrum of the bright LED recorded with the PMT `DM00231` at a voltage of 95 V with an average charge of 44.8 pC (∼ 56 photoelectrons) per pulse. The value of the capacitor C_D was 1.2 nF.

the same channel and will not be compared to each other. However, a comparable result is required for classification into voltage classes, so the fluctuations in the different channels will be considered in this work.

To calculate the charge from a pulse, the gain of the AFE must also be factored out since the amount of charge at the output of the PMT is critical to the gain. The gain of the AFE is determined by simulations of the AFE electronics considering an average pulse shape. Measurements on PMTs in Aachen with an external FADC show that the simulated factor differs by 30 to 40% from the factor measured with the FADC. Two PMTs (DM07124 and DM07525) calibrated in Aachen with an external FADC are used here to calibrate the channels' gain. At the same time, this calibration enables an alignment of the target voltage measurement between the two test benches in Aachen and Dortmund.

The measurements for the calibration can be divided into two steps:

1. Measure all positions in the rack with 12 PMTs on a Vogelstange. The positions of the PMTs on the Vogelstange remain the same throughout this measurement. Only the Vogelstangen moves in the rack.
2. In one row (here, row 02), every PMT is permuted so that every position in this row is measured with every PMT.

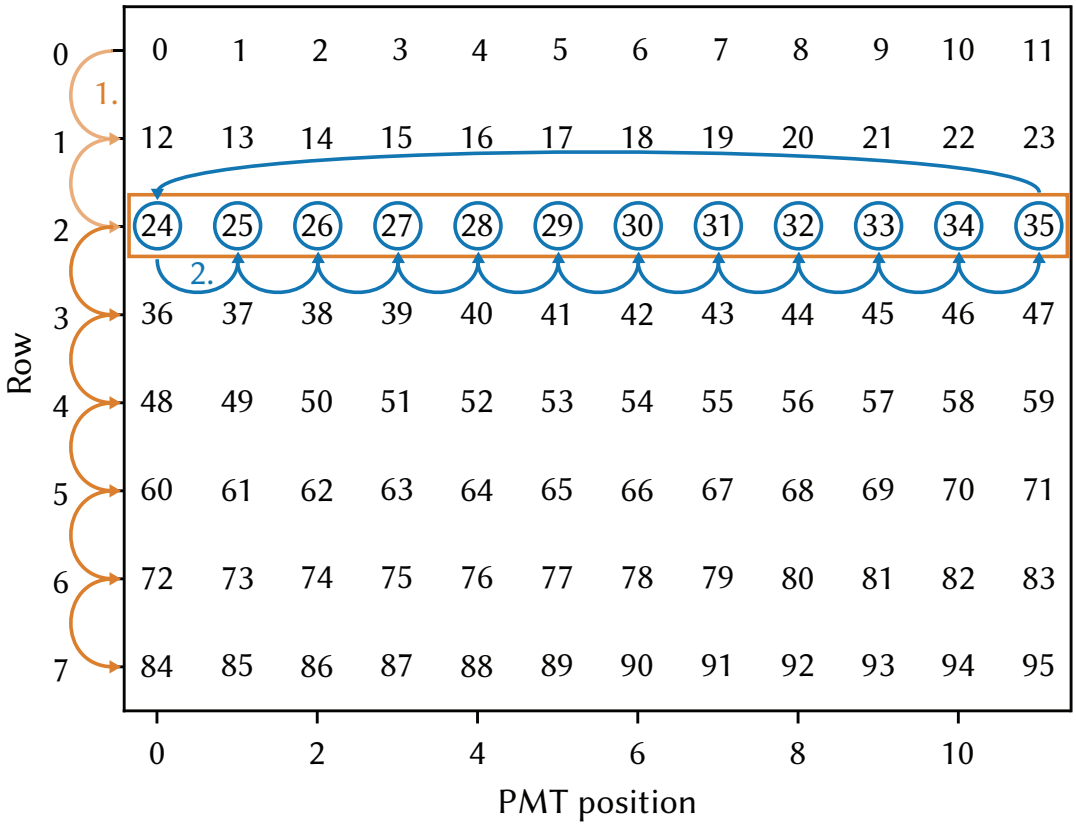

Figure 5.19: Measurement scheme for the AFE gain calibration.

For each measurement a fixed operating voltage ($U_{\mathrm{dy10}} = 93\,\mathrm{V}$) of the PMTs is used. This voltage corresponds to the one used to measure the reference values with the external FADC. The gains obtained with the external FADC measurements are [92]:

DM07124: 11.091×10^6
DM07525: 11.471×10^6

Three steps are performed along the same lines as above to calculate the correction values.

1. The eight measurements of all rows are normalized to the values of the second row for each PMT (position on the Vogelstangen). Each column was measured with a different PMT, and the differences in the PMTs must be considered in the next step.

[92]: Halve (2022),

2. Each PMT was measured at each position of the Vogelstangen. The results of each position are now normalized to the first position. Resulting in correction values for each PMT for each position on the Vogelstange. Each column from step one is now corrected with the mean value for the corresponding PMT.
3. The final step is to normalize using the external FADC values.

Figure 5.20 shows the normalized values after step 3. The values for each channel are now comparable, and the differences between the channels represent the variations in AFE gain for each channel. The values are greater than one, indicating a higher gain measured with the testing setup compared to the FADC measurements. This is expected as the mainboards further amplify the PMT output before digitizing it.

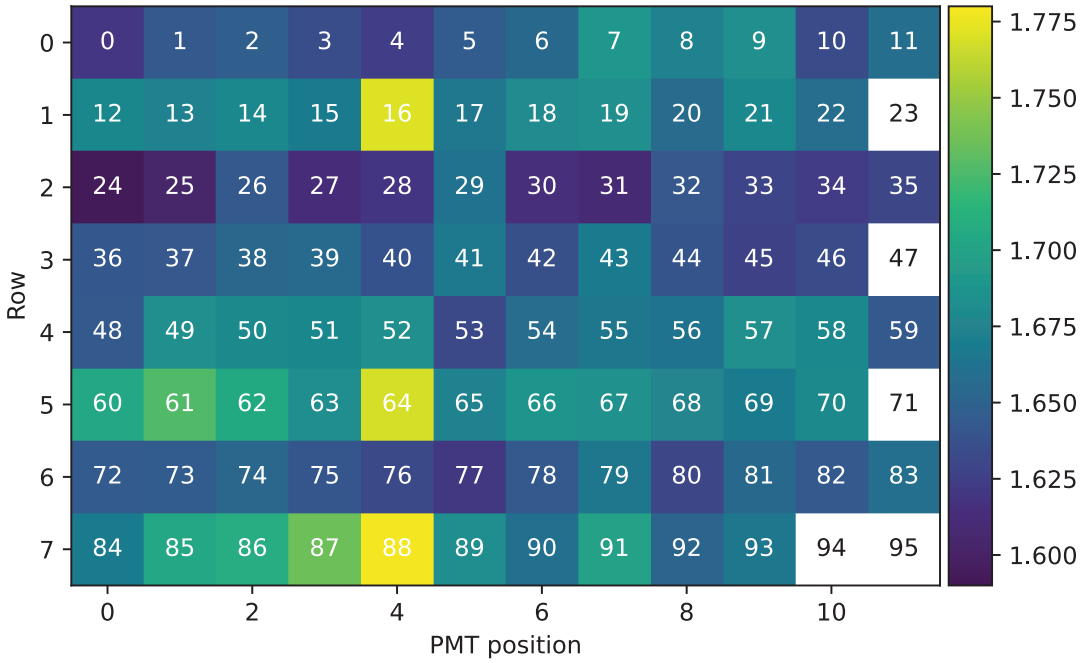

Figure 5.20: The figure shows the values normalized to the FADC measurements. The different AFE gains for each channel are visible as variations between the channels.

5.3.3 Light Distribution at the Rack

The incident light intensity at each rack position is crucial for the QE measurement, see subsection 5.5.3, and is defined by the isotropy of the diffuser. For a perfectly isotropic diffuser, the number of photons decreases with the distance squared:

$$N = A \cdot \frac{N_0}{4\pi R^2} \tag{5.3}$$

where N_0 is the number of emitted photons, R is the distance of the PMT from the source, and A describes the effective area of the PMT. The effective area of the PMT can be approximately described by an ellipse:

$$A = \pi r^2 \cos(\phi) \tag{5.4}$$

with the radius r of the PMT and the angle ϕ between the vertical link line and the position of the PMT, as shown in Figure 5.21.

The number of photons measured can be derived from the formulas (5.3) and (5.4). To do this, R is expressed by equation (5.5) with the distance R_0 from the diffuser to the center of the rack and the distance d from the PMT to the same point.

$$R^2 = R_0^2 + d^2 \tag{5.5}$$

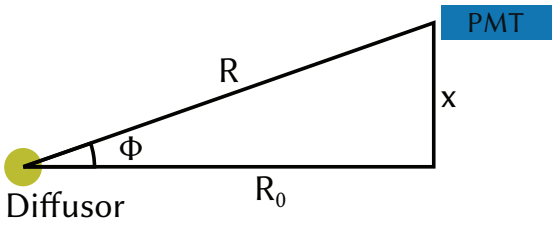

Figure 5.21: 1D illustration of the geometric considerations for the light intensity measurements.

The angle $\cos(\phi)$ can also be described by R and R_0.

$$\cos(\phi) = \frac{R_0}{R} \tag{5.6}$$

Thus, the number of photons depends solely on the PMT's distance from the center of the rack, which is given by its position in the rack.

$$N = \frac{N_0 r^2}{4} \frac{R_0}{(R_0^2 + d^2)^{\frac{3}{2}}} \tag{5.7}$$

If the light intensities are measured at different distances from the center of the rack, the relative light intensity at each point on the rack can be determined using

a fit function. The fit function can be defined as follows:

$$f(d) = a \cdot \left(\frac{R_0}{(R_0^2 + d^2)^{\frac{1}{2}}} \right)^b \tag{5.8}$$

The fit parameter a normalizes the light intensity, the distance between the diffuser and the rack R_0 is 2.26 m, and b describes the isotropy of the diffuser. For an ideal diffuser, the value of b would be equal to 3.

The distances from the center of the rack can be calculated with the positions.

$$d_{ij} = \sqrt{(i \cdot x - x_0)^2 + (j \cdot y - y_0)^2} \text{ with } i \in [0, 11], j \in [0, 7] \tag{5.9}$$

i and j define the position in the rack as described in section 5.2. The center of the rack is given by $x_0 = 0.605\,\text{m}$ in the vertical and $y_0 = 0.490\,\text{m}$ in the horizontal. Between two positions in the rack is a horizontal distance of $x = 0.11\,\text{m}$ and a vertical distance of $y = 0.14\,\text{m}$.

Four PMTs are connected to channels 40 to 43 in the center of the rack to compensate for fluctuations in the intensity of the light source. If the relative number compared to the four stationary PMTs is considered instead of the absolute number of pulses, the fit parameter a is expected to be 1. The relative number of pulses for the PMT at channel k can be calculated as follows:

$$N_{k,\text{rel}} = \frac{4 \cdot N_k}{N_{40} + N_{41} + N_{42} + N_{43}} \tag{5.10}$$

Instead of measuring all positions with one PMT, four PMTs are used. This considerably reduces the measurement time since, instead of 94, only 23 measurements have to be performed. For each PMT, the relative number is plotted against the distance, and the fit is conducted according to the equation (5.8). For PMT `DM00231`, this is shown in Figure 5.22. Figure 5.23a depicts the measured light distribution in the rack. Single PMTs can be identified due to their different acceptances.

The relative number of pulses can be normalized using parameter a from (5.8). This normalization eliminates the varying acceptance of the PMTs used and allows any position in the rack to be plotted, see Figure 5.23b. This determines the exact position of the light source in the plane of the rack. For this purpose, each row and column is fitted with the function

$$f(x) = q \cdot \frac{1}{|x - p|^2 + R_0^2} \tag{5.11}$$

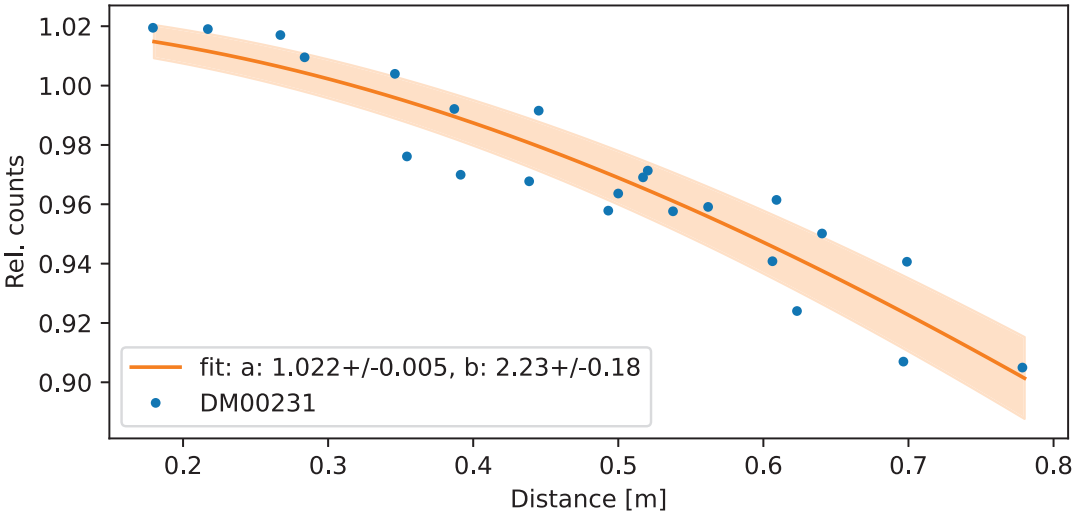

Figure 5.22: The measurement results of PMT `DM00231` are shown as blue dots in the plot. A dependence of the intensity on the distance from the center of the rack can be seen. The fit result is plotted as an orange line with an error band.

Here, p describes the distance of the maximum intensity from the edge of the rack. The values of p result in

$$p_{\text{hor}} = (0.607 \pm 0.006)\,\text{m} \text{ and } p_{\text{vert}} = (0.462 \pm 0.008)\,\text{m}$$

When comparing the intensity maximum and the geometric center (0.605 m, 0.490 m) of the rack, a difference in the vertical position of (0.028 ± 0.008) m can be noticed.

Using the values of the intensity maximum to recalculate the distances and refitting the value of the isotropy results in an averaged b over all four PMTs:

$$b = 1.98 \pm 0.07$$

The deviation from the ideal value $b = 3$ can be explained by the fact that, on the one hand, the PMTs have an acceptance dependent on the angle of incidence and, on the other hand, a diffuser made of ordinary PTFE is used in Dortmund. In comparison, the POCAM and the setup at RWTH Aachen use optical PTFE, and in Aachen, the value for b is 2.64 ± 0.07 [93].

[93]: Scheiter (2020), "Messungen Der Relativen Photodetektionseffizienz von Photomultipliern Für Das IceCube Upgrade Projekt"

Figure 5.23c shows the measured relative brightness calibrated by the calculated light yield from the fit of equation (5.8). The distribution is flat and shows no systematic shape, proving a successful calibration. A more detailed description of the calibration can be found in the bachelor's thesis of M. Freienhofer [94].

[94]: Freienhofer (2022), "Vermessen Der Referenz-PMTs Und Bestimmen Der Lichtverteilung Im Teststand Für Die mDOM-PMTs Des IceCube-Upgrades in Dortmund"

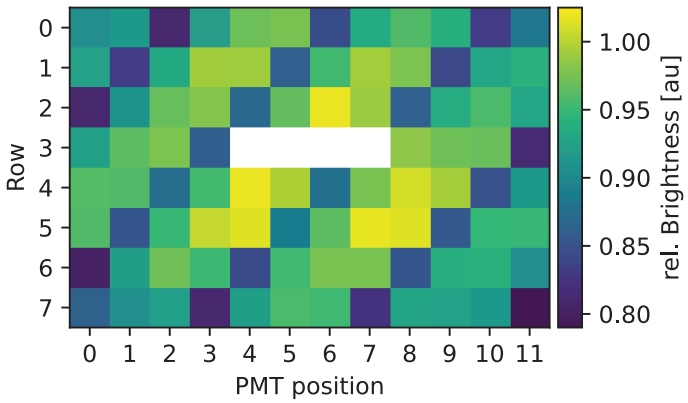

(a) Normalized light yield

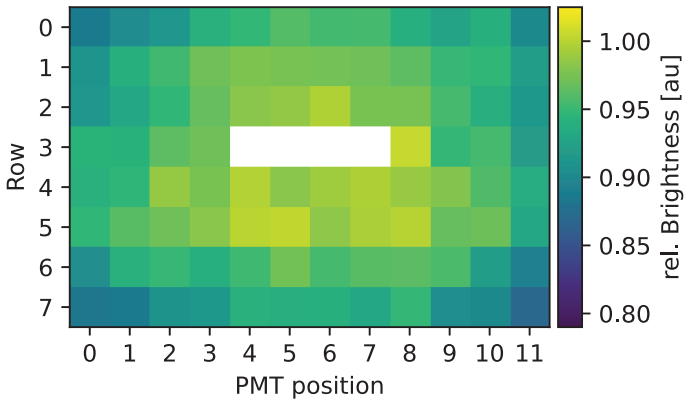

(b) Corrected light yield.

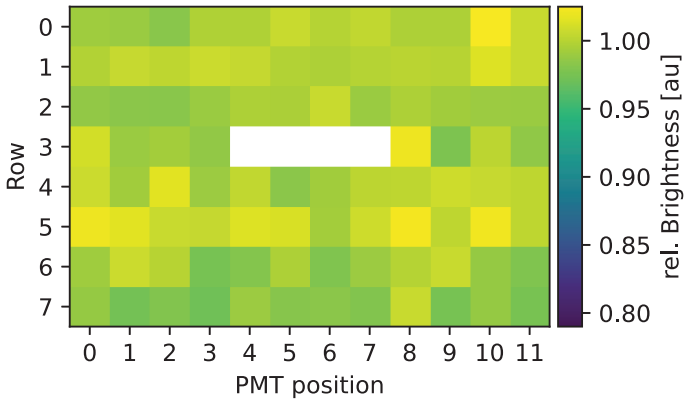

(c) Calibrated light yield.

Figure 5.23: (a): The measured light distribution in the rack. Artifacts, caused by the different acceptances of the PMTs, can be identified. The measurements are normalized to the average light yield of the four reference PMTs in the middle of the rack, represented by a white square.
(b): Acceptance corrected light yield. Single PMTs can no longer be identified, and the distribution now exhibits the expected behavior of decreasing intensity toward the edges.
(c): Calibrated light yields. The measured light yield is calibrated with the results from the fit of equation (5.8). The distribution shows no systematic shape, proving a successful calibration.

5.4 A Complete Testing Cycle

The entire cycle of a test procedure is highly automated and designed to take less than 24 h. The shifter's intervention is only necessary at the beginning of the testing cycle for exchanging the PMTs and starting the sequence of measurements, called a *run*. The sequence of a whole testing cycle is shown in Figure 5.24.

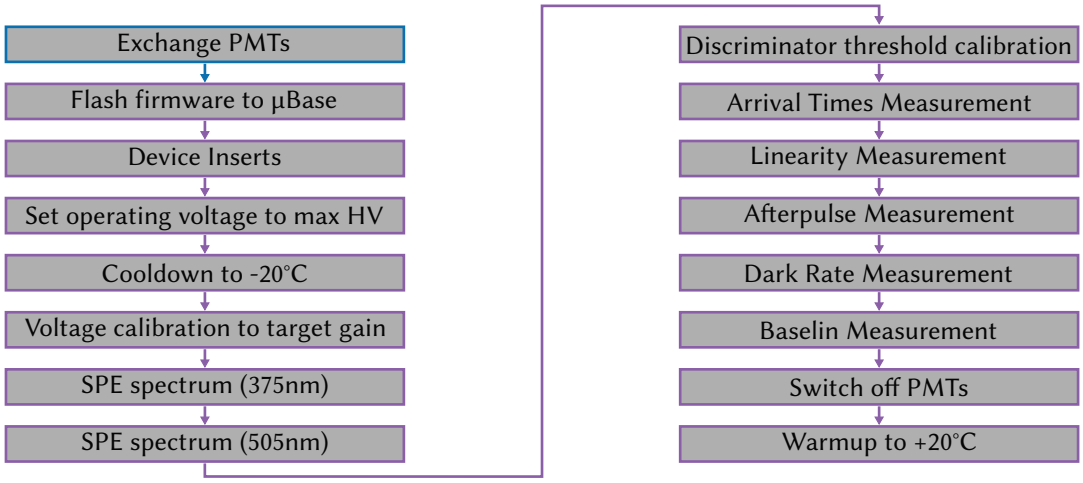

Figure 5.24: Sequence of a standard testing cycle starting with the exchange of PMTs and the start of a *run*. The *run* is a series of measurements (in the scope of the software, see subsection 5.1.2) and depicted in purple.

Preparing the Measurement

Step 1: The PMTs are inserted into the holders on the Vogelstangen and screwed tight. The PMT serial number and the holder's ID are then scanned in pairs with the `Scanner Service`. The `Scanner Service` links both values and adds them to the database. This makes it possible to trace PMT positions.

Step 2: The Vogelstangen are inserted into the rack, and the number of the Vogelstangen is linked to the row in the rack via the `Scanner Service`. It is now possible to assign a PMT to a channel on the mainboards, as a fixed channel is assigned to each position in a row in the rack.

Start the Measurement

Step 3: The script `run_testing_cycle_dortmund.py` is executed in a tmux session to ensure that the software runs in the background even if the shifter logs out of the PC. This allows them to log in remotely and access the output of the program over the entire test cycle of approx. 24 hours. Before the measurement program starts, the PMT to channel assignment is checked.

For each row, the shifter must enter the serial number of the connected PMT for a randomly selected channel. This is compared with the serial number in the database for this channel. If an error occurs, all PMT/PMT holder IDs and Vogelstangen/row pairs need to be scanned again. The script is then executed again. After a successful check, the shifter is prompted to close the cooling chamber, turn off the lights, and ensure the heater fan is turned off.

The shifter enters their name and a comment on the test cycle (if required) in the input window, and the test cycle begins. From now on, everything will run automatically. The progress of the measurement can be followed in the terminal. If an error occurs, a message with error details is sent to a specific Slack channel, and the shifter is notified. Depending on the type of error, the shifter can correct the error via a remote connection or restart the test cycle.

During the test *run*, the next cycle can be prepared. The PMTs from the previous *run* can be unmounted and sorted into shipping boxes based on their voltage classes. Faulty PMTs are sorted out and shipped separately. The location of a PMT is tracked via the `Scanner Service`. Step 1 can now be executed, and the next cycle can start with step 2.

The Test *Run*

The automated test cycle consists of a sequence of measurements. Measurements in the scope of the software can be from either hardware measurements, analysis measurements, or special measurements. The hardware measurements set up hardware and record actual data (e.g., SPE measurements, dark rate measurements). Analysis measurements analyze the data recorded in hardware measurements (e.g., SPE analysis, arrival times analysis). A special measurement is everything that does not fall into the previously mentioned categories (e.g., device inserts, cooldown).

1. **Device Inserts**: Up to this point the µBase and the PMT were two separate devices in the IceCube-wide FatCat database. To link them together, the mainboards read the unique ID (UID) of the µBase and link them to the serial number of the PMT on this channel. This device pair is then inserted into the FatCat database. All test results for a PMT can later be looked up either via the PMT serial number or the UID.
2. **max HV**: The cathode voltage of the PMTs is set to the maximum operating voltage (113 V at the 10th dynode). This burn-in phase of the PMTs reduces the dark rate of the PMT and allows all components to settle into the operating state and ensure consistent quality of the PMT results.
3. **Cooldown**: The cooling chamber is switched on, and the target temperature is set to −20 °C. It takes approx. 3 h until the cooling chamber has cooled down from ∼ 25 °C to −20 °C. This is also the time available for the burn-in phase.
4. **Gain Calibration**: Find the target voltage at which a gain of 5×10^6 is achieved.
5. **SPE spectrum (375 nm)**: Recording and analysis of a Single Photoelectron spectrum with the 375 nm LED.
6. **SPE spectrum (505 nm)**: Recording and analysis of a Single Photoelectron spectrum with the 505 nm LED.
7. **Discriminator Calibration**: Calibration of the discriminator to 0.5 PE.
8. **Arrival times**: Measurement of arrival times, pre- and late-pulse with charge stamps.
9. **Linearity**: Measurement series with the bright LED and analysis of the linearity of the PMT.
10. **Afterpulses**: Recording long light curves to analyze the afterpulses.
11. **Dark Rate**: Measurement of the dark rate for slightly more than one hour.
12. **Switch Off PMT**: The PMTs are switched off, and the supply voltage is interrupted.
13. **Warmup**: The cooling chamber is switched off. The cooling chamber slowly warms up to room temperature. Due to the good insulation of the chamber, this process takes longer than 12 h. For this reason, a heater in the cooling chamber can be switched on manually to speed up the process.

5.5 The Measurements

In this chapter, the different PMT calibration measurements are described. Each section begins with a tabular representation of the hardware settings for each measurement, followed by a detailed analysis of the data collected and the results obtained.

5.5.1 SPE Spectrum

Component	Configuration	
Container	Temperature	$-20\,°\mathrm{C}$
Light Source Sys.	Wavelength	$\lambda = 375\,\mathrm{nm}$ or $\lambda = 505\,\mathrm{nm}$
	Brightness	$\mathrm{bias}_{375} = -0.1\,\mathrm{V}$ or $\mathrm{bias}_{505} = -0.9\,\mathrm{V}$
PMT high voltage	Voltage at 10th dynode	$78\,\mathrm{V}$ to $113\,\mathrm{V}$
DAQ Settings	Readout Mode	Charge stamps
	Trigger Mode	Global
	Trigger Treshold	$5\,\mathrm{mV}$
	Num. of Chrg. Stamps	$100\,000$ or $300\,000$

Most measurements for the PMT calibration are based on the SPE spectrum. PMT waveforms are recorded and analyzed and then combined to the SPE spectrum. To ensure accurate results, an occupancy level of around 10% is maintained and ensures that multi-photon events remain below 1%.

Waveforms for all channels are acquired through an electronic trigger pulse generated by the ps-pulser. Each trigger initiates the readout of one waveform from each channel. Around 10% of the recorded waveforms contain actual pulses. The detected pulses consistently occur within a similar time window due to similar transit times. The waveforms are processed on the mDOM mainboard to reduce bandwidth requirements and faster transfer to the DAQ PC. For the readout mode *charge stamps*, a baseline correction is applied to the waveform. The correction factor is determined in a continuous rolling time window before the readout is triggered.

Charge integration then occurs over a fixed time window in which a pulse is expected. The measured charge is corrected for AFE gain before being transmitted to the DAQ PC. The arrival time of the pulse is determined by identifying the first non-zero entry of the discriminator flag. The resulting data package transmitted from this process is referred to as a charge stamp.

The charges of a measurement series are plotted in the SPE spectrum. The pulse generators trigger the mainboards; the charge stamps are recorded and filled into a histogram. The SPE spectrum consists of several components: the noise peak and the PE peaks. Contributions with different photoelectron numbers can be distinguished in the histogram. An exemplary SPE spectrum is shown in Figure 5.25, and various parameters can be extracted from the characteristic charge distribution.

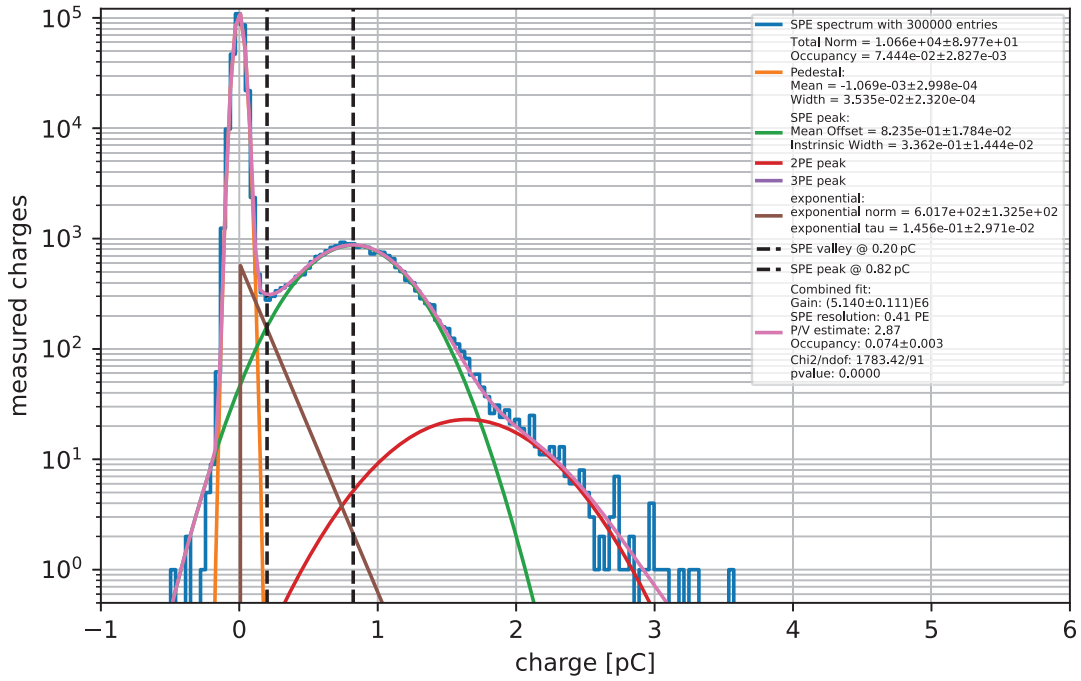

Figure 5.25: An exemplary SPE spectrum, recorded at −20 °C and an operating voltage of 94.19 V. The charge is plotted in pC on the x-axis. The y-axis shows how often the corresponding charge was measured. The SPE spectrum of the measured charges is shown in blue. The individual components of the fit function are also shown: in orange, the noise peak; in green, the SPE peak; in red, the 2 PE peak; and in brown, an exponential function representing poorly amplified photons. The fit results are given in the legend on the right.

The fit function is structured as follows:

$$f(x) = f_{\text{ped}}(x) + \sum_{i=1}^{3} f_{i\text{PE}}(x) + f_{\text{exp}}(x) \tag{5.12}$$

The terms of the fit function and their explanation are described below.

Noise Peak

The peak around 0 pC is referred to as the noise peak and is generated by the waveforms without a pulse. The range in which a pulse is expected for each waveform is integrated, and the charge in this interval is calculated. If there is no pulse in the integration window, only noise is integrated. Due to the base correction, the charge fluctuates around 0 pC and follows a Gaussian distribution. $f_{\text{ped}}(x)$ describes the noise peak and is also called pedestal:

$$f_{\text{ped}}(x) = a_{\text{ped}} \cdot \frac{1}{\sqrt{2\pi\sigma_{\text{ped}}^2}} \cdot \exp\left(-\frac{(x-\mu_{\text{ped}})^2}{2\sigma_{\text{ped}}^2}\right) \tag{5.13}$$

PE Peaks

In Figure 5.25, the charge distribution of the waveforms containing a pulse can be seen to the right of the noise peak. The prominent peak directly next to the noise peak is the SPE peak. Here, the pulse was triggered by a single photon, and the mean value $\sigma_{1\text{PE}}$ indicates the average charge of these pulses. The photoelectron amplification can be determined from the mean value by dividing by the elementary charge e.

$$\text{Gain}Y = \frac{\mu_{1\text{PE}-\mu_{\text{ped}}}}{\text{e}} \tag{5.14}$$

$$\sigma_Y = \frac{\sigma_{1\text{PE}}}{\text{e}} \tag{5.15}$$

The SPE peak, the 2 PE peak, and the 3 PE peak are described in the fit function (5.12). i describes the number of photoelectrons emitted by the cathode, and the function is described as follows:

$$f_{i\mathrm{PE}}(x) = B \cdot a_{i\mathrm{PE}} \cdot \frac{1}{\sqrt{2\pi\sigma_{i\mathrm{PE}}^2}} \cdot \exp\left(-\frac{(x-\mu_{i\mathrm{PE}})^2}{2\sigma_{i\mathrm{PE}}^2}\right) \tag{5.16}$$

$$B = \frac{1}{2}\left[1 + \mathrm{erf}\left(\frac{10x}{\sqrt{2}}\right)\right] \tag{5.17}$$

Introducing an attenuation term B for the PE peaks has proven helpful in tests. The error function erf limits the influence of pulses with very small or negative charges and stabilizes the fit.

Incompletely Amplified Photoelectrons

The last component of the fit function represents the electrons that are not fully amplified in the PMT and is described by an exponential function. An attenuation term B (5.17) also suppresses unphysical results with negative charges.

$$f_{\mathrm{exp}}(x) = B \cdot a_{\mathrm{exp}} \cdot \exp\left(-\frac{x}{\tau}\right) \tag{5.18}$$

Occupancy

For low light intensities, the single components of the fit are no longer independent. Poisson's statistics can describe the number of triggered photoelectrons.

$$P(i,\lambda) = \frac{\lambda^i e^{-\lambda}}{i!} \tag{5.19}$$

The occupancy is defined as the ratio between the waveforms containing a pulse and the total of the measured waveforms and can be written as:

$$\mathrm{occupancy} = \sum_1^3 \frac{\int f_{i\mathrm{PE}}(x)dx}{\int f(x)dx} = \sum_1^3 P(i,\lambda) = 1 - P(0,\lambda) \tag{5.20}$$

This results in a correlation between the PE peaks and the noise peak, which reduces the number of fit parameters from 14 to 8.

$$\mu_{\text{ped}} = \mu_0 \qquad \mu_{i\text{PE}} = \mu_0 + i \cdot \mu_1$$
$$\sigma_{\text{ped}} = \sigma_0 \qquad \sigma_{i\text{PE}} = \sigma_0 + i \cdot \sigma_1$$
$$a_{\text{ped}} = h \cdot e^{-\lambda} \qquad a_{i\text{PE}} = a \cdot e^{-\lambda} \cdot \frac{\lambda^i}{i!}$$

Several more properties can be extracted from this type of measurement and will be explained in subsection 5.5.3.

5.5.2 HV vs. Gain

Component	**Configuration**	
Container	Temperature	$-20\,°\text{C}$
Light Source Sys.	Wavelength	$\lambda = 375\,\text{nm}$
	Brightness	$\text{bias}_{375} = -0.1\,\text{V}$
PMT high voltage	Voltage at 10th dynode	[78 V, 86 V, 95 V, 104 V, 113 V]
DAQ Settings	Readout Mode	Charge stamps
	Trigger Mode	Global
	Trigger Treshold	5 mV
	Num. of Chrg. Stamps	100 000

The target gain of the PMTs is 5×10^6 at a cathode voltage between 950 V to 1350 V. The voltage needed to achieve the target gain is called the target voltage U_{target}. The cathode voltage cannot be read out directly. Instead, the voltage is measured at the 10th dynode. The required voltage range is therefore 79 V to 113 V. As described in subsection 3.3.2, gain and supply voltage are related via a power law, and formula (3.4) can be written with a coefficient A and the exponent x as:

$$G(U) = A * U_{\text{dy10}}^x \tag{5.21}$$

Five SPE measurements are carried out at 78, 86, 95, 104, 113 V and a power law according to (5.21) is fitted to the values.

The target voltage for a gain of $G_{\text{target}} = 5 \times 10^6$ can then be calculated with the inverse of the fit function:

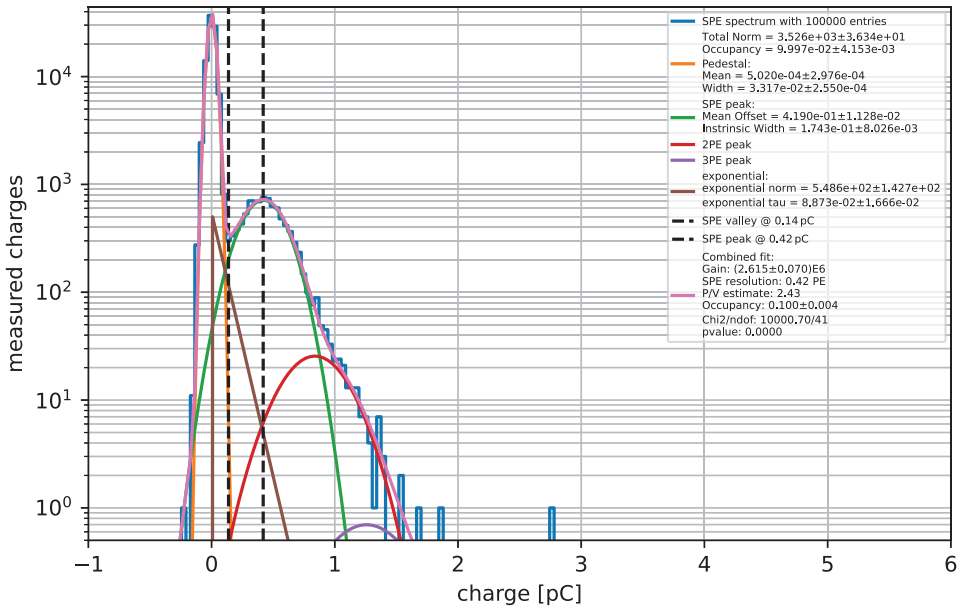

(a) SPE spectrum with $U_{\mathrm{dy10}} = 86\,\mathrm{V}$.

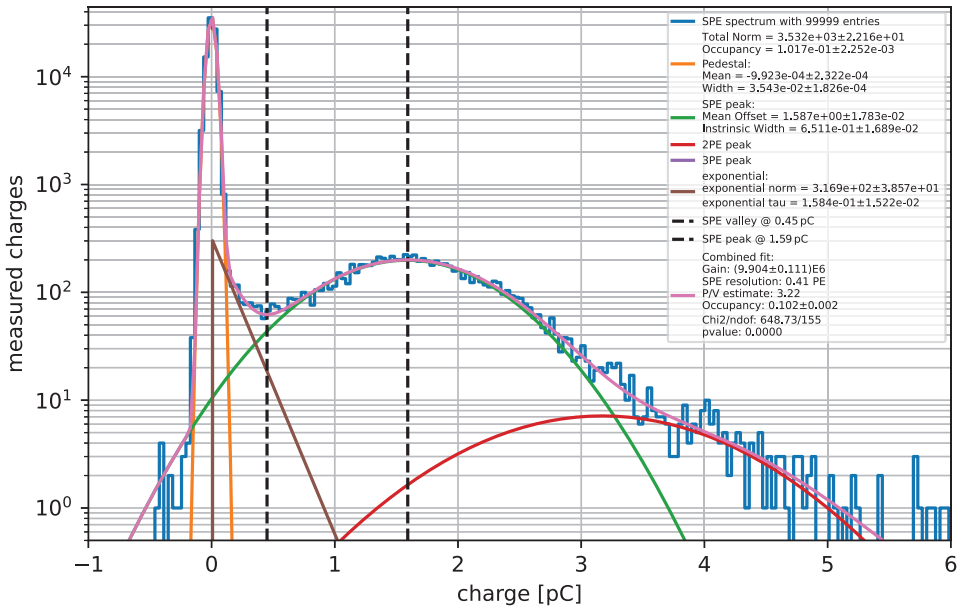

(b) SPE spectrum with $U_{\mathrm{dy10}} = 104\,\mathrm{V}$.

Figure 5.26: Two SPE spectra of PMT `DM00231` with $U_{\mathrm{dy10}} = 86\,\mathrm{V}$ (top) and $U_{\mathrm{dy10}} = 104\,\mathrm{V}$ (bottom). The different measured gain for both supply voltages is $G_{86\,\mathrm{V}} = 2.6$ and $G_{104\,\mathrm{V}} = 9.9$ respectively.

$$U_{\text{target}} = \left(\frac{G_{\text{target}}}{A}\right)^{\frac{1}{x}} \tag{5.22}$$

For a more stable fit, the gain and the voltage are rescaled to values close to one before fitting:

$$G_{\text{rescaled}} = \frac{G_{\text{i}}}{G_{\text{target}}} \tag{5.23}$$

$$U_{\text{rescaled}} = \frac{U_{\text{i}}}{\overline{U}} \tag{5.24}$$

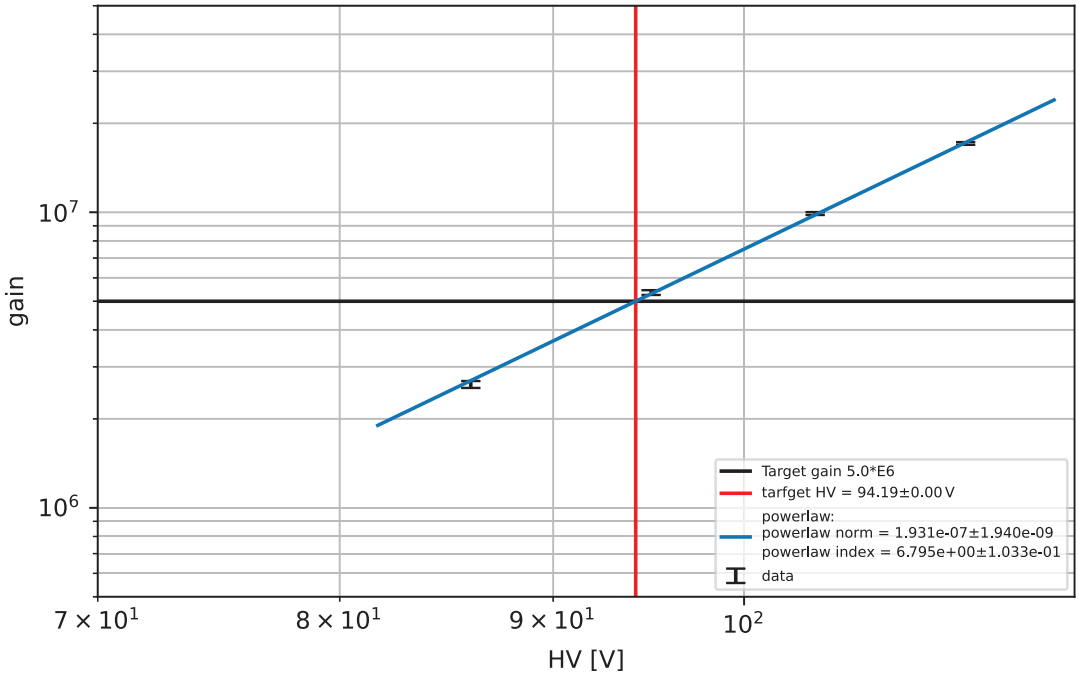

Figure 5.27: An exemplary representation of the high voltage calibration. The voltage at the 10th dynode is plotted on the x-axis, and the measured gain is on the y-axis. Both axes are logarithmic, and the fitted power law is shown as a straight line in blue. The target gain of 5×10^6 is achieved at a target HV of 94.19 V.

In Figure 5.27, an exemplary HV vs. gain calibration is shown. It shows the measured data points (black), the fit (blue), the target gain (horizontal black line),

and the target voltage (vertical red line). The determined target voltage is used for all subsequent measurements.

5.5.3 Properties from the SPE Spectrum

Component	Configuration	
Container	Temperature	$-20\,°\mathrm{C}$
Light Source Sys.	Wavelength	$\lambda = 375\,\mathrm{nm}$ or $\lambda = 505\,\mathrm{nm}$
	Brightness	$\mathrm{bias}_{375} = -0.1\,\mathrm{V}$ or $\mathrm{bias}_{505} = -0.9\,\mathrm{V}$
PMT high voltage	Voltage at 10th dynode	PMT target voltage
DAQ Settings	Readout Mode	Charge stamps
	Trigger Mode	Global
	Trigger Treshold	5 mV
	Num. of Chrg. Stamps	300 000

The SPE spectrum as shown in Figure 5.25 can be used to calculate several PMT properties: The gain Y, the SPE resolution σ_{SPE}, the peak-to-valley ratio (PVR), the occupancy, and the photo detection efficiency (PDE).

For the **SPE resolution** the width of the SPE peak is expressed in units of the expected SPE charge:

$$\sigma_{\mathrm{SPE}} = \frac{\sigma_{\mathrm{1PE}}}{\mu_{\mathrm{1PE}}} \tag{5.25}$$

The **PVR** is computed by dividing the position of the maximum by the position of the minimum of the fit function, excluding the pedestal peak. Determining the positions of the valley is done by minimizing the fit function in the interval $[0\,\mathrm{pC}, 0.9 \cdot \mu_{\mathrm{1PE}}]$. The position of the maximum differs slightly from the position of the SPE peak due to contributions of the 2PE peak and the exponential. The inverse of the fit function is minimized in the interval $[q_{\mathrm{valley}}, \infty]$ and the PVR is calculated as

$$\mathrm{PVR} = \frac{\max(f(x)[q_{\mathrm{valley}}, \infty])}{\min(f(x)[0\,\mathrm{pC}, 0.9 \cdot \mu_{\mathrm{1PE}}])}. \tag{5.26}$$

The QE stated in the manufacturer's specifications for the PMTs cannot be measured directly. Instead, the PDE is used to determine the QE. They are connected to each other via the collection efficiency (CE):

$$\mathrm{PDE} = \mathrm{QE} \cdot \mathrm{CE} \tag{5.27}$$

Variations in the CE are neglected as the voltage between the photocathode and first dynode is $U_{\mathrm{cat}} = 3 \cdot U_{\mathrm{dy10}} > 200\,\mathrm{V}$. For such voltages, the CE is close to one and can be considered constant [60].

The **PDE**, similar to the occupancy, is defined as the ratio of the measured pulses to the incident photons. Due to this close relationship, the PDE is proportional to the occupancy for low light intensities:

$$\mathrm{occ_i} = \mathrm{PDE_i} \tag{5.28}$$

Simultaneously measured SPE spectra from all PMTs in a run are compared against four reference PMTs present in the same run with known QEs. The QEs for 10% of the PMTs are measured by the manufacturer and delivered with the PMTs. The measured occupancies are corrected for the channel-specific light yield $f_{\mathrm{corr}}(\mathrm{ch})$ at each position utilizing the correction factors from subsection 5.3.3. The quantum efficiencies $\mathrm{QE_i}$ are then computed as the median of the scaled QEs of the reference PMTs $\mathrm{QE_{j,ref}}$:

$$\mathrm{QE_i} = \mathrm{median}\left(\mathrm{QE_{j,ref}} \cdot \frac{\mathrm{occ_i}}{f_{\mathrm{corr}}(\mathrm{i,\ ch})} \cdot \frac{f_{\mathrm{corr}}(\mathrm{j,\ ch})}{\mathrm{occ_{j,\ ref}}}\right) \tag{5.29}$$

[60]: Hamamatsu (2017), *Photomultiplier Tubes: Basics and Applications*

5.5.4 Discriminator Calibration

Component	Configuration	
Container	Temperature	$-20\,°C$
Light Source Sys.	Wavelength	$\lambda = 375\,nm$
	Brightness	$bias_{375} = -0.1\,V$
PMT high voltage	Voltage at 10th dynode	PMT target voltage
DAQ Settings	Readout Mode	Charge stamps
	Trigger Mode	Global
	Trigger Treshold	$5\,mV$
	Discriminator Setting	$3\,mV$ to $8\,mV$
	Num. of Chrg. Stamps	100 000

The mDOM mainboards can trigger the data readout in two ways:
Firstly, the readout can be triggered *globally* for all channels simultaneously via an external trigger connection or by a predefined channel. Secondly, each channel can be read out *independently* of the other channels.

If the external trigger connection is not used, the readout is triggered by a discriminator threshold value. The threshold value can be specified either in analog-to-digital converter (ADC) counts or volts. For the trigger channels, the threshold is $0.005\,V$ and the main board automatically determines the voltage above the dark current. The threshold value is specified directly in ADC counts for all other channels. Whether the discriminator threshold has been exceeded is stored in the readout data of every channel, even if the readout data was triggered globally.

A threshold value of $0.2\,PE$ is specified in the specification for the dark rate measurement. The relationship between PE and voltage or ADC counts is established in the discriminator calibration. For this purpose, several SPE measurements with different discriminator thresholds are carried out, and the cumulative ratio of waveforms with and without exceeding the threshold is calculated for each measurement. Such a measurement is shown in Figure 5.28.

If the ratio reaches the value 0.5, the corresponding charge is assigned to the threshold value in ADC counts. The conversion from charge to photoelectrons is described in the formula (5.30).

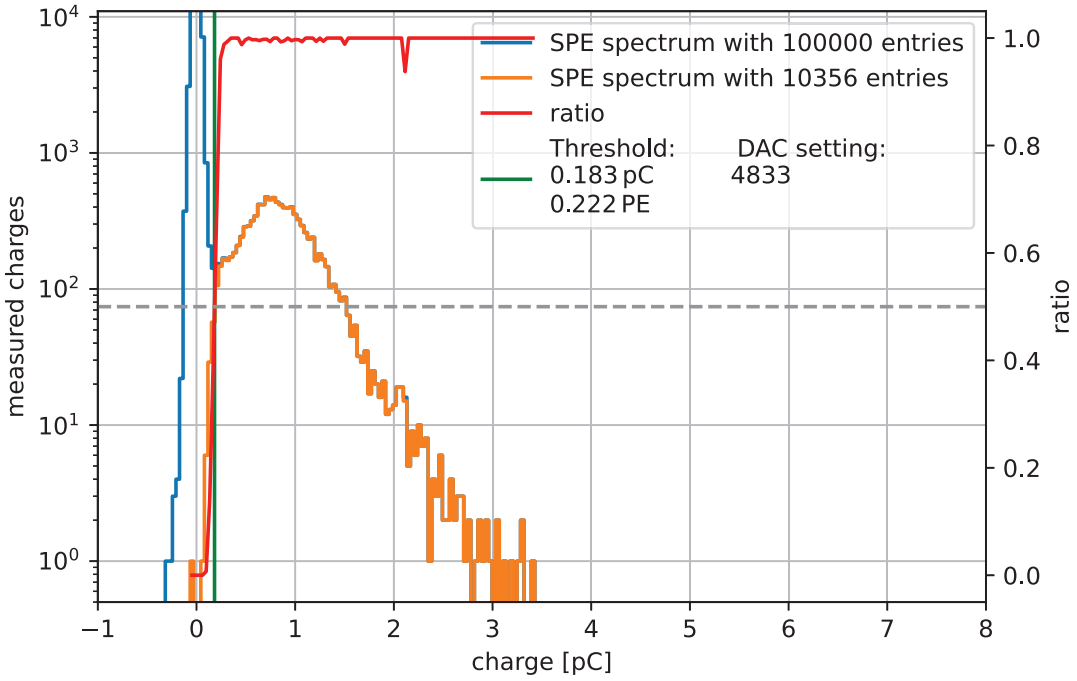

Figure 5.28: The SPE spectrum consists of two populations; all externally triggered events are shown in blue, and all events in which the discriminator threshold was exceeded are shown in orange. Exceeding the threshold would trigger the channel to be read out without an external trigger. The cumulative ratio of all events to the internally triggered events is shown in red. The threshold value in PE is defined at a ratio of 0.5 (green vertical line).

$$N_{\text{photons}} = \frac{Q}{\mu_{\text{1PE}}} \tag{5.30}$$

Figure 5.29 shows the Discriminator DAQ setting for the corresponding charge thresholds. A linear function fitted to the data can be used to calculate the associated threshold value in ADC counts for any given charge.

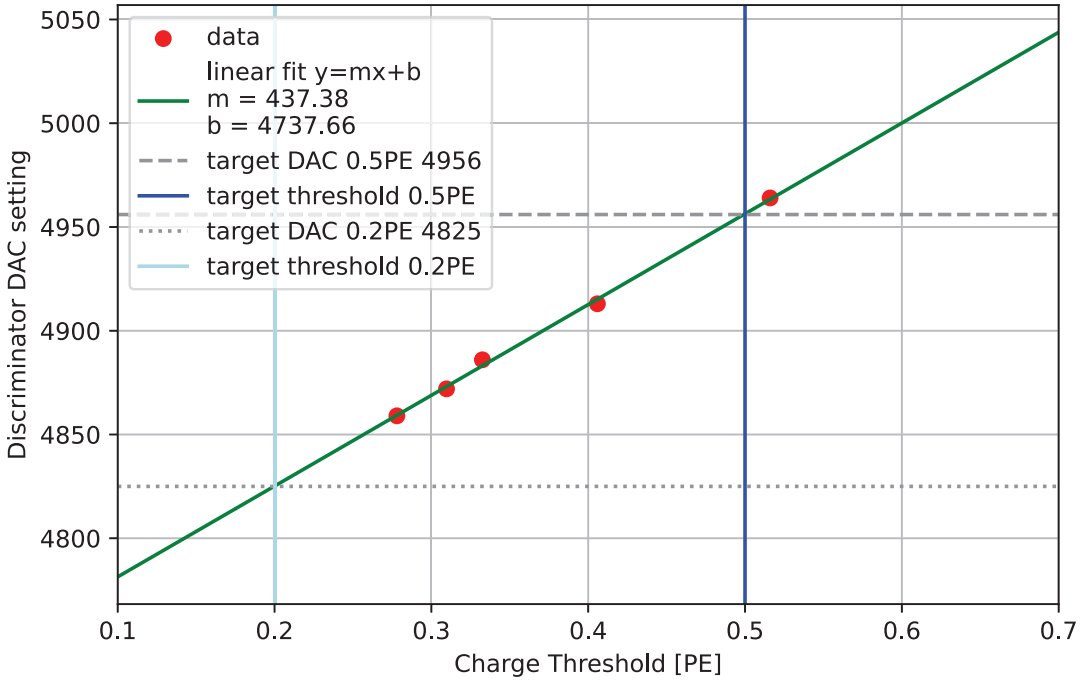

Figure 5.29: The recorded data is shown in red, and the linear fit is in green. The two threshold values at which the channel should trigger are marked as vertical lines in blue. The 0.2 PE threshold value is given in the specifications of the PMTs, and the 0.5 PE threshold value is used in the acceptance tests. The horizontal lines indicate the respective DAC settings for the threshold value in ADC counts.

5.5.5 Arrival Time Measurement

Component	Configuration	
Container	Temperature	−20 °C
Light Source Sys.	Wavelength	$\lambda = 375\,\text{nm}$
	Brightness	$\text{bias}_{375} = -0.1\,\text{V}$
PMT high voltage	Voltage at 10th dynode	PMT target voltage
DAQ Settings	Readout Mode	Waveforms
	Trigger Mode	Global
	Trigger Treshold	0.5 PE
	Num. of Waveforms	100 000

The arrival times of the pulses in the PMT play an essential role in the performance of IceCube, as they are the primary factor for estimating distances between modules and determining the trajectory of the particle. Uncertainties in the arrival times affect the reconstructions. These uncertainties are called transit time spread. Therefore, the strength of the TTS is determined and corrected by the factor of the variance in the light system used. Only PMTs with a TTS below the specification of 2 ns are included in the mDOMs.

Full waveforms with a 0.5 PE discriminator threshold are recorded for the arrival times. Charge stamps carry only the first discriminator crossing as the arrival time of the pulse, as opposed to waveforms, where every crossing of the discriminator threshold is extracted as an arrival time. This measurement can obtain several values simultaneously: the TTS, the pre- and the latepulses.

Each mainboard has a dedicated trigger channel that is issued by the FPGA on a 120 MHz clock. This introduces an inherent fluctuation of approximately 8 ns in the arrival times of both the trigger and PMT pulse within the waveform. The discriminator flag is sampled at 960 MS/s resulting in a DAQ timing resolution of $\Delta t_{\mathrm{DAQ}} = 1.04\,\mathrm{ns}$. A special channel (channel 23) of each mainboard is used as the trigger channel for this purpose. The recorded arrival times for the trigger pulses are then subtracted from those of the PMT pulses.

In Figure 5.30, a corrected arrival time spectrum is shown. An arrival time of 0 ns means the pulse was measured simultaneously with the trigger pulse. In the figure, the main peak is around 54 ns. This indicates the time it takes for the generated pulse in the pulser module to switch the avalanche transistor, convert the energy in the LED into light, pass through a 3 m optical fiber, and the diffuser to the PMT and run through all dynodes in the PMT until it can be measured at the anode. More important than this absolute transit time are the differences in the arrival times caused by slightly different paths of the electrons in the PMTs. This variance in transit time is referred to as the TTS.

The TTS is determined by fitting a Gaussian curve to the main peak. For this purpose, a time window of ± 5 ns is selected around the maximum of the distribution. In Figure 5.30, the main peak is highlighted in green and the fit to the peak is shown in red. The standard deviation of the Gaussian function describes the TTS of the entire distribution. The transit time can be broken down into three independent components: the transit time from the pulser to the PMT t_{ls}, the transit time

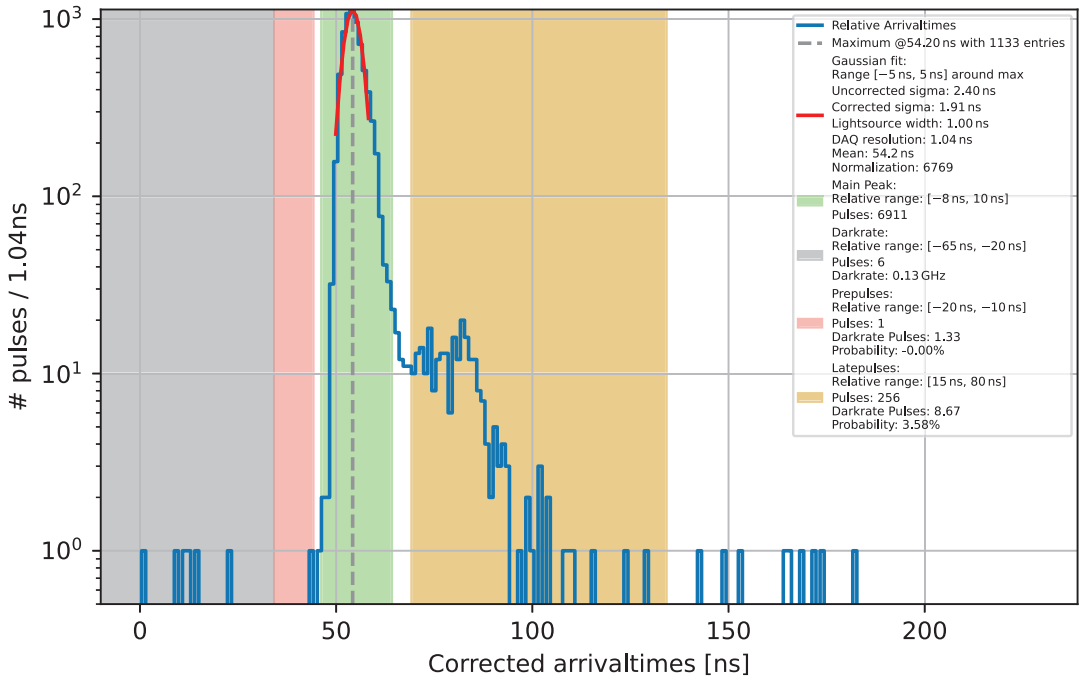

Figure 5.30: A arrival time spectrum at target voltage is shown in blue. A Gaussian is fitted to the main peak to determine the arrival time spread. The colored bands indicate the time windows for dark rate pulses (gray), prepulses (red), main peak (green), and latepulses (yellow).

in the PMT t_{PMT} and the resolution of the main board t_{res}. The resolution does not directly contribute to the runtime but influences the variance of the measured transit time through discretization.

$$t_{\mathrm{tot}} = t_{\mathrm{ls}} + t_{\mathrm{PMT}} + t_{\mathrm{res}} \tag{5.31}$$

The variances of uncorrelated variables can be expressed by the sum of the individual variances. Therefore, the TTS of the PMT is given by:

$$\sigma_{\mathrm{pmt}} = \sqrt{\sigma_{\mathrm{tot}}^2 - \Delta t_{\mathrm{ls}}^2 - \Delta t_{\mathrm{res}}^2} \tag{5.32}$$

With $t_{\mathrm{ls}} = 1\,\mathrm{ns}$ and $t_{\mathrm{res}} = 1.04\,\mathrm{ns}$ given by the hardware limitiations of the test bench.

The probability of pre- and latepulses can also be derived from the measurement of the arrival time. In addition to the main peak, three further areas are defined. The contribution of the dark rate is determined in a time window of −65 ns to −20 ns before the maximum of the main peak. These pulses occur randomly, do not correlate with the actual pulse, and are therefore excluded. The prepulses occur a few nanoseconds before the main peak and are counted in a time window of −20 ns to −10 ns. The late pulses occur after the main peak in a time window between 15 ns and 80 ns. The entries in a 5 ns window around the expectation value of the Gaussian fit are summed to the normalization factor n_{main}. The probabilities can then be calculated by:

$$P_{\text{pre}} = \frac{n_{\text{pre}} - n_{\text{dark}} \frac{\Delta t_{\text{pre}}}{\Delta t_{\text{dark}}}}{n_{\text{main}}} \tag{5.33}$$

$$P_{\text{late}} = \frac{n_{\text{late}} - n_{\text{dark}} \frac{\Delta t_{\text{late}}}{\Delta t_{\text{dark}}}}{n_{\text{main}}} \tag{5.34}$$

5.5.6 Bright LED Charge Spectrum

Component	Configuration	
Container	Temperature	−20 °C
Light Source Sys.	Wavelength	$\lambda = 505\,\text{nm}$
	Brightness	$\text{bias}_{505} = 0.7\,\text{V}$
	Pulser	modified ps-pulser
PMT high voltage	Voltage at 10th dynode	[69 V, 78 V, 86 V, 95 V, 100 V, 104 V, 109 V, 113 V]
DAQ Settings	Readout Mode	charge stamps
	Trigger Mode	Global
	Trigger Treshold	5 mV
	Num. of Chrg. Stamps	100 000

The linearity of PMT response needs to be within 10% for an optical input corresponding to approximately 100 PE within a time frame of 10 ns. The linearity of the PMT response is influenced by two primary factors:

- Current Supply from the µBase: If not enough current is provided by the voltage supply, the PMT response flattens at high incident light. The µBase is designed to provide sufficient current to the PMT.
- Space Charge Effect: The space charge effect occurs if a significant number of charged particles, such as electrons, accumulate near the anode during operation. This accumulation can lead to a local electric field that affects the motion of subsequent electrons emitted from the photocathode. As these secondary electrons encounter this field, their trajectories are altered, resulting in reduced efficiency and non-linear responses due to varying electron distributions.

A modified ps-pulser is employed to generate bright pulses for the measurement as described in section 5.3.1. The expected charge corresponding to 100 PE is approximately 80 pC; however, the light system is only capable of achieving around 40 pC, which corresponds to approximately 52 PE. To achieve a similar anode current as compared to 100 PE, the amplification of the PMT is increased. In order to stay consistent with the measurements conducted in Aachen, the linearity was evaluated at 50 PE.

It is important to note that these results are not factored into decisions regarding the acceptance or rejection of a PMT. The reason for this decision is that the high number of produced secondary electrons creates a different electron distribution inside the PMT and therefore a different PMT response compared to a 100 PE light pulse.

Several measurements are carried out at maximum LED brightness and different operating voltage settings at the PMT to detect possible saturation effects. As a result, a high anode current is measured at the anode despite the low light intensity. The results of the measurements with a bright LED and different voltages for the PMT `DM00231` are shown in Figure 5.31 as an example.

The measured charges at different operating voltages are converted into the number of measured electrons. For this, a Gaussian is fitted to the charge spectrum in an interval of 0.7 standard deviations around the maximum of the distribution $[q_{\max} - 0.7\sigma,\, q_{\max} + 0.7\sigma]$. The expectation value μ of the fit is then used to calculate the number of electrons N_e recorded at the anode:

$$N_e = \frac{\mu}{e} \tag{5.35}$$

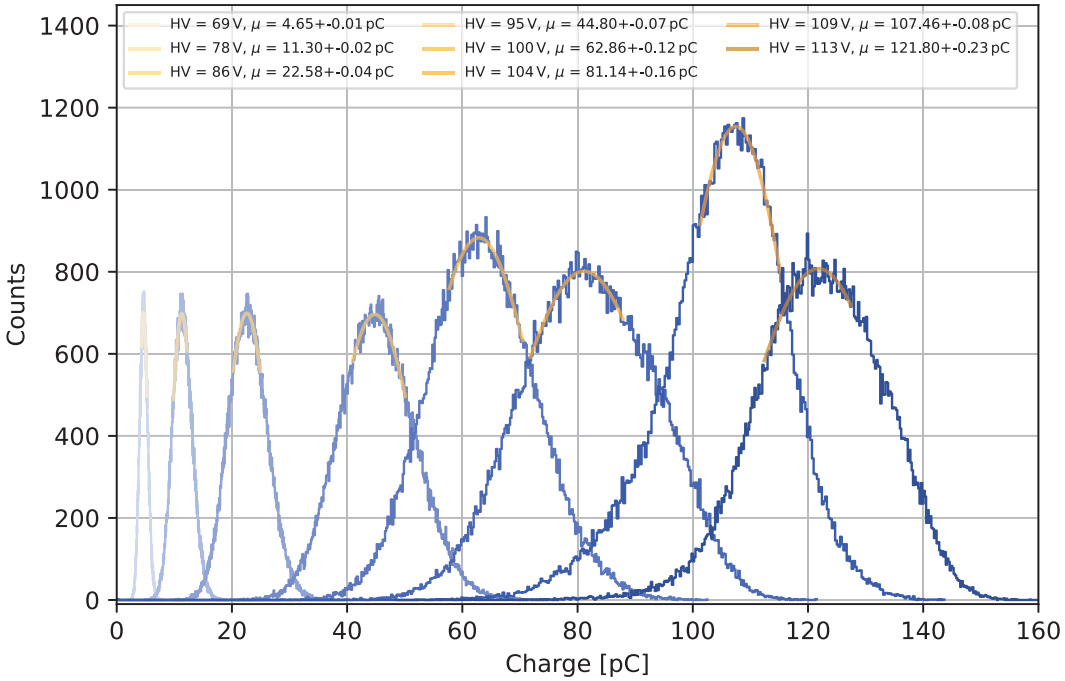

Figure 5.31: The charge spectrum of all bright LED measurements of PMT `DM00231`. A higher charge is measured with a higher operating voltage (HV). A Gaussian is fitted to the peak of each distribution, and the mean of the fit is given by μ.

and the number of photos N_γ is obtained by dividing the number of electrons N_e by the gain $G_{\text{SPE, @sup. voltage}}$ at this supply voltage (Equation (5.36)).

$$N_\gamma = \frac{N_e}{G_{\text{SPE, @sup. voltage}}} \tag{5.36}$$

The amplification depends on the set voltage and is only available for the voltages of the SPE measurements. Therefore, the charges for the SPE voltages are interpolated for voltages below the target voltage. This holds true because by definition the number of photoelectrons in the SPE measurements is $N_\gamma = 1$.

Each bright LED pulse releases the same number of photons, and the detected number of photons should be the same for all supply voltages. If the PMT runs into non-linear conditions, the number of detected photons is reduced. The number of released photons per pulse is measured at supply voltages U below the target voltage

U_{target} because no saturation effects are expected at these operating conditions. The mean number of photoelectrons N_{mean} is calculated.

$$N_{\text{mean}} = \langle N_\gamma \rangle_{U<U_{\text{target}}} \tag{5.37}$$

With the knowledge of N_{mean}, it is possible to calculate the amplification gain to simulate an anode signal corresponding to $N_{100} = 100\,\text{PE}$:

$$G_{\text{new}} = \frac{N_{100}}{N_{\text{mean}}} \cdot G_{\text{@target voltage}} \tag{5.38}$$

From the HV vs. gain measurement, the read-off voltage can be determined using the formula (5.21). The number of measured electrons $N_{\text{e, new}}$ is read from the interpolation of the curve recorded with the bright LED and converted to the number of photoelectrons $N_{\gamma,\text{ new}}$:

$$N_{\gamma,\text{ new}} = \frac{N_{\text{e, new}}}{G_{\text{new}}} \tag{5.39}$$

The linearity can then be defined as:

$$\text{Linearity} = \frac{N_{\gamma,\text{ new}}}{N_{\text{mean}}} \tag{5.40}$$

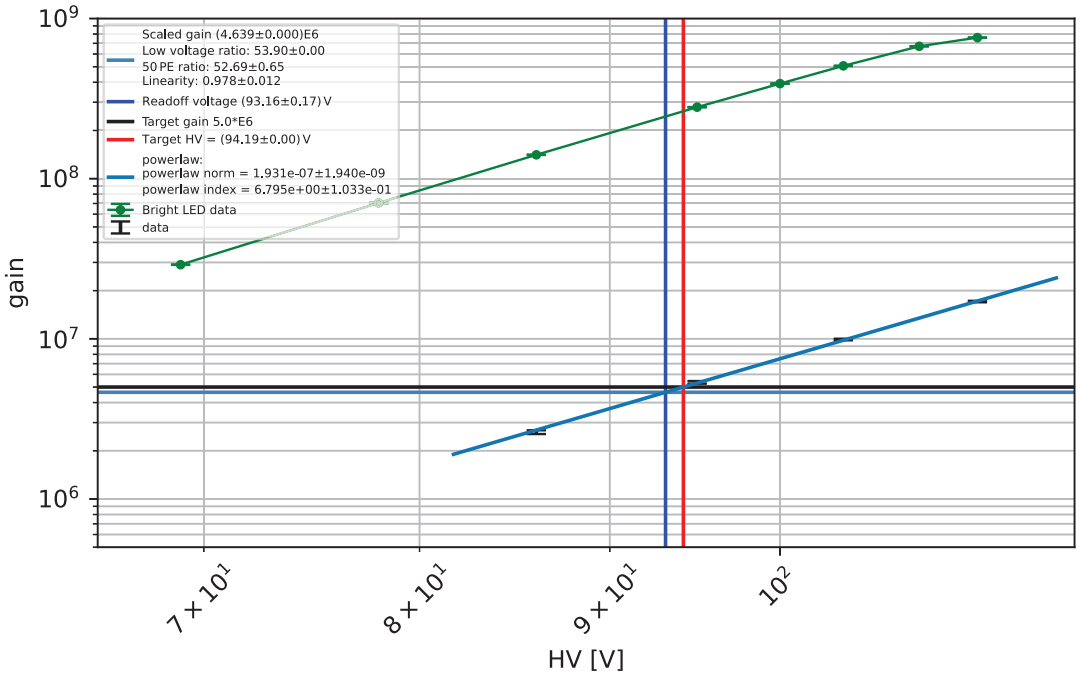

Figure 5.32: The charge linearity is determined by comparing measured bright charge spectra (green line) with the ones obtained from high voltage calibration (blue line). The red vertical line denotes the target voltage of the PMT, whereas the blue vertical line indicates the voltage at which linearity is assessed.

5.5.7 Afterpulse

Component	Configuration	
Container	Temperature	$-20\,°C$
Light Source Sys.	Wavelength Brightness	$\lambda = 375\,nm$ $bias_{375} = -0.1\,V$
PMT high voltage	Voltage at 10th dynode	PMT target voltage
DAQ Settings	Readout Mode Trigger Mode Trigger Treshold Num. of Waveforms Num. of Samples	Waveforms Global 0.5 PE 1000 1500

Afterpulses are generated by excited residual gas in the vacuum tube of the PMT. They are expected in a few hundred nanoseconds to a few microseconds after the actual pulse [95]. To determine the number of afterpulses, the time window of the individual measurements is extended to 12 µs. To reduce the total measurement time, a smaller set of 1000 lightcurves is recorded and analyzed as described previously in subsection 5.5.5.

A trigger-corrected arrival time spectrum of the long light curves is shown in Figure 5.33. The prominent peak around 50 ns is the main peak, as already described in Figure 5.30. In addition, all afterpulses are recorded in the time window [100 ns, 12 µs] after the main peak highlighted in yellow. The probability of an afterpulse is 3.42% for this PMT. The probability was calculated by dividing the number of pulses in the time window of the afterpulse N_{after} by the number of pulses in the main peak N_{main}. Before division, the contribution from dark rate pulses in the time window of the afterpulses is subtracted.

$$P_{\text{after}} = \frac{N_{\text{after}} - N_{\text{dark}} \frac{\Delta t_{\text{after}}}{\Delta t_{\text{dark}}}}{N_{\text{main}}} \cdot \frac{1}{c_{\text{2pe}}} \tag{5.41}$$

To return the probability of afterpulses per single incoming photon, the factor c_{2pe} corrects the main peak N_{main} to just single photons.

$$c_{\text{2pe}} = \frac{\overline{q}_{\text{main}}}{q_{\text{spe}}} \tag{5.42}$$

The number of photons in the main peak can be determined using the mean value of all charges in the main peak $\overline{q}_{\text{main}}$:

$$q_{\text{spe}} = G_{\text{targetHV}} \cdot \text{e} \tag{5.43}$$

The expected average charge q_{spe} for a single photon can be calculated from the measured amplification at the target voltage G_{targetHV} and the elementary charge e.

[95]: Lubsandorzhiev et al. (2000), "Studies of Prepulses and Late Pulses in the 8 Electron Tubes Series of Photomultipliers"

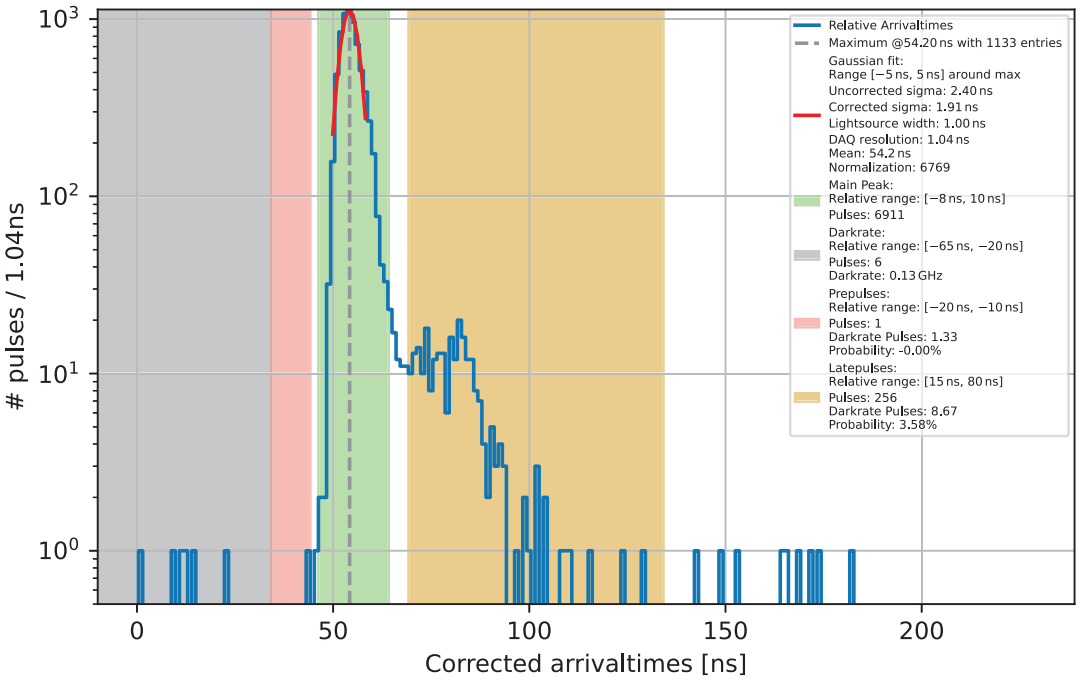

Figure 5.33: Distribution of trigger-corrected arrival times for afterpulse measurements. The gray area [−65 ns, −20 ns] indicates the area used to estimate the dark rate contribution. The red band [−10 ns, 15 ns] shows the region of the main peak. The yellow area [100 ns, 12 µs] shows the afterpulse region.

5.5.8 Dark Rate Measurement

Component	Configuration	
Container	Temperature	−20 °C
Light Source Sys.		Off
PMT high voltage	Voltage at 10th dynode	PMT target voltage
DAQ Settings	Readout Mode	Scalers
	Trigger Mode	Discriminator
	Trigger Treshold	0.5 PE
	Num. of Scalar reads	100
	Scaler Integration Time	10 s
	Deadtime	$\delta t_{\text{dead}} = 100\,\text{ns}$

To determine the dark rate of a PMT, all discriminator crossings are counted in a time interval of $T = 10\,\mathrm{s}$. After each counted event, there is a dead time of $\delta t_{\mathrm{dead}} = 100\,\mathrm{ns}$ during which no further threshold violations are counted. The measured scaler count N_{dark} needs to be corrected for the higher discriminator threshold 0.5 PE, as described in section 6.1, and is converted to a rate:

$$R = \frac{N_{\mathrm{dark}}}{T} \cdot r \tag{5.44}$$

Possible fluctuations and external events influence the measurement of the dark rates. To minimize statistical fluctuations, the measurement is carried out 100 times, and then the median and standard deviation of all measurements are calculated. In Figure 5.34, the measurement of the dark rate is shown using the example of PMT DM00373.

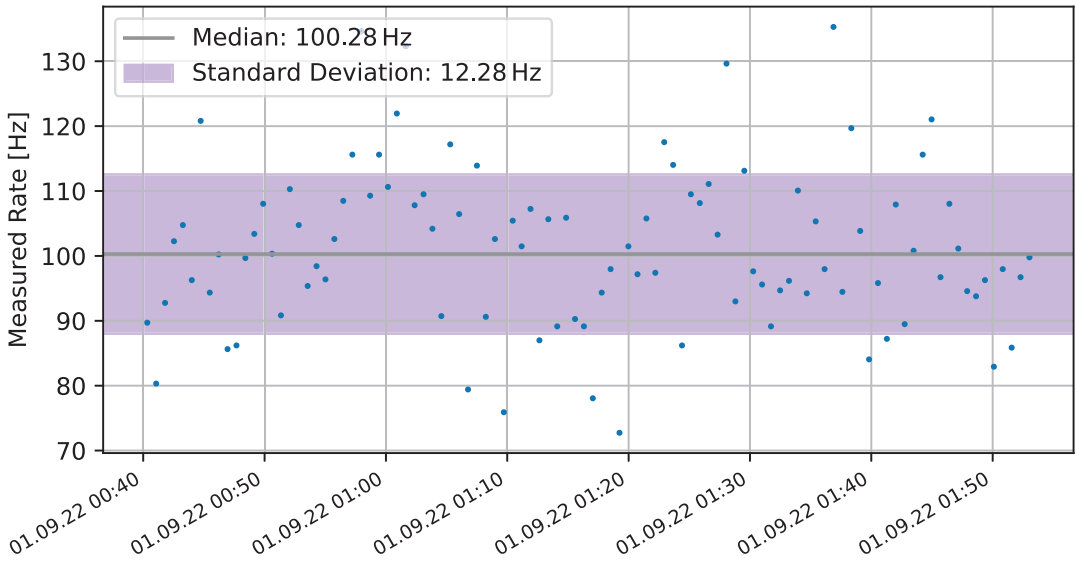

Figure 5.34: 100 dark rate measurements with a measurement length of $T = 10\,\mathrm{s}$ each. This PMT exhibits a stable dark rate.

5.5.9 Baseline Measurement

Component	Configuration	
Container	Temperature	−20 °C
Light Source Sys.		Off
PMT high voltage	Voltage at 10th dynode	PMT target voltage
DAQ Settings	Readout Mode	Waveforms
	Trigger Mode	Global
	Trigger Treshold	5 mV
	Num. of Waveforms	5000

Electronic noise in the µBase and the AFE of the mainboard results in a non-zero baseline. Electromagnetic interference (EM), temperature fluctuations and other factors can cause unstable or drifting baselines. Software-triggered waveforms are recorded over a time period of 10 min to validate the performance of the baseline. The median, mean, and standard deviation of a waveform are calculated and used as indicators of baseline stability.

Figure 5.35 shows the median and standard deviation of a PMT. The median of waveforms without illumination (top) is stable over 10 min with a standard deviation of 0.51 ADC counts. The standard deviation of each waveform without illumination is shown in the bottom plot and exhibits a stable behavior with a mean of 0.74 ADC counts.

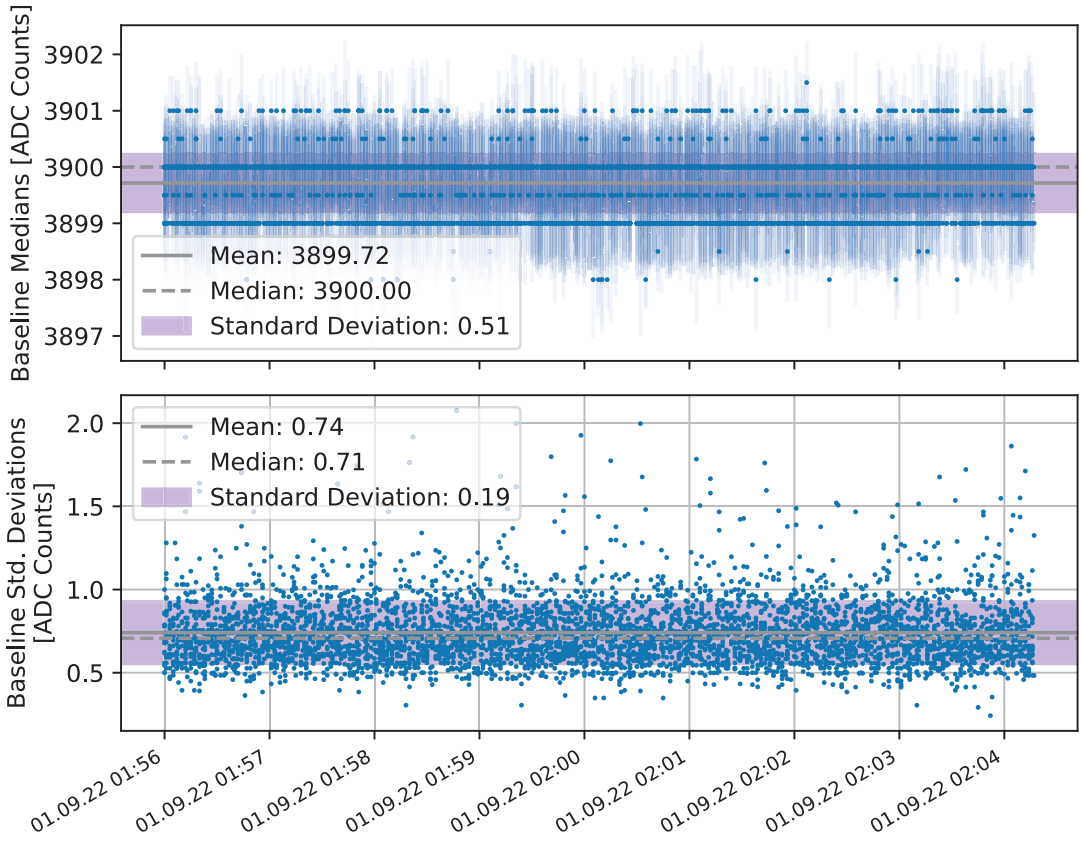

Figure 5.35: Baseline measurement with the median (top) and standard deviation (bottom) of the waveforms over a time of 10 min.

6 Results

Contents

6.1 Technical Challenges of the Test Bench 119

6.2 Summary of PMT Testing Results and Voltage Classifications 122

6.3 Key Findings from PMT Testing 124

6.4 Stability and Channel Dependency of the Results 129

6.5 Comparison with Aachen and Hamamatsu 136

The test bench was developed and built for the acceptance tests of the mDOM PMTs. The primary objective is to perform function tests, check if the PMTs meet the requirements, and categorize them into six different voltage classes. A high throughput of around 500 PMTs per week, expandability to other PMT types, and easy scaling by setting up additional test benches are secondary objectives of this development. As such, the test bench was very successful in all respects.

The next chapter gives an overview of technical challenges faced during mass testing, followed by a summary of the test bench results. The results of the acceptance tests for each measured quantity are found in Appendix A. The dark rate, afterpulse, and TTS measurements will be discussed in detail in section 6.3. Section 6.4 aims to quantify the accuracy of the measurements. A cross-check between the Dortmund and Aachen setups is conducted to ensure comparable testing results, and a comparison to the manufacturer's reported data of the PMTs is made in section 6.5.

6.1 Technical Challenges of the Test Bench

For the timing and dark rate measurements, the discriminator threshold of 0.2 PE is specified in Table 4.1. Measurements with 0.2 PE during the initial dark rate measurements of 1000 PMTs exhibited an inconsistent high dark rate that stabilized for higher threshold settings. Figure 6.1 shows a comparison of the dark rates with different thresholds. The higher dark rate results from triggering on electronic

noise. To avoid this behavior, a higher threshold of 0.5 PE is used for the timing and dark rate measurements. The higher threshold does not influence the timing measurements, and a correction factor r is applied to the measured dark rates to scale the measurements from 0.5 PE to 0.2 PE.

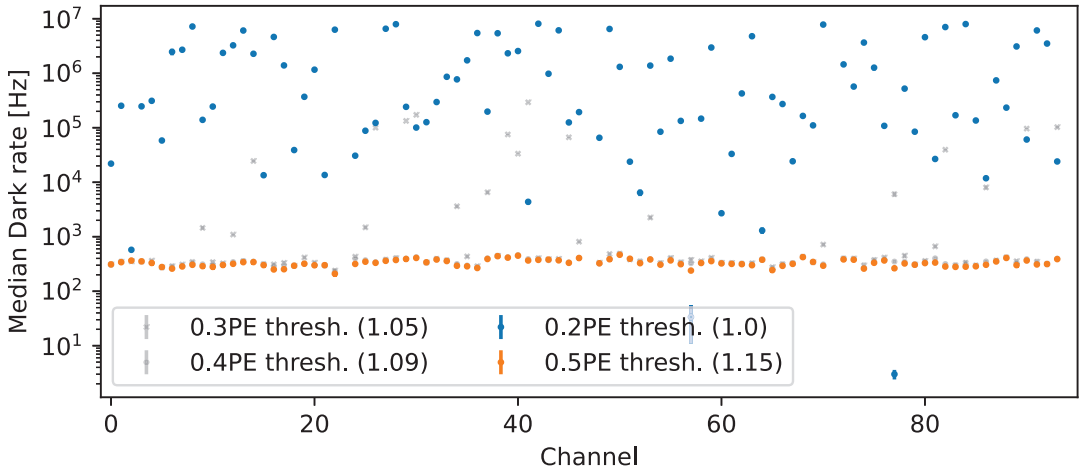

Figure 6.1: The influence of the discriminator threshold is shown. The required threshold of 0.2 PE (blue) shows high scalar measurements, and it can be assumed that electronic noise contributes to these results. The chosen threshold of 0.5 PE is shown in orange and scaled with a correction factor (1.15).

The SPE spectrum from previous measurements at target voltage $U_{\text{dy10, target}}$ can be used to calculate r.

To do so the best-fit parameterization of the exponential function and the SPE peak is integrated across two distinct regions: one beginning at $q_{0.2} = 0.2\,\text{PE} \sim 0.16\,\text{pC}$ and another starting at $q_{0.5} = 0.5\,\text{PE} \sim 0.4\,\text{pC}$. The integrals are defined as follows:

$$\begin{aligned} I_{0.2} &= \int_{0.2\,\text{PE}}^{\infty} (\exp + \text{SPE}) dQ \\ I_{0.5} &= \int_{0.5\,\text{PE}}^{\infty} (\exp + \text{SPE}) dQ \end{aligned} \tag{6.1}$$

resulting in a scaling parameter r:

$$r = \frac{I_{0.2}}{I_{0.5}} \tag{6.2}$$

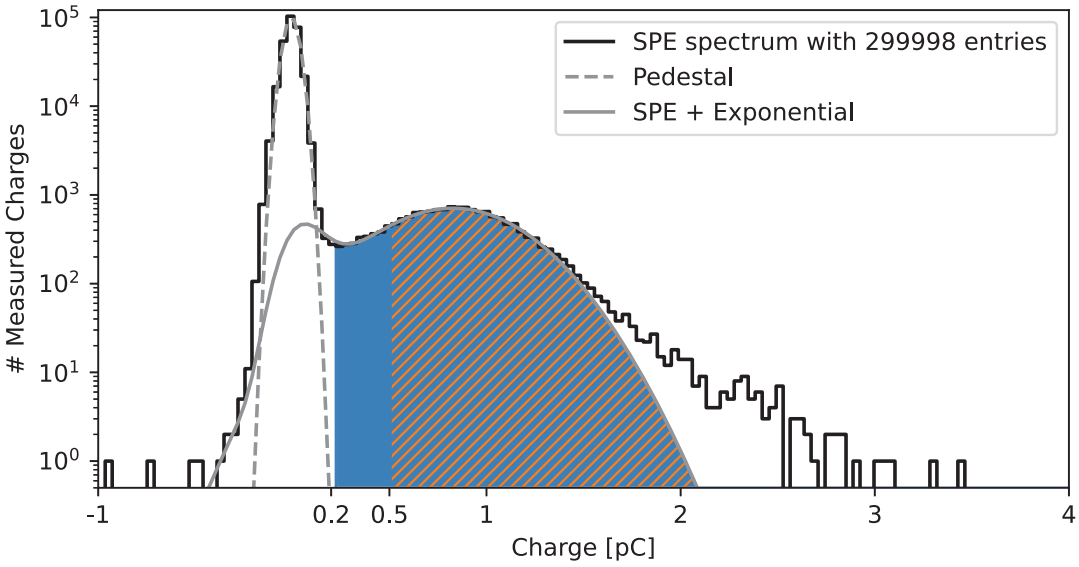

Figure 6.2: The SPE spectrum at target voltage U_{target} is used to calculate the estimated contribution of below threshold events to the dark rate. The blue region is integrated above $q_{0.2} = 0.2\,\text{PE}$ and divided by the integrated area above $q_{0.5} = 0.5\,\text{PE}$ shown in orange.

Failure Modes of the Test Bench

The targeted 500 PMTs per week corresponds to one successful run per day, and the test cycle is designed accordingly. However, some runs had to be restarted during the mass testing, resulting in a lower throughput of 360 PMTs per week. The failure modes can be divided into two categories:

1. **High dark rates in all PMTs:** In some runs, a 10 to 20 times increased dark rate was measured with all PMTs. The run was restarted, and the dark rates were within the expected range during the second run. The entire testing cycle was repeated to ensure that the transient event did not influence other measurements as well. It was not possible to identify a source for this error.
2. **Communication error:** Several types of communication errors between one or more test bench components occurred during operation. These errors were

related to different test bench components or the IceCube database. All errors could be resolved by restarting the measurement or the component. Three sources of the error can be identified:

- Communication interruption to the light source control during a run. If the EV3 is operated for too long without a restart, it results in too many open channels to the PC, reaching the permitted file limit. A new connection is no longer possible, and the run aborts with a communication error. A scheduled restart of the EV3 at the beginning of each test cycle would prevent this error and should be implemented in a future update of the test bench.
- Communication loss to the FatCat-DB. The results of an analysis are transferred to the IceCube-wide database. The connection to FatCat is established at the start of a run and kept open throughout. The run stops with an error if the connection is interrupted and cannot be renewed.
- Communication with one of the mainboards was interrupted once. The reason for this could not be reproduced and did not occur again.

6.2 Summary of PMT Testing Results and Voltage Classifications

In 2022, 10 427 PMTs were tested at TU Dortmund University and RWTH Aachen. A total of 4793 PMTs were tested at the Dortmund site within 15 weeks. For 601 PMTs, the acceptance tests were run a second time because they had failed one or more tests during their first run. This results in a throughput of around 360 PMTs per week.

An overview of all compliant and accepted PMTs tested in Dortmund and Aachen is given in Table 6.1. Nearly all PMTs failed to meet the specified dark rate requirements. This issue was caused by an elevated concentration of radioactive isotopes within the glass envelope of the PMTs. Based on a subsequent study [39, p. 111], the IceCube collaboration concluded that the PMTs could still be utilized, and an agreement was reached with the manufacturer to address and acknowledge

[39]: Unland Elorrieta (2023), "Development, Simulation, and Characterisation of a Novel Multi-PMT Optical Module for IceCube Upgrade with Emphasis on Detailed Understanding of Photomultiplier Performance Parameters"

these findings. The second-highest failure rate is found in the linearity measurements. This can be traced back to the weak design of the light source systems in Aachen and Dortmund, which do not reach the required 100 photons per pulse, and no PMT was rejected due to failed charge linearity requirements. Five PMTs were sent back to the manufacturer. Four of them were unable to reach the maximum voltage. One expressed extreme darkrates in the order of kHz. Other non-conformant PMTs are held back to be used in spare mDOMs.

Specification	**conformant PMTs**	**non-conformant PMTs**	**accepted PMTs**
Dark rate	351	10 076	10 426
Linearity	7237	3190	10 427
TTS	10 255	172	10 427
Afterpulse probability	10 317	110	10 427
quantum efficiency	10 336	91	10 427
Target voltage	10 349	78	10 423
Latepulse probability	10 381	46	10 427
Prepulse probability	10 383	44	10 427
Peak-to-Valley ratio	10 390	37	10 427
SPE resolution	10 396	31	10 427
Total	147	10 280	10 422

Table 6.1: Statistics of the acceptance testing results. A total of 10 427 PMTs were tested. Five PMTs were sent back to the manufacturer. Four of them were unable to reach the maximum voltage. One expressed extreme darkrates. Other non-conformant PMTs are held back for spare mDOMs.

Another important task of the test bench was to sort the PMTs into different voltage classes based on the voltage at target gain. The PMTs are divided into six different voltage classes. The voltage is measured at the 10th dynode.

A	(78 V to 84 V)	■	1198	D	(96 V to 102 V)	□	381
B	(84 V to 90 V)	■	1984	E	(102 V to 108 V)	■	88
C	(90 V to 69 V)	■	1125	F	(108 V to 114 V)	■	14

Table 6.2: The voltage classes and number of PMTs falling into each class measured in Dortmund.

6.3 Key Findings from PMT Testing

This section presents a detailed analysis of key findings obtained from the PMT testing, focusing on dark rates, afterpulses, and TTS. Results of the other measured values from the testing campaign are summarized in Appendix A for reference.

6.3.1 Darkrates

As noted in Table 6.1, the majority of the PMTs fail the specification of a dark rate below $R_{\text{dark}} < 150\,\text{Hz}$. In Figure 6.3 two populations at $(114 \pm 39)\,\text{Hz}$ and $(350 \pm 52)\,\text{Hz}$ are clearly visible.

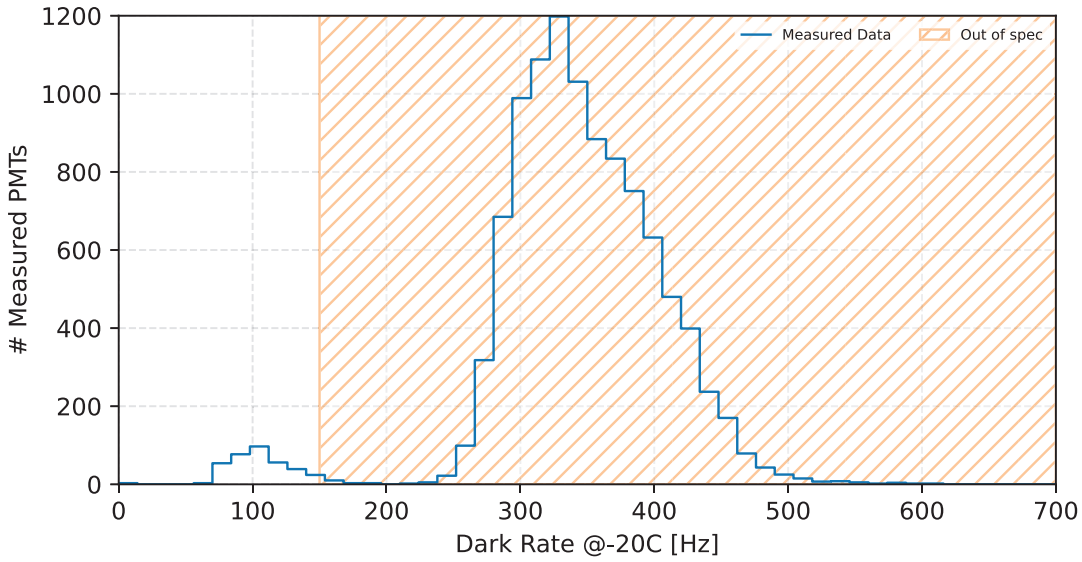

Figure 6.3: Histogram of dark rates measured in Aachen and Dortmund. Two populations are clearly visible: One around $\sim 114\,\text{Hz}$ and one around $\sim 350\,\text{Hz}$. The two populations correspond to PMTs with serial numbers below and above `DM01130` respectively, as shown in Figure 6.4, and the difference in dark rates can be explained by a change in the production process.

Figure 6.4 shows the behavior of the dark rates with respect to their serial numbers. The serial number can be seen as an indication of when in the production process the PMT was produced, with lower numbers corresponding to earlier production dates. Most compliant PMTs were manufactured early in the production. A clear

transition to high dark rates can be observed for PMTs with serial numbers above DM01130.

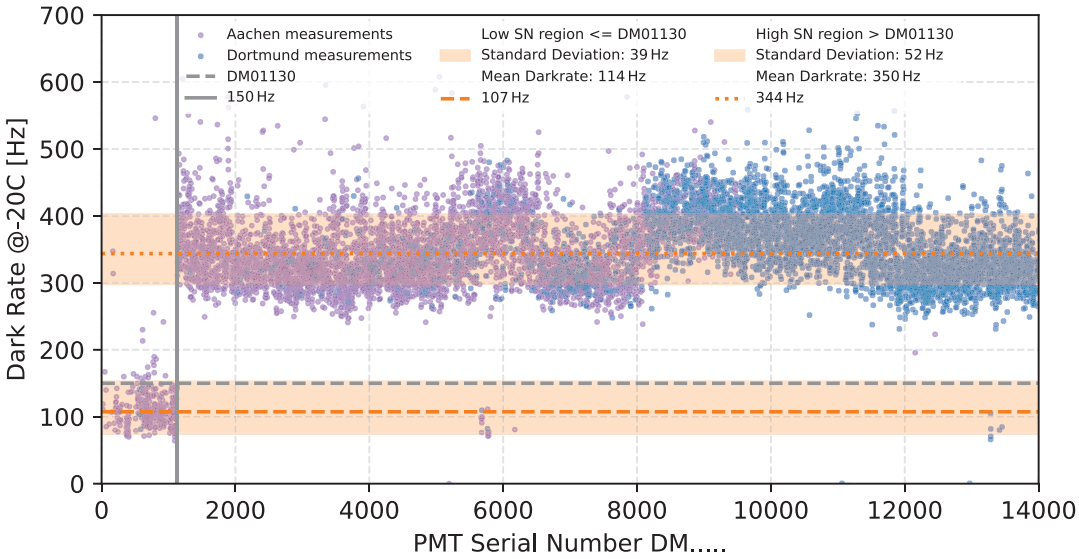

Figure 6.4: The dark rates plotted against the serial number of the PMTs. A change in the production quality can be seen at the serial number DM01130 (gray vertical line). The blue points show PMTs tested in Aachen, and the purple points show PMTs tested in Dortmund.

These high dark rates were discovered during the commissioning of the testing facilities. To rule out an error in the measurement, the dark rates of 1000 PMTs were measured in Aachen and Dortmund before the mass testing started. Additional dark rate measurements at the University of Münster vetted the findings. Elevated concentrations of radioactive isotopes within the glass envelope of the PMTs are the reason for the high dark rates. The cause was discussed with the manufacturer and is well understood. Based on a subsequent study [39, p. 111], the IceCube collaboration concluded that the PMTs could still be utilized. This early discovery enabled the IceCube collaboration to perform the study and reach an agreement with the manufacturer to address and acknowledge these findings.

The manufacturer measured the dark rate of each PMT at room temperature before delivery. In Figure 6.5, the dark rates reported by the manufacturer are compared

[39]: Unland Elorrieta (2023), "Development, Simulation, and Characterisation of a Novel Multi-PMT Optical Module for IceCube Upgrade with Emphasis on Detailed Understanding of Photomultiplier Performance Parameters"

to the dark rates measured in Aachen and Dortmund at −20 °C. The figure shows no visible difference in the dark rates at room temperature.

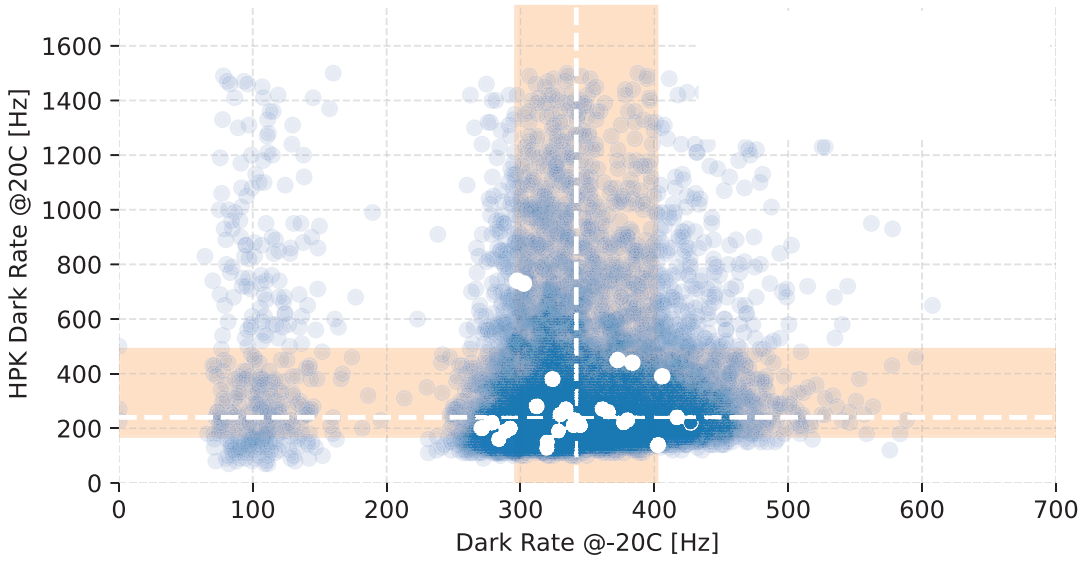

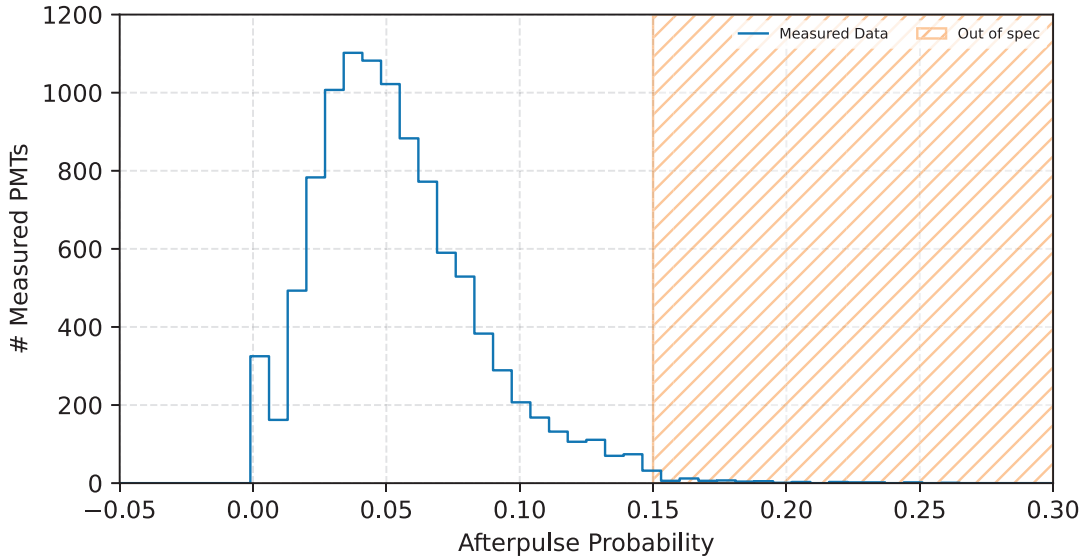

Figure 6.6: Histogram of the afterpulse probabilities. The blue histogram shows the measured probabilities, and the area marked with orange slanted lines highlights the specification boundary.

4793 PMTs measured in Dortmund is depicted in Figure 6.7. A falling spectrum is visible in the arrival time window, highlighted in orange. A more complex structure with several smaller peaks is present between 1 µs to 3 µs. This structure is more clearly visible in Figure 6.8. The distribution continues to fall until indistinguishable from the dark noise level at around 5 µs.

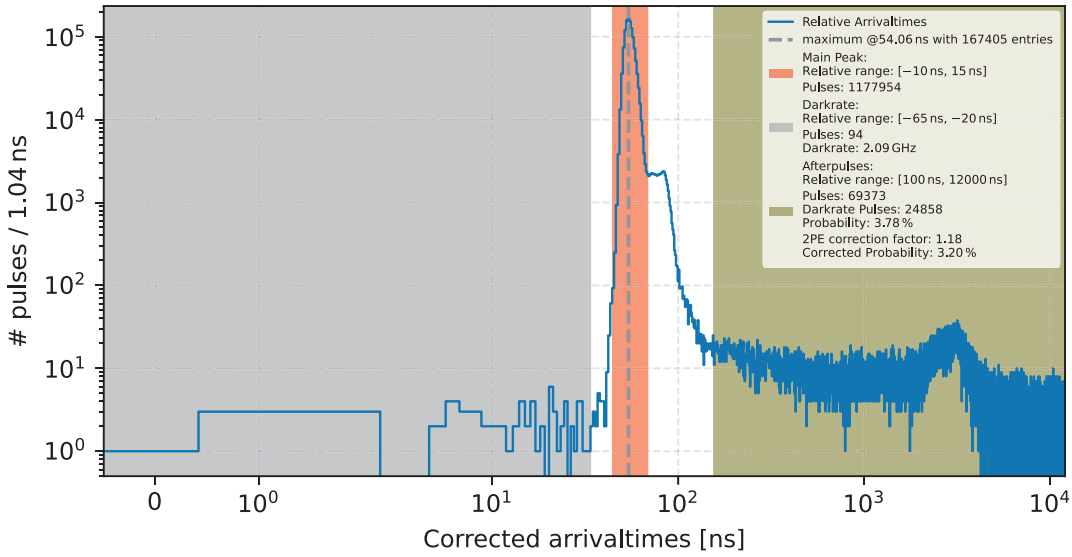

Figure 6.7: The combined arriaval times of 4793 PMTs measured in Dortmund are shown in the blue histogram. The vertical dashed gray line marks the expected arrival time of the main pulse. The afterpulse region is highlighted in yellow. A falling spectrum with a distinct structure at 3 µs is visible.

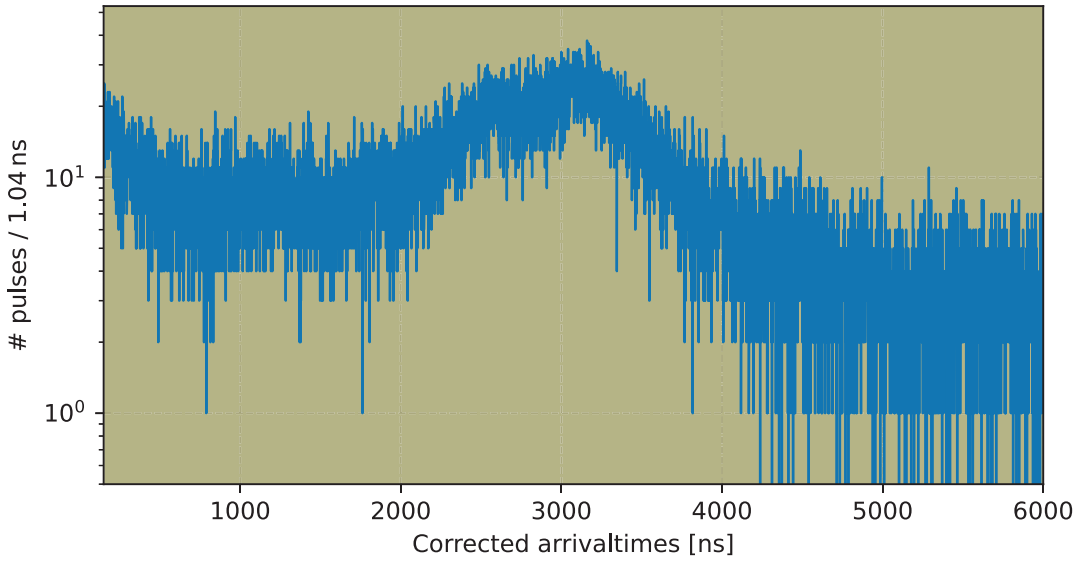

Figure 6.8: The combined arrival times of pulses in the afterpulse time window are shown in the blue histogram. The area around the peak at 3 µs indicates a more complex structure.

6.3.3 Transit time spread

The TTS is determined by analysing the main peak in the arrival time spectrum as described in subsection 5.5.5. Figure 6.9 shows the distribution of TTSs. The distribution peaks at $\sigma_{\mathrm{TTS}} = 1.7\,\mathrm{ns}$ and shows a distinct edge at the specification boundary. Several PMTs failed to meet the specification during the initial testing phase. These PMTs were retested, and after retesting, most of these PMTs were found to now comply with the specifications, resulting in the distinct edge. 175 PMTs are finally not compliant with the specification of $\sigma_{\mathrm{TTS}} < 2\,\mathrm{ns}$.

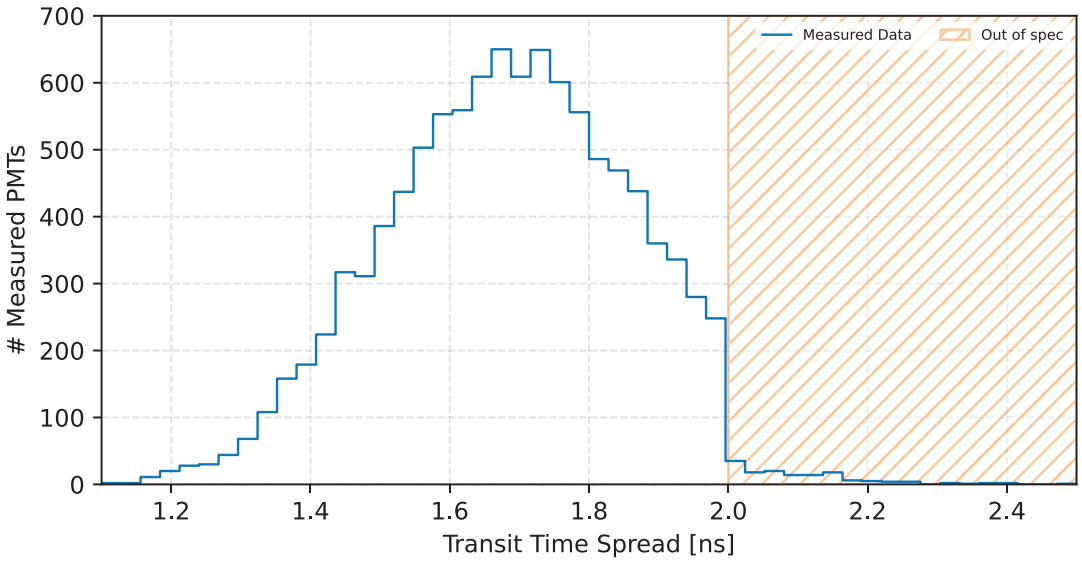

Figure 6.9: Histogram of the TTS. The blue histogram shows the measured TTS, and the area highlighted by orange slanted lines indicates the specification boundary.

6.4 Stability and Channel Dependency of the Results

A closer look at the results of the measurements reveals that most of the failed PMTs exceed the specification for the TTS. After retesting, most restested PMTs now comply with the specifications. This discrepancy between initial and subsequent

results raises questions about the stability and potential systematic uncertainties that may affect the consistency of the measurements.

This section describes the search for these systematic effects on the PMTs measurements at the testing facilities. The reference PMTs present in each run is the basis for channel-to-channel and same-channel variation analysis. Differences in the measured values between the runs can be analysed to find the influence of statistical variations. The focus is placed on results obtained at TU Dortmund University, as the underlying effects and calibrations are unique to the testing facilities (see section 5.3).

6.4.1 Transit time spread

A systematic effect becomes apparent looking at the 2D distribution of the median of the TTS for each channel plotted in Figure 6.10. The layout resembles the physical rack as seen from behind. The values decrease from $\sigma_{\mathrm{TTS}} = 1.78\,\mathrm{ns}$ at the top to $\sigma_{\mathrm{TTS}} = 1.62\,\mathrm{ns}$ at the bottom of the rack. This is also visible when plotting the TTSs against each channel as in Figure 6.11.

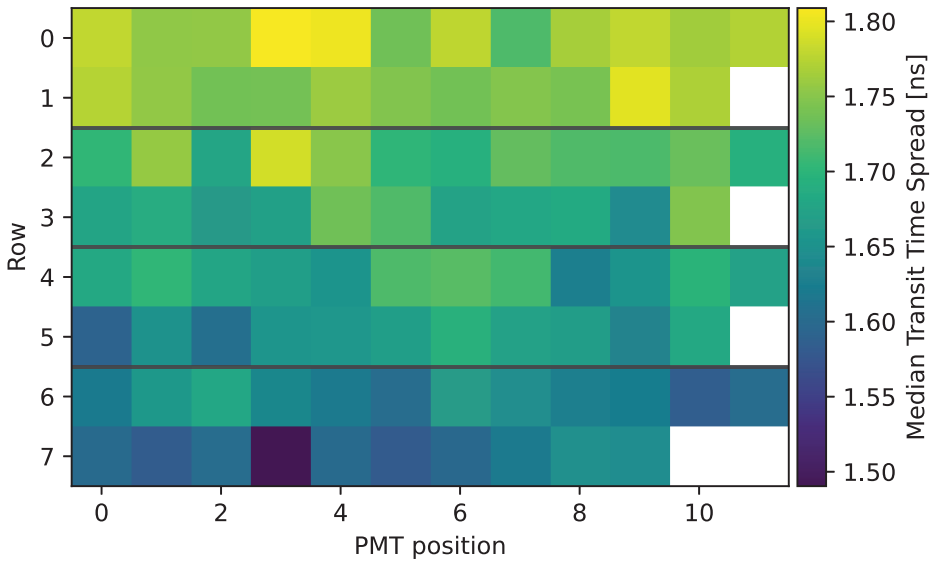

Figure 6.10: The median of measured TTSs for each channel in the rack layout as seen from behind. White positions are either used for the trigger signal (1-11, 3-11, 5-11, and 7-11) or not used at all (7-10) during mass testing.

One possible cause could be the scattering processes inside the diffusion sphere: The TTS can increase, if more scattering inside the sphere is required to illuminate the upper PMTs. The differences between top and bottom measurements are, with $t = 0.16\,\text{ns} \rightarrow \approx 4.7\,\text{cm}$, on the same length scale as the diameter of the diffusion sphere of $d = 2.4\,\text{cm}$.

Figure 6.11 shows the same systematic effect caused by the retesting as in Figure 6.9. A clear edge at the specification boundary is visible. The finite measurement accuracy and the geometrical effect of the diffusion sphere can lead to PMTs being accepted during the retesting.

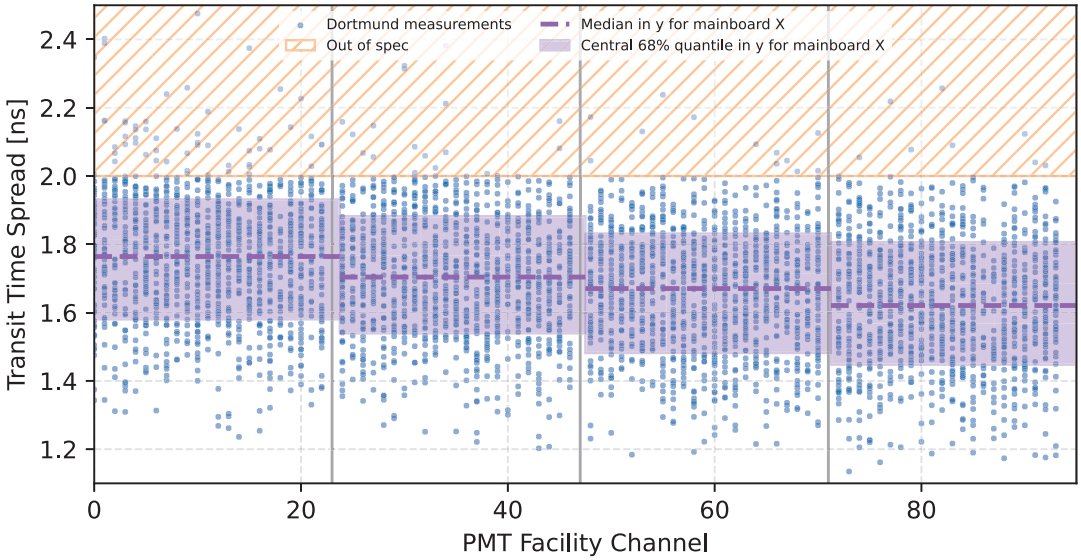

Figure 6.11: Measured TTSs as a function of the channel. Each segment represents the 24 channels of a mDOM mainboard, and the median and standard deviation for each mainboard are printed in purple.

The measurement standard deviation can be estimated by analyzing the differences between the measured TTSs for each PMT. The differences in the TTS are shown in dark blue in Figure 6.12. A sum of two Gaussian functions describes the distribution of Δtts well and is fitted to the data. The broad Gaussian distribution, shown in dashed orange, describes the scatter of the measured values when measured on different channels. These variations are affected by the mDOM mainboard electronics, the geometrical effect, and the target voltage of the PMTs, which varies slightly between the channels, see Figure 6.15. The second Gaussian distribution,

highlighted in dotted orange, is much narrower and follows a population of Δtts between measurements at the same channel. The same-channel data is plotted in light blue. The standard deviation of the TTS measurement can be extracted from the same-channel Gaussian as δtts,methode = 60 ps. The broader Gaussian describes the channel-to-channel fluctuations and introduces a lager uncertainty of δtts,channels = 260 ps. The combined standard deviation δtts, comb. = 267 ps of the TTS measurement can be the cause of PMTs passing the specifications after a second measurement.

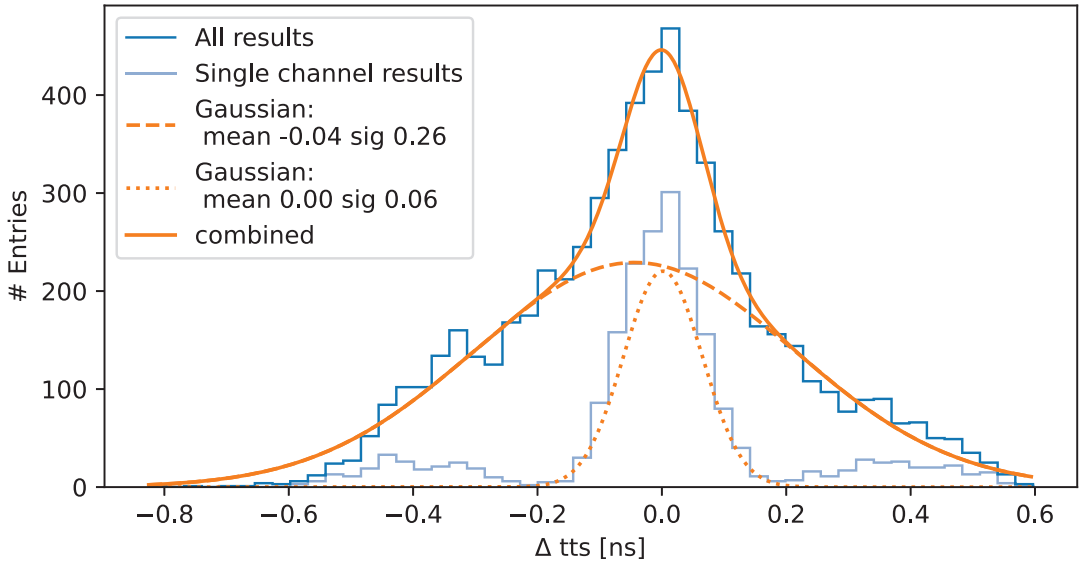

Figure 6.12: Plotted are the differences in TTS between different runs for the reference PMTs. The same-channel contribution to the overall distribution is shown in light blue.

In the case of Δtts, two additional distributions to the left and right of the same-channel distribution at ± 4 ns are striking. These deviations are due to the Gaussian fit, which does not always accurately represent the measured distribution. The arrival time spectrum is skewed towards higher arrival times. In a few cases, the fit cannot describe the peak of the distribution correctly, and thus the TTS is underestimated. This can be seen in Figure 6.13, showing the main peak of the arrival times for two measurements for PMT `DM00373`. The right histogram shows the fit with an underestimated standard deviation. In the left histogram, the fit result better describes the peak of the distribution, and a higher standard deviation is determined. In this example, the difference between the two standard deviations

is 0.41 ns, which corresponds to the distance of the two peaks towards the main peak in Figure 6.12.

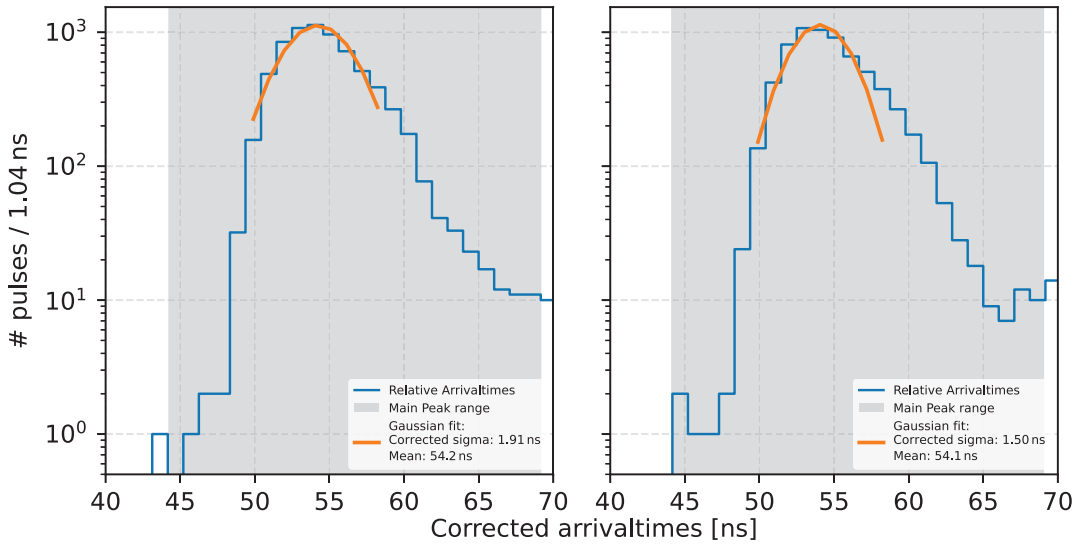

Figure 6.13: Two examples of a "good" fit of the arrival times (left) and an "underestimated" fit (right). Underestimating the standard deviation of the Gaussian function leads to the two distributions to the right and left of the same-channel main peak in Figure 6.12.

6.4.2 Target Voltage

In subsection 5.3.2, the channel-to-channel calibration of the mDOM mainboard AFE gain was described. As this calibration directly affects the measured PMT gain and, consequently, the target voltage U_{target}, any miscalibration could lead to systematic shifts in the target voltages. The median of all measured target voltages for each channel is displayed in Figure 6.14. The geometrical layout of the rack is preserved in the plot. No significant systematic effects can be observed in the medians of target voltages.

A closer look at the differences in target voltage for the same PMT between different runs indicates a channel-dependent result. The distribution in Figure 6.15 is well-described by the sum of two Gaussians.

The fluctuations in the target voltage of a PMT on different channels indicate that this correction does not always work as intended and leads to a broad channel-to-

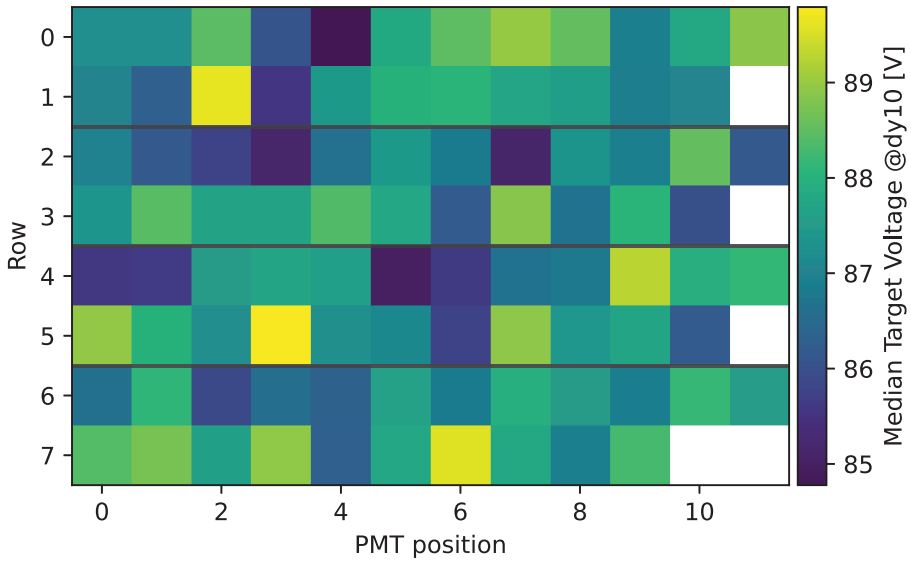

Figure 6.14: The median of measured target voltage for each channel in the rack layout as seen from behind.

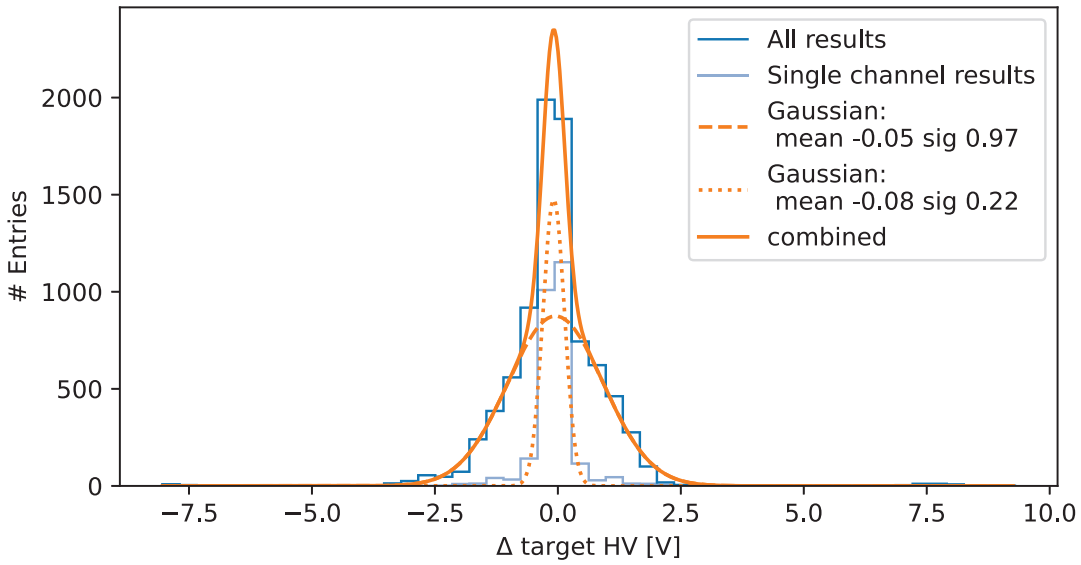

Figure 6.15: The differences in target voltage between different runs for the reference PMTs are plotted here. The same-channel contribution to the overall distribution is shown in light blue.

channel distribution. The left plot in Figure 6.16 shows an example of the two most distinguishable channels 40 and 67. Other channels are not distinguishable by eye, as shown on the right. A better AFE gain correction would be desirable, but has no influence on the performance of the PMTs in the final mDOM modules as the PMT is connected and calibrated to a single channel. For the testing facility in Dortmund, the measurement standard deviation of the target voltage can be estimated to $\delta_U \text{target} = 1\,\text{V}$.

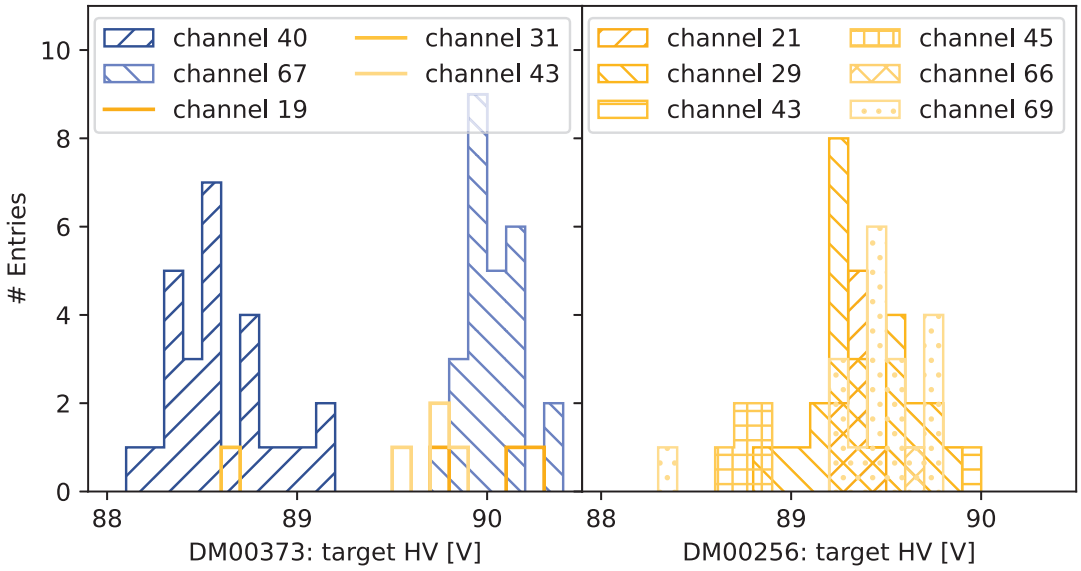

Figure 6.16: The influence of the channel on the target voltage is visible for the two channels 40 and 67 (measured with PMT `DM00373`, left). Other channels show no such distinct distributions as seen on the right (measured with PMT `DM00256`).

6.4.3 Quantum efficiency

The measurement of the QE is described in subsection 5.5.3, and the occupancy correction, as detailed in subsection 5.3.3, directly influences the results of the tests. An analysis of the median QE @ 375 nm for each channel depicted in Figure 6.17 reveals a systematic deviation.

The correction assumes that the detection area of the PMTs depends solely on the geometric angle of incidence of light. However, metal strips are affixed to the PMTs,

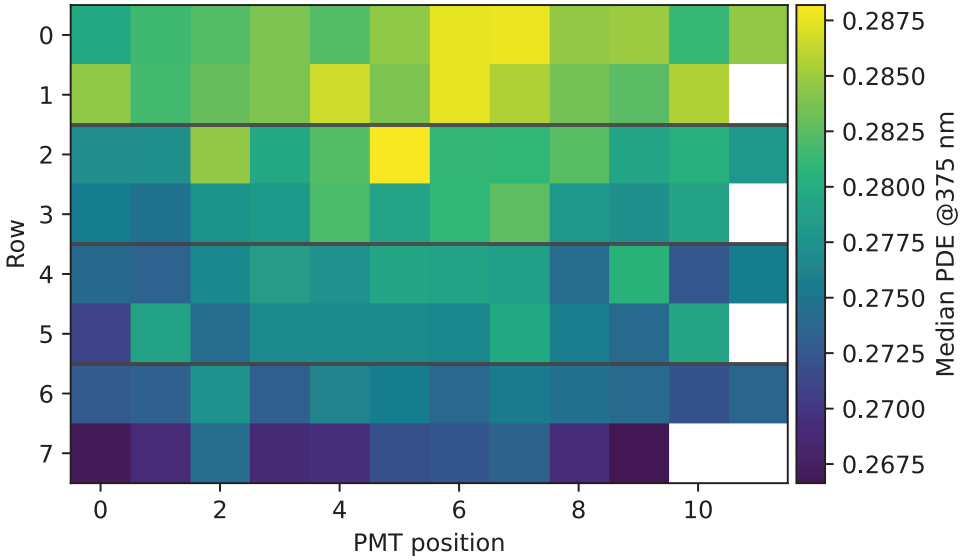

Figure 6.17: The median of measured QE @ 375 nm for each channel in the rack layout as seen from behind.

connecting the photocathode to the reflector ring in the final mDOM module. These metal strips were not removed during acceptance testing. Due to their alignment, less light reaches PMTs located beneath the light source, as these metal strips shade portions of their photocathodes. This angular dependency introduces a bias towards the measured QEs and is visible in Figure 6.17.

6.5 Comparison with Aachen and Hamamatsu

This section looks into the measurement results from the test benches in Aachen and Dortmund, highlighting potential differences and comparing the measured data with the reported data supplied by the manufacturer. Further data and plots are found in Appendix A.

6.5.1 Target Voltage

Figure 6.18 compares the operating voltage reported by the manufacturer to the target voltage at the 10th dynode U_{target} measured in Aachen (blue data) and

Dortmund (purple data). Both measurement sites show a clear correlation with Pearson correlation coefficients of $p_U = 0.88$. A slight shift towards higher voltages can be observed for values measured in Dortmund and might be the result of a systematic error during the cross-calibration between the two sites as described in subsection 5.3.2. This systematic shift has no influence on the results as the target voltage is determined in the final mDOM assembly and PMTs are not moved between channels.

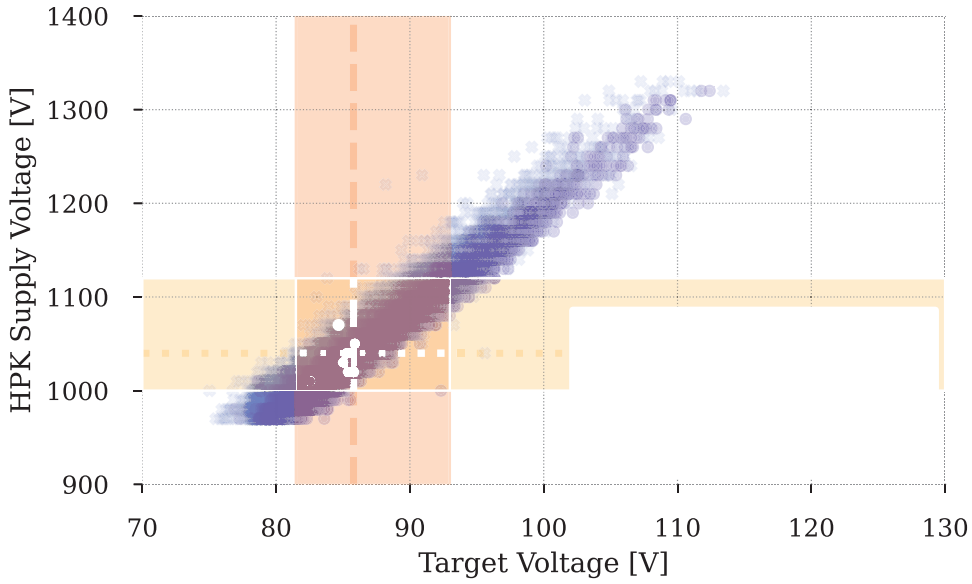

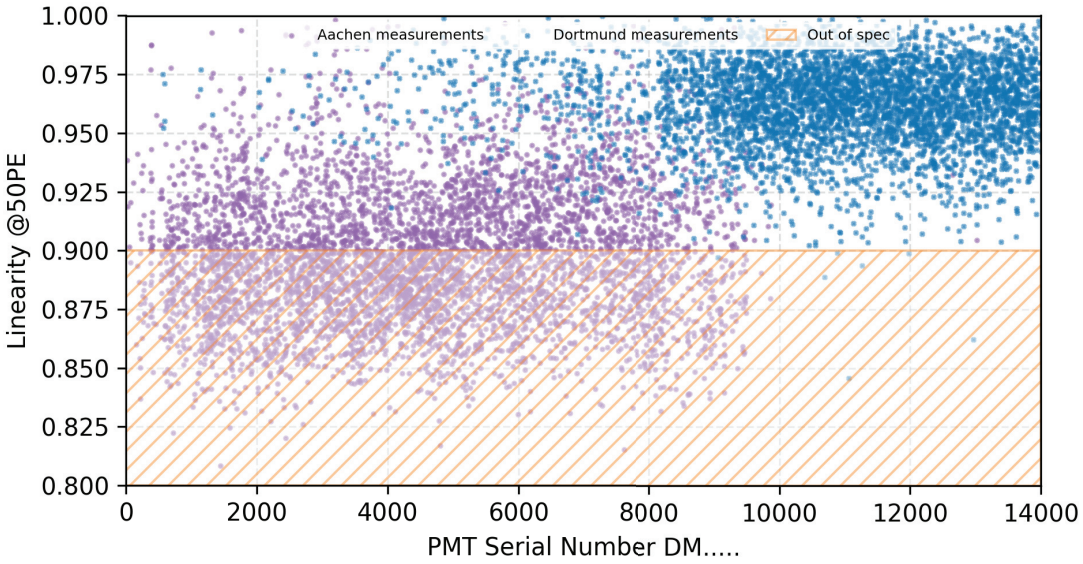

Figure 6.19: Measured charge linearities plotted against the PMT serial numbers. Blue points show PMTs tested in Dortmund and purple ones PMTs tested in Aachen. The area marked with orange slanted lines highlights the specification boundaries.

6.5.3 Baseline Characteristics

Figure 6.20 shows the mean of measured baseline deviations plotted agains the PMT serial numbers. Figure 6.21 shows the mean of the baseline spread plotted agains the PMT serial numbers. In both figures, the data recorded at TU Dortmund University exhibit a slightly wider shift than that measured in Aachen. This suggests a higher level of noise at the testing site in Dortmund, which does not influence the acceptance decisions.

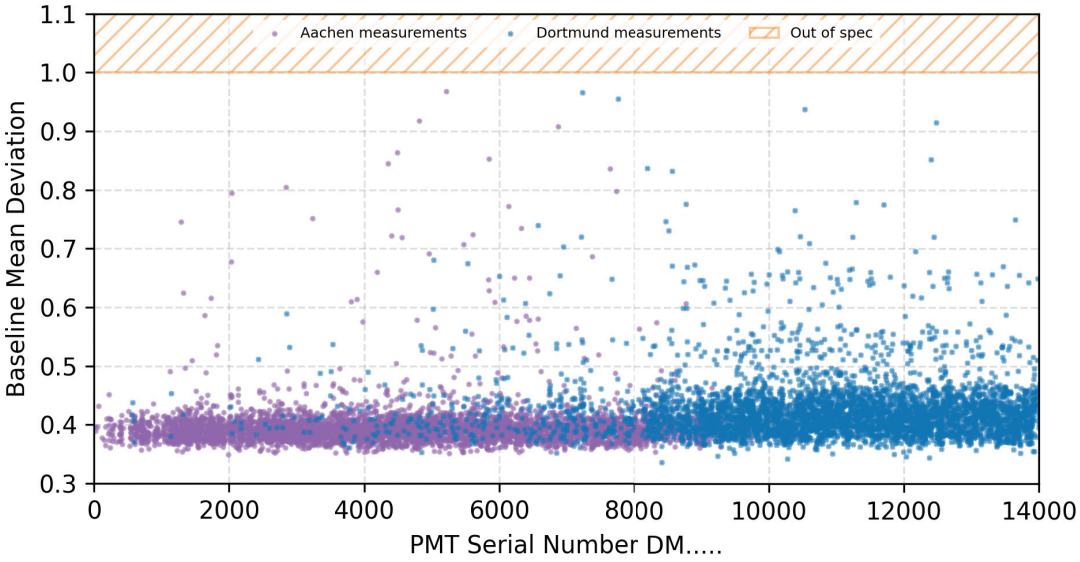

Figure 6.20: The mean of measured baseline deviations plotted against the PMT serial numbers. Blue points show PMTs tested in Dortmund and purple ones PMTs tested in Aachen.

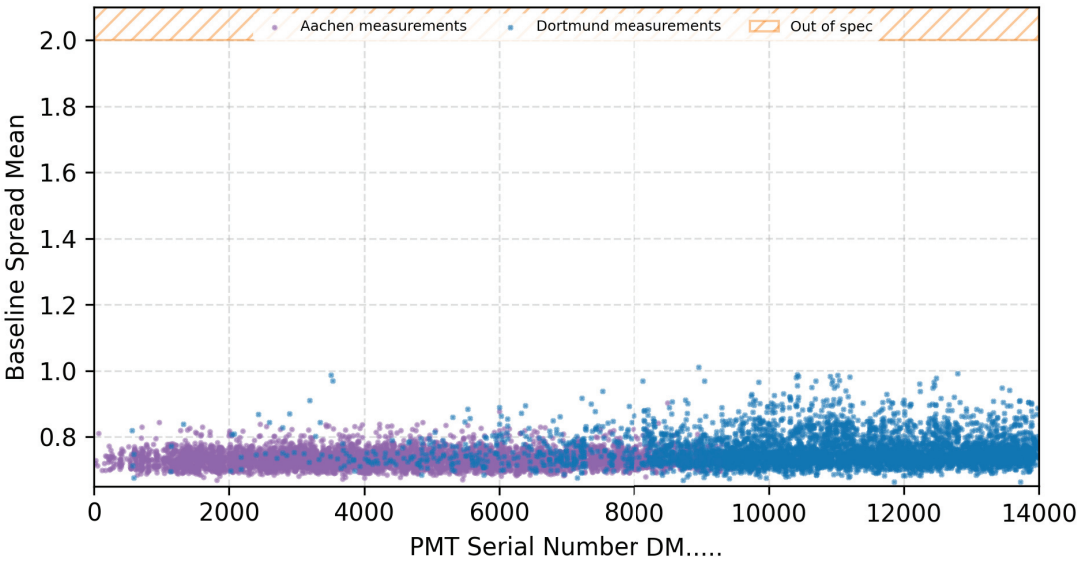

Figure 6.21: Mean of the measured baseline spread plotted against the PMT serial numbers. Blue points show PMTs tested in Dortmund and purple ones PMTs tested in Aachen.

7 Resume and Outlook

This work aimed to plan, build, and operate a test bench for the IceCube upgrade mDOM PMTs. The PMTs undergo initial acceptance tests to determine whether they meet the requirements defined by the IceCube collaboration. In addition, the PMTs were divided into six voltage classes according to their operating voltage at the target gain. This allows PMTs with the same operating voltage to be preferably installed in an mDOM, reducing possible leakage currents. In addition to the operating voltage, twelve other parameters were measured, such as the transit time spread and the dark rate.

The test bench's mass test capability and scalability are important aspects of the concept, particularly with the expected quantities of PMTs for the IceCube-Gen2 upgrade planned in 2033 [19]. For the IceCube upgrade mDOMs, more than 10 000 PMTs had to be tested, of which 4793 PMTs were tested in Dortmund. The parallel testing of 92 PMTs per cycle and a cycle duration of less than 24 h have made this possible. In addition, the test bench can be easily expanded and adapted to other conditions. If compatible microbases are used on the PMTs, these can be tested with just minor adjustments. As a proof of concept, some Pacific Ocean Neutrino Experiment (P-ONE) [96] PMTs have already been successfully tested in the Aachen test bench [74]. The test bench can also be easily adapted to PMTs with different dimensions by replacing the PMT brackets on the Vogelstangen. All brackets are 3D printed and flexibly mounted on the profile rails, facilitating adaptation.

This work proves that the development of the Dortmund test bench has been successful and that all required values could be measured reliably. The test bench design can be transferred to other locations and is easy to implement by using the mDOM mainboards as readout electronics. The capacity can also be easily expanded by adding further mainboards to the existing locations. The shared software is flexible and can be adapted to other conditions via configuration files. Additional tests or analyses can be easily implemented thanks to the modular structure of the software. The script-controlled test cycle runs automatically after the start and

[19]: Aartsen et al. (2021), "IceCube-Gen2: The Window to the Extreme Universe"
[96]: Malecki (2024), "Pacific Ocean Neutrino Experiment"
[74]: Halve (2024), "Validation of Optical Sensors for the mDOM of the IceCube Upgrade"

sends messages to a shifter in case of an error. This enables a high throughput of around 500 PMTs per week.

It was shown that consistent results can be delivered at two locations with the same concept and slightly different realizations of the light sources and cooling chambers. This means that the PMTs can be checked during production, and any changes that occur can be detected at an early stage. At the beginning of the tests, higher dark rates were noticed for PMTs with serial numbers greater than `DM01130` and were consistently documented at both locations. A change in the manufacturer's production process was identified as the cause of this increase in dark rates. Further investigations within the IceCube upgrade community led to the conclusion that the PMTs can be used despite the higher dark rates and that there will be no significant impact on the goals and results of the IceCube upgrade.

Outlook

The test bench can also be upgraded for precision measurements by making minor changes. The most significant improvement is a different light system. Lasers can generate much more regular pulses than ps pulsers and LEDs. The maximum brightness of a laser also allows correct linearity measurements, and the higher amount of light does not have to be interpolated using a higher operating voltage. Filters mounted on motorized filter wheels can be used to send single photons. With this upgrade, the intensity of the laser does not need to be adapted, and the amount of light at the PMTs is realized via different filter combinations. Such a light system was used at the University of Chiba for the final acceptance test of the D-Egg modules and can be used as a model for a light system. Several lasers can be coupled into the beam path to realize measurements with different wavelengths.

Furthermore, a bundle of optical fibers can be used instead of the diffuser. The individual ends of the bundle are positioned on the rack so that they are in the same place for each PMT and are not blocked by the copper strip. This also allows for a much more compact cooling chamber, as the optical fibers are positioned directly on the rack, and there is no longer any need for a gap between the diffuser and the rack. A lens widens the laser beam to the size of the optical fiber bundle. The occupancies still need to be calibrated with this setup, if the photodetection efficiency is to be measured using reference PMTs.

In addition to the changes to the light system, it is also possible to measure the transit time. For this purpose, several FastPhoto diodes can be installed in the rack, and the mainboard can be read out via the signal at one of these diodes. This allows the transit time to be measured and not just the scattering of the transit time. As the light intensity was selected when setting the ps pulsers so that a pulse could only be measured in a PMT for approximately every ten triggers, several FastPhoto diodes can be used to increase the number of successful triggers. This procedure extends the measurement times, as triggering no longer occurs with every pulse.

The mainboards of the mDOMs have the option of calibrating the internal clocks. A special command is sent to all mainboards simultaneously, and they send back their current time. This time synchronization makes it possible to measure coincident events in the rack. It is also possible to synchronize the clocks of the mainboards via a GPS clock, as used in the IceCube detector. This is currently not implemented in the test bench software, and it is only possible to search for coincident results within a mainboard's 24 channels. Such coincident events are radioactive isotopes in the glass of the PMTs, cosmic showers, or spontaneous light emissions of the bases. A first search for coincident events in Aachen found coincident events, but could not assign them to a cause due to the large uncertainties. [97]

The separation of signal and supply lines, as well as the additional shielding of the signal lines and the mainboards, probably positively influences the noise behavior of the readout electronics. The database can also be revised for larger projects. With the current implementation, each waveform is stored as an individual object in the database. This has the advantage that each waveform can be accessed individually, but it also means that the database builds up a large index and, therefore, loses performance. In the current configuration, the index size is approximately as large as the amount of stored data.

These changes allow the successful test bench to be modernized and used for more precise tests.

[97]: Behrens (2022), "Studies of Correlated Noise Events in the PMT Testing Facility for the mDOMs of the IceCube Upgrade"

Appendix

A Results of Single Measurements

Here, the result for each measured quantity is discussed. The histograms show the combined results from the measurements in Aachen and Dortmund. A separate distribution shows the measured value plotted against the serial number of the PMT. It is reasonable to assume that the serial number increases with later production dates. In this plot, the two measurement sites are differentiated to show potential systematic differences.

The manufacturer performs an in-house calibration of the PMTs with a subset of the tests conducted at the PMT testing facilities. Where applicable, the manufacturer's in-house calibration data is compared to that recorded at the testing facilities.

A.0.1 Voltage at Target Gain

Figure A.1 shows the distribution of voltages U_{target} resulting in a target amplification gain of $Y_{\text{target}} = 5 \times 10^6$. Most PMTs fall into voltage classes A or B, see Table 6.2, and the distribution as a whole is well-behaved. Out of the 10 427 tested PMTs, 78 do not meet the specification. One PMT has a target voltage of $U_{\text{target}} = 113.43\,\text{V}$ and exceeds the upper boundary of $U_{\text{max}} = 113\,\text{V}$ slightly. The remaining 77 PMTs show a target voltage below $U_{\text{min}} = 78\,\text{V}$. All other specifications were met, and the non-conforming PMTs are accepted and used in spare mDOMs.

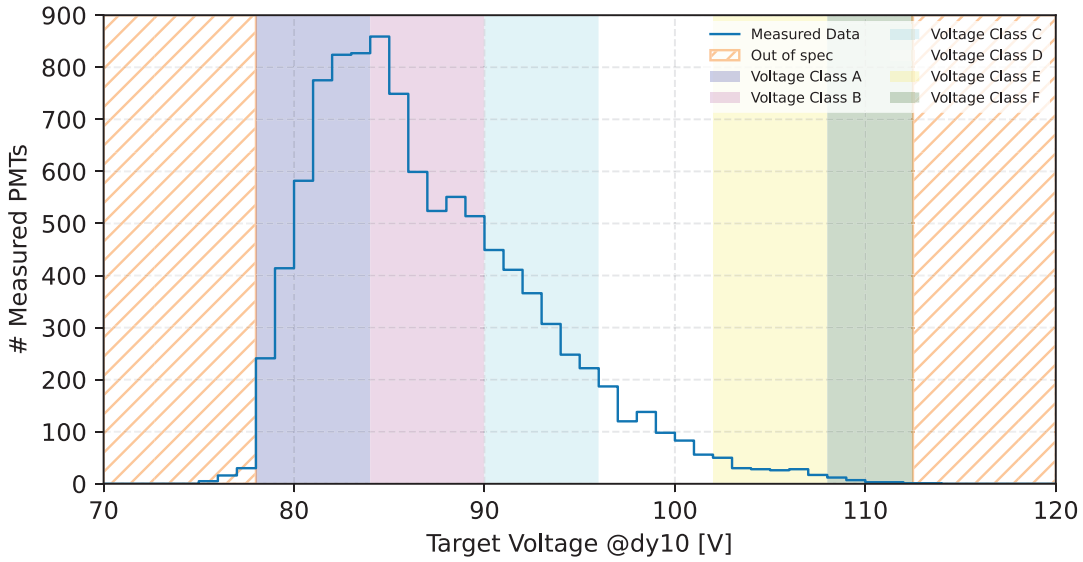

Figure A.1: Histogram of the target voltages resulting in a gain of $Y_{\text{target}} 5 \times 10^6$. Blue histogram shows the measured voltages, the colored bands depict the voltage classes defined in Table 6.2, and the area marked with orange slanted lines highlights the specification boundaries.

Figure A.2 shows the target voltages as a function of the PMT serial numbers. A disjoint set of PMTs were tested at the two testing facilities at the RWTH Aachen and TU Dortmund University. An overlap exists between the serial numbers `DM08000` and `DM10000`, as well as some random PMTs with smaller serial numbers. An overall consistent image of the measured target voltages is seen.

Figure A.3 shows the target voltages at 10th dynode U_{target} plotted against the full supply voltage U_{tot} measured by the manufacturer resulting in a gain of $Y_{\text{target}} =$

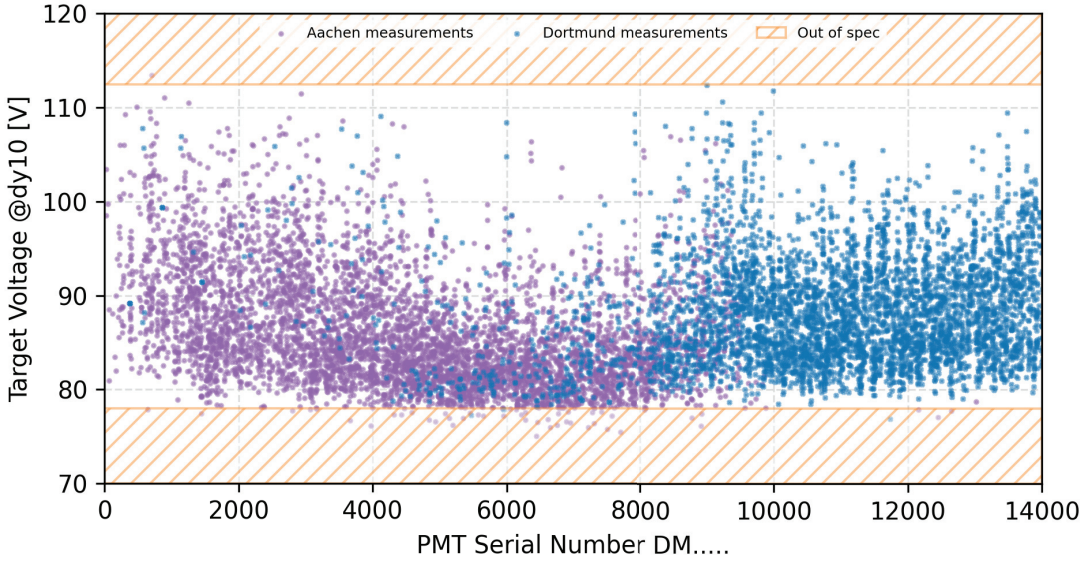

Figure A.2: Measured target voltages resulting in a gain of $Y_{\text{target}} = 5 \times 10^6$ plotted against the PMT serial numbers. Blue points show PMTs tested in Dortmund and purple ones PMTs tested in Aachen. The area marked with orange slanted lines highlights the specification boundaries.

5×10^6. A clear correlation is observed with a Pearson correlation coefficient of $p_U = 0.75$.

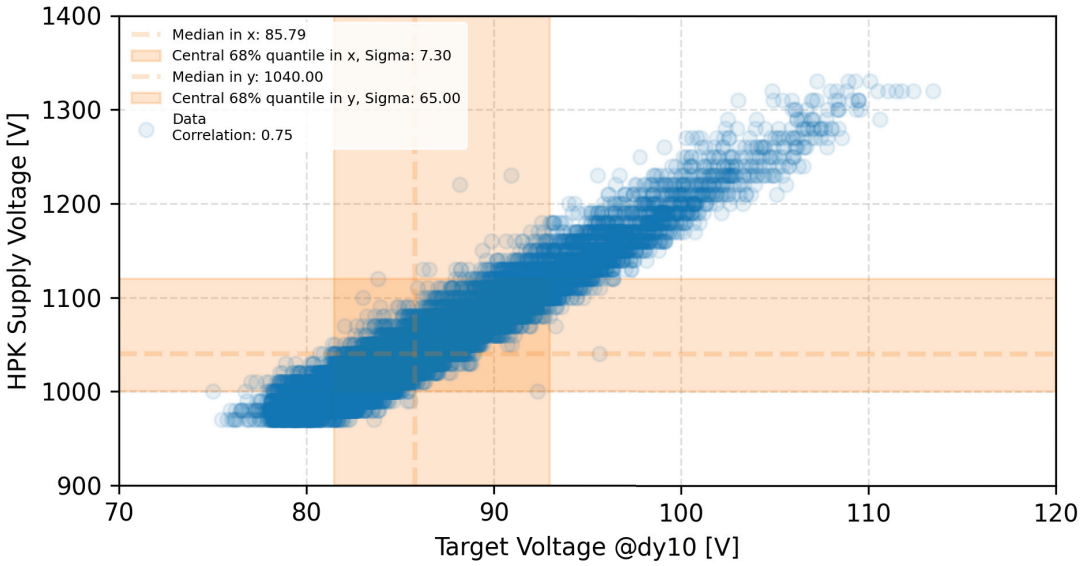

Figure A.3: Measured target voltages plotted against the manufacturer supply voltage resulting in a gain of $Y_{\text{target}} 5 \times 10^6$ are represented by blue points. The orange bands show the central 68% quantiles for the measured values and manufacturer data for all PMTs.

A.0.2 SPE Characteristics

The SPE characteristics are described by the peak-to-valley ratio (PVR) and the SPE resolution σ_{SPE}. Both are extracted from the SPE spectrum measured at target voltage as described in subsection 5.5.3.

Figure A.4 shows the distribution of PVRs. The distribution is smooth and peaks at PVR = 3.2. 37 PMTs have a PVR < 2.0 and do not meet the specification. They are accepted and used in spare mDOMs.

Figure A.5 shows the PVRs as a function of the PMT serial numbers. A small difference between the testing sites can be observed. The measurements conducted at TU Dortmund University result in slightly larger PVRs than the ones taken at RWTH Aachen. A slightly higher noise environment at the TU Dortmund University is the most probable cause for the differences, as the baseline measurements (cmp. Section 6.5) indicate. They do not influence the decision whether or not to accept the PMTs.

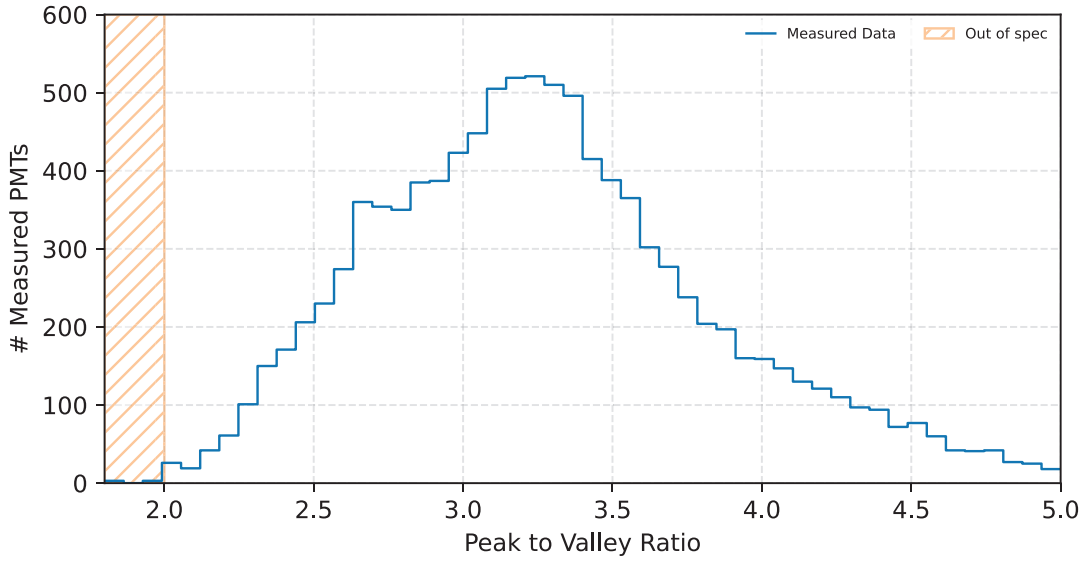

Figure A.4: Histogram of the PVRs. The blue histogram shows the measured ratios, and the area marked with orange slanted lines highlights the specification boundary.

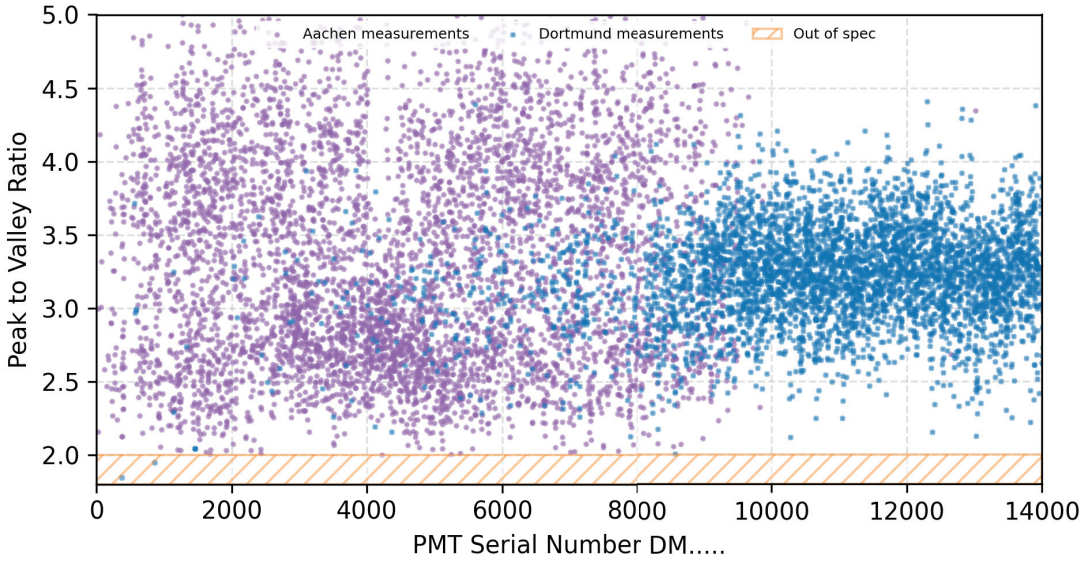

Figure A.5: Measured PVRs plotted against the PMT serial numbers. Blue points show PMTs tested in Dortmund and purple ones PMTs tested in Aachen. The area marked with orange slanted lines highlights the specification boundaries.

Figure A.6 shows the distribution of SPE resolutions. The distribution is well-bahved and all PMTs are within the specification $\sigma_{\mathrm{SPE}} < 0.7\,\mathrm{PE}$.

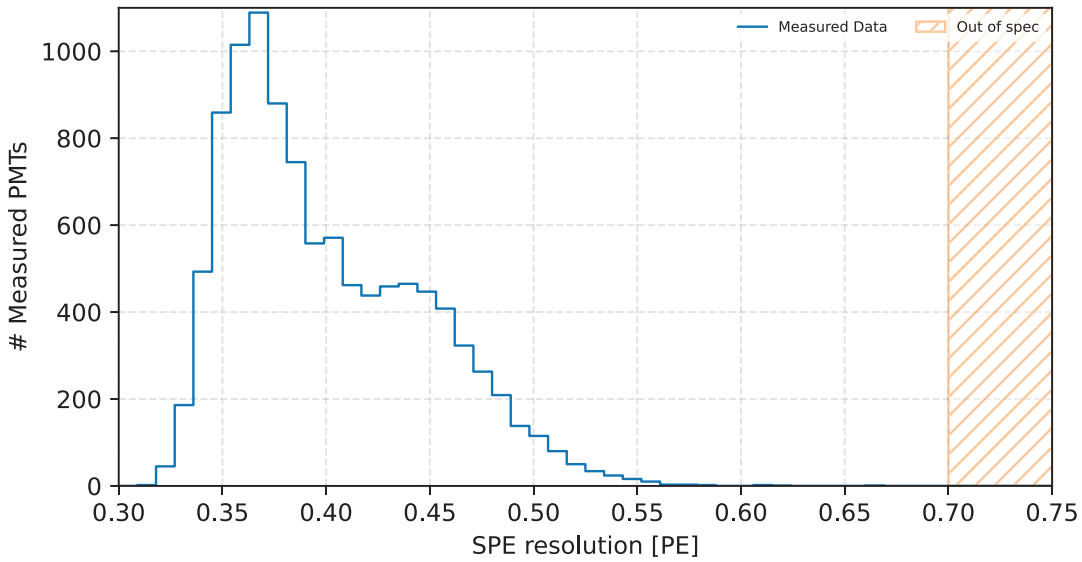

Figure A.6: Histogram of the SPE resolutions. The blue histogram shows the measured resolutions, and the area marked with orange slanted lines highlights the specification boundary.

Figure A.7 shows the SPE resolutions as a function of the PMT serial numbers. A small difference between the testing sites can be observed as well. The measurements conducted at TU Dortmund University result in slightly smaller SPE resolutions than the ones taken at RWTH Aachen.

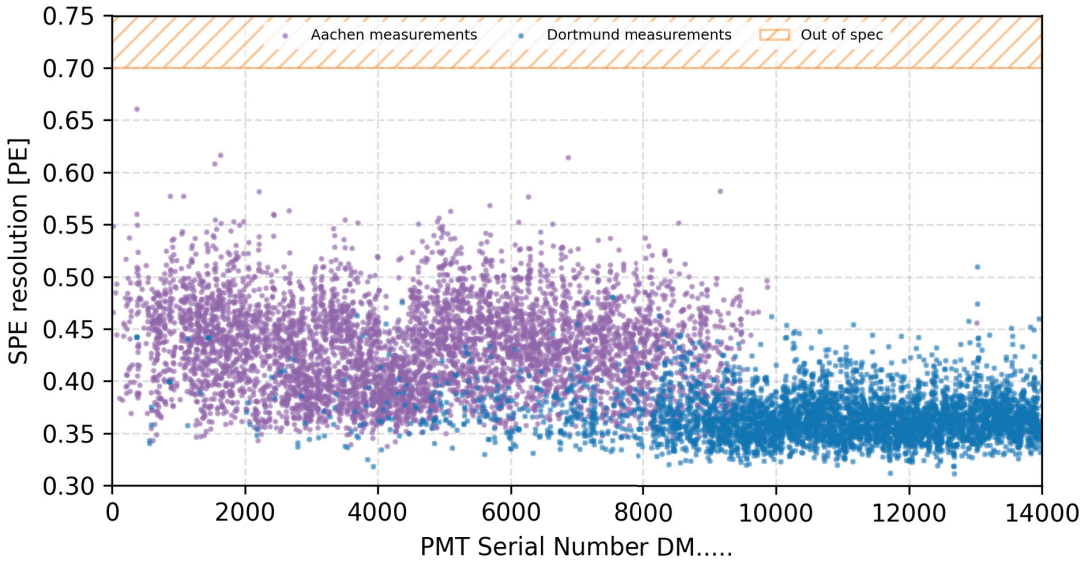

Figure A.7: Measured SPE resolutions plotted against the PMT serial numbers. Blue points show PMTs tested in Dortmund and purple ones PMTs tested in Aachen. The area marked with orange slanted lines highlights the specification boundaries.

A.0.3 Quantum efficiency

The QE measurement is not a direct measurement. It depends on the measured occupancies and the reported QE for several reference PMTs as described in subsection 5.5.3.

Figure A.8 shows the distribution of QEs at $\lambda_1 = 375\,\text{nm}$ and $\lambda_2 = 505\,\text{nm}$. The distributions are well-behaved and peak at 27% and 18% respectively. 24 PMTs have a $\text{QE}_{375} < 25\%$ and do not meet the specification. 27 PMTs do not fullfill the specifications and have a $\text{QE}_{505} < 15\%$. Eight of those PMTs fail both criteria. All are accepted and used in spare mDOMs.

Figure A.9 shows the QEs as a function of the PMT serial numbers. No differences between the testing sites can be observed. A minor increase of QEs for low serial numbers can be observed. The increase could correlate with a change in the production process as discussed in subsection 6.3.1.

The manufacturer reported quantum efficiencies for 10% of the delivered PMTs, and Figure A.10 shows the correlation of these data with the ones measured in the

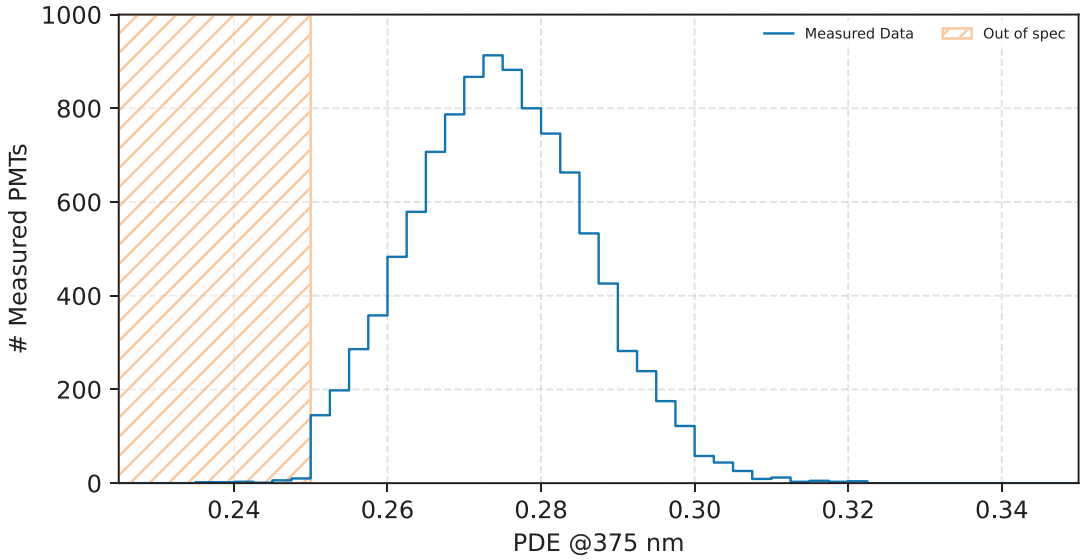

(a) $\lambda_1 = 375\,\text{nm}$

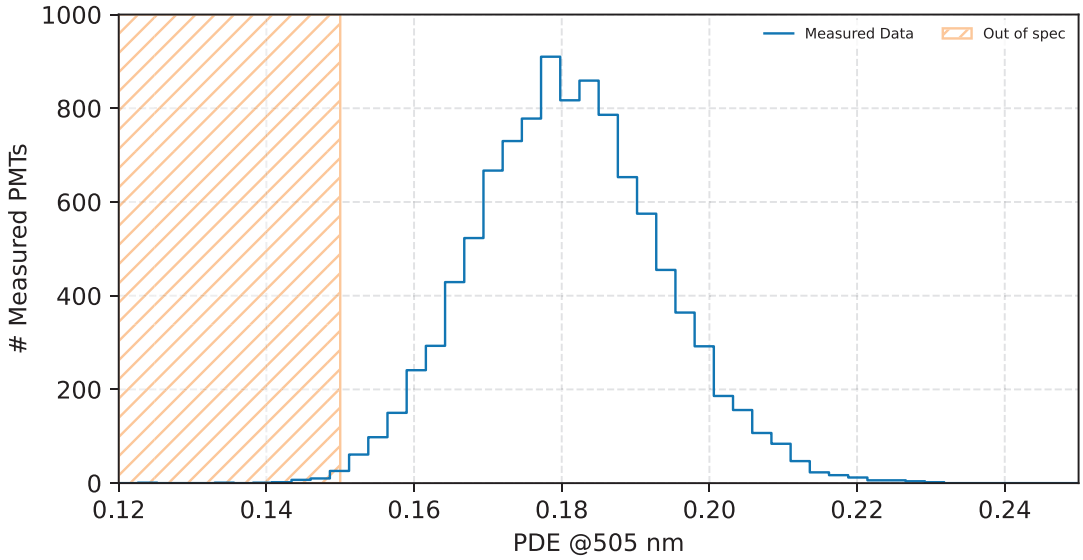

(b) $\lambda_2 = 505\,\text{nm}$

Figure A.8: Histograms of the relative QEs at $\lambda_1 = 375\,\text{nm}$ (a) and at $\lambda_2 = 505\,\text{nm}$ (b). The blue histogram shows the measured efficiencies, and the area marked with orange slanted lines highlights the specification boundaries.

testing facilities for two wavelengths. The upper Figure A.10a shows data recorded at $\lambda_1 = 375\,\text{nm}$ and $\lambda_{\text{hpk}} = 380\,\text{nm}$ and exhibits a small correlation coefficient of

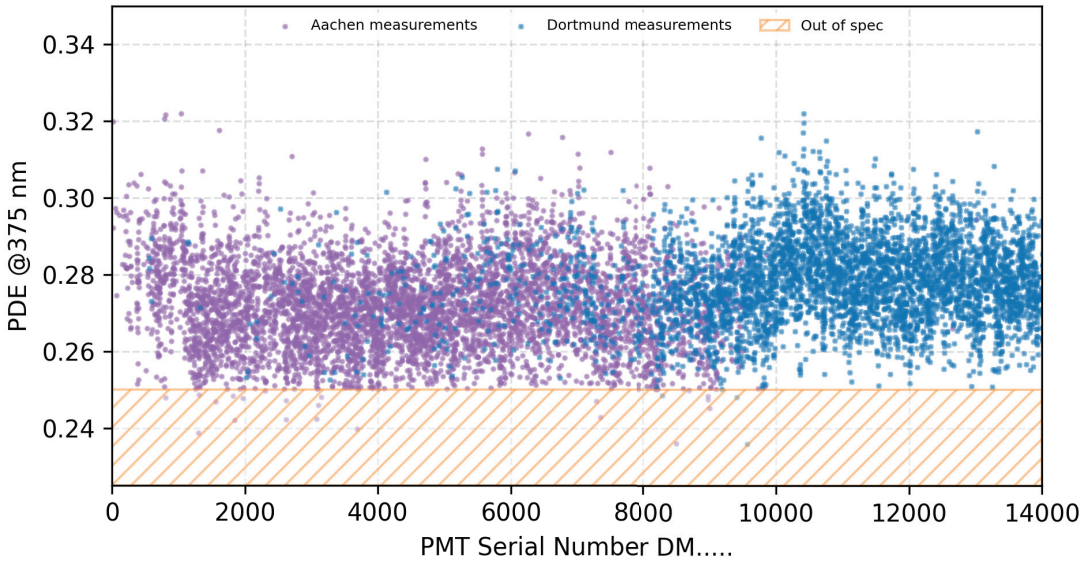

(a) $\lambda_1 = 375\,\mathrm{nm}$

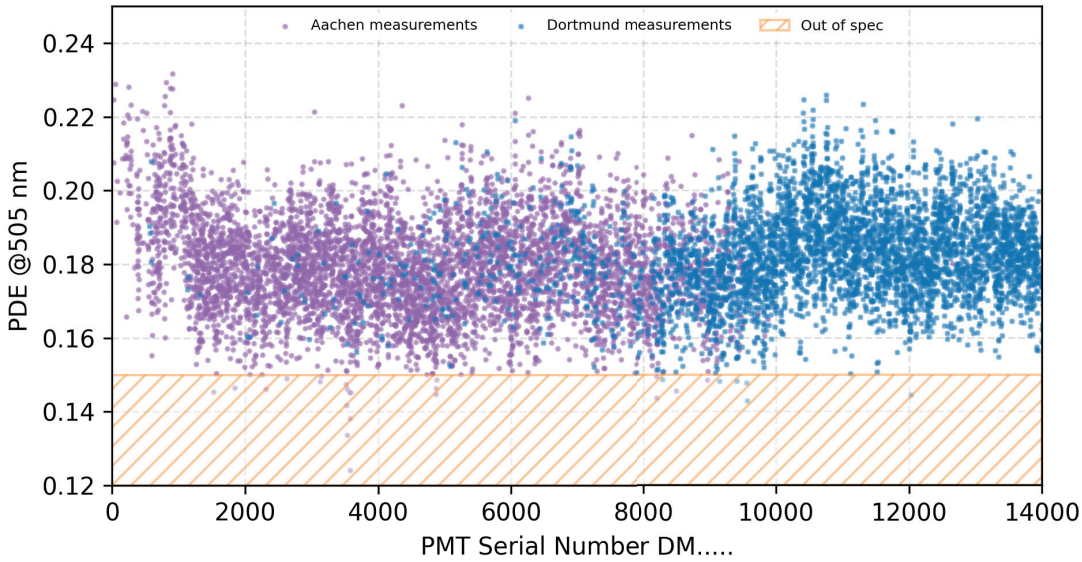

(b) $\lambda_2 = 505\,\mathrm{nm}$

Figure A.9: Measured relative QEs at $\lambda_1 = 375\,\mathrm{nm}$ (a) and at $\lambda_2 = 505\,\mathrm{nm}$ (b) plotted against the PMT serial numbers. Blue points show PMTs tested in Dortmund and purple ones PMTs tested in Aachen. The area marked with orange slanted lines highlights the specification boundaries.

$P_{\mathrm{QE,\,375\,nm}} = 0.3$. The lower Figure A.10b shows data recorded at $\lambda_2 = 505\,\mathrm{nm}$ and $\lambda_{\mathrm{hpk}} = 500\,\mathrm{nm}$ and exhibits a lager correlation coefficient of $P_{\mathrm{QE,\,505\,nm}} = 0.66$ than the one at $\lambda_1 = 375\,\mathrm{nm}$. Since the measurement relies on comparison of the measured occupancies and the reported QEs for the reference PMTs, the low correlation coefficients are unexpected. This hints at an unsuitable light source system, and the measured QEs should not be used as calibration data but can be understood as validation measurements. The QE is measured again during the FAT of the mDOMs for each mDOM PMT.

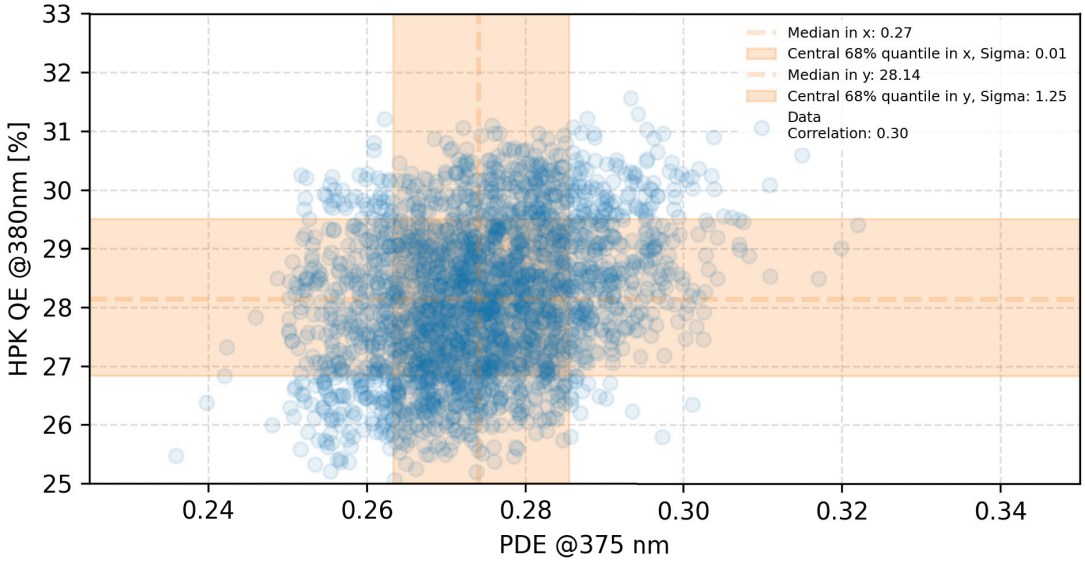

(a) $\lambda_1 = 375\,\mathrm{nm}$, $\lambda_{\mathrm{hpk}} = 380\,\mathrm{nm}$

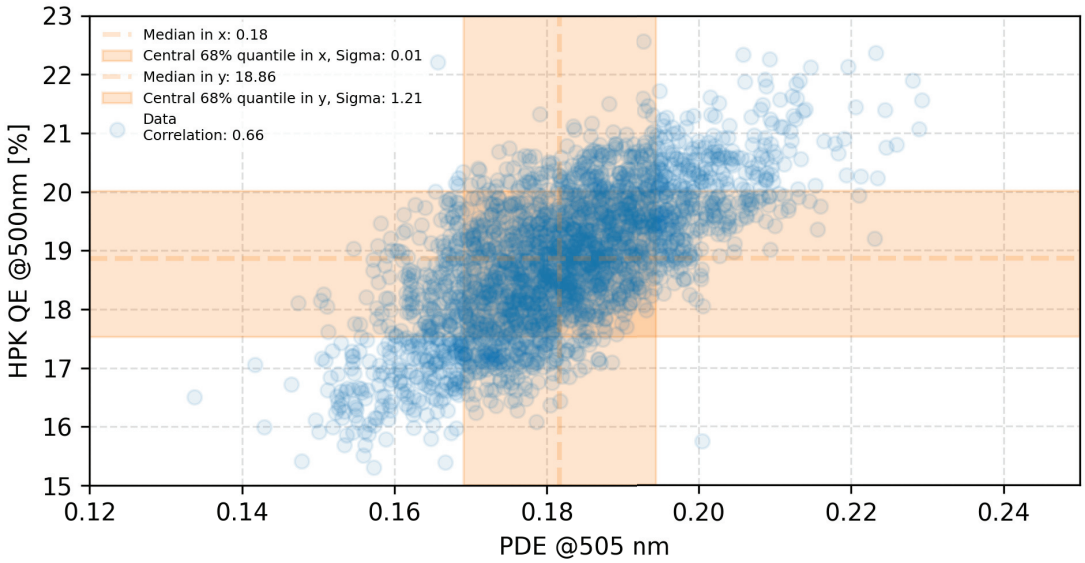

(b) $\lambda_2 = 505\,\mathrm{nm}$, $\lambda_{\mathrm{hpk}} = 500\,\mathrm{nm}$

Figure A.10: Measured relative QEs plotted against the manufacturer data are represented by blue points. The orange bands show the central 68% quantiles for the measured values and manufacturer data. Data in (a) is recorded at $\lambda_1 = 375\,\mathrm{nm}$ for the testing facilities and at $\lambda_{\mathrm{hpk}} = 380\,\mathrm{nm}$ for the manufacturer data. (b) shows the data recorded at $\lambda_2 = 505\,\mathrm{nm}$ and $\lambda_{\mathrm{hpk}} = 500\,\mathrm{nm}$ respectively.

A.0.4 Transit time spread

Figure A.11 shows the distribution of TTSs. The distribution peaks at $\sigma_{\mathrm{TTS}} = 1.7\,\mathrm{ns}$ and shows a distinct edge at the specification boundary. This edge is caused by retesting previously failed PMTs and is discussed in section 6.4. 175 PMTs are not compliant with the specification of $\sigma_{\mathrm{TTS}} < 2\,\mathrm{ns}$. All PMTs are accepted because their TTSs are just slightly above the specification and used in spare mDOMs.

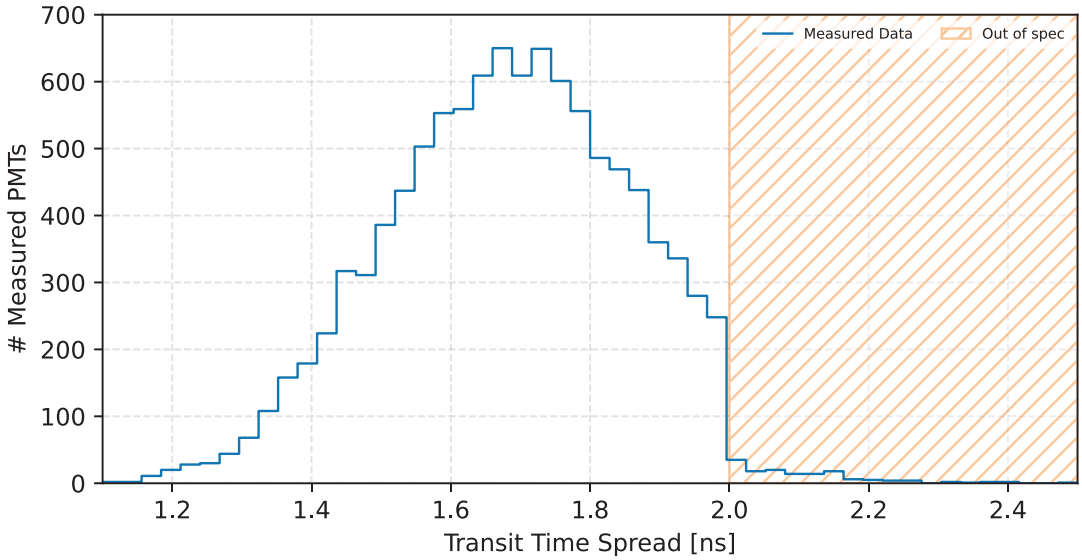

Figure A.11: Histogram of the TTS. The blue histogram shows the measured TTS, and the area highlighted by orange slanted lines indicates the specification boundary.

Figure A.12 shows the TTSs as a function of the PMT serial numbers. No deviations between the testing sites can be observed. The TTSs show a steady production quality.

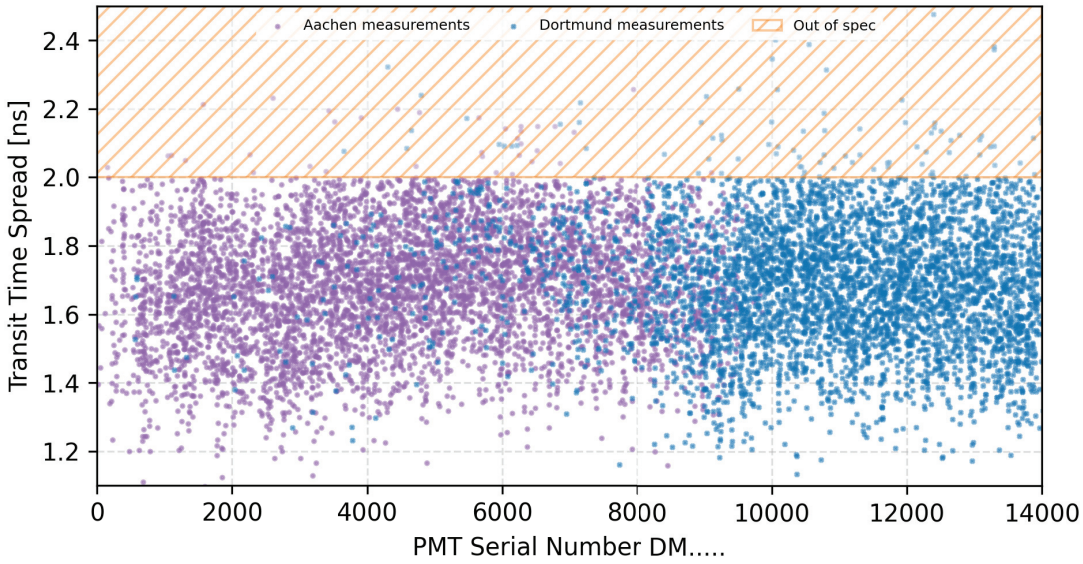

Figure A.12: Measured TTSs plotted against the PMT serial numbers. Blue points show PMTs tested in Dortmund and purple ones PMTs tested in Aachen. The area marked with orange slanted lines highlights the specification boundaries.

A.0.5 Prepulse Probability

Figure A.13 shows the distribution of prepulse probabilities. The distribution peaks around $p_{\text{pre}} = 0.0\%$ and shows a spiky pattern (more prominent with smaller bin sizes). These spikes arise from the binary nature of pulse counting. Negative values occur when the associated PMT dark rate contribution exceeds the measured number of prepulses. 44 PMTs are not compliant with the specification of $p_{\text{pre}} < 1\%$ and are used in spare mDOMs.

Figure A.14 shows the prepulse probabilities as a function of the PMT serial numbers. A larger spread can be observed for PMTs measured in Dortmund, with all probabilities still much smaller than the specification.

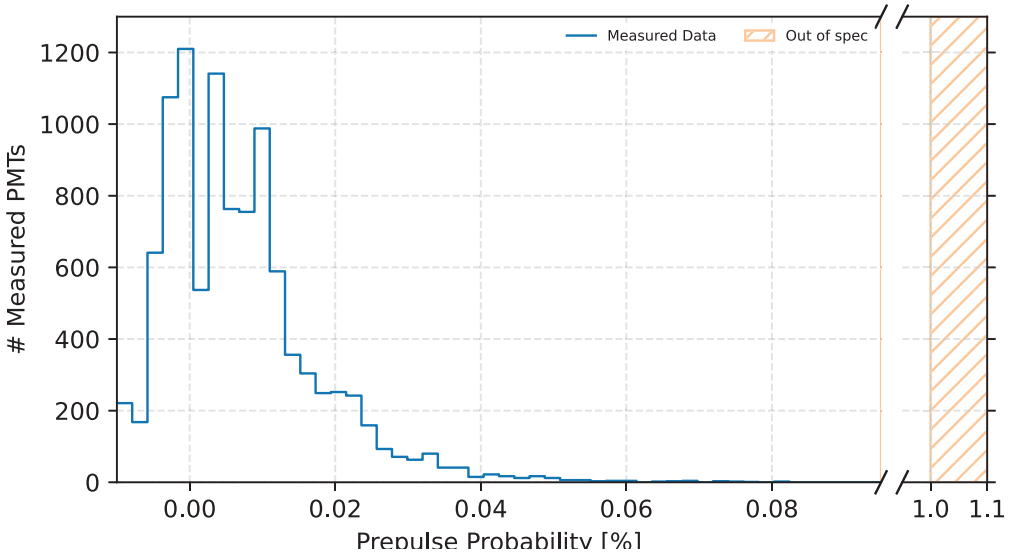

Figure A.13: Histogram of the prepulse probabilities. The blue histogram shows the measured probabilities, and the area marked with orange slanted lines highlights the specification boundary. Note the broken x-axis.

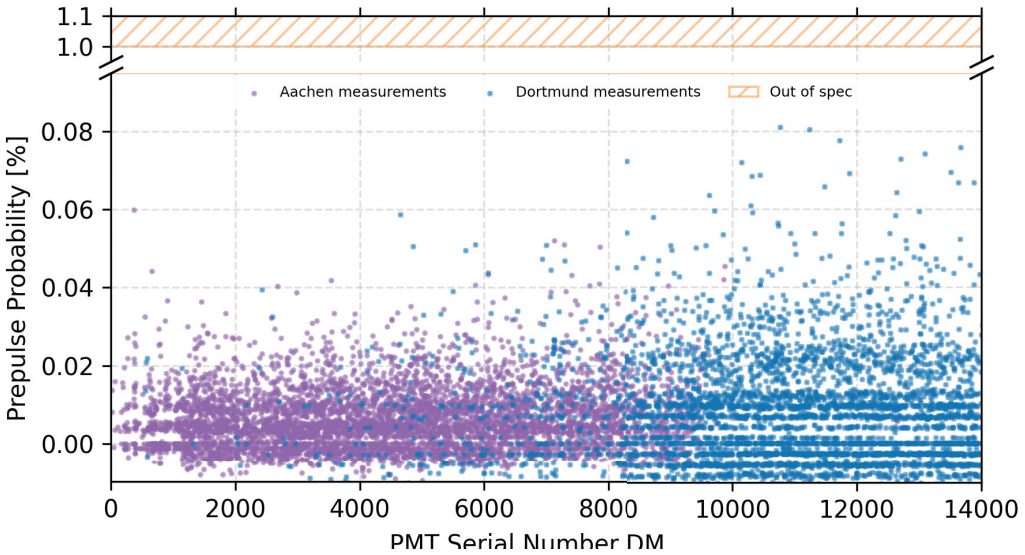

Figure A.14: Measured prepulse probabilities plotted against the PMT serial numbers. Blue points show PMTs tested in Dortmund and purple ones PMTs tested in Aachen. The area marked with orange slanted lines highlights the specification boundaries.

A.0.6 Latepulse Probability

Figure A.15 shows the distribution of latepulse probabilities. The distribution is well-behaved and peaks around $p_{\text{late}} = 4.25\%$. 46 PMTs are not compliant with the specification of $p_{\text{late}} < 5\%$ and are used in spare mDOMs.

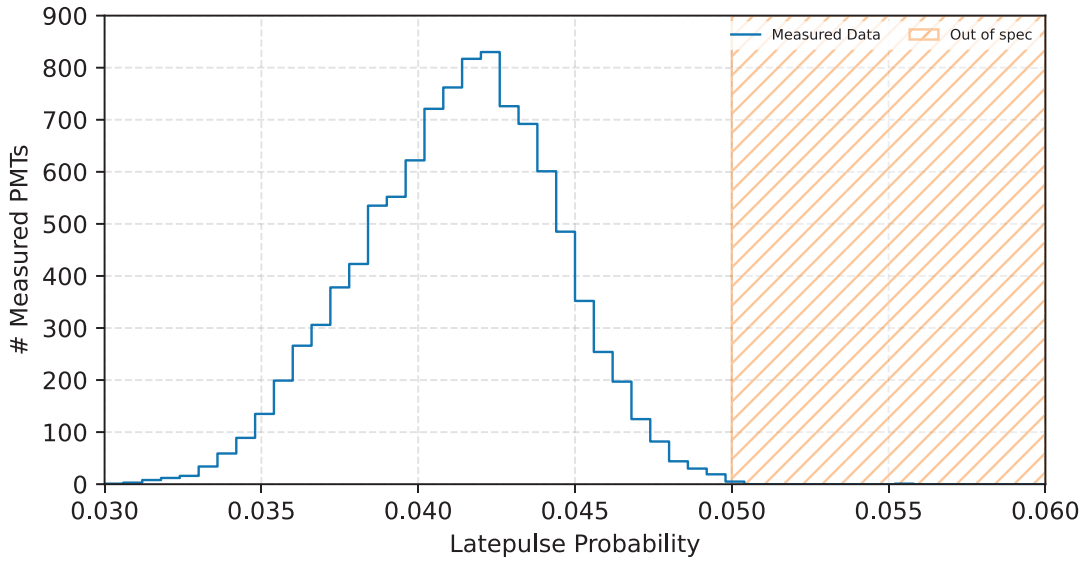

Figure A.15: Histogram of the latepulse probabilities. The blue histogram shows the measured probabilities, and the area marked with orange slanted lines highlights the specification boundary.

Figure A.16 shows the latepulse probabilities as a function of the PMT serial numbers. There is a visible systematic difference between the two measurement sites. The site at TU Dortmund University exhibits a slightly larger spread and a lower overall probability.

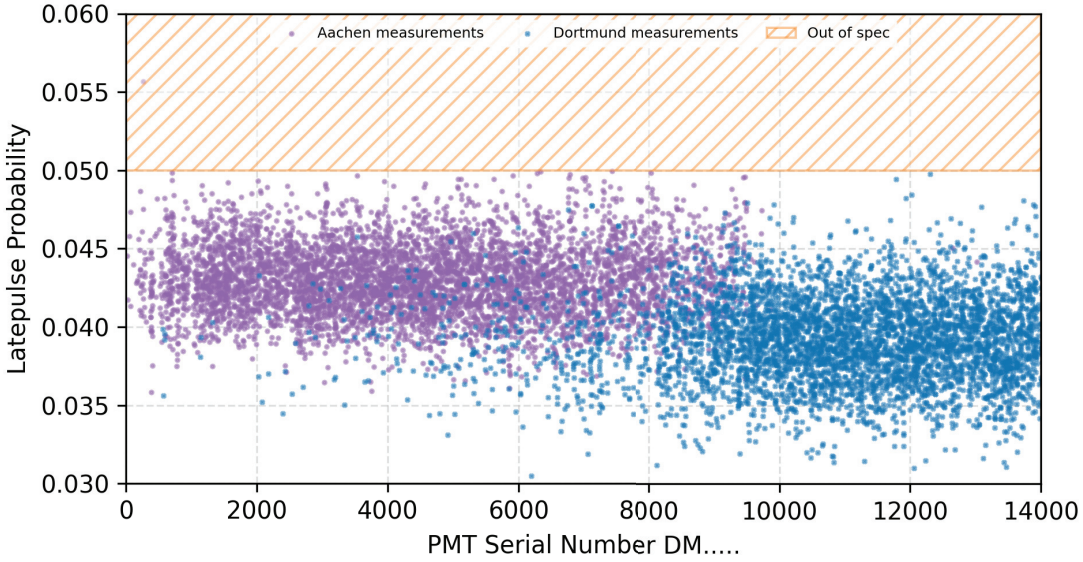

Figure A.16: Measured latepulse probabilities plotted against the PMT serial numbers. Blue points show PMTs tested in Dortmund and purple ones PMTs tested in Aachen. The area marked with orange slanted lines highlights the specification boundaries.

A.0.7 Afterpulse Probability

Figure A.17 shows the distribution of afterpulse probabilities. The distribution peaks around $p_{\text{after}} = 4.25\%$, with a longer tail towards higher probabilities. The spike at zero contains all values without a pulse in the afterpulse time window. 110 PMTs are not compliant with the specification of $p_{\text{after}} < 15\%$.

Figure A.18 shows the afterpulse probabilities as a function of the PMT serial numbers. Here, a slightly larger spread in the data measured in Dortmund can also be observed.

The charge-timing distribution is shown in Figure A.19. Most pulses have charges corresponding to SPEs. The same is true for pulses within the peaks of Figure 6.8. After 500 ns, a population of pulses with higher charges can be observed.

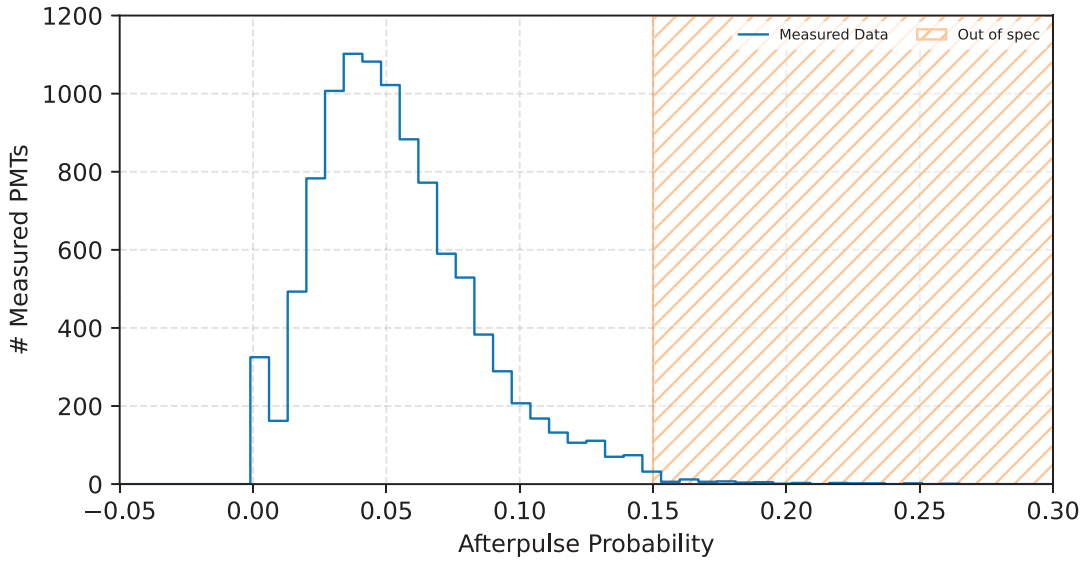

Figure A.17: Histogram of the afterpulse probabilities. The blue histogram shows the measured probabilities, and the area marked with orange slanted lines highlights the specification boundary.

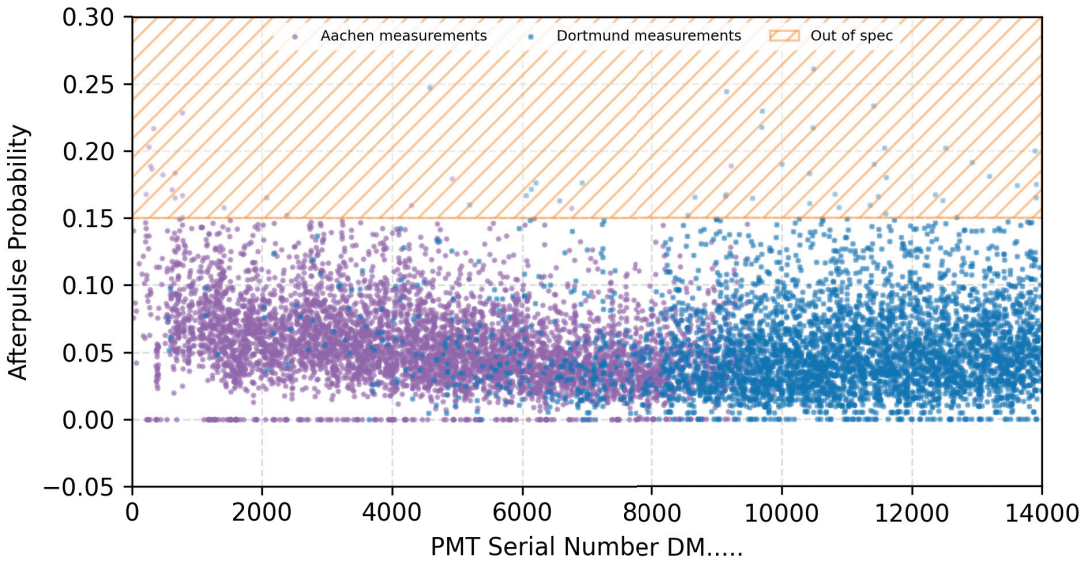

Figure A.18: Measured afterpulses probabilities plotted against the PMT serial numbers. Blue points show PMTs tested in Dortmund and purple ones PMTs tested in Aachen. The area marked with orange slanted lines highlights the specification boundaries.

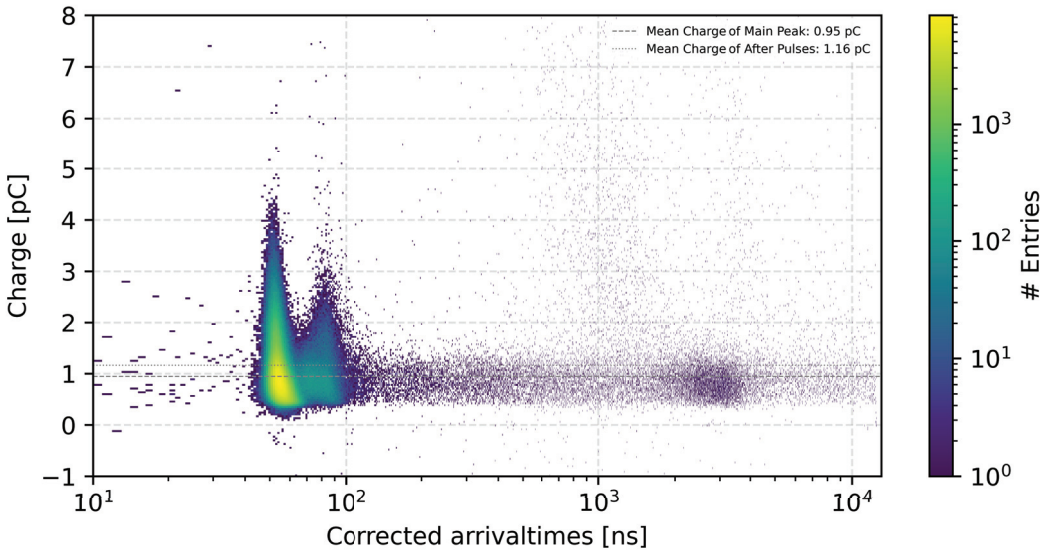

Figure A.19: The arrival time vs. charge spectrum for all pulses within the afterpulse time window. Most pulses exhibit SPE charges with a small distribution of higher charges beginning after 500 ns.

A.0.8 Linearity

Figure A.20 shows the distribution of charge linearities. A bimodal distribution is visible. 3190 PMTs are not compliant with the specification.

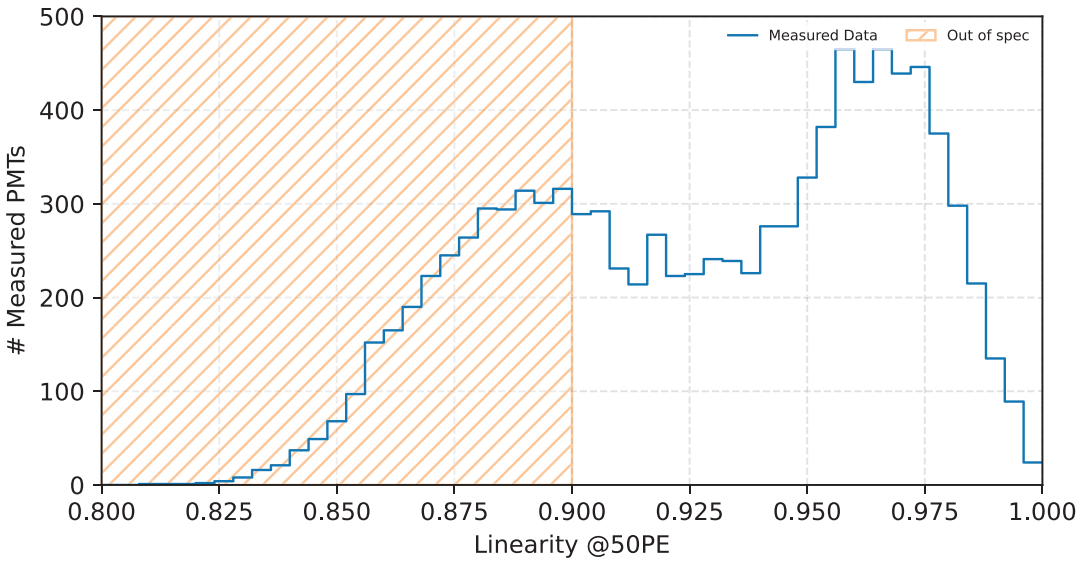

Figure A.20: Histogram of the charge linearities. The blue histogram shows the measured linearities, and the area marked with orange slanted lines highlights the specification boundary. The unreliable measurements do not affect the decision to accept the PMTs.

Figure A.21 shows the charge linearities as a function of the PMT serial numbers. The bimodal distribution in Figure A.20 results from a different implementation of the light source system at the two testing sites.

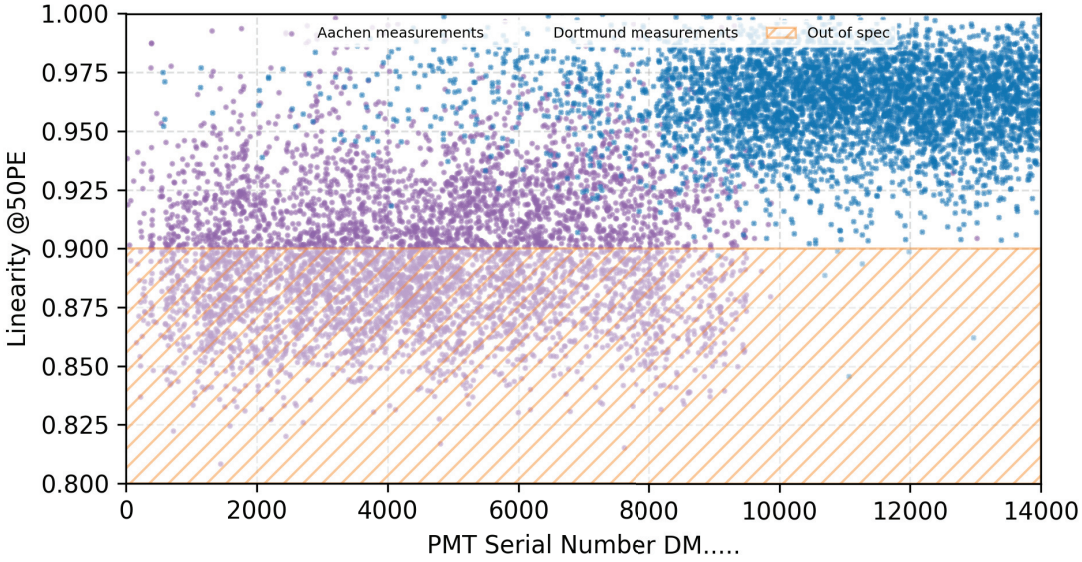

Figure A.21: Measured charge linearities plotted against the PMT serial numbers. Blue points show PMTs tested in Dortmund and purple ones PMTs tested in Aachen. The area marked with orange slanted lines highlights the specification boundaries.

A.0.9 Baseline Characteristics

No specifications were formally established with the manufacturer. However, baseline mean and electronic noise variability measurements were conducted to identify and rule out potential defects. Self-set specification boundaries were defined before mass testing and set to $\sigma_{\text{mean-baseline}} = 1\,\text{ADCcount}$ for the deviation of baseline means and $\bar{\sigma}_{\text{baseline}} = 2\,\text{ADCcount}$.

Figure A.22 shows the distribution of baseline mean deviations. The distribution peaks slightly below 0.4 ADC counts and has a wider tail towards higher baseline mean deviations with two more less prominent contributions at around 0.54 ADC counts and 0.65 ADC counts.

Figure A.23 shows the baseline mean deviations as a function of the PMT serial numbers. A wider spread of the data measured in Dortmund can be observed. Here, it is also visible that the main contribution to the secondary peaks at 0.54 ADC counts and 0.65 ADC counts is coming from data measured in Dortmund.

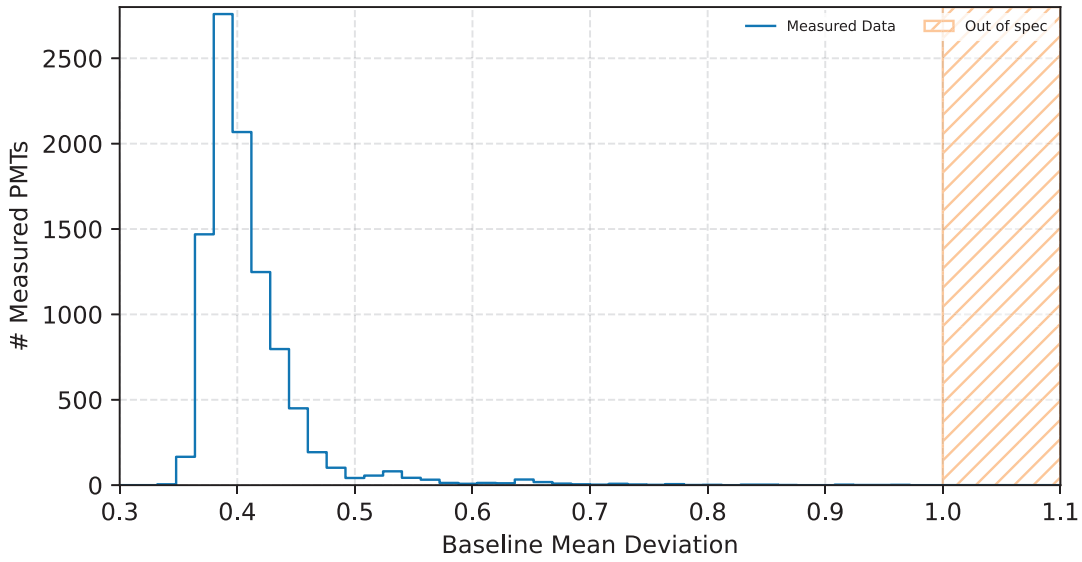

Figure A.22: Histogram of baseline mean deviations. The blue histogram shows the measured data, and the area marked with orange slanted lines highlights the self-set specification boundary.

Figure A.24 shows the distribution of the mean of the measured baseline spread. The distribution peaks slightly below 0.73 ADC counts and has a wider tail towards higher ADC counts.

Figure A.25 shows the mean of the measured baseline spread as a function of the PMT serial numbers. As seen in Figure A.23, a wider spread of the data measured in Dortmund can also be observed here. This hints towards a noisier environment. All self-set specification boundaries are met.

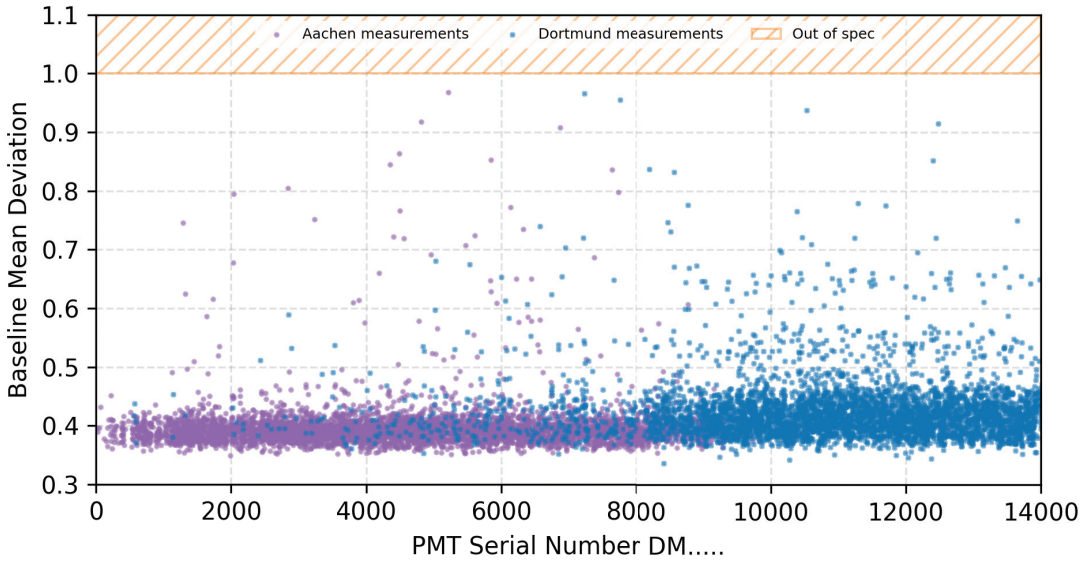

Figure A.23: The mean of measured baseline deviations plotted against the PMT serial numbers. Blue points show PMTs tested in Dortmund and purple ones PMTs tested in Aachen. The area marked with orange slanted lines highlights the self-set specification boundaries.

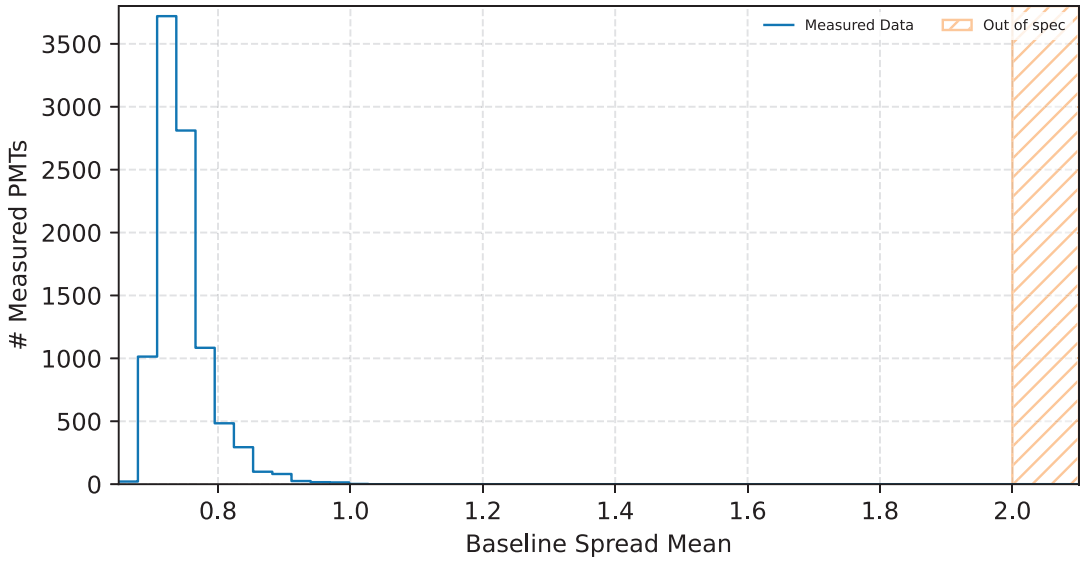

Figure A.24: Histogram of the baseline spreads. The blue histogram shows the measured mean baseline spreads, and the area marked with orange slanted lines highlights the self-set specification boundary.

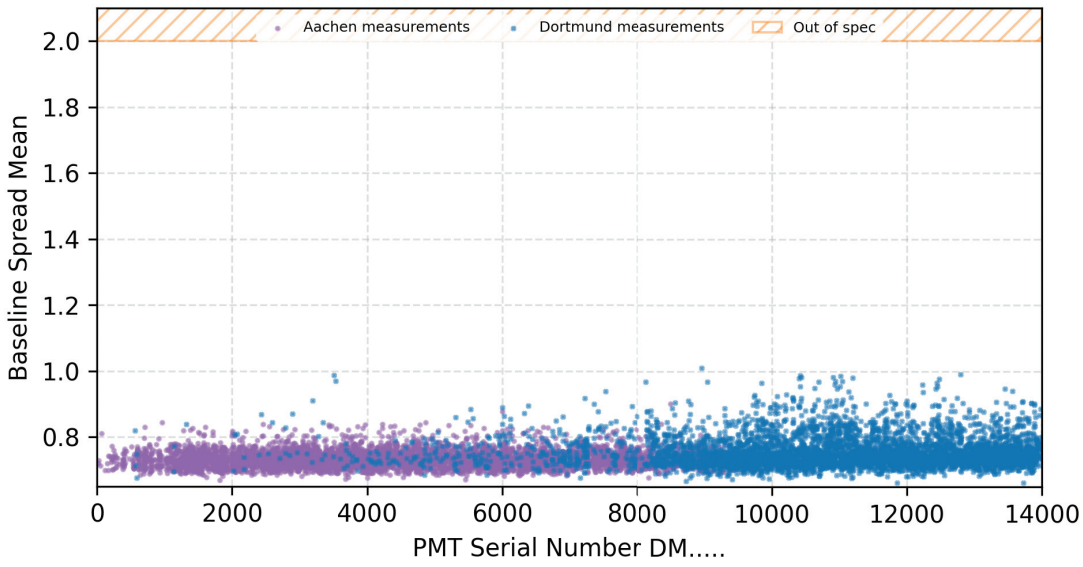

Figure A.25: Mean of the measured baseline spread plotted against the PMT serial numbers. Blue points show PMTs tested in Dortmund and purple ones PMTs tested in Aachen. The area marked with orange slanted lines highlights the self-set specification boundaries.

A.0.10 Dark Rates

Figure A.26 shows the distribution of dark rates. Two populations at (114 ± 39) Hz and (350 ± 52) Hz are clearly visible. The reason and consequences are discussed in subsection 6.3.1.

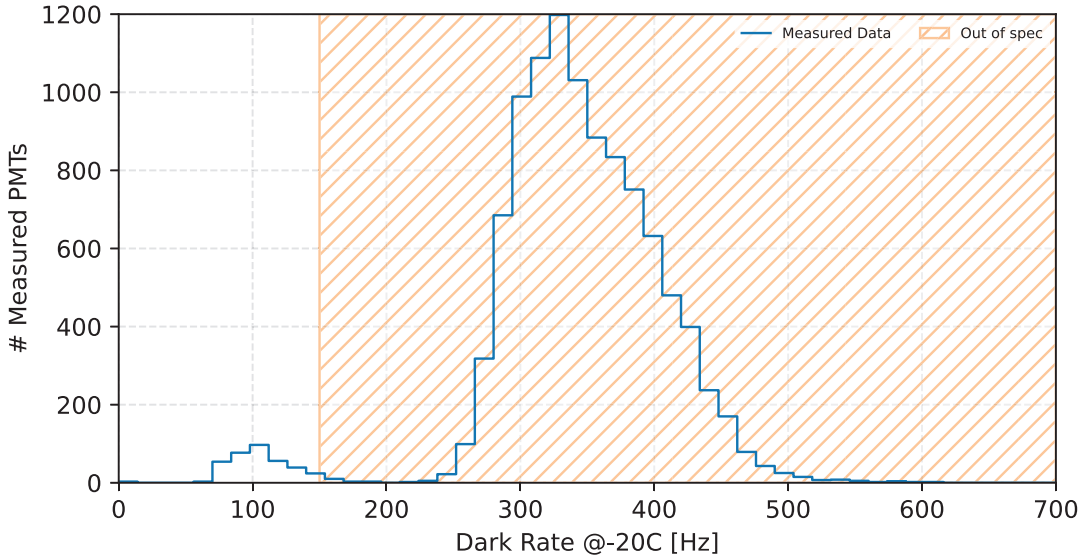

Figure A.26: Histogram of dark rates measured in Aachen and Dortmund. The blue histogram shows the measured dark rates, and the area marked with orange slanted lines highlights the specification boundary.

Figure A.27 shows the behavior of the dark rates in relation to their serial numbers. A clear transition to high dark rates can be observed for PMTs with serial numbers above `DM01130`.

Figure A.28 shows the dark rates measured at $-20\,°C$ plotted against the dark rates at room temperature as reported by the manufacturer. The figure shows no visible difference in the dark rates at room temperature.

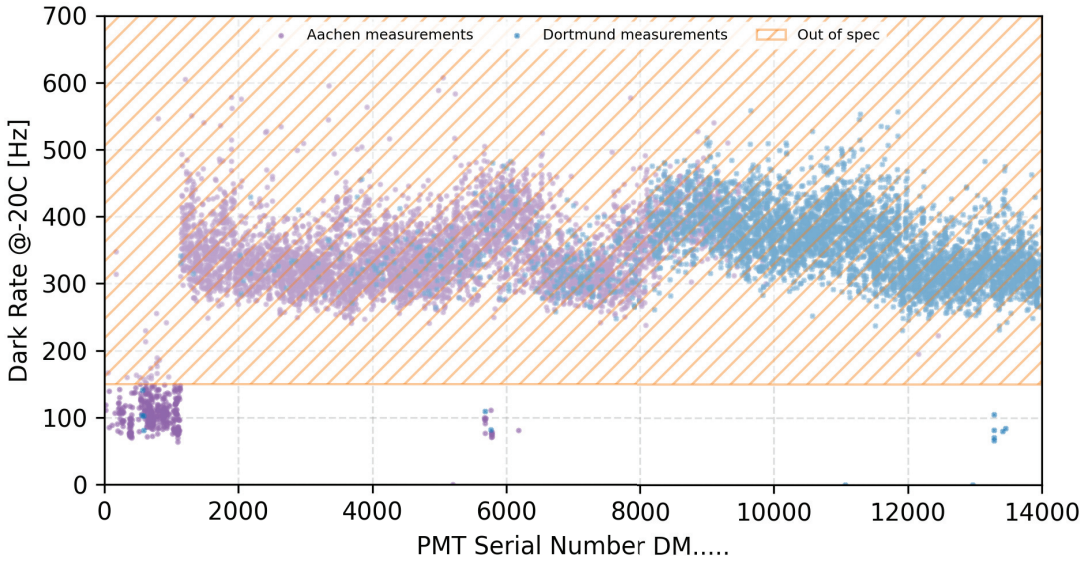

Figure A.27: The dark rates plotted against the serial number of the PMTs. Blue points show PMTs tested in Dortmund and purple ones PMTs tested in Aachen. The area marked with orange slanted lines highlights the self-set specification boundaries.

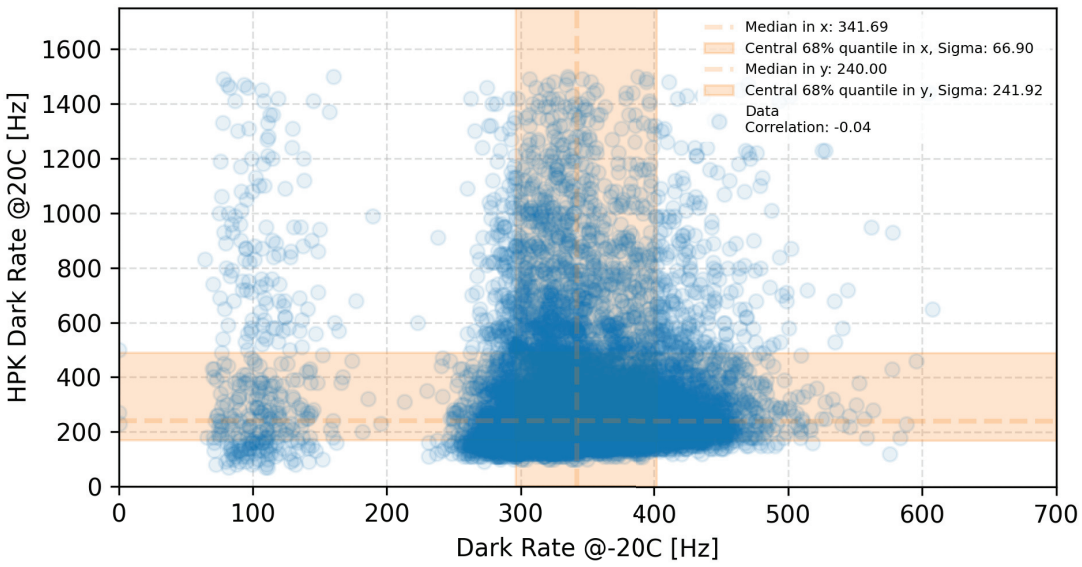

Figure A.28: A comparison of the dark rates reported by the manufacturer at 20 degreeCelsius with the results of the test benches at −20 degreeCelsius. The higher dark rate is not observable at room temperature and could not have been detected in the tests carried out by the manufacturer.

B Estimation of the Measurement Precision

Here, an estimation of the measurement precision of the facility at TU Dortmund University is discussed. The basis for this estimation is channel-to-channel and same-channel variations. Several PMTs were measured more than once, and especially the reference PMTs were present in each run. Most measurements were repeated with the PMT in a different channel of the testing facility. A smaller subset of measurements was repeated with the PMT connected to the same channel; plotted in light blue. The complete data is plotted in blue.

All measured values can be divided into two categories: those described by a single Gaussian and those better represented by the sum of two Gaussians. The broad Gaussian describes the channel-to-channel contribution, and the narrow Gaussian the same-channel contribution. It can be observed that, in particular, values dependent on the target voltage show a two-distribution contribution. The measurement precision can be extracted from these Gaussians.

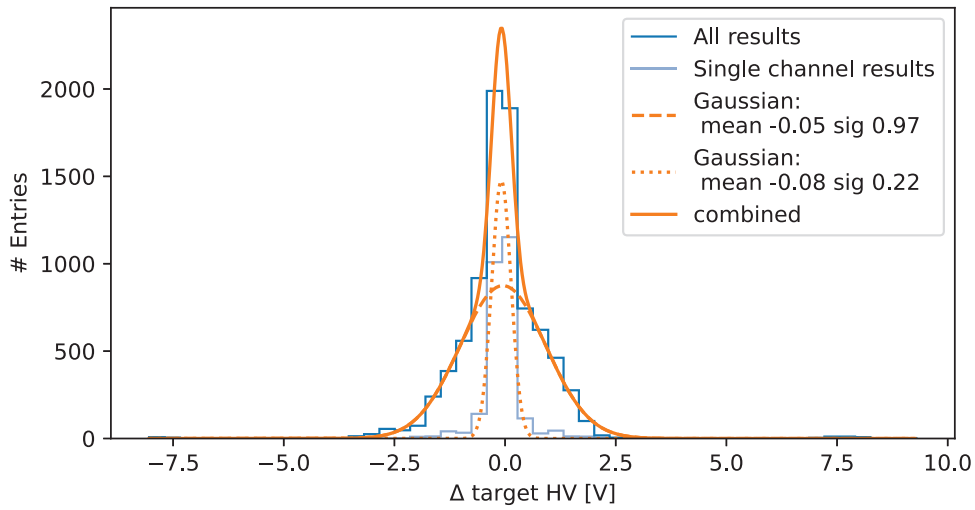

Figure B.1: Plotted are the differences in target voltage between different runs for the reference PMTs. The same-channel contribution to the overall distribution is shown in light blue.

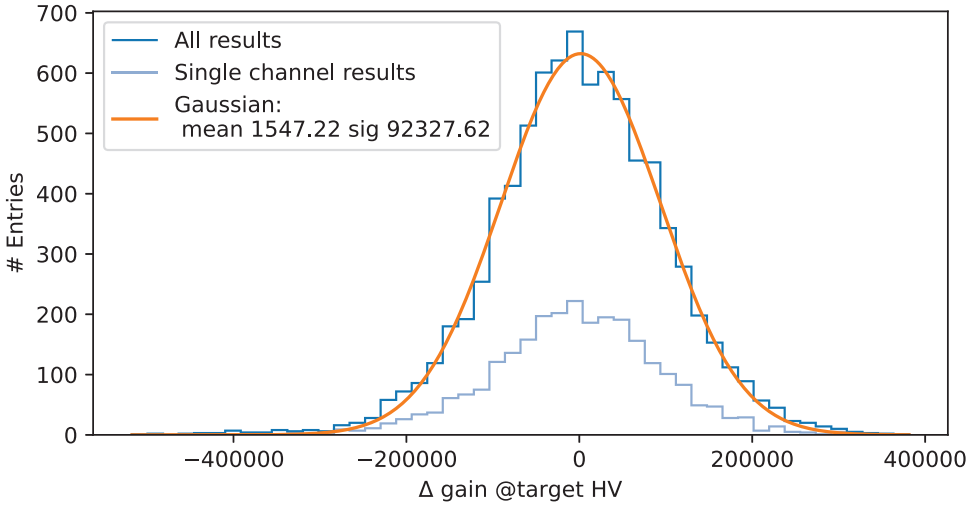

Figure B.2: Plotted are the differences in gain at target voltage between different runs for the reference PMTs. The same-channel contribution to the overall distribution is shown in light blue.

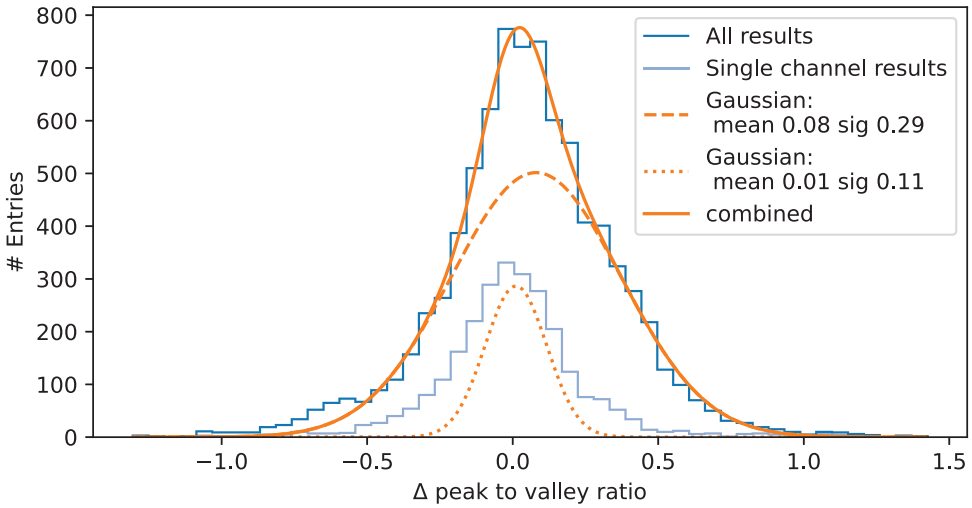

Figure B.3: Plotted are the differences in peak to valley between different runs for the reference PMTs. The same-channel contribution to the overall distribution is shown in light blue.

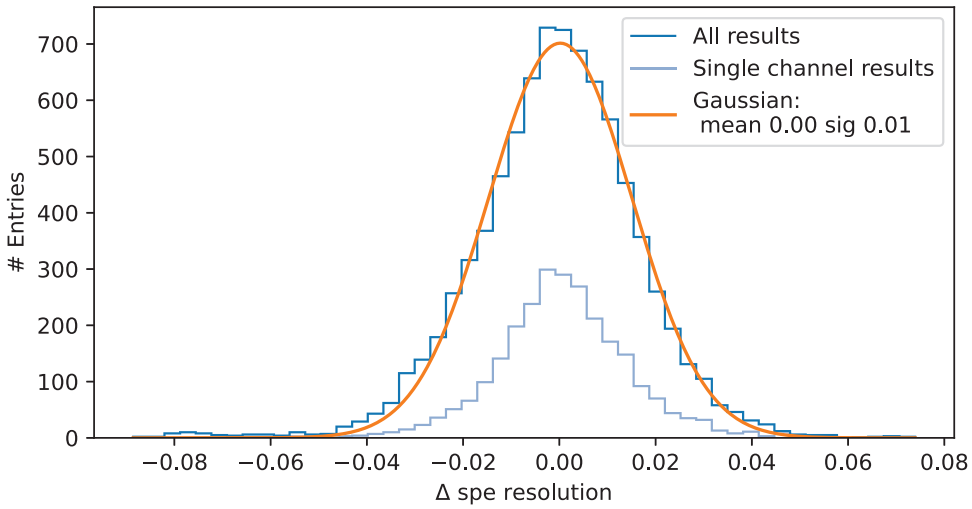

Figure B.4: Plotted are the differences in SPE resolution between different runs for the reference PMTs. The same-channel contribution to the overall distribution is shown in light blue.

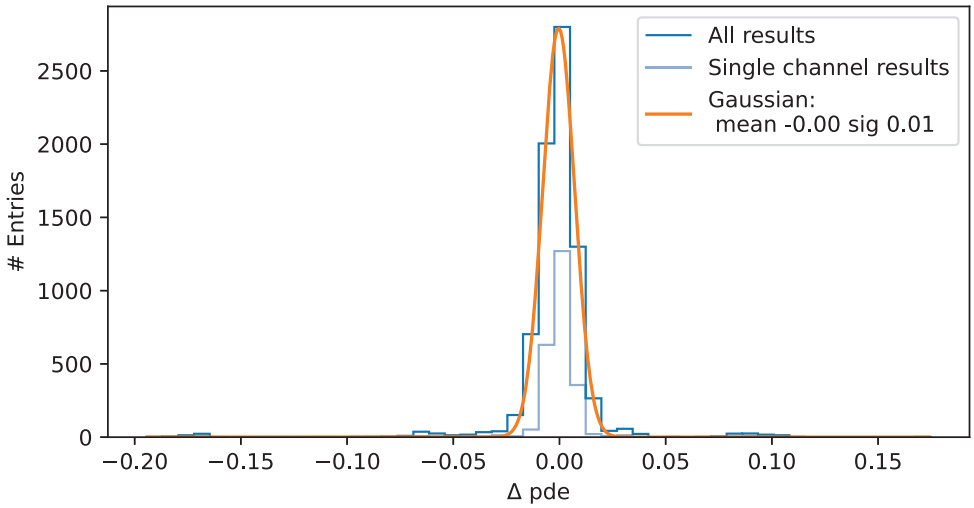

Figure B.5: Plotted are the differences in QE @ 375 nm between different runs for the reference PMTs. The same-channel contribution to the overall distribution is shown in light blue.

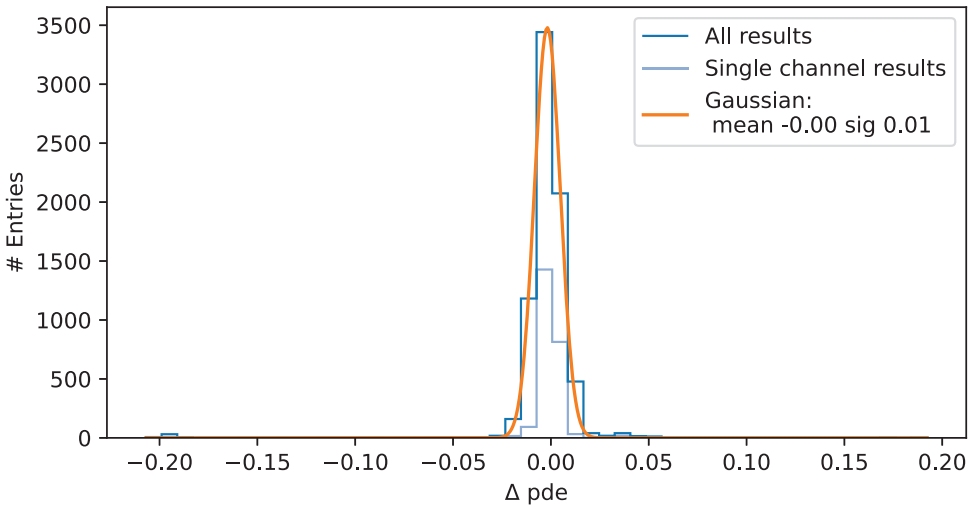

Figure B.6: Plotted are the differences in QE @ 505 nm between different runs for the reference PMTs. The same-channel contribution to the overall distribution is shown in light blue.

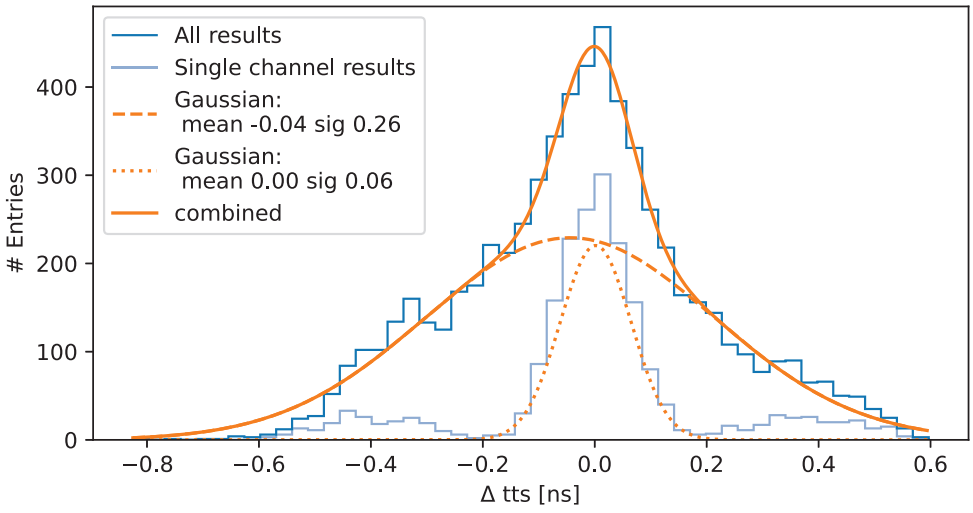

Figure B.7: Plotted are the differences in TTS between different runs for the reference PMTs. The same-channel contribution to the overall distribution is shown in light blue.

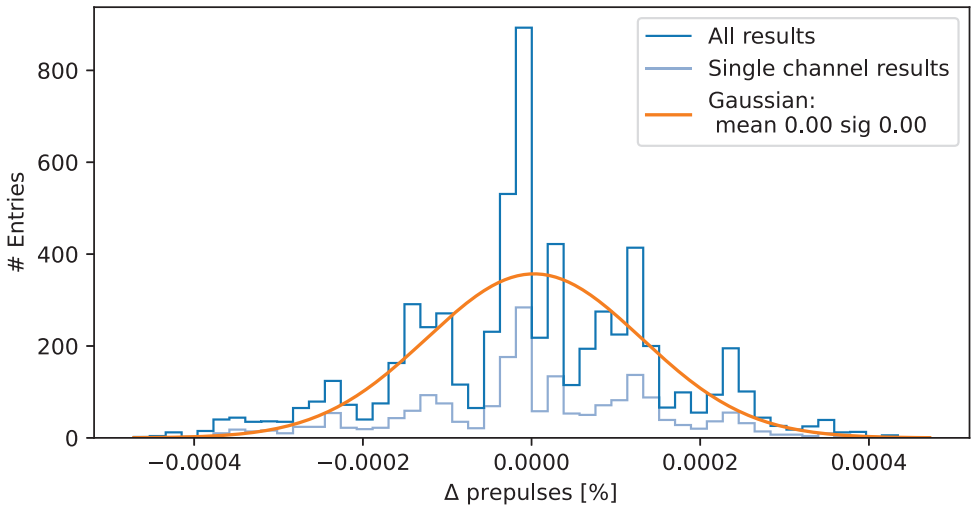

Figure B.8: Plotted are the differences in prepulse probability between different runs for the reference PMTs. The same-channel contribution to the overall distribution is shown in light blue.

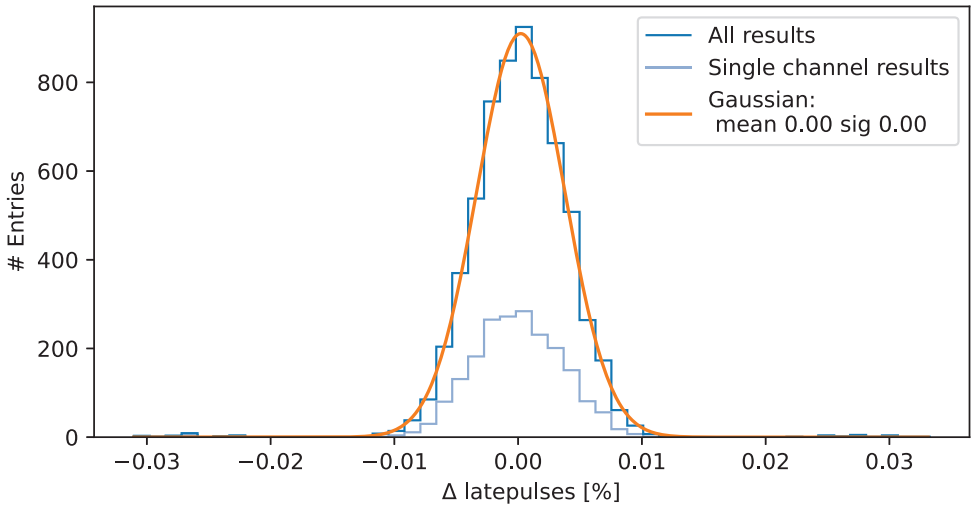

Figure B.9: Plotted are the differences in latepulse probability between different runs for the reference PMTs. The same-channel contribution to the overall distribution is shown in light blue.

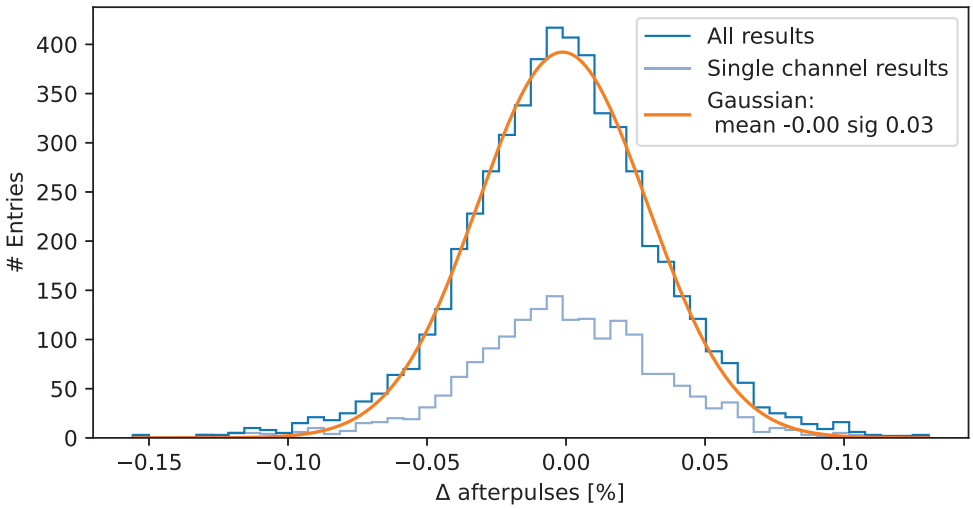

Figure B.10: Plotted are the differences in afterpulse probability between different runs for the reference PMTs. The same-channel contribution to the overall distribution is shown in light blue.

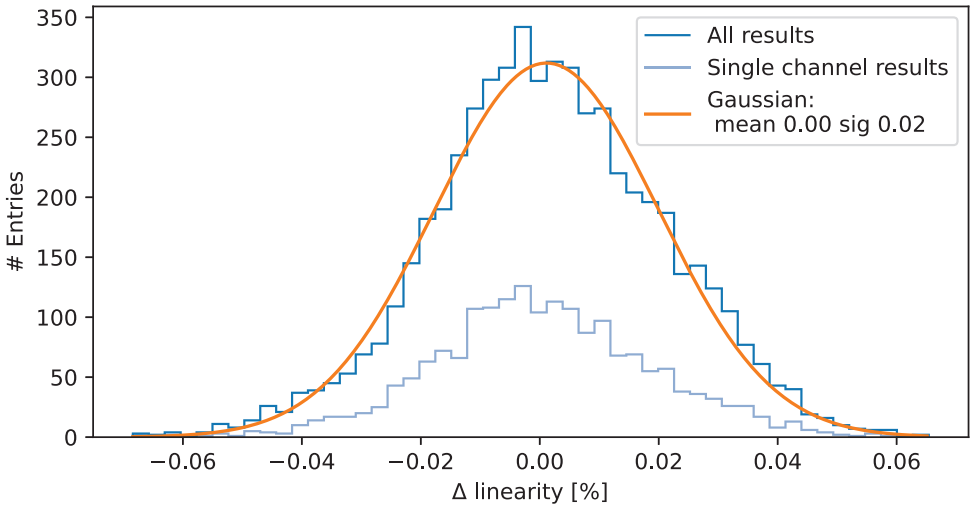

Figure B.11: Plotted are the differences in charge linearitiy between different runs for the reference PMTs. The same-channel contribution to the overall distribution is shown in light blue.

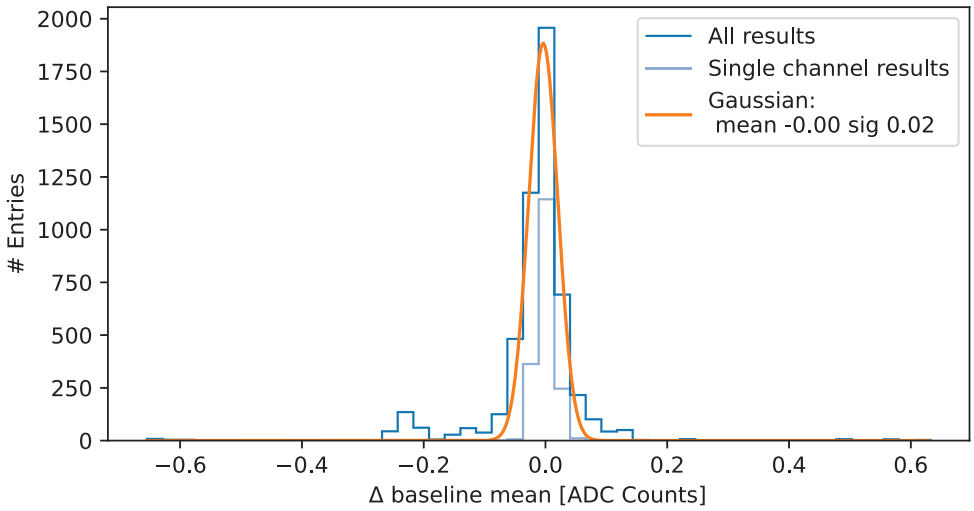

Figure B.12: Plotted are the differences in the mean of the baseline deviation between different runs for the reference PMTs. The same-channel contribution to the overall distribution is shown in light blue.

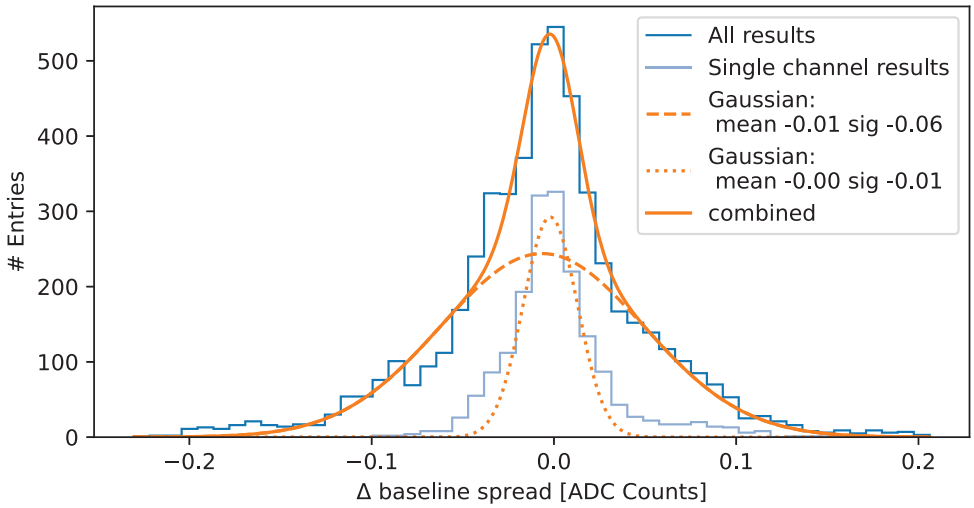

Figure B.13: Plotted are the differences in the mean of the baseline spread between different runs for the reference PMTs. The same-channel contribution to the overall distribution is shown in light blue.

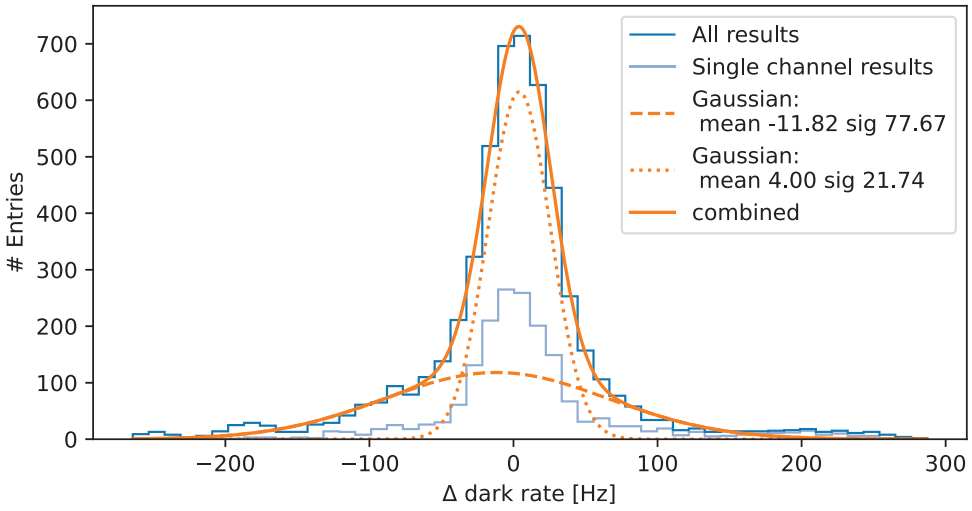

Figure B.14: Plotted are the differences in dark rate between different runs for the reference PMTs. The same-channel contribution to the overall distribution is shown in light blue.

Bibliography

[1] R. Abbasi et al. "Acceptance Tests of More than 10 000 Photomultiplier Tubes for the Multi-PMT Digital Optical Modules of the IceCube Upgrade." In: *J. Inst.* 19.07 (July 1, 2024), P07038. DOI: 10.1088/1748-0221/19/07/P07038. (Visited on 11/07/2024) (cited on page iii).

[2] Lasse Halve and Johannes Werthebach. "Design of an Efficient, High-Throughput Photomultiplier Tube Testing Facility for the IceCube Upgrade." July 21, 2021 (cited on page iii).

[3] Timothy Darvill. "Keeping Time at Stonehenge." In: *Antiquity* 96.386 (Apr. 2, 2022), pp. 319–335. DOI: 10.15184/aqy.2022.5 (cited on page 3).

[4] J. McKim Malville. "Astronomy at Nabta Playa, Southern Egypt." In: *Handbook of Archaeoastronomy and Ethnoastronomy*. Ed. by Clive L.N. Ruggles. New York, NY: Springer New York, 2015, pp. 1079–1091. DOI: 10.1007/978-1-4614-6141-8_101. (Visited on 02/14/2025) (cited on page 3).

[5] V. Hess. "Über Beobachtungen Der Durchdringenden Strahlung Bei Sieben Freiballonfahrten." In: *Physikalische Zeitschrift* 13 (1912) (cited on page 3).

[6] Cecilia Helena Payne-Gaposchkin. "Stellar Atmospheres: A Contribution to the Observational Study of High Temperature in the Reversing Layers of Stars." PhD thesis. Jan. 1, 1925. (Visited on 06/17/2025) (cited on page 3).

[7] A. Hewish et al. "Observation of a Rapidly Pulsating Radio Source." In: *Nature* 217.5130 (Feb. 1968), pp. 709–713. DOI: 10.1038/217709a0. (Visited on 06/17/2025) (cited on page 3).

[8] M G Aartsen et al. "Evidence for High-Energy Extraterrestrial Neutrinos at the IceCube Detector." In: *Science* 342.6161 (Nov. 22, 2013). DOI: 10.1126/science.1242856 (cited on pages 3, 51).

[9] B. P. Abbott et al. "Observation of Gravitational Waves from a Binary Black Hole Merger." In: *Phys. Rev. Lett.* 116.6 (Feb. 11, 2016), p. 061102. DOI: 10.1103/PhysRevLett.116.061102. (Visited on 06/17/2025) (cited on page 3).

[10] Frank Close. *Neutrino*. 1. publ. in paperback. Popular Science. Oxford: Oxford University Press, 2012. 181 pp. (cited on pages 4, 6).

[11] William Giaré et al. “Cosmological Forecasts on Thermal Axions, Relic Neutrinos and Light Elements.” In: *Monthly Notices of the Royal Astronomical Society* (Jan. 18, 2022), stac126. DOI: 10.1093/mnras/stac126. (Visited on 01/31/2025) (cited on page 4).

[12] Maurizio Spurio. “Low-Energy Neutrino Physics and Astrophysics.” In: *Probes of Multimessenger Astrophysics*. Cham: Springer International Publishing, 2018, pp. 441–488. DOI: 10.1007/978-3-319-96854-4_12. (Visited on 01/31/2025) (cited on page 5).

[13] Ivan Esteban et al. “NuFit-6.0: Updated Global Analysis of Three-Flavor Neutrino Oscillations.” In: *J. High Energ. Phys.* 2024.12 (Dec. 30, 2024), p. 216. DOI: 10.1007/JHEP12(2024)216. (Visited on 02/16/2025) (cited on page 6).

[14] Carlo Giunti. “Neutrino Oscillations In Matter.” In: Carlo Giunti and Chung W. Kim. *Fundamentals of Neutrino Physics and Astrophysics*. Oxford University Press, Mar. 15, 2007, pp. 322–351. DOI: 10.1093/acprof:oso/9780198508717.001.0001. (Visited on 11/27/2024) (cited on page 6).

[15] Ivan Esteban et al. “The Fate of Hints: Updated Global Analysis of Three-Flavor Neutrino Oscillations.” In: (2020). DOI: 10.48550/ARXIV.2007.14792. (Visited on 11/28/2024) (cited on page 6).

[16] The KATRIN Collaboration et al. “Direct Neutrino-Mass Measurement with Sub-Electronvolt Sensitivity.” In: *Nat. Phys.* 18.2 (Feb. 2022), pp. 160–166. DOI: 10.1038/s41567-021-01463-1. (Visited on 01/31/2025) (cited on page 6).

[17] F. Vannucci. “Interactions of Neutrinos with Matter.” In: *Progress in Particle and Nuclear Physics* 95 (July 2017), pp. 1–47. DOI: 10.1016/j.ppnp.2017.03.003. (Visited on 01/31/2025) (cited on page 7).

[18] Sheldon L. Glashow. “Resonant Scattering of Antineutrinos.” In: *Phys. Rev.* 118.1 (Apr. 1, 1960), pp. 316–317. DOI: 10.1103/PhysRev.118.316. (Visited on 01/31/2025) (cited on page 7).

[19] M. G. Aartsen et al. “IceCube-Gen2: The Window to the Extreme Universe.” In: *Journal of Physics G: Nuclear and Particle Physics* 48.6 (2021). DOI: 10.1088/1361-6471/abbd48 (cited on pages 7, 18, 31–33, 141).

[20] David Maurin et al. “A Cosmic-Ray Database Update: CRDB v4.1.” In: *Eur. Phys. J. C* 83.10 (Oct. 29, 2023), p. 971. DOI: 10.1140/epjc/s10052-023-12092-8. (Visited on 01/31/2025) (cited on page 8).

[21] Alberto Daniel Supanitsky. "Determination of the Cosmic-Ray Chemical Composition: Open Issues and Prospects." In: *Galaxies* 10.3 (June 17, 2022), p. 75. DOI: 10.3390/galaxies10030075. (Visited on 01/31/2025) (cited on page 8).

[22] Alessandro De Angelis. "The Highest Energies in the Universe." In: *Cosmic Rays*. Cham: Springer International Publishing, 2023, pp. 1–21. DOI: 10.1007/978-3-031-38560-5_1. (Visited on 01/31/2025) (cited on page 8).

[23] Maurizio Spurio. *Probes of Multimessenger Astrophysics*. Cham: Springer International Publishing, 2018 (cited on page 8).

[24] R L Workman et al. "Review of Particle Physics." In: *Progress of Theoretical and Experimental Physics* 2022.8 (Aug. 8, 2022). DOI: 10.1093/ptep/ptac097 (cited on page 9).

[25] Thomas K. Gaisser, Ralph Engel, and Elisa Resconi. *Cosmic Rays and Particle Physics*. Cambridge University Press, June 2, 2016 (cited on page 9).

[26] Maurizio Spurio. "The Extragalactic Sources and Ultra High Energy Cosmic Rays." In: *Probes of Multimessenger Astrophysics*. Cham: Springer International Publishing, 2018, pp. 225–267. DOI: 10.1007/978-3-319-96854-4_7. (Visited on 01/31/2025) (cited on page 9).

[27] P. Abreu et al. "Update on the Correlation of the Highest Energy Cosmic Rays with Nearby Extragalactic Matter." In: *Astroparticle Physics* 34.5 (Dec. 2010), pp. 314–326. DOI: 10.1016/j.astropartphys.2010.08.010. (Visited on 01/31/2025) (cited on page 9).

[28] O. Adriani et al. "Measurements of Cosmic-Ray Proton and Helium Spectra with the PAMELA Calorimeter." In: *Advances in Space Research* 51.2 (Jan. 2013), pp. 219–226. DOI: 10.1016/j.asr.2012.09.029. (Visited on 01/31/2025) (cited on page 9).

[29] M. Ackermann et al. "Detection of the Characteristic Pion-Decay Signature in Supernova Remnants." In: *Science* 339.6121 (Feb. 15, 2013), pp. 807–811. DOI: 10.1126/science.1231160. (Visited on 01/31/2025) (cited on page 9).

[30] M.G. Aartsen et al. "Astrophysical Neutrinos and Cosmic Rays Observed by IceCube." In: *Advances in Space Research* 62.10 (Nov. 2018), pp. 2902–2930. DOI: 10.1016/j.asr.2017.05.030. (Visited on 02/14/2025) (cited on page 11).

[31] Mark Aartsen et al. “Multimessenger Observations of a Flaring Blazar Coincident with High-Energy Neutrino IceCube-170922A.” In: *Science* 361.6398 (July 13, 2018). DOI: 10.1126/science.aat1378 (cited on pages 11, 21, 51).

[32] R. Abbasi et al. “Evidence for Neutrino Emission from the Nearby Active Galaxy NGC 1068.” In: *Science* 378.6619 (Nov. 4, 2022), pp. 538–543. DOI: 10.1126/science.abg3395 (cited on pages 11, 51).

[33] Maurizio Spurio. “The Sky Seen in -Rays.” In: *Probes of Multimessenger Astrophysics*. Cham: Springer International Publishing, 2018, pp. 269–312. DOI: 10.1007/978-3-319-96854-4_8. (Visited on 01/31/2025) (cited on page 12).

[34] U.F. Katz and Ch. Spiering. “High-Energy Neutrino Astrophysics: Status and Perspectives.” In: *Progress in Particle and Nuclear Physics* 67.3 (July 2012), pp. 651–704. DOI: 10.1016/j.ppnp.2011.12.001. (Visited on 11/13/2024) (cited on pages 12–14).

[35] Robert Marcus Wagner. “Measurement of Very High Energy Gamma-Ray Emission from Four Blazars Using the MAGIC Telescope and a Comparative Blazar Study.” PhD thesis. Munich, Tech. U., 2006 (cited on page 13).

[36] Jakob Van Santen. “Probing Extraterrestrial Neutrino Fluxes and Atmospheric Charm with Contained Neutrino Events above 1 TeV in IceCube.” In: *Physics Procedia* 61 (2015), pp. 633–640. DOI: 10.1016/j.phpro.2014.12.063. (Visited on 11/13/2024) (cited on page 14).

[37] Maurizio Spurio. “Indirect Cosmic Ray Detection: Particle Showers in the Atmosphere.” In: *Probes of Multimessenger Astrophysics*. Cham: Springer International Publishing, 2018, pp. 101–148. DOI: 10.1007/978-3-319-96854-4_4. (Visited on 01/31/2025) (cited on page 15).

[38] Peter K.F. Grieder. “Cosmic Rays Underground, Underwater and Under Ice.” In: *Cosmic Rays at Earth*. Elsevier, 2001, pp. 459–668. DOI: 10.1016/B978-044450710-5/50006-3. (Visited on 01/31/2025) (cited on page 16).

[39] Martin Antonio Unland Elorrieta. “Development, Simulation, and Characterisation of a Novel Multi-PMT Optical Module for IceCube Upgrade with Emphasis on Detailed Understanding of Photomultiplier Performance Parameters.” Universität Münster, July 2023. DOI: 10.5281/zenodo.8121321 (cited on pages 16, 122, 125).

[40] Thomas Gaisser and Francis Halzen. "IceCube." In: *Annu. Rev. Nucl. Part. Sci.* 64.1 (Oct. 19, 2014), pp. 101–123. DOI: 10.1146/annurev-nucl-102313-025321. (Visited on 01/31/2025) (cited on pages 17, 20).

[41] M.G. Aartsen et al. "The IceCube Realtime Alert System." In: *Astroparticle Physics* 92 (June 2017), pp. 30–41. DOI: 10.1016/j.astropartphys.2017.05.002. (Visited on 11/17/2024) (cited on page 21).

[42] Sebastian Euler. "Observation of Oscillations of Atmospheric Neutrinos with the IceCube Neutrino Observatory." PhD thesis. Aachen, 2014 (cited on page 22).

[43] M. Ackermann et al. "Optical Properties of Deep Glacial Ice at the South Pole." In: *J. Geophys. Res.* 111.D13 (July 16, 2006), 2005JD006687. DOI: 10.1029/2005JD006687. (Visited on 11/17/2024) (cited on pages 21, 22).

[44] T. Uchida et al. "Refractive-Index Measurements of Natural Air–Hydrate Crystals in an Antarctic Ice Sheet." In: *Appl. Opt.* 34.25 (Sept. 1, 1995), p. 5746. DOI: 10.1364/AO.34.005746. (Visited on 12/20/2024) (cited on page 21).

[45] The IceCube Collaboration. "South Pole Glacial Climate Reconstruction from Multi-Borehole Laser Particulate Stratigraphy." In: *J. Glaciol.* 59.218 (2013), pp. 1117–1128. DOI: 10.3189/2013JoG13J068. (Visited on 11/17/2024) (cited on page 22).

[46] M.G. Aartsen et al. "Measurement of South Pole Ice Transparency with the IceCube LED Calibration System." In: *Nuclear Instruments and Methods in Physics Research Section A: Accelerators, Spectrometers, Detectors and Associated Equipment* 711 (May 2013), pp. 73–89. DOI: 10.1016/j.nima.2013.01.054. (Visited on 11/17/2024) (cited on page 22).

[47] Martin Rongen and Dmitry Chirkin. *A Novel Microstructure-Based Model to Explain the IceCube Ice Anisotropy*. 2021. DOI: 10.48550/ARXIV.2107.08692. URL: https://arxiv.org/abs/2107.08692 (visited on 11/17/2024). Prepublished (cited on page 23).

[48] Aya Ishihara. "The IceCube Upgrade - Design and Science Goals." In: *Proceedings of Science* 358 (2019). DOI: 10.22323/1.358.1031 (cited on pages 23, 29, 30).

[49] Aya Ishihara and Ayumi Kiriki. *Calibration LEDs in the IceCube Upgrade D-Egg Modules*. Aug. 29, 2019. DOI: 10.48550/arXiv.1908.10780. URL: http://arxiv.org/abs/1908.10780 (visited on 01/30/2025). Pre-published (cited on pages 23, 30, 31).

[50] M. G. Aartsen et al. "The IceCube Neutrino Observatory: Instrumentation and Online Systems." In: *Journal of Instrumentation* 12.3 (2017). DOI: 10.1088/1748-0221/12/03/P03012 (cited on pages 24–27, 52, 61).

[51] Vedant Basu et al. "A Next-Generation Optical Sensor for IceCube-Gen2." In: (2021). DOI: 10.48550/ARXIV.2107.08837. (Visited on 11/26/2024) (cited on pages 29, 30, 33).

[52] T. Anderson et al. "Design and Performance of the Multi-PMT Optical Module for IceCube Upgrade." July 23, 2021 (cited on page 29).

[53] Colton Hill et al. *Performance of the D-Egg Optical Sensor for the IceCube Upgrade*. Aug. 11, 2021. DOI: 10.48550/arXiv.2108.05353. URL: http://arxiv.org/abs/2108.05353 (visited on 01/30/2025). Pre-published (cited on page 29).

[54] John Rack-Helleis, Anna Pollmann, and Martin Rongen. *The Wavelength-shifting Optical Module (WOM) for the IceCube Upgrade*. July 21, 2021. DOI: 10.48550/arXiv.2107.10194. URL: http://arxiv.org/abs/2107.10194 (visited on 01/30/2025). Pre-published (cited on page 29).

[55] Yoichiro Suzuki. "The Super-Kamiokande Experiment." In: *Eur. Phys. J. C* 79.4 (Apr. 2019), p. 298. DOI: 10.1140/epjc/s10052-019-6796-2. (Visited on 06/20/2025) (cited on page 30).

[56] Jianming Bian. *The NOvA Experiment: Overview and Status*. 2013. DOI: 10.48550/ARXIV.1309.7898. URL: https://arxiv.org/abs/1309.7898 (visited on 02/16/2025). Pre-published (cited on page 30).

[57] K. Abe et al. "The T2K Experiment." In: *Nuclear Instruments and Methods in Physics Research Section A: Accelerators, Spectrometers, Detectors and Associated Equipment* 659.1 (Dec. 2011), pp. 106–135. DOI: 10.1016/j.nima.2011.06.067. (Visited on 02/16/2025) (cited on page 30).

[58] Justin Evans. *The MINOS Experiment: Results and Prospects*. 2013. DOI: 10.48550/ARXIV.1307.0721. URL: https://arxiv.org/abs/1307.0721 (visited on 02/16/2025). Pre-published (cited on page 30).

[59] M. Rongen and D. Chirkin. "Advances in IceCube Ice Modelling & What to Expect from the Upgrade." In: *J. Inst.* 16.09 (Sept. 1, 2021), p. C09014. DOI: 10.1088/1748-0221/16/09/C09014. (Visited on 11/17/2024) (cited on page 31).

[60] Hamamatsu. *Photomultiplier Tubes: Basics and Applications*. 2017. (Visited on 02/18/2025) (cited on pages 35, 37, 38, 103).

[61] S. O. Flyckt and Carole Marmonier. *Photomultiplier Tubes: Principles and Applications*. 2nd ed. Photonis, 2002. (Visited on 02/18/2025) (cited on page 35).

[62] Photonis. *Photomultiplier Tube Basics*. 2002. (Visited on 02/18/2025) (cited on page 35).

[63] Heinrich Hertz. "Über Einen Einfluss Des Ultravioletten Lichtes Auf Die Elektrische Entladung." In: *Annalen der Physik* 267.8 (1887), pp. 983–1000. DOI: 10.1002/andp.18872670827 (cited on page 36).

[64] A. Einstein. "Über Einen Die Erzeugung Und Verwandlung Des Lichtes Betreffenden Heuristischen Gesichtspunkt." In: *Annalen der Physik* 322.6 (1905), pp. 132–148. DOI: 10.1002/andp.19053220607 (cited on page 36).

[65] L. Austin and H. Starke. "Ueber Die Reflexion Der Kathodenstrahlen Und Eine Damit Verbundene Neue Erscheinung Secundärer Emission." In: *Annalen der Physik* 314.10 (Jan. 14, 1902), pp. 271–292. DOI: 10.1002/andp.19023141003 (cited on page 38).

[66] J. Reubelt. *PMT Characterization: Hamamatsu R12199 Tests*. IceCube Internal Document, 2018 (cited on page 40).

[67] Owen W. Richardson. *Thermionic Phenomena and the Laws Which Govern Them*. Stokholm, Dec. 12, 1929 (cited on page 45).

[68] P B Coates. "Thermionic Emission from Photocathodes." In: *Journal of Physics D: Applied Physics* 5.8 (Aug. 1, 1972), p. 319. DOI: 10.1088/0022-3727/5/8/319 (cited on page 45).

[69] M. G. Aartsen et al. "First Observation of PeV-Energy Neutrinos with IceCube." In: *Physical Review Letters* 111.2 (July 8, 2013), p. 021103. DOI: 10.1103/PhysRevLett.111.021103 (cited on page 51).

[70] M. G. Aartsen et al. "Measurement of Atmospheric Neutrino Oscillations at 6–56 GeV with IceCube DeepCore." In: *Physical Review Letters* 120.7 (Feb. 13, 2018), p. 071801. DOI: 10.1103/PhysRevLett.120.071801 (cited on page 51).

[71] Ronald Bruijn. "The KM3NeT Digital Optical Module and Detection Unit." In: *EPJ Web of Conferences* 207 (May 10, 2019), p. 06002. DOI: 10.1051/epjconf/201920706002 (cited on page 52).

[72] Lew Classen. "The mDOM - a Multi-PMT Digital Optical Module for the IceCube-Gen2 Neutrino Telescope." Friedrich-Alexander-Universität Erlangen-Nürnberg (FAU), 2017. 271 pp. (cited on pages 52, 53).

[73] Alexander Kappes. *mDOM PMT Tender Specifications*. IceCube Internal Document, 2019 (cited on page 56).

[74] Lasse Yannik Halve. "Validation of Optical Sensors for the mDOM of the IceCube Upgrade." RWTH Aachen University, 2024, pages x, 205 Seiten : Illustrationen. DOI: 10.18154/RWTH-2024-05501. (Visited on 02/25/2025) (cited on pages 61, 141).

[75] P. Buford Price et al. "Temperature Profile for Glacial Ice at the South Pole: Implications for Life in a Nearby Subglacial Lake." In: *Proceedings of the National Academy of Sciences* 99.12 (June 11, 2002), pp. 7844–7847. DOI: 10.1073/pnas.082238999 (cited on page 61).

[76] M. Rongen and M. Schaufel. "Design and Evaluation of a Versatile Picosecond Light Pulser." In: *Journal of Instrumentation* 13.06 (June 5, 2018), P06002–P06002. DOI: 10.1088/1748-0221/13/06/P06002 (cited on pages 63, 72, 74).

[77] Jim Williams. "Practical Circuitry for Measurement and Control Problems." In: *Linear Technology* Application Note.61 (1994) (cited on page 72).

[78] *XSL-375-3E Data Sheet*. Roithner Lasertechnik GmbH, 2014. URL: https://roithner-laser.com/datasheets/led_div/xsl-375-3e.pdf (visited on 03/05/2025) (cited on page 73).

[79] *B3B-443-B505 Data Sheet*. Roithner Lasertechnik GmbH, 2010. URL: https://roithner-laser.com/datasheets/led_div/b3b-443-b505.pdf (visited on 03/05/2025) (cited on page 73).

[80] *LEGO MINDSTORMS EV3*. LEGO System A/S, 2013. URL: https://education.lego.com/en-us/products/lego-mindstorms-education-ev3-core-set/5003400/ (visited on 03/05/2025) (cited on page 74).

[81] *Ev3dev - Debian Linux for LEGO MINDSTORMS EV3*. ev3dev.org, 2025. URL: https://www.ev3dev.org/ (cited on page 74).

[82] Nikhita Khera and Felix Henningsen. *POCAM in the IceCube Upgrade*. 2021. DOI: 10.48550/ARXIV.2108.05298. URL: https://arxiv.org/abs/2108.05298 (visited on 11/16/2024). Pre-published (cited on page 75).

[83] IceCube et al. "Design and Performance of the mDOM Mainboard for the IceCube Upgrade." In: *Proceedings of 38th International Cosmic Ray Conference — PoS(ICRC2023)*. 38th International Cosmic Ray Conference. Nagoya, Japan: Sissa Medialab, July 25, 2023, p. 967. DOI: 10.22323/1.444.0967. (Visited on 03/05/2025) (cited on page 76).

[84] K. H. Sulanke. *mDOM Mainboard Design Status and Notes (DSN)*. IceCube Internal Document, 2023 (cited on pages 76, 77).

[85] K. H. Sulanke. *Mini Fieldhub Design Status and Notes (DSN)*. IceCube Internal Document, 2023 (cited on page 77).

[86] *American National Standard for VME64*. ANSI/VITA, 1995. URL: https://www.ge.infn.it/~musico/Vme/Vme64.pdf (cited on page 77).

[87] LeCroy. *429A QUAD LOGIC FAN-IN/FAN-OUT*. LeCroy Corporation, 1995. URL: https://www.lnf.infn.it/esperimenti/finuda/Trigger/Datasheet/LeCroy%20429A%20Logic%20Fan-In-Out.htm (visited on 03/05/2025) (cited on page 79).

[88] otom Group GmbH. *Kabelfühler - Durchmesser 4mm (KS-PT100A-4L-5.0-430)*. otom Group GmbH, 2025. URL: https://www.sensorshop24.de/productpdf/download/file/id/1746/name/Kabelf%25C3%25BChler_-_Durchmesser_%25C3%25984mm.pdf (visited on 03/05/2025) (cited on page 80).

[89] Lady ada. *Adafruit MAX31865 RTD PT100 or PT1000 Amplifier*. Adafruit Industries, 2024. URL: https://cdn-learn.adafruit.com/downloads/pdf/adafruit-max31865-rtd-pt100-amplifier.pdf (visited on 03/05/2025) (cited on page 80).

[90] Kattni Rembor. *Adafruit AHT20 Temperature & Humidity Sensor*. Adafruit Industries, 2024. URL: https://cdn-learn.adafruit.com/downloads/pdf/adafruit-aht20.pdf (visited on 03/05/2025) (cited on page 80).

[91] Arduino. *Arduino Uno R3 Data Sheet*. Arduino S.r.L., 2025. URL: https://docs.arduino.cc/resources/datasheets/A000066-datasheet.pdf (visited on 03/05/2025) (cited on page 80).

[92] Lasse Halve. personal communication. Mar. 28, 2022 (cited on page 85).

[93] Marco Scheiter. "Messungen Der Relativen Photodetektionseffizienz von Photomultipliern Für Das IceCube Upgrade Projekt." Aachen: RWTH Aachen, 2020 (cited on page 89).

[94] Maja Freienhofer. "Vermessen Der Referenz-PMTs Und Bestimmen Der Lichtverteilung Im Teststand Für Die mDOM-PMTs Des IceCube-Upgrades in Dortmund." Dortmund: TU Dortmund University, 2022 (cited on page 90).

[95] B.K Lubsandorzhiev et al. "Studies of Prepulses and Late Pulses in the 8 Electron Tubes Series of Photomultipliers." In: *Nuclear Instruments and Methods in Physics Research Section A: Accelerators, Spectrometers, Detectors and Associated Equipment* 442.1–3 (Mar. 2000), pp. 452–458. DOI: 10.1016/S0168-9002(99)01272-3 (cited on page 114).

[96] Paweł Malecki. "Pacific Ocean Neutrino Experiment." In: *Universe* 10.2 (Jan. 23, 2024), p. 53. DOI: 10.3390/universe10020053. (Visited on 02/03/2025) (cited on page 141).

[97] Philipp Behrens. "Studies of Correlated Noise Events in the PMT Testing Facility for the mDOMs of the IceCube Upgrade." RWTH Aachen, 2022 (cited on page 143).

List of Acronyms

`pmt_taco` **PMT** **T**esting **A**nd **Co**ntrol
ADC analog-to-digital converter
AFE analog front-end
AGN active galactic nucleus
CE collection efficiency
CMB cosmic microwave background
CR cosmic ray
D-Egg dual Optical Sensors in Ellipsoid Glassdome
DAQ Data Acquisition
DOM Digital Optical Module
DSA diffuse shock acceleration
EM electromagnetic interference
FADC flash analog-to-digital converter
FAT Final Acceptance Testing
FPGA field-programmable gate array
GZK Greisen-Zatsepin-Kuzmin
HLC Hard Local Coincidence
HV high voltage
I3MS IceCube Messaging System
ICL IceCube Laboratory
ICRC International Cosmic Ray Conference
ID identification
JADE Java Archival and Data Exchange
LOM Long Optical Module
mDOM Multi-PMT Digital Optical Module
MIS4 marine isotope stage 4
MSW Mikheyev–Smirnov–Wolfenstein
P-ONE Pacific Ocean Neutrino Experiment
PA12 nylon 12
PDE photo detection efficiency
PE photoelectron
PMNS Pontecorvo–Maki–Nakagawa–Sakata
PMT photomultiplier tube

PnF Processing and Filtering
POCAM Precision Optical Calibration Module
PTFE Polytetrafluorethylen
PVR peak-to-valley ratio
QE quantum efficiency
R&D research and development
RAPCal Reciprocal Active Pulsing Calibration
RK Rose+Krieger
SLC Soft Local Coincidence
SPE Single Photoelectron
SPS South Pole System
SSC Synchrotron Self-Compton
TDRS Tracking and Data Relay Satellites
TTS transit time spread
UID unique ID
UTC Coordinated Universal Time
VCSEL vertical-cavity surface-emitting laser
VLT Very Large Telescope
VME Versa Module Eurocard
WOM Wavelength-Shifting Optical Module